

JOHANNES REIFF

Advances in Transition-State Theory and Applications to Driven Systems

Von der Fakultät Mathematik und Physik der Universität Stuttgart zur
Erlangung der Würde eines Doktors der Naturwissenschaften
(Dr. rer. nat.) genehmigte Abhandlung

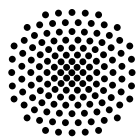
Vorgelegt von Johannes Reiff aus Berlin

Hauptbericht **Prof. Dr. Jörg Main**
Institut für Theoretische Physik I
Universität Stuttgart

Mitbericht **Prof. Dr. Udo Seifert**
Institut für Theoretische Physik II
Universität Stuttgart

Prüfungsvorsitz **Prof. Dr. Ronny Nawrodt**
5. Physikalisches Institut
Universität Stuttgart

Tag der mündlichen Prüfung: 19. April 2023



Universität Stuttgart
Institut für Theoretische Physik I

2023

Johannes Reiff

Advances in Transition-State Theory and Applications to Driven Systems

Von der Fakultät Mathematik und Physik der Universität Stuttgart zur
Erlangung der Würde eines Doktors der Naturwissenschaften (Dr. rer. nat.)
genehmigte Abhandlung, 2023

Hauptbericht: Prof. Dr. Jörg Main

Mitbericht: Prof. Dr. Udo Seifert

Prüfungsvorsitz: Prof. Dr. Ronny Nawrodt

Tag der Abgabe: 2. Februar 2023

Tag der mündlichen Prüfung: 19. April 2023

Universität Stuttgart

Institut für Theoretische Physik I

Pfaffenwaldring 57

70569 Stuttgart

ABSTRACT

Chemical reactions are often described via the motion of an effective particle on a Born–Oppenheimer potential-energy surface. In this picture, trajectories typically turn from reactants to products when crossing a rank-1 saddle on the energy surface. The geometric properties of this bottleneck and its associated [transition state](#) play an important role for the dynamics of activated trajectories, i. e., trajectories that cross near threshold energy. [Transition-state theory](#) is a well-established framework that can be used to analyze the dynamics near the rank-1 saddle. It focuses particularly on the determination of rates via the flux through the [transition state](#), which has been investigated since the early 20th century and continues to be of relevance today.

In this work, we focus mainly on the geometrical formulation of [transition-state theory](#). This description formalizes the distinction between reactants and products by defining a [dividing surface](#) in phase space based on the hyperbolic dynamics near the saddle. Specifically, a formally exact [dividing surface](#) can be constructed by anchoring it to the saddle’s [normally hyperbolic invariant manifold](#). This invariant manifold and its associated stable and unstable manifolds determine the fate of activated trajectories, and so they are of great interest in the field of chemical reaction kinetics.

This dissertation is concerned with the development and application of numerical methods in the framework of [transition-state theory](#). We address the emergent dynamics of time-dependent chemical and physical model systems under periodic external driving of the transition barrier. In particular, we focus on the structure of the [normally hyperbolic invariant manifold](#), its associated decay rates, and whether these rates can somehow be connected to Kramers’s notion of escape rates. The range of models we investigate includes two simple but prototypical test cases with one and two driven saddles as well as the $\text{LiCN} \rightarrow \text{LiNC}$ isomerization reaction. We further show how [transition-state theory](#) can be applied to celestial-mechanics, where it can be used to optimize orbits of satellites with respect to fuel consumption while accounting for time-dependent perturbations from the moon. The systems are mostly treated deterministically, but we also make use of the (generalized) [Langevin equation](#) when examining the absolute LiCN isomerization rates. In this context, we ask the fundamental question of how to define a rate, which is especially important at high temperatures.

INHALTSANGABE IN DEUTSCHER SPRACHE

Chemische Reaktionen werden häufig durch die Bewegung eines effektiven Teilchens auf einer Born-Oppenheimer-Potentialfläche beschrieben. Der Übergang von Reaktant zu Produkt ist dabei typischerweise mit der Überquerung eines Rang-1-Sattels auf der Potentialfläche verbunden. Die geometrischen Eigenschaften dieses Engpasses und des zugehörigen **Übergangszustands** spielen eine wichtige Rolle für die Dynamik aktivierter Trajektorien. Diese Trajektorien überqueren den Sattel mit nur wenig mehr als der Aktivierungsenergie und halten sich daher vergleichsweise lang in dessen Nähe auf. Für die Analyse der Dynamik nahe dem Rang-1-Sattel hat sich die **Theorie des Übergangszustands** (engl. *transition state theory*) bewährt. Sie beschäftigt sich insbesondere mit der Bestimmung der Raten über den Fluss durch den **Übergangszustand**. Die Forschung hierzu begann bereits im späten 19. Jahrhundert und ist auch heute noch von Bedeutung.

Im Zuge dieser Arbeit beschäftigen wir uns primär mit der geometrischen Formulierung der Theorie. Diese Variante formalisiert die Unterscheidung zwischen Reaktanten und Produkten durch die Definition einer **Trennfläche** im Phasenraum basierend auf der hyperbolischen Dynamik des Systems. Durch Anheften an der sogenannten **normal-hyperbolisch invarianten Mannigfaltigkeit** des Sattels kann eine formal exakte **Trennfläche** konstruiert werden. Die invariante Mannigfaltigkeit bestimmt zusammen mit ihren stabilen und instabilen Mannigfaltigkeiten maßgeblich den Verlauf aktivierter Trajektorien, und ist daher von großem Interesse für die Reaktionskinetik.

Die vorliegende Dissertation widmet sich der Entwicklung und Anwendung numerischer Methoden im Rahmen der **Theorie des Übergangszustands**. Wir befassen uns mit der emergenten Dynamik von zeitabhängigen chemischen und physikalischen Modellsystemen unter dem Einfluss von externem periodischen Treiben. Im Besonderen konzentrieren wir uns dabei auf die Struktur der **normal-hyperbolisch invarianten Mannigfaltigkeit**, die mit ihr verbundenen Zerfallsraten sowie der Frage, ob diese Raten mit dem von Kramers geprägten Begriff der Fluchraten verbunden werden können. Die Palette der untersuchten Modelle umfasst dabei zwei einfache, aber prototypische Testsysteme mit ein respektive zwei getriebenen Sätteln sowie die Isomerisierungsreaktion $\text{LiCN} \rightarrow \text{LiNC}$. Wir zeigen außerdem, wie die Theorie auf die Himmelsmechanik angewandt werden kann. Hier lassen

sich Umlaufbahnen von Satelliten im Hinblick auf den Treibstoffverbrauch optimieren, während vom Mond verursachte zeitabhängige Störungen berücksichtigt werden. Die Systeme werden dabei zumeist deterministisch behandelt. Um die absoluten Isomerisierungsraten von LiCN zu bestimmen, machen wir jedoch auch von der (verallgemeinerten) [Langevin-Gleichung](#) Gebrauch. In diesem Kontext stellen wir uns die fundamentale Frage nach der Definition einer Rate, die insbesondere bei hohen Temperaturen eine große Rolle spielt.

CONTENTS

ABSTRACT	III
INHALTSANGABE IN DEUTSCHER SPRACHE	V
1 INTRODUCTION	1
1-1 Outline	4
1-2 List of author's publications	5
<hr/> THEORY & METHODS <hr/>	
2 TRANSITION-STATE THEORY	9
2-1 Geometrical formulation	10
2-2 Langevin equation	14
2-3 Rates	16
2-4 Floquet theory	19
3 NUMERICAL METHODS	21
3-1 Integrating ordinary differential equations	21
3-2 Revealing the phase-space geometry	23
3-3 Binary-search methods	27
3-4 Dynamics on the NHIM	30
3-5 Decay rates	31
3-6 Integrating the Langevin equation	39
3-7 Mean first-passage times	40
<hr/> APPLICATIONS & PERSPECTIVE <hr/>	
4 BIFURCATIONS IN A TWO-DIMENSIONAL MODEL SYSTEM	43
4-1 Two-dimensional model system	43
4-2 Overview of phenomena resulting from the driving	44
4-3 Decay rate enhancement	50
4-4 Reaction geometry	55
4-5 Reaction probability	58
4-6 Conclusion and outlook	59

5	SELF-SIMILARITY IN A DRIVEN TWO-SADDLE SYSTEM	65
5-1	Two-saddle model system	66
5-2	Fractal phase space	68
5-3	Geometric cross	71
5-4	Decay rates	78
5-5	Conclusion and outlook	80
6	THE MOON'S INFLUENCE ON STABILITY NEAR SUN-EARTH L_2	83
6-1	Solar system model	84
6-2	Reframing TST in terms of celestial mechanics	89
6-3	Dynamics on the NHIM and the L_2 orbit	90
6-4	Stability of satellites	93
6-5	Conclusion and outlook	95
7	KRAMERS RATES OF LITHIUM-CYANIDE ISOMERIZATION	97
7-1	Lithium-cyanide model	98
7-2	Summary of previous results	101
7-3	Kramers turnover	105
7-4	Temperature dependence	107
7-5	Conclusion and outlook	113
8	REVIEW AND FUTURE PERSPECTIVE	115
8-1	Decay rates in driven systems	115
8-2	Absolute reaction rates in thermal systems	116

APPENDICES

A	FLAWS OF DISCONTINUOUS DIVIDING SURFACES	121
B	LITHIUM-CYANIDE POTENTIAL-ENERGY SURFACE	123
C	APPROXIMATIVE REACTION-RATE FORMULAS	127
C-1	Polanyi–Wigner rate	127
C-2	Eyring–Polanyi rate	128
D	SOFTWARE	129
D-1	RODEO	129
D-2	mfptlib	129
D-3	Lithium-cyanide isomerization potential	130
	SYMBOLS AND NOTATION	131

GLOSSARY	135
BIBLIOGRAPHY	139
ZUSAMMENFASSUNG IN DEUTSCHER SPRACHE	161
Teil I: Theorie & Methoden	162
Teil II: Anwendungen & Ausblick	168
DANKSAGUNG	175
CURRICULUM VITAE	179

INTRODUCTION

Various phenomena in physics and chemistry can be described by the dynamics of a system on a potential-energy surface. Local minima on such surfaces are commonly associated with discrete states like spin up and spin down in spintronics, or reactant and product in a chemical reaction. To transition from one state to the other, the system must overcome the barrier in between. While doing so, the minimum-energy path usually passes over a rank-1 saddle point.

One of the central aims in the field of physical chemistry is the accurate determination of a chemical reaction's rate. Pioneered, amongst others, by Waage and Guldberg in 1864, [12–15] and later by van 't Hoff in 1884 [16], the discipline of chemical kinetics remains highly relevant even after one and a half centuries. The determination of rates is not just an abstract problem of academic (or basic) concern [17–20] but also a practical problem with many potential applications in complex reactions [21–25]. The possibility of optimizing reaction rates by external driving could perhaps take these applications further in offering improvements to throughput and efficiency.

Transition-state theory (TST) [19, 20, 26–47] is well established for the computation of rates in systems with a rank-1 saddle. In these systems, two different states — viz., reactants and products — are classified and separated by an appropriately chosen *dividing surface* (DS). TST uses the flux through the DS to determine the rate of a chemical reaction or a similar process. This rate is only formally exact if the DS is recrossing-free, meaning that trajectories crossing the DS from the reactant side do not return before reaching the product well. It has been applied to a broad range of problems in a broad range of fields including atomic physics [48], solid state physics [10, 11, 49–52], cluster formation [53, 54], diffusion dynamics [55, 56], cosmology [57], celestial mechanics [6, 58–60], and Bose–Einstein condensates [61–65].

In this work, we focus on a geometrical formulation of TST. In a system with d *degrees of freedom* (DoFs), the DS embedded in phase space has dimension $2d - 1$. It is attached to a $(2d - 2)$ -dimensional *normally hyperbolic invariant manifold* (NHIM) [66–71], which has the property that every particle on the NHIM will never leave this manifold when propagated forward or backward in time. The importance of the geometric structure of the NHIM on dynamical systems without driving has been understood for some time [69] and continues to receive attention [72–74]. For example, the bifurcation of the periodic-orbit DS in two DoFs upon varying the total

energy was revealed by Pechukas, Pollak, and Child [75–77]. Li et al. [78] extended their work to three DoFs, showing that the bath modes' invariants of motion can be used to control the bifurcation of the NHIM. In general, bifurcations of the NHIM give rise to its breakdown leading to switching between the dominant reaction coordinate as a function of the system's total energy [79, 80], and further leads to the possibility of experimental control [81].

An alternative ansatz for experimental control is the implementation of a time-dependent driving, e. g., via oscillating external fields [8, 82–87]. Here, the situation becomes more challenging because the NHIM and, hence, the DS themselves become time-dependent. They depend nontrivially on the moving saddle of the potential [30, 31], but they can nevertheless be obtained by time-dependent perturbation theory [88], through a minimization procedure based on a Lagrangian descriptor [1, 89–91], and other approaches [1, 87, 92]. Furthermore, machine learning techniques have been leveraged recently to construct representations of the time-dependent NHIM and its dynamical properties [93–99].

In this work, we address the emergent dynamics of chemical and physical model systems under time-periodic external driving of the transition barrier. In periodically driven systems with only one degree of freedom, the NHIM reduces to a point that oscillates with the same period as the driving potential [30, 31, 100–107]. This periodic orbit is the one-dimensional *transition state* (TS) trajectory. In systems with two or more degrees of freedom, the structure of the NHIM itself and the dynamics of trajectories on it become nontrivial [2, 3, 5, 6, 108]. These systems commonly show torus structures with elliptic and hyperbolic fixed points that can bifurcate as a function of the driving parameters.

Such phenomena raise the fundamental questions [5]: Does the structure *on* the NHIM also have an influence on the dynamics *off* the NHIM? And can we use our knowledge of the NHIM's properties to predict the behavior of trajectories starting in the reactant or product basin? After all, slowly reacting trajectories cross the DS close to the NHIM and spend a relatively long time in its vicinity. This issue is closely related to the important distinction between decay rates [2, 4, 6], which assess the stability of trajectories near the NHIM, and absolute reaction rates [109–111], where the full path from reactant to product well is considered. The challenge arises whether these can be linked in a meaningful way.

We pursue these questions by investigating chemically inspired model systems. The challenges in a system with multiple DoFs lie in the inner structure of the NHIM. Metrics like the decay rate can unveil this structure. Hence, they are a useful tool to investigate whether the reaction geometry

can be influenced or even controlled via external driving. The case of only one DoF but multiple saddles, on the other hand, gives rise to a different type of complexity [4]. Here, the NHIM still only consists of individual points as discussed above; this time, however, time-dependent driving can cause the NHIM to develop into a fractal set of disjoint TS trajectories connecting the barriers. This fractal structure makes it very challenging to determine a proper DS. To do so, one has to ask whether a dominant TS trajectory can still be identified in a specific scenario.

Besides these fundamental questions, this thesis also focuses on concrete applications of TST to systems inspired by the real world. One such system is the Sun–Earth libration point L_2 . Here, the effective potential — generated by the gravitational forces of Sun and Earth — exhibits a rank-1 saddle in a rotating frame. This potential is perturbed by the Moon, which serves as the external driving [6, 60]. The NHIM at L_2 is highly relevant for real-world space missions. It allows a spacecraft to stay far enough from Earth to minimize electromagnetic interferences but close enough for easy communication. In addition, a carefully chosen orbit keeps the craft out of Earth’s shadow, thereby preventing constant heating and cooling of its instruments. It has therefore been the target of numerous scientific satellite missions [112–115] in recent years. These missions may have a number of different requirements. But all of them have in common that the mission duration is ultimately limited by the amount of fuel available for course corrections. TST can help to reduce the fuel consumption by providing measures for the stability of orbits at L_2 , i. e., decay rates.

While the stability of the TS as revealed by decay rates can also be investigated for real chemical molecules [87, 116], the results are much harder to observe and utilize in practice. Our second real-world example instead addresses the absolute reaction rate of the lithium-cyanide (LiCN) isomerization reaction. This reaction has already been examined by multiple groups and, thus, a potential-energy surface [117] is readily available. Various rate methods have been tested and compared previously [7, 116, 118–120] based on this surface, but they left some questions unanswered. Here, we revisit the *mean first-passage time* (MFPT) calculations published in References [7, 116]. In particular, we focus on the partially conflicting results between MFPT rates on the one hand, and *Pollak–Grabert–Hänggi* (PGH) and *all-atom molecular dynamics* (AAMD) rates from References [7, 116, 118, 119] on the other hand. The new MFPT results are in better agreement with PGH and AAMD; they also shed new light upon the influence of solvent memory on the lithium-cyanide isomerization reaction.

A substantial part of the earlier analysis on LiCN rates focused on high temperatures, i. e., the regime where the average thermal energy is larger

than the barrier height. This raises questions about the definition of a reaction rate, namely: Do trajectories have to only reach the product well to constitute a reaction? Or do they also have to get captured to prevent correlations between individual reactions? The way in which ballistic trajectories are treated can have a significant influence on the rate. One needs to be especially careful when comparing different methods as they may each make different assumptions. After all, rates can only be compared in a meaningful way when everyone agrees on what they deem a *rate*.

1-1 Outline

This thesis is organized as follows:

In part one we present the theoretical and methodical foundations of this work. We start off by introducing the geometrical formulation of TST in Section 2-1 along with a brief overview of Floquet theory in Section 2-4. Kramers's notion of escape rates and the important distinction between reaction and decay rates are subsequently discussed in Section 2-3. Proper reaction rates usually imply solvent-induced noise and friction; the Langevin theory, which we use to implement such effects, is summarized in Section 2-2. Chapter 3 then presents the methods that are necessary to reveal the geometric structure described in Section 2-1. This includes the integration of ordinary differential equations in Section 3-1, the concepts of Lagrangian descriptors and reactive regions in Section 3-2, and the *binary-contraction method* (BCM) in Section 3-3. Based on this, Section 3-4 gives a short overview of typical structures in dynamical systems and how to reveal them using *Poincaré surfaces of section* (PSOSs). More information about the phase-space structure of the NHIM can be determined from decay rates, which is why we review three such methods in Section 3-5. The numerical methods we use to solve the stochastic differential equations resulting from the Langevin ansatz follow in Section 3-6. Finally, we show in Section 3-7 how Kramers's escape rates can be calculated using MFPTs.

The second part of this thesis is dedicated to selected examples of applications in prototypical and real-world models. First, we have a detailed look at a prototypical 2-DoF model in Chapter 4. We apply the theoretical and methodical framework developed in Chapters 2 and 3 and show how the structure on the NHIM can be connected to the dynamics happening far from the saddle. The challenges that arise in multi-saddle systems are then discussed in Chapter 5, where we illustrate the complicated fractal structure that can develop in seemingly simple systems. As demonstrated, a mostly recrossing-free DS can still be constructed using adapted variants of our methods. This discussion is continued in Appendix A.

Next, we turn to more realistic models. Chapter 6 applies TST methods to celestial mechanics as a concrete example of how decay rates can be useful in practice. Specifically, we showcase how the methods presented in Chapter 3 can be used to optimize the fuel consumption of satellites near the libration point L_2 . We conclude part two by investigating MFPT rates of the lithium-cyanide isomerization reaction in Chapter 7. We focus on the results that have previously been obtained in References [7, 116] and how we can improve on them. The new results are compared with rates determined from PGH theory and via AAMD simulations, and the concept of rates at high temperatures is discussed. Supplementary information on the lithium-cyanide potential-energy surface and approximative reaction-rate formulas can be found in Appendices B and C, respectively.

Parts of the software developed for this thesis has been made open source. Details hereof are given in Appendix D.

1-2 List of author's publications

Parts of this thesis are based on the following publications:

- [1] M. Feldmaier, P. Schraft, R. Bardakcioglu, J. Reiff, M. Lober, M. Tschöpe, A. Junginger, J. Main, T. Bartsch, and R. Hernandez, “Invariant manifolds and rate constants in driven chemical reactions,” *J. Phys. Chem. B* **123**, 2070–2086 (2019).
- [2] M. Feldmaier, R. Bardakcioglu, J. Reiff, J. Main, and R. Hernandez, “Phase-space resolved rates in driven multidimensional chemical reactions,” *J. Chem. Phys.* **151**, 244108 (2019).
- [3] M. Kuchelmeister, J. Reiff, J. Main, and R. Hernandez, “Dynamics and bifurcations on the normally hyperbolic invariant manifold of a periodically driven system with rank-1 saddle,” *Regul. Chaotic Dyn.* **25**, 496–507 (2020).
- [4] J. Reiff, M. Feldmaier, J. Main, and R. Hernandez, “Dynamics and decay rates of a time-dependent two-saddle system,” *Phys. Rev. E* **103**, 022121 (2021).
- [5] J. Reiff, R. Bardakcioglu, M. Feldmaier, J. Main, and R. Hernandez, “Controlling reaction dynamics in chemical model systems through external driving,” *Physica D* **427**, 133013 (2021).
- [6] J. Reiff, J. Zatsch, J. Main, and R. Hernandez, “On the stability of satellites at unstable libration points of sun–planet–moon systems,” *Commun. Nonlinear Sci. Numer. Simul.* **104**, 106053 (2022).

- [7] M. M. Schlee, J. Reiff, P. L. García-Müller, R. M. Benito, F. Borondo, J. Main, and R. Hernandez, “Mean first-passage times for solvated LiCN isomerization at intermediate to high temperatures,” *J. Chem. Phys.* **156**, 034103 (2022).

Work related to this thesis has been published by the author in:

- [8] M. Feldmaier, J. Reiff, R. M. Benito, F. Borondo, J. Main, and R. Hernandez, “Influence of external driving on decays in the geometry of the LiCN isomerization,” *J. Chem. Phys.* **153**, 084115 (2020).
- [9] R. Bardakcioglu, J. Reiff, M. Feldmaier, J. Main, and R. Hernandez, “Thermal decay rates of an activated complex in a driven model chemical reaction,” *Phys. Rev. E* **102**, 062204 (2020).
- [10] J. Mögerle, R. Schuldt, J. Reiff, J. Main, and R. Hernandez, “Transition state dynamics of a driven magnetic free layer,” *Commun. Nonlinear Sci. Numer. Simul.* **105**, 106054 (2022).
- [11] M. Maihöfer, J. Reiff, J. Main, and R. Hernandez, “Transition state theory characterizes thin film macrospin dynamics driven by an oscillatory magnetic field: inertial effects,” *Commun. Nonlinear Sci. Numer. Simul.* **115**, 106764 (2022).

Part I

THEORY & METHODS

Transition-state theory has a long history in the field of chemical reaction kinetics, from its roots in the early 20th century to the modern geometrical formulations developed in more recent years. In this first part, we summarize the necessary theoretical background, review existing methods, and present new developments while staying mostly system-agnostic.

TRANSITION-STATE THEORY

Parts of this chapter have previously been published by the author in References [3, 4, 6].

A pair of fundamental assumptions in the original construction of *transition-state theory* (TST) [19, 20, 26–47] is that chemical reaction kinetics can be modeled by nuclear motion on a Born–Oppenheimer surface [121], and that said motion can be described by classical mechanics. In this framework, the system can be represented as an effective particle in a d -dimensional coordinate space. Its evolution is a trajectory on the potential-energy surface connecting reactant and product regions or valleys. In a typical scenario, there exists a *rank-1 saddle* between these regions, i. e., a critical point where exactly one direction is unstable, and all others are stable. The unstable direction locally identifies the *reaction coordinate* x [122, 123], which indicates the progress of the reaction. The $d - 1$ stable directions are referred to as the *orthogonal modes* y .

The saddle is associated with a *dividing surface* (DS) that formally separates reactant and product states by dividing the phase space into two parts. Located on the DS is the *transition state* (TS) [19, 26, 35, 43] — an unstable set of configurations that are neither reactants nor products. All reactive trajectory in the system have to cross the DS and, therefore, pass through the TS. In thermal systems with thermal energies $k_{\text{B}}T$ well below the barrier height, trajectories can only cross once they have been activated by the bath. Hence, the TS is also known as the *activated complex*. The umbrella term TST commonly refers to all theories that make use of this concept, especially when they concern themselves with the calculation of rates (cf. Section 2-3). Classical TST rates are calculated via the directional flux through the DS weighted by the (reactant) population [124]. This connection, however, is exact only if the DS is recrossing-free. Thus, the concept of recrossing-free DSs is very important for TST in general and the determination of rates in particular.

A DS is *locally recrossing-free* [73, 78, 125, 126] if no particle pierces it more than once before leaving some pre-determined interaction region around the saddle. In this case, any rates as determined by the DS are locally exact. We refer to a DS as being *globally exact* or recrossing-free if the above is true independent of the choice of the interaction region — as long as said region does not overlap with the stable reactant or product regions [1, 4].

Using this definition avoids inherent recrossings caused by reflections in closed reactant or product basins [127]. Global recrossings, though, may still occur if closed basins are excluded. Nonlinearities in the potential or fictitious forces like the Coriolis force, for example, can lead a trajectory to turn around after leaving the local interaction region, causing the DS to be crossed again. This distinction between locally and globally recrossing-free DSs is especially important when a system contains multiple saddles. Here, every saddle can potentially be associated with its own locally recrossing-free DS. Yet, none of these DSs might be globally recrossing-free if the dynamics over all barriers is considered. In this work, we only address transitions over barriers in series, and we do not address the parallel case in which a reaction could access more than one distant barrier. The scope of the definitions of globally exact and recrossing-free is therefore limited accordingly.

Determining a globally exact DS in a static 1-degree of freedom (DoF) system uncoupled from any other mode (e. g., without thermal bath) is almost trivial: If and only if a particle crosses the highest barrier, it has demonstrated to possess enough energy to react over all barriers. A globally recrossing-free DS can therefore be defined simply via the global maximum of the potential-energy surface. Additional layers of complexity arise when the system is multidimensional [128], driven by time-dependent potentials [34], or includes random noise from a thermal bath [9]. For now, we assume an isolated system, but we will come back to the issue of random noise in Section 2-3.

2-1 Geometrical formulation

While it is straightforward to define a recrossing-free DS for a static 1-DoF system, differentiating between reactants and products in higher-dimensional or driven systems requires a more sophisticated mathematical framework. One way of determining the DS is by means of variational TST [129]. This variant starts with an arbitrary guess for the DS and variationally optimizes this surface to minimize the flux through it. In contrast to traditional TST, the DS may detach from the actual saddle point in this process. As every crossing of the DS increases the rate, this approach makes sure to exclude as many recrossings as possible. Although this approach works well in many cases, it does not allow the construction of the DS from first principles. Indeed, with variational TST, one only knows *what* a DS looks like, not *why* it looks the way it does. For these reasons, we focus on a different approach in this thesis, namely, the geometrical formulation of TST.

We begin by considering the time-invariant case of a reactive 1-DoF system as sketched in Figure 2-1(a) (dark blue potential). An energy barrier

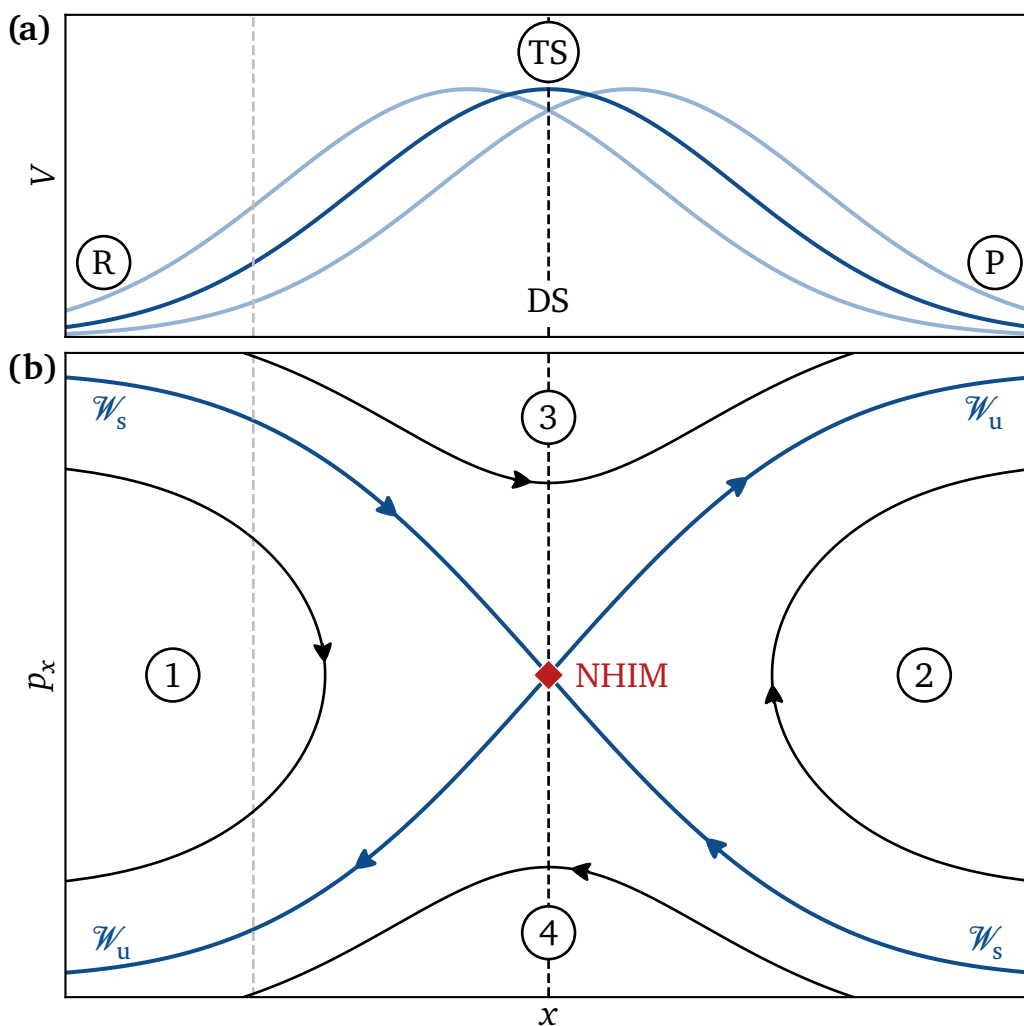


Figure 2-1: (a) Potential energy V as a function of reaction coordinate x for a generic example system. A DS associated with the energy barrier separates the reactant (R) from the product (P) state. The TS is located on the DS in between reactants and products. The addition of a time-dependent driving — indicated via faint versions of the potential at different points in time — leaves the general structure intact. In this case, however, the DS can detach from the top (see text). (b) The phase space of the model system shown in panel (a) for fixed time t_0 . The bulk of the phase space consists of four distinct, numbered regions associated with four qualitatively different classes of trajectories. One example trajectory each is shown as a solid black line with the forward time direction indicated via an arrow head. These regions are separated by the stable and unstable manifolds \mathcal{W}_s and \mathcal{W}_u , whose closures intersect in the NHIM. A DS cutting through regions 1 or 2 (gray dashed line) inevitably leads to recrossings. Higher-dimensional systems can show the same structure in an x - p_x section with fixed orthogonal modes y and p_y .

along the reaction coordinate x separates reactants (R) from products (P). Depending on the initial conditions and thus the energy, most particles can be classified as either

1. nonreactive reactants $R \rightarrow R$,
2. nonreactive products $P \rightarrow P$,
3. reactive reactants $R \rightarrow P$, or
4. reactive products $P \rightarrow R$.

This results in four distinct *reactive and nonreactive regions* in phase space, as indicated in Figure 2-1(b). In this simple example, all trajectories with a total energy above the barrier height are reactive (regions 3 and 4), whereas those below are nonreactive (regions 1 and 2).

The regions are separated by two kinds of critical trajectories. Their energy equals exactly the barrier height in time-invariant 1-DoF case. The first kind move towards the barrier top, progressively slowing down while converting kinetic into potential energy. They approach the barrier top without reaching it as $t \rightarrow +\infty$, and they leave the barrier's vicinity when propagating backward in time. Together, they form the *stable manifold* \mathcal{W}_s . The reverse, trajectories that reach the top for $t \rightarrow -\infty$, is called the *unstable manifold* \mathcal{W}_u . Both manifolds are shown as blue lines in Figure 2-1(b).

The closures of the manifolds \mathcal{W}_s and \mathcal{W}_u intersect in the so-called *normally hyperbolic invariant manifold* (NHIM) [66–70, 130] [red diamond in Figure 2-1(b)]. All trajectories started on this object are bound indefinitely to the saddle, both forward and backward in time. The NHIM thus combines the properties of \mathcal{W}_s and \mathcal{W}_u in this regard. Furthermore, it is this object that trajectories on \mathcal{W}_s and \mathcal{W}_u converge towards for $t \rightarrow +\infty$ and $-\infty$, respectively. Its name comes about as follows: Invariant manifolds are subspaces that cannot be entered or left. A state initialized *on* a NHIM may move within that NHIM but may never deviate from it (except for numerical errors). Similarly, states started *off* the NHIM may approach it via the stable manifold, but they may never reach it. Normally hyperbolic roughly means that the instability or decay away from (normal to) the NHIM dominates any possible instabilities within the NHIM itself [128]. Thus, the NHIM can be seen as the generalization of a hyperbolic fixed point to arbitrarily many DoFs (see below).

Looking at Figure 2-1(b), it becomes clear that all DSs cutting through regions 1 or 2 (gray dashed line) inevitably lead to recrossings. One can always find a trajectory with an energy just below the barrier height that enters the interaction region close to \mathcal{W}_s , pierces the DS twice, and leaves the interaction region close to \mathcal{W}_u . Any recrossing-free DSs — if they exist — must therefore be anchored at the NHIM. As shown in previous work [1, 91, 128,

131, 132], a (locally) recrossing-free DS can indeed often be constructed by attaching it to the NHIM [128, 131, 133]. In the simplest case, this is done by extending the NHIM in the p_x direction, as shown in Figure 2-1(b). The DS then divides the phase space into a reactant and a product domain. This ansatz is neither guaranteed to work globally, nor is it necessarily the only possible choice. In the case of Figure 2-1(b), for example, a slightly tilted surface could still divide the phase space without cutting through regions 1 or 2. Such a choice, however, entails increased complexity without providing additional benefits. Thus, we restrict ourselves to vertical DSs akin to Figure 2-1(b).

This general geometry of the phase space remains when driven systems are considered. In the special case of a time-invariant 1-DoF Hamiltonian, the NHIM is associated with the unstable trajectory for which a particle remains precariously fixed at the barrier maximum. We can extend this structure to time-dependently driven systems. Now, the NHIM will be time-dependent as well, but it detaches from the barrier's maximum. Its defining property — a set of unstable trajectories trapped indefinitely in the vicinity of the barrier — still applies, and it is still a good anchor for a DS. A similar behavior was mentioned for the variational TST ansatz, although this time, we have a formal framework that allows us to construct the DS from first principles.

The one-dimensional picture presented above can be extended to systems with arbitrarily many DoFs. The potential-energy landscape in a d -DoF system typically features a rank-1 saddle separating reactants from products. While there is still a single unstable reaction coordinate x , we now have $d - 1$ additional stable orthogonal modes y . As a consequence, the stable and unstable manifolds become hypersurfaces with codimension 1, i. e., they are $(2d - 1)$ -dimensional subspaces in $2d$ -dimensional phase space. Similarly, the NHIM becomes a codimension-2 manifold (dimension $2d - 2$) located at the intersection of the closures of \mathcal{W}_s and \mathcal{W}_u . If coordinates are chosen well, every x - p_x section of the phase space for a given position y and momentum p_y shows the cross-like structure shown in Figure 2-1(b). Numerical algorithms computing the NHIM in 1-DoF systems can, therefore, be used with minimal modifications to compute individual points on the NHIM in higher-dimensional systems. This can be done on demand for many applications. Alternatively, an interpolated representation of the NHIM can be constructed from precalculated points via classical or machine learning techniques [93–98].

Finally, a word of caution regarding the term *transition state*: It is commonly used in the chemical physics literature to describe the set of configurations in between the reactant and the product state, i. e., those located on the codimension-1 DS in phase space. Frequently, it is also used as a synonym to

the 0-dimensional saddle point. The more mathematical literature, however, uses this phrase to refer to the ensemble of states bound indefinitely to the saddle region, i. e., those located on the codimension-2 **NHIM**. This is effectively a generalization of the saddle-point definition. See footnote 6 of Reference [33] for a more detailed discussion. In this work, we adopt the former definition for the **TS** but use the phrase *TS trajectory* for trajectories bound to the **NHIM**.

2-2 Langevin equation

So far, we have assumed that the systems under investigation are completely isolated. In practice, however, this is rarely the case for chemical reactions. Instead, many of them take place in a solution or are connected to a thermal bath in some other way. Here, energy can transfer between the system and the bath, typically in the form of collisions with the solvent particles.

The *Langevin equation (LE)* [134–137] includes such solvent effects by way of coarse graining via a random-noise term ζ and a friction term $-\gamma\mathbf{p}$. The resulting stochastic differential equation reads

$$\begin{aligned} (2-1a) \quad & \dot{\mathbf{q}}(t) = \mathbf{M}^{-1} \mathbf{p}(t) \\ (2-1b) \quad & \text{and } \dot{\mathbf{p}}(t) = \mathbf{F}(\mathbf{q}(t), \mathbf{p}(t), t) - \gamma \mathbf{p}(t) + \zeta(t) \\ (2-1c) \quad & \text{with } \zeta(t) = \sqrt{2\gamma k_B T \mathbf{M}^{1/2}} \xi(t), \end{aligned}$$

where \mathbf{M} is the system's mass matrix (diagonal in this work), \mathbf{F} is the deterministic force (e. g., exerted by a potential or external driving), γ is the friction coefficient, and ξ is a temporally uncorrelated random variable with standard normal distribution (white noise). The components of the stochastic force ζ_j satisfy the *fluctuation-dissipation theorem* [134, 136]

$$(2-2) \quad \langle \zeta_j(t) \zeta_k(t') \rangle = 2\gamma k_B T M_{jk} \delta(t - t').$$

The *generalized Langevin equation (GLE)* [134, 136–138] extends the **LE**, allowing for memory effects to be taken into account (colored noise). This is achieved by introducing a *friction kernel* Γ that also considers previous momenta \mathbf{p} starting from initial time t_0 . The generalized version of Equation (2-1) then reads

$$\begin{aligned} (2-3a) \quad & \dot{\mathbf{q}}(t) = \mathbf{M}^{-1} \mathbf{p}(t) \\ (2-3b) \quad & \text{and } \dot{\mathbf{p}}(t) = \mathbf{F}(\mathbf{q}(t), \mathbf{p}(t), t) - \int_{t_0}^t dt' \Gamma(t - t') \mathbf{p}(t') + \zeta(t). \end{aligned}$$

for $t \geq t_0$, and the fluctuation-dissipation theorem (2-2) becomes

$$\langle \zeta_j(t) \zeta_k(t') \rangle = k_B T M_{jk} \Gamma(t - t'). \quad (2-4)$$

In this framework, the LE can be recovered with a Dirac-delta kernel

$$\Gamma(s) = 2\gamma \delta(s). \quad (2-5)$$

Other common choices are so-called Prony-series memory kernels [139, 140]. These are kernels of the form

$$\Gamma(s) = \sum_j \frac{\gamma_j}{\tau_j} \exp\left(-\frac{s}{\tau_j}\right), \quad (2-6)$$

where τ_j are the memory timescales of the series components. In this work, we focus on the simplest variant

$$\Gamma(s) = \frac{1}{\alpha} \exp\left(-\frac{s}{\alpha\gamma}\right) \quad (2-7)$$

with bath parameter α and memory timescale $\tau = \alpha\gamma$.

The statements above make use of the so-called *Stratonovich convention* [141, 142], as is common in this field. This is important to state so as to assign any meaning at all to certain types of equations. Specifically, the integral over the infinitesimally-wide Dirac delta distribution δ is undefined if one of the integral's limits coincides with the position of the peak as in

$$\int_a^b dx f(x) \delta(x - b). \quad (2-8)$$

Here, it is unclear whether the distribution is still fully within the limits, which would yield $f(b)$, or whether the integral stops just before. The latter interpretation, known as the *Itô convention*, would assign zero to the same integral. Stratonovich takes the middle ground by assigning the average $f(b)/2$, i. e., it treats half of the Dirac delta distribution to be within the integral limits. With this convention, the integral in the GLE (2-3b) evaluated for the LE friction kernel (2-5) yields

$$\int_{t_0}^t dt' 2\gamma \delta(t - t') \mathbf{p}(t') = \gamma \mathbf{p}(t), \quad (2-9)$$

which recovers the LE (2-1b). A more detailed discussion about Itô versus Stratonovich and their physical interpretation can be found in References [141, 142].

2-3 Rates

In the previous sections, we discussed which requirements we have for an ideal DS, how the geometric formulation of TST can help to meet these requirements, and how we can model the solvent for processes such as a chemical reaction. These concepts form the basis for the determination of rates. In this section, we present two different types of rates that both originate from the same fundamental consideration—the normalized flux through a DS—but lead to vastly different outcomes.

(a) Absolute reaction rates

The original goal of TST—and one that is still pursued today—is the accurate determination of *absolute reaction rates* [109]. There exists a plethora of rate theories [110, 111] that has been developed since the early 20th century. Two such examples, the Polanyi–Wigner equation [143] and the Eyring–Polanyi rate [26, 110, 144], are presented in Appendix C. Yet, many of these simpler rate equations are quite limited in their applicability.

An important step towards a more complete description happened in 1940 when Kramers [111] formulated a scenario that is now known as *Kramers's escape-rate problem*. Therein, he describes a simple 1-DoF system featuring a reactant well separated from a lower-energy product basin by a barrier. He considers an activated process, i. e., a process where the temperature $k_B T$ is small compared to the barrier height E^\ddagger . The flux of particles escaping the reactant well is therefore assumed to be small and stationary, and the rate is given by the flux divided by the reactant population. This is commonly known as a *flux-over-population rate*.

From these assumptions, Kramers was able to derive the expressions

$$(2-10) \quad k(\gamma) = \frac{\gamma E^\ddagger}{k_B T} \exp\left(-\frac{E^\ddagger}{k_B T}\right)$$

for reaction or escape rates in the low-friction regime and

$$(2-11) \quad k(\gamma) = \left[\sqrt{\left(\frac{\gamma}{2\omega^\ddagger}\right)^2 + 1} - \frac{\gamma}{2\omega^\ddagger} \right] \frac{\omega_0}{2\pi} \exp\left(-\frac{E^\ddagger}{k_B T}\right)$$

for rates in the high-friction regime. In these equations, γ denotes the friction coefficient, ω^\ddagger the inverse barrier frequency, and ω_0 the vibrational frequency of the reactant well. In between these limits, his theory predicts a turnover but fails to specify it quantitatively.

This theory was later extended by Mel'nikov and Meshkov [145] as well as by Pollak, Grabert, and Hänggi [146], who were able to connect Kramers's limiting cases. Besides fully resolving the turnover, the *Pollak–Grabert–Hänggi* (PGH) theory also generalizes Kramers's ideas to include memory effects based on the GLE. This generality has led to widespread adoption within the TST community [27, 147–153]. Ultimately, however, both theories still involve a number of assumptions that are not always justified, such as being able to treat the reaction as a one-dimensional process [27]. Notably, they are typically only valid for $k_{\text{B}}T \ll E^{\ddagger}$ and begin to break down for thermal energies near or above the barrier height.

More universally accurate — but also computationally expensive — results can be obtained, e. g., from flux-over-population rates in *all-atom molecular dynamics* (AAMD) [154–157] or Langevin-based [134–138] ensemble simulations. These types of calculations require the definition of a DS or similar means to differentiate between reactants and products. As with Kramers, the idea is to inject a constant flux of reactants into the system. These reactants will eventually cross the DS on their way towards the product state. At this point, they are removed from the simulation, which is known as an *absorbing boundary condition* [158]. The rate is then given by the flux of new reactants divided by their equilibrium population.

The geometrical formulation of TST from Section 2-1 could, in principle, be used to calculate an ideal, recrossing-free DS for these types of calculations [9, 94]. Such a DS, however, would have to depend on the dynamics of the solvent particles or the exact noise sequence, depending on how the bath is modeled. This would make the calculations extremely expensive while providing limited benefit in terms of accuracy compared to other approaches. Therefore, simpler approximations are used in practice.

A traditional choice is to construct the DS as follows: We start by approximating the reaction coordinate x via the potential's minimum-energy path. The rank-1 saddle point then corresponds to the maximum along x . At this point, we attach a planar DS such that it is orthogonal to the local direction of the reaction coordinate [43, 159], i. e., such that the DS's normal vector points along the minimum-energy path's tangent vector. This choice is simple but has the same drawback as many traditional TST rate formulas [27] in that its accuracy suffers from recrossings. Notably, a particle could be thrown back by the solvent just after crossing the DS. Counting these events as positive flux through the DS may be undesirable. Further recrossings can be caused by, e. g., nonlinear coupling between the reaction coordinate and the orthogonal modes.

Luckily, the time it takes a reactant to climb the barrier in an activated process in many cases vastly exceeds the time it takes to fall down on the

product side. Pushing the **DS** some distance to the product side [158] (or the reactant side for the backward reaction) will thus only have a small impact on the escape time of recrossing-free trajectories while simultaneously reducing the likelihood of recrossings. This can filter out many recrossings without affecting the rate obtained from the recrossing-free sub-ensemble too much. Alternatively, energy constraints for the **DS** have been studied [149, 160], which are especially relevant for cases with slow energy relaxation [149]. Many more schemes have been proposed — variational **TST** [129, 161] being a notable one — for which we refer the reader to the literature.

Thus, there are many options available, and the best choice is not obvious in many cases. What constitutes a good **DS** and what does not can also depend significantly on the physical (or chemical) problem to be solved. This is especially true at high temperatures $k_{\text{B}}T \gtrsim E^{\ddagger}$ where the barrier is not much of an obstacle anymore for many trajectories. Such high-energy trajectories may enter the product well, get reflected at the potential walls, and immediately react back without getting captured in the product state. Should such reaction paths be treated as a forward reaction followed by a backward reaction? Or do we require their capture, e. g., by introducing an energy constraint for the **DS**? The answer to these questions can have a significant influence on the result as shown in Chapter 7 for a concrete example.

(b) Decay rates

As mentioned above, determining a formally correct **DS** in a thermal system via the geometrical formulation of **TST** can be unfeasibly expensive. Hence, to the best knowledge of the author, this formulation is rarely used in practice to determine absolute reaction rates of real chemical processes. It does, however, provide useful insights into the reaction geometry and the dynamics of systems near the **TS**. As shown in Reference [9], it is even possible to correlate the deterministic dynamics on the **NHIM** of a system without solvent with the stochastic dynamics of that same system in a noisy environment. Furthermore, such knowledge about the reaction geometry can be used for limited predictions about the dynamics away from the **TS**, as demonstrated in Chapter 4. This, however, requires that trajectories pass close to the **NHIM**, and so far has only been demonstrated without noise or friction.

Now that we have established that the framework presented in Section 2-1 will mostly be useful near the **TS**, we can reconsider the concept of flux-over-population rates. Indeed, such a rate can still be defined in this context (cf. Section 3-5), but it does not represent an absolute reaction rate anymore.

Instead, this so-called *decay rate* constitutes a measure for the instability of the **TS**. It is discussed in detail in Section 3-5 and Chapters 4 to 6. This rate is different from the absolute reaction rate in that it only describes how an ensemble falls down from the saddle and not how it climbs it in the first place. The latter is what takes far more time in an activated process and therefore dominates the reaction rate. Thus, if a reaction rate formula incorporates decay rates in the future, it is possible that they will only be a small correction in most cases. Chapter 6 shows that the stability properties revealed by decay rates can nevertheless be useful on their own.

2-4 Floquet theory

It can be useful to linearize the dynamics near the **NHIM** when investigating stability properties. The linearized dynamics near a reference trajectory $\boldsymbol{\gamma}_0(t)$ can be described via the *Jacobian matrix* $\mathbf{J}(t; \boldsymbol{\gamma}_0)$ of the system's equations of motion. Given a set of differential equations

$$\dot{\boldsymbol{\gamma}}(t) = \mathbf{f}(\boldsymbol{\gamma}(t), t), \quad (2-12)$$

the elements of the Jacobian are defined via the partial derivatives

$$J_{jk} = \frac{\partial f_j}{\partial \gamma_k}. \quad (2-13)$$

The linearized form of the differential equations (2-12) then reads

$$\frac{d}{dt} \delta\boldsymbol{\gamma}(t) = \mathbf{J}(t; \boldsymbol{\gamma}_0) \delta\boldsymbol{\gamma}(t), \quad (2-14)$$

where $\delta\boldsymbol{\gamma}(t) = \boldsymbol{\gamma}(t) - \boldsymbol{\gamma}_0(t)$ is the deviation from the reference trajectory $\boldsymbol{\gamma}_0$.

The effect in the interval from t_0 to t can be summarized with the *fundamental matrix* $\boldsymbol{\sigma}(t; \boldsymbol{\gamma}_0, t_0)$. It is calculated by solving the system of differential equations

$$\dot{\boldsymbol{\sigma}}(t; \boldsymbol{\gamma}_0, t_0) = \mathbf{J}(t; \boldsymbol{\gamma}_0) \boldsymbol{\sigma}(t; \boldsymbol{\gamma}_0, t_0) \quad \text{with} \quad \boldsymbol{\sigma}(t_0; \boldsymbol{\gamma}_0, t_0) = \mathbf{1}_{2d}, \quad (2-15)$$

where $\mathbf{1}_{2d}$ is the $(2d \times 2d)$ -dimensional identity matrix and d is the number of **DoFs**. The fundamental matrix can then be used as

$$\delta\boldsymbol{\gamma}(t) = \boldsymbol{\sigma}(t; \boldsymbol{\gamma}_0, t_0) \delta\boldsymbol{\gamma}(t_0) \quad (2-16)$$

to propagate the trajectory $\boldsymbol{\gamma}$ from time t_0 to a later time t .

It seems natural to consider the effect after one period T if the reference trajectory \boldsymbol{y}_0 is periodic. The fundamental matrix $\boldsymbol{\sigma}(t_0 + T; \boldsymbol{y}_0, t_0)$ in this case is known as the *monodromy matrix* and provides the basis for Floquet theory [162, 163]. Its eigenvalues $m_j \in \mathbb{C}$ are called characteristic or *Floquet multipliers*. Any value $\mu_j \in \mathbb{C}$ that fulfills $\exp(\mu_j T) = m_j$ is denoted as a characteristic or *Floquet exponent*. Generally, these exponents are only unique up to an additive multiple of $2\pi i/T$ since $\exp(2\pi i) = 1$. The exponents' real parts

$$(2-17) \quad \lambda_j = \operatorname{Re}(\mu_j) = \frac{1}{T} \ln |m_j|$$

coincide with the *Lyapunov exponents* λ_j of the system and can thus be used to shed light upon the stability properties of the reference trajectory \boldsymbol{y}_0 .

NUMERICAL METHODS

3

Parts of this chapter have previously been published by the author in References [3–6].

The geometrical formulation of TST introduced in Section 2-1 provides an elegant, conceptually simple framework for the investigation of chemical reaction dynamics. Trying to apply it analytically to specific systems, however, quickly gets unwieldy, especially if systems are driven time-dependently. One way of dealing with such systems is by means of perturbative methods [20, 54, 88]. These, however, can only ever yield approximative solutions. In this work, we instead use numerical methods based on the systems' full dynamics in order to achieve results that are exact up to numerical errors. The most important numerical methods and algorithms used in Chapters 4 to 6 are presented in Sections 3-1 to 3-5.

The calculation of absolute reaction rates usually implies a coupling to some kind of thermal bath. The geometrical methods mentioned above can, in principle, also be used within the context of noise and friction [9]. This, however, is of limited value in the calculation of reaction rates (cf. Section 2-3), which is why we do not employ them in Chapter 7. Instead, we rely on the algorithms described in Sections 3-6 and 3-7 for the investigations in this final chapter. They have been implemented in the open-source library *mfptlib*, see Section D-2.

3-1 Integrating ordinary differential equations

The propagation of trajectories forms the core of our analysis. We exclusively use explicit methods, i. e., methods of the form

$$\boldsymbol{\gamma}(t + \delta t) = \boldsymbol{F}(\boldsymbol{\gamma}(t), t), \quad (3-1)$$

where $\boldsymbol{\gamma}(t)$ is the trajectory's state (position and momentum) at time t and \boldsymbol{F} is the stepper function implementing a concrete integration scheme for a particular system. The step length δt has to be chosen appropriately for each system to capture the relevant dynamics. This can, in principle, be done automatically using so-called adaptive methods, which estimate a step's error and dynamically adapt δt if necessary. Such adaptive methods, however, are

not employed in this work to avoid subtle inconsistencies between unstable trajectories.

In this framework, whole trajectories can be obtained by iteratively applying F to some initial conditions $\boldsymbol{\gamma}(t_0)$. We utilize the following integration schemes.

(a) Velocity Verlet

We choose the *velocity-Verlet* scheme [164] in all systems without velocity-dependent forces, i. e., those investigated primarily in Chapters 4 and 5. In these systems, the equations of motion can be written as

$$(3-2) \quad \dot{\boldsymbol{q}}(t) = \boldsymbol{v}(t) \quad \text{and} \quad \dot{\boldsymbol{v}}(t) = \boldsymbol{a}(\boldsymbol{q}(t), t),$$

where \boldsymbol{q} is the position, \boldsymbol{v} is the velocity, and \boldsymbol{a} is the acceleration. The velocity-Verlet scheme discretizes the time step, resulting in

$$(3-3a) \quad \boldsymbol{q}(t + \delta t) = \boldsymbol{q}(t) + \boldsymbol{v}(t) \delta t + \frac{1}{2} \boldsymbol{a}(t) \delta t^2 + \mathcal{O}(\delta t^3)$$

$$(3-3b) \quad \text{and} \quad \boldsymbol{v}(t + \delta t) = \boldsymbol{v}(t) + \frac{\boldsymbol{a}(t) + \boldsymbol{a}(t + \delta t)}{2} \delta t + \mathcal{O}(\delta t^2).$$

It is typically implemented using the sequence of operations

$$(3-4a) \quad \boldsymbol{v}_{n+1/2} = \boldsymbol{v}_n + \boldsymbol{a}_n \frac{\delta t}{2},$$

$$(3-4b) \quad \boldsymbol{q}_{n+1} = \boldsymbol{q}_n + \boldsymbol{v}_{n+1/2} \delta t,$$

$$(3-4c) \quad t_{n+1} = t_n + \delta t,$$

$$(3-4d) \quad \boldsymbol{a}_{n+1} = \boldsymbol{a}(\boldsymbol{q}_{n+1}, t_{n+1}),$$

$$(3-4e) \quad \text{and} \quad \boldsymbol{v}_{n+1} = \boldsymbol{v}_{n+1/2} + \boldsymbol{a}_{n+1} \frac{\delta t}{2},$$

where the acceleration \boldsymbol{a}_n is cached between iterations.

A major advantage of the velocity-Verlet scheme is that it conserves the symplectic structure of Hamiltonian systems. This minimizes long-term energy drifts caused by the discretization of the time propagation [165].

(b) Runge–Kutta

The velocity-Verlet scheme loses its symplecticity if velocity-dependent forces — such as the Coriolis force — are at play [166]. We therefore implement a

classical fourth-order *Runge–Kutta* scheme [167, 168] for the calculations performed in Chapter 6.

Runge–Kutta-type steppers can be applied to any first-order system of ordinary differential equations

$$\dot{\boldsymbol{\gamma}}(t) = \mathbf{f}(\boldsymbol{\gamma}(t), t) \quad (3-5)$$

and, therefore, have less restrictions than the velocity-Verlet algorithm outlined in Section 3-1 (a). They enjoy great popularity because of their flexibility and ease of implementation. The classical fourth-order form reads

$$\mathbf{k}_n^{(1)} = \mathbf{f}(\boldsymbol{\gamma}_n, t_n), \quad (3-6a)$$

$$\mathbf{k}_n^{(2)} = \mathbf{f}\left(\boldsymbol{\gamma}_n + \mathbf{k}_n^{(1)} \frac{\delta t}{2}, t_n + \frac{\delta t}{2}\right), \quad (3-6b)$$

$$\mathbf{k}_n^{(3)} = \mathbf{f}\left(\boldsymbol{\gamma}_n + \mathbf{k}_n^{(2)} \frac{\delta t}{2}, t_n + \frac{\delta t}{2}\right), \quad (3-6c)$$

$$\mathbf{k}_n^{(4)} = \mathbf{f}\left(\boldsymbol{\gamma}_n + \mathbf{k}_n^{(3)} \delta t, t_n + \delta t\right), \quad (3-6d)$$

$$\boldsymbol{\gamma}_{n+1} = \boldsymbol{\gamma}_n + \frac{1}{6} \left[\mathbf{k}_n^{(1)} + 2\mathbf{k}_n^{(2)} + 2\mathbf{k}_n^{(3)} + \mathbf{k}_n^{(4)} \right] \delta t, \quad (3-6e)$$

$$\text{and } t_{n+1} = t_n + \delta t. \quad (3-6f)$$

3-2 Revealing the phase-space geometry

Many means of revealing the phase-space structure have been discussed over the years [1, 89, 90, 169, 170]. Two of them — the Lagrangian descriptor and the concept of reactive regions — have proven to be particularly useful for this work. In the following, we give a short review of these methods. We demonstrate their advantages, drawbacks, and potential use cases by means of the static example potential

$$V(x) = \frac{x^4}{4} - \frac{x^2}{2} \quad (3-7)$$

shown in Figure 3-1. Using such a simple 1-DoF model without driving allows us to focus on the methods without worrying about any difficulties arising from the model itself. Yet, none of the methods presented in this chapter rely on these simplifications. On the contrary, they make no assumptions about the dimensionality or time dependence of the model at all and are only applied to individual points at once. The methods thus have to be

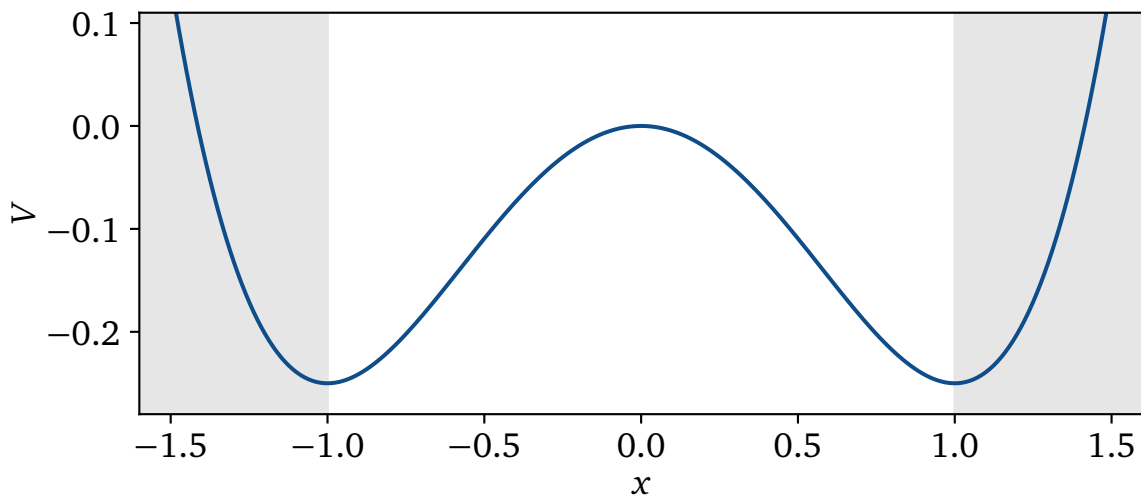


Figure 3-1: Quartic double-well potential V from Equation (3-7) as a function of reaction coordinate x . States in the shaded regions $x \leq -1$ and $x \geq +1$ are unambiguously identified as reactants and products, respectively. States in the interaction region in between could also be identified analytically due to the trivial nature of the model. Still, we consider those states to be ambiguous for the sake of demonstration of the methods.

sampled over the relevant parts of the phase space to resolve extended structures. Nevertheless, a time dependence or additional DoFs would make visualization more challenging. Only sections of the full phase space could be shown in such cases.

(a) Lagrangian descriptors

The geometric structure of the phase space can be revealed using the *Lagrangian descriptor* [89, 90, 100, 106, 169, 171] defined by

$$(3-8) \quad \mathcal{L}(\mathbf{q}_0, \mathbf{v}_0, t_0) = \int_{t_0-\tau}^{t_0+\tau} dt \|\mathbf{v}(t; \mathbf{q}_0, \mathbf{v}_0, t_0)\|_2$$

for a given initial position \mathbf{q}_0 , velocity \mathbf{v}_0 , and time t_0 . The classical version shown here measures the arc length of a trajectory $\mathbf{q}(t; \mathbf{q}_0, \mathbf{v}_0, t_0)$ in the time interval $t_0 - \tau \leq t \leq t_0 + \tau$. Other measures such as the integral of the modulus of acceleration $\|\mathbf{a}(t)\|_2 = \|\dot{\mathbf{v}}(t)\|_2$ have also been investigated [90] but will not be discussed in this work.

Sampling the Lagrangian descriptor \mathcal{L} over the phase space of the example potential (3-7) yields Figure 3-2(a). A local minimum in \mathcal{L} arises when the particle covers the minimum distance in the interval $t_0 - \tau \leq t \leq t_0 + \tau$. It consequently remains longer in the interaction region when integrating

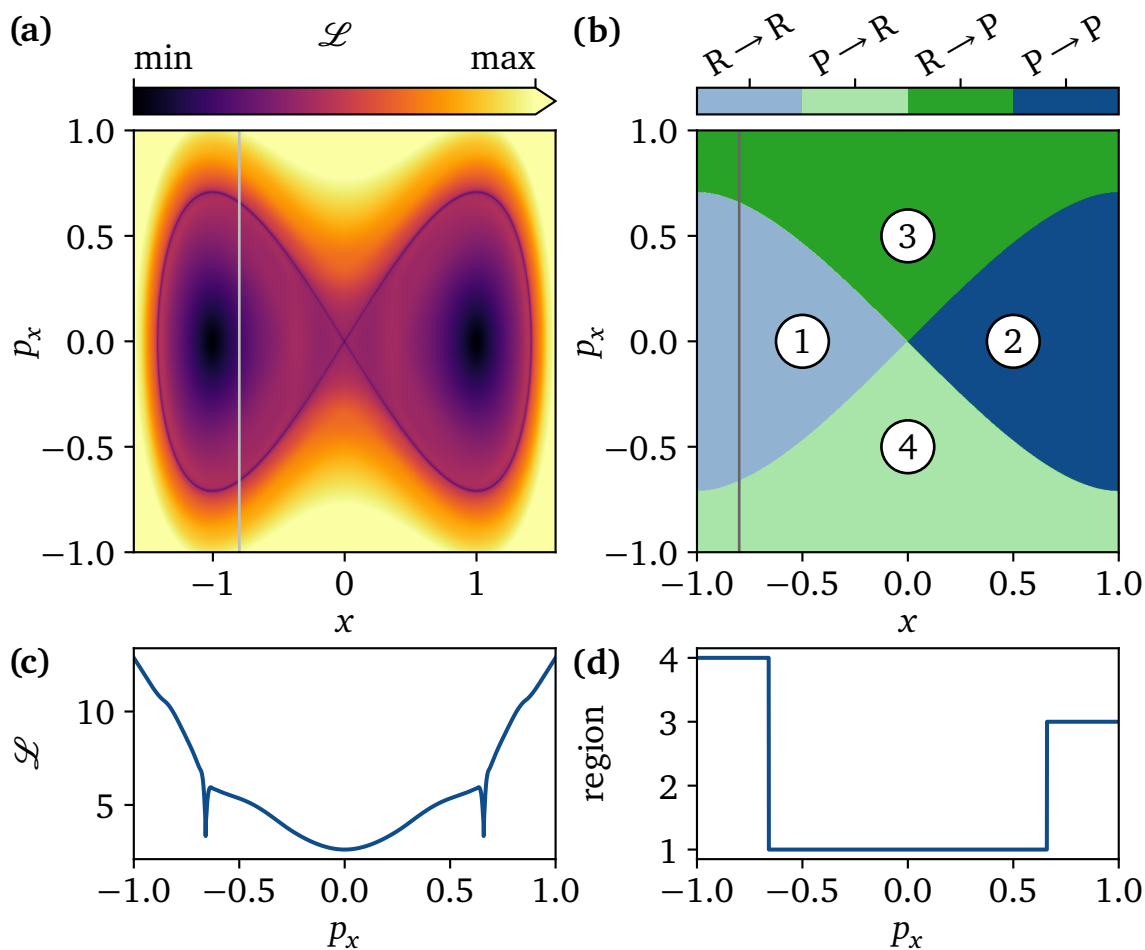


Figure 3-2: (a) Phase-space structure for the potential (3-7) as revealed by the Lagrangian descriptor \mathcal{L} given in Equation (3-8) with $\tau = 8$. The stable and unstable manifolds \mathcal{W}_s and \mathcal{W}_u —connected to homoclinic orbits—are clearly visible. Their apparent intersection reveals the position of the NHIM. The color scale is capped at $\mathcal{L} = 13$. (b) Reactive regions of the same system. The manifolds \mathcal{W}_s and \mathcal{W}_u lie at the borders between the regions. (c) Cut at $x \approx -0.8$ through the Lagrangian descriptor \mathcal{L} shown by the vertical line in panel (a). The stable and unstable manifolds \mathcal{W}_s and \mathcal{W}_u signify their presence via sharp local minima. The lowest minimum corresponds to the reactant well. (d) Equivalent cut through the reactive regions in panel (b). The different regions show as plateaus in the numeric data, and the manifolds \mathcal{W}_s and \mathcal{W}_u manifest in clean steps between these plateaus.

forward or backward in time, and thus provides a signature for the presence of a stable or unstable manifold, respectively. Specifically, the manifolds \mathcal{W}_s and \mathcal{W}_u manifest as sharp dips in \mathcal{L} [cf. Figure 3-2(c)]. The NHIM lies at the intersection of these low- \mathcal{L} lines, which is located at $(x = 0, p_x = 0)^T$ in our example. We caution the reader that this location as well as any symmetries in \mathcal{L} are specific properties of the example system; other models can differ in

this regard. This is especially true for driven systems, where the phase-space structure—including the positions of \mathcal{W}_s , \mathcal{W}_u , and the NHIM—is a function of the initial time t_0 .

Not all minima can generally be attributed to the stable or unstable manifolds. And even if they can, they might not always be easy to find numerically. Reference [1], for instance, shows an example where the minima heralding the existence of the manifolds are accompanied by additional minima in close proximity for which no relevant phase-space geometry could be identified.

All in all, the Lagrangian descriptor has the advantage that it is conceptually very simple and that it can be applied to practically any system. This makes it suitable for a first visual inspection. As discussed in Reference [1] and shown in Figure 3-2(c), however, it features a nontrivial internal structure. Numerically determining the exact position of stable and unstable manifolds is therefore difficult.

(b) Reactive regions

A numerically simpler scheme for systems with a rank-1 saddle is based on the concept of *reactive (and nonreactive) regions* as described in References [1, 87, 92] and Chapter 2. It discriminates initial conditions by first defining an interaction region in position space—typically an interval along the reaction coordinate x —outside of which the system is *clearly* in the reactant or product state. In the example from Figure 3-1, we assume that the interaction region is given by $-1 < x < +1$ (nonshaded). Particles are then propagated forward and backward in time until they leave said region. In both directions of time, a particle can end up as either reactant (R) or product (P). This leads to four possible classifications for a given initial condition as shown in Figure 3-2(b), namely

1. nonreactive reactants $R \rightarrow R$,
2. nonreactive products $P \rightarrow P$,
3. reactive reactants $R \rightarrow P$, and
4. reactive products $P \rightarrow R$.

Similar concepts have been introduced in, e. g., Reference [169].

Using the concept of reactive regions, stable and unstable manifolds can be revealed as borders between adjacent regions. In the numeric data, these manifest as clean steps [see Figure 3-2(d)] which can easily be resolved numerically.

3-3 Binary-search methods

We can leverage the concept of reactive and nonreactive regions discussed in the previous section to efficiently determine the precise position of the stable and unstable manifolds as well as the **NHIM**. These calculations are quite straightforward for the manifolds \mathcal{W}_s and \mathcal{W}_u when based on sections akin to Figure 3-2(d). Here, we first guess an interval that contains the relevant manifold, e. g., $0 \leq p_x \leq 1$ for the \mathcal{W}_s . The correctness of the guess can be verified by checking that the interval limits, $p_x = 0$ and $p_x = 1$ in this example, are located in the expected regions [cf. Figure 3-2(b)]. From here on, a simple binary search [172] can be leveraged to determine the momentum p_x of the step and, thus, the manifold. For the **NHIM**, however, a more sophisticated ansatz is necessary.

(a) Binary-contraction method

The **NHIM** can be obtained using several perturbative [20, 54] and direct [40, 91, 171] methods, but we have found that the *binary-contraction method* (**BCM**) introduced in Reference [92] is effective and efficient for systems such as the ones addressed in this work. A sketch of this algorithm can be found in Figure 3-3.

The algorithm is initialized by defining a quadrangle with each of its corners lying exclusively within one of the four regions shown in Figure 3-2(b). In each iterative step, we first determine an edge's midpoint. Then, the adjacent corner corresponding to the same region as that midpoint is moved to the midpoint's position, cf. Figure 3-3(a). By repeating this interleaved bisection procedure in turn for all edges, the quadrangle successively contracts and converges towards the **NHIM**, as shown in Figures 3-3(b) to 3-3(d).

The **BCM** operates exclusively within an x - p_x section of phase space, keeping any orthogonal modes $(\mathbf{y}, \mathbf{p}_y)^\top$ fixed (see Section 2-1). Any trajectories started in this section, however, are propagated in the full phase space. The calculations can be repeated for various values of $(\mathbf{y}, \mathbf{p}_y)^\top$ to sample the full codimension-2 **NHIM**.

(b) Finding an initial quadrangle

In order to apply the **BCM** reliably, it needs to be initialized with four points in four different reactive regions without human intervention. In many cases, these regions are clearly located to the left, right, top, and bottom of the **NHIM** in a given x - p_x section of phase space [cf. Figure 3-2(b)]. Here, the quadrangle can be initialized in the following way [92, 94]: We first guess

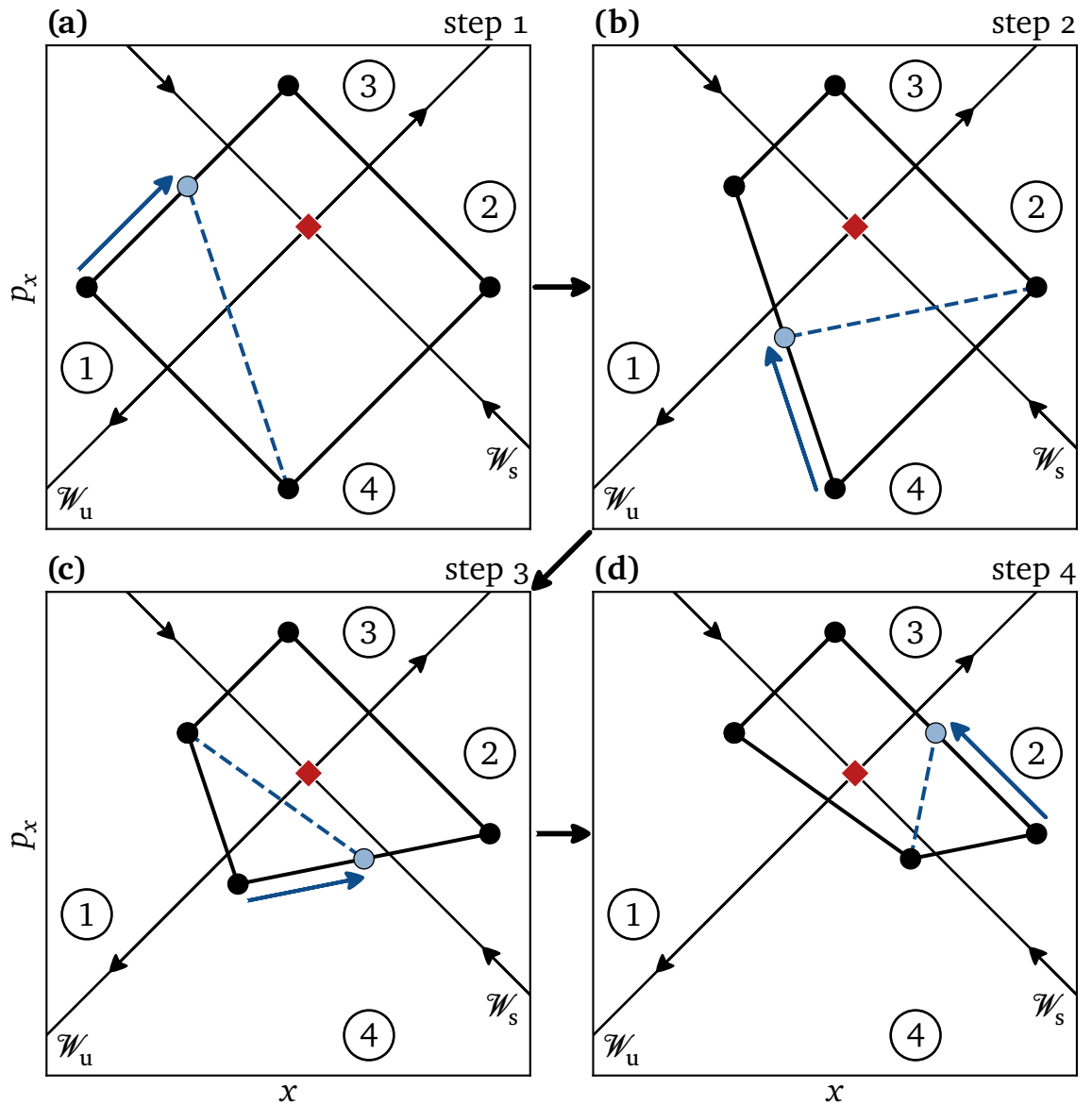


Figure 3-3: Use of the BCM to uncover the NHIM in phase space. (a) The stable and unstable manifolds \mathcal{W}_s and \mathcal{W}_u associated with the barrier divide the phase space into distinct regions labeled 1 through 4. The NHIM is located at the intersection of the two manifolds' closures and is marked with a diamond. To numerically obtain this point, a quadrangle with one corner in each region is set up. In turn, the midpoint for every edge is determined, shown as a light blue circle. Depending on which region the midpoint is in, it subsequently replaces one of the previous corners. (b)–(d) This procedure is repeated until the quadrangle is sufficiently small.

the NHIM's position $\mathbf{y}_{\text{guess}}^\ddagger$ in the x – p_x section. Candidates for the quadrangle corners can then be defined at fixed empirical distances Δx and Δp_x along a horizontal and a vertical line through this guess, i. e., at $\mathbf{y}_{\text{guess}}^\ddagger \pm \Delta x \hat{x}$ and $\mathbf{y}_{\text{guess}}^\ddagger \pm \Delta p_x \hat{p}_x$ (light gray markers and blue marker 1 in Figure 3-4).

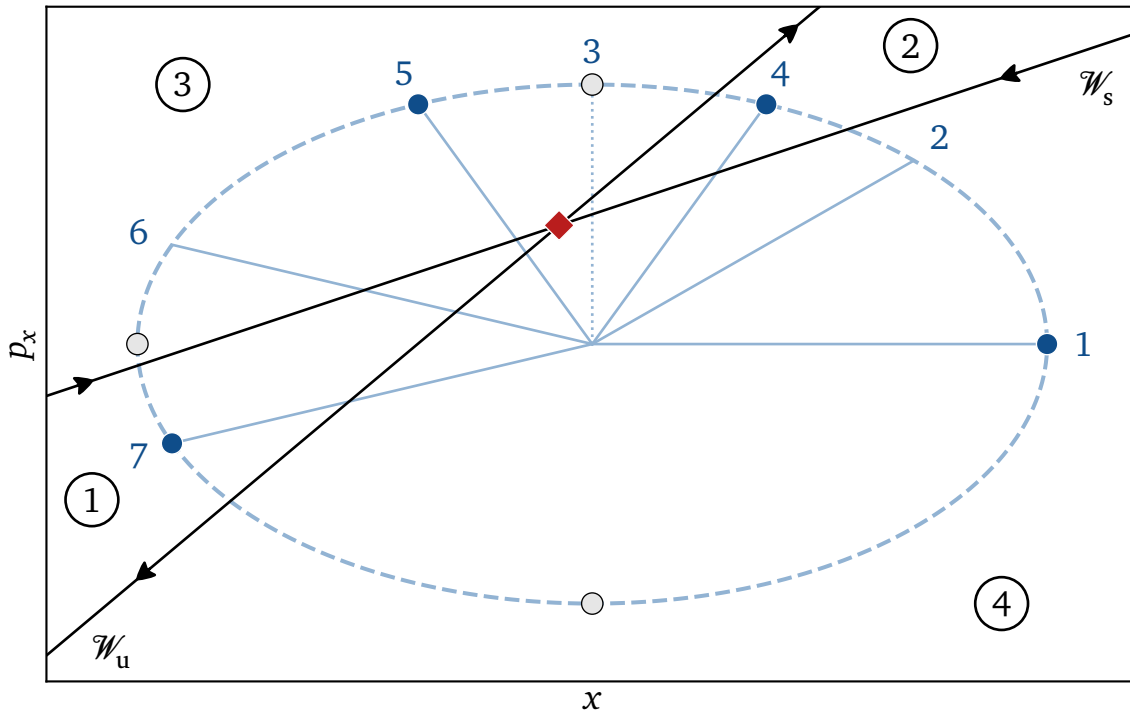


Figure 3-4: Sketch of an algorithm for finding the inputs to the BCM, namely, four arbitrary initial phase-space coordinates representative of the four regions associated with the NHIM. Naively choosing coordinates on two right-angled axes (light gray circles) would not work in the case shown here as only regions 3 and 4 would be covered. Instead, an ellipse enclosing the geometric cross is constructed. The first point (dark blue circle on right-hand side) is selected arbitrarily at coordinates with angle $\alpha = 0$. Subsequent coordinates are found by incrementing α in steps of $\Delta\alpha = \pi/4$ (solid lines), and confirming that said point satisfies the condition of a new region. If a region is skipped — e. g., as shown in the dotted line in step 3 — the increment $\Delta\alpha$ is temporarily reduced until a point in the region in between is found (step 4). The points considered in each step of the example are numbered sequentially.

These initial guesses may not always be unique, especially in driven systems. Different strategies can be employed [92] to handle such cases. One option is to sample multiple positions along the horizontal and vertical line corresponding to different values for Δx and Δp_x . Appropriate initial corners can then be chosen from these samples. Other possibilities include interpolation or extrapolation of the initial guess $\mathbf{y}_{\text{guess}}^{\ddagger}$ from known points on the NHIM. This is especially useful in systems with many DoFs. These strategies can also be combined, making the initialization routine even more robust.

Since the geometry of the stable and unstable manifolds can be quite distorted in some systems, the BCM can not always be initialized precisely in the way described above. In these cases, we still require a guess of the NHIM's position. However, instead of choosing the coordinates on a horizontal and a vertical line, we first define an ellipse centered on the guess. This ellipse must be large enough to enclose the NHIM in the given section of phase space. The initial corners of the quadrangle are then selected on the ellipse according to the algorithm described in Figure 3-4 [4, 173].

3-4 Dynamics on the NHIM

Despite the fact that the NHIM is a mathematically invariant subspace, trajectories started on it deviate exponentially fast as time goes by because of limited numerical precision. Therefore, numerically calculated trajectories have to be stabilized explicitly on the NHIM, e. g., using the BCM. Therein, after each time interval Δt , the coordinates x and p_x are recalculated to project the particle back onto the NHIM. A similar projection has been used in Reference [174]. Care has to be taken to ensure that this projection does not introduce significant errors. To achieve this, the projected distance in x and p_x is measured. If a maximum distance is exceeded, the projection is rejected and the particle is reset to an earlier time and position. The propagation is then repeated with a smaller value of Δt . This procedure effectively reduces the dimensionality of the subspace traversed by the trajectories from the $2d$ dimensions of the full phase space to the $2d - 2$ dimensions of the NHIM. In higher dimensions, one could instead take advantage of an artificial neural network as recently done in Reference [174] to stabilize the trajectories at the price of some loss in accuracy.

The systems discussed in Chapters 4 and 6 have two DoFs, and consequently a four-dimensional phase space. Although the NHIM in these cases is only a two-dimensional subspace, visualizing many trajectories on it can still get confusing quickly. A reliable method for such a task is the Poincaré map, also known as the *Poincaré surface of section (PSOS)* [66]. Using this method, the dimensionality of the phase space is reduced by only showing intersection points with a given sectional surface instead of the whole trajectory. When the system has a natural period, such as in the present case of a periodically driven system, one can effect a similar dimensional reduction using a stroboscopic map capturing periodic sections at corresponding intervals in time. For a time-dependent, effectively two-dimensional system, the stroboscopic PSOS corresponds to a set Σ given by

$$(3-9) \quad \Sigma = \{ \boldsymbol{\gamma}(t_n) \in \mathbb{R}^2 \mid t_n = t_0 + nT, n \in \mathbb{N}_0 \},$$

where $\boldsymbol{\gamma}(t) = (y(t), p_y(t))^T$ denotes the phase-space vector of the system constrained to the **NHIM** and T is the period of the driving. The formerly continuous trajectory thus becomes discretized under the stroboscopic map.

Using this stroboscopic map, dynamical properties such as the integrability of the system can be determined. Near integrability is revealed by the existence of torus-like structures in the system's **PSOS**. Changes in the system's parameters can lead to a transition from near integrable to chaotic as revealed by the emergence of stochastic structure in the **PSOS**.

A periodic trajectory with the property

$$\boldsymbol{\gamma}_n = \boldsymbol{\gamma}_{n+1}, \quad \text{where } \boldsymbol{\gamma}_n := \boldsymbol{\gamma}(t_0 + nT) \quad \text{and } n \in \mathbb{N}_0, \quad (3-10)$$

manifests as a fixed point with period T in the **PSOS**. Fixed points with periodicity sT , where $s \in \mathbb{N}_0$, analogously fulfill $\boldsymbol{\gamma}_n = \boldsymbol{\gamma}_{n+s}$. They appear as s -cycles in the **PSOS** since the stroboscopic map records a point once per system period T . The difference $\boldsymbol{\gamma}_{n+1} - \boldsymbol{\gamma}_n$ is a vector whose length increases monotonically with distance from the fixed point within the fixed point's neighborhood. This can be exploited to find fixed points through a root search algorithm. In the numerical results presented in this work, the fixed points of the map are found using the modified Powell method, `scipy.optimize.root(method='hybr')`, implemented in the Python library SciPy [175].

There are two kinds of fixed points that must be distinguished: Elliptic fixed points belong to stable periodic orbits. Trajectories that start in the vicinity of such an orbit stay in its vicinity indefinitely. In the **PSOS**, these show up as concentric, possibly deformed torus-like structures. Hyperbolic fixed points, on the other hand, correspond to unstable orbits. Trajectories started in their vicinity act as if they were being repelled by the fixed point, leading to hyperbola-shaped structures in the **PSOS**.

When varying a system's parameters, its dynamics can change qualitatively in so-called bifurcations. Local bifurcations are identifiable via the creation or annihilation of fixed points. Most important for this work is the saddle-node bifurcation, in which a pair of an elliptic and a hyperbolic fixed point emerges or vanishes. A typical path from regular to chaotic, nonintegrable dynamics is via an infinite series of bifurcations.

3-5 Decay rates

The existence of a **NHIM** of codimension 2 and its role in determining the chemical reaction rate brings an additional concern. Namely, what is the degree of instability of the **TS** as determined by the decay of trajectories that

start in the proximity of the **NHIM**? In a time-dependent — e. g., driven — environment, this instantaneous decay will be time-dependent as well. Nevertheless, it can be assigned a single characteristic decay rate constant when the time dependence is periodic by taking the average over the period [2, 176].

The stability of the **TS** near threshold energy can be quantified via the decay of trajectories near the **NHIM**. This is equivalent to the rate at which an ensemble of reactants moves through the **DS** and can thus be seen as a local flux-over-population rate as described in Section 2-3. The decay of this reactant population is exponentially fast because of the hyperbolic nature of the **NHIM**. We can therefore define an instantaneous decay rate $k(t)$ via the differential equation [2, 4, 8, 176]

$$(3-11) \quad k(t) = -\frac{\dot{N}(t)}{N(t)},$$

where $N(t)$ is the time-dependent size of the reactant population. Compared to other measures of instability, instantaneous decay rates have the advantage that they can be evaluated for a specific point in time. Floquet multipliers and Lyapunov exponents, for instance, only yield average values for a whole period and long-term limits, respectively.

In this work, we implement three different methods, summarized below, for calculating decay rates:

1. The ensemble rate method [2, 176] yields instantaneous (i. e., time-resolved) rates $k(t)$ by propagating a large number of particles. It is computationally expensive but conceptually simple.
2. The **local manifold analysis** [2, 6] accelerates the computation of instantaneous rates by leveraging the linearized dynamics near the **NHIM**.
3. If only time-averaged rate constants $\langle k \rangle_t$ are desired, the Floquet rate method [2, 103] can be used instead, requiring even less computational resources.

In the cases presented in this work, the three algorithms all generally converge within reasonable time. However, they each involve different assumptions which might lead to different results, and which can provide complementary interpretations about the underlying dynamics of the system. As shown in Chapters 5 and 6, all three lead to decay rates in excellent agreement. The repetition thus also serves to provide assurance in the reported values.

(a) Ensemble rate method

The conceptually simplest method for calculating decay rates k_e is by means of propagation of an ensemble. The *ensemble rate method* [2, 4, 8, 87] can be used to obtain the instantaneous decay rate of a reactant population close to the **NHIM**, which anchors the **TS**. A homogeneous and linear ensemble of N reactive trajectories is initialized on the reactant side of the full phase space. Specifically, they are placed on an x - p_x cross-sectional surface at a small distance δx from a given position $\mathbf{y}^\ddagger(t) = (x^\ddagger(t), \mathbf{y}^\ddagger(t), p_x^\ddagger(t), \mathbf{p}_y^\ddagger(t))^\top$ of an arbitrarily chosen trajectory on the **NHIM** (see light blue bullets in Figure 3-5). After propagating this ensemble for a time δt , a subdomain will have pierced the **DS** and entered the product side (diamonds in Figure 3-5) while the remainder will still be located on the reactant side (dark blue bullets in Figure 3-5). As the **DS** is non-recrossing, the resulting decrease of the reactant population in a close neighborhood of the **NHIM** [cf. Equation (3-11)] is associated with a decay rate

$$k_e(\mathbf{y}, \mathbf{p}_y, t; t_0) = -\frac{d}{dt} \ln[N(\mathbf{y}, \mathbf{p}_y, t; t_0)]. \quad (3-12)$$

It is referred to as the *instantaneous ensemble rate* to emphasize that it is obtained by propagating an ensemble of reactive trajectories according to the equations of motion. In general, the **DS** has to be computed individually for each trajectory of the ensemble and each time step as the ensemble may turn out of the x - p_x plane. An analogous definition has been used in Reference [176] for escape rates over a potential barrier.

As shown in Figure 3-5, we prepare the ensemble parallel to the unstable manifold \mathcal{W}_u ; other initial orientations will, in general, entail different rates k_e . This choice may seem arbitrary but is justified for two reasons. First, it can be shown analytically and numerically that this ansatz leads to consistency with the Floquet rate method discussed in Section 3-5 (c). And second, any ensemble in the linear regime of the **NHIM** will converge towards \mathcal{W}_u for $t \rightarrow \infty$. Any rates derived from such ensembles thus have to converge as well.

Finally, the ensemble can be propagated not just for a small time step δt but for longer times when computing the time-dependent ensemble rate according to Equation (3-12). As the reactant population decreases exponentially when propagating the ensemble, a new ensemble can be initialized close to the corresponding point of the respective trajectory on the **NHIM** after an appropriately chosen propagation time. Such technical details are discussed in Reference [2] and Section 5-4. Although the implementation of the ensemble method is straightforward, it can be numerically expensive

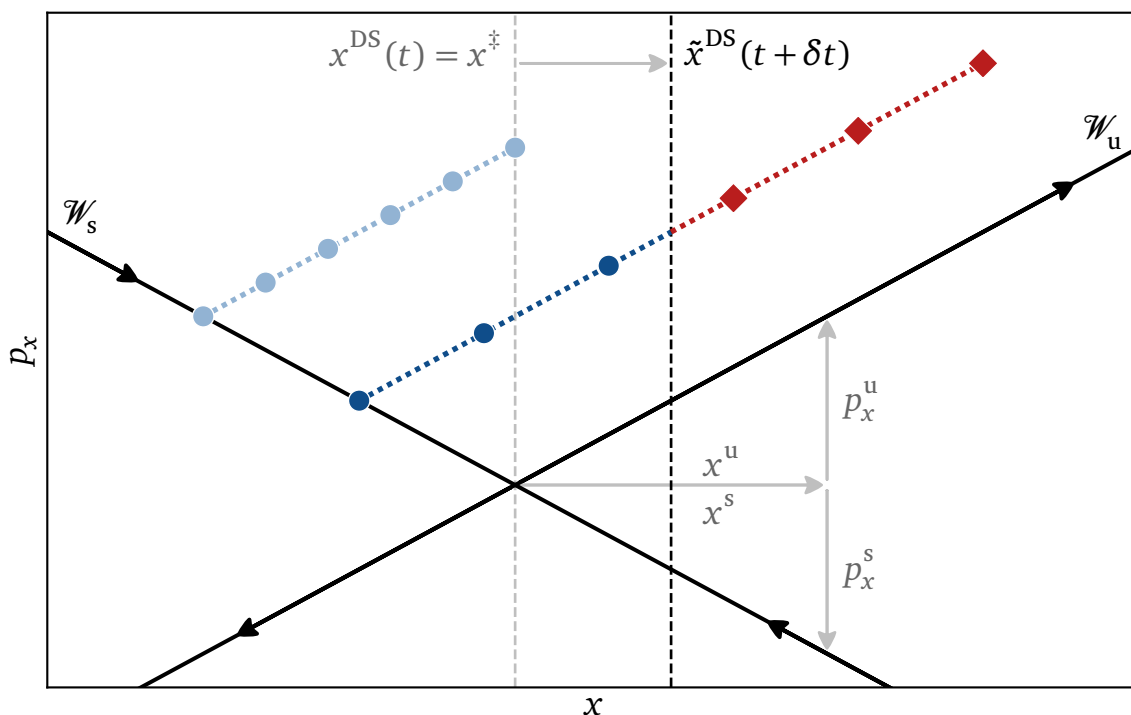


Figure 3-5: Schematic of instantaneous rate calculations. An equidistant ensemble is initialized parallel to \mathcal{W}_u such that it connects \mathcal{W}_s on the reactant side with the DS. Upon time propagation, parts of the ensemble react through the DS. The resulting ensemble is still equidistant, parallel to \mathcal{W}_u , and connected to \mathcal{W}_s . In the general case, ensembles can move out of the x - p_x plane during propagation and may therefore pierce the DS at $\tilde{x}^{\text{DS}}(t + \delta t) \neq x^\ddagger$.

because the ensemble consists of many trajectories and the DS is obtained individually for each reactive trajectory using the BCM [see Section 3-3 (a)].

(b) Local manifold analysis

The accuracy of the ensemble-method decay rates decreases with time because of the reduction of the density of reactants. However, the inaccuracy can be reduced at the cost of larger computational expense by starting bigger ensembles or starting the ensembles staggered. Alternatively, we can avoid most of the expensive particle propagation of the ensemble method by leveraging the geometry of the stable and unstable manifolds to effectively describe the linearized dynamics near the NHIM. The resulting *local manifold analysis (LMA)* [2, 6] can thus be seen as an extension to the ensemble method with the difference that the time when trajectories have reached the DS can now be determined analytically through the linearization, thereby avoiding a costly numerical integration. As a result, the computational ef-

fort required to calculate instantaneous decay rates is significantly reduced while numerical precision is simultaneously enhanced. Additionally, these calculations can be trivially parallelized for entire trajectories. Compared to previous publications, the LMA was extended in Reference [6] to account for velocity-dependent forces (e. g., the Coriolis force).

As in the ensemble method described in Section 3-5 (a), we consider the region of phase space close to a reference trajectory $\boldsymbol{\gamma}^\ddagger = (x^\ddagger, \boldsymbol{y}^\ddagger, p_x^\ddagger, \boldsymbol{p}_y^\ddagger)^\top$ on the NHIM, as shown in Figure 3-5. For simplicity, we choose a moving coordinate frame in which the origin is at $\boldsymbol{\gamma}^\ddagger = \mathbf{0}$ for all times t . The decay rate is determined by two components:

1. The first contribution k_m^{ens} arises from the movement of the ensemble akin to Section 3-5 (a) relative to $\boldsymbol{\gamma}^\ddagger$. The resulting flux through the associated DS at $x^{\text{DS}} = x^\ddagger = 0$ [markers to the right of $x^{\text{DS}}(t) = x^\ddagger$ in Figure 3-5] is then obtained via the slopes of the stable and unstable manifolds defined by the variables $x^s = x^u$, p_x^s , and p_x^u .
2. The second contribution k_m^{DS} accounts for the fact that in systems with more than one degree of freedom, the ensemble can turn out of the x - p_x plane associated with $\boldsymbol{\gamma}^\ddagger$. This can happen if the system's orthogonal modes are coupled to the reaction-coordinate momentum p_x and leads to an apparent movement of the DS relative to $\boldsymbol{\gamma}^\ddagger$ (represented by the top arrow in Figure 3-5). As a result, the instantaneous flux through the DS is modified. To quantify this effect, we first propagate the top particle of the ensemble initially located on the DS numerically by a small time step δt . The related shift of the DS $\tilde{x}^{\text{DS}}(t + \delta t)$ can then be determined by projecting the propagated particle back onto the NHIM using the BCM.

Combining the two terms, the instantaneous decay rate can be written as

$$k_m(t; \boldsymbol{\gamma}^\ddagger) = J_{x, p_x}(t) \frac{p_x^u(t) - p_x^s(t)}{x^u(t)} - \frac{\tilde{x}^{\text{DS}}(t + \delta t)}{x^u(t) \delta t}, \quad (3-13)$$

where $J(t)$ is the Jacobian of the system's equations of motion evaluated for the trajectory $\boldsymbol{\gamma}^\ddagger$ at time t .

For a more detailed derivation of Equation (3-13) we consider a trajectory $\boldsymbol{\gamma}^\ddagger(t) = (x^\ddagger, \boldsymbol{y}^\ddagger, p_x^\ddagger, \boldsymbol{p}_y^\ddagger)^\top$ starting at some arbitrary time t_0 on the NHIM. All the statements in this section depend implicitly on $\boldsymbol{\gamma}^\ddagger$ and t_0 , which we neglect in our notation for simplicity. Without loss of generality, we choose coordinates such that $x^\ddagger(t) = p_x^\ddagger(t) = 0$ for all times t .

Figure 3-5 sketches an x - p_x section of phase space in close proximity to $\boldsymbol{y}^\ddagger(t_0)$. We can assume that the manifold fibers in this section are straight lines since we only look at the dynamics very close to the NHIM. Therefore, the stable and unstable manifolds for fixed $(\boldsymbol{y}^\ddagger, \boldsymbol{p}_y^\ddagger)^\top$ can be described using only two vectors $\boldsymbol{y}^s = (x^s, p_x^s)^\top$ and $\boldsymbol{y}^u = (x^u, p_x^u)^\top$. These vectors will be squeezed and stretched as a function of time if subjected to the equations of motion. Without loss of generality, we initially choose a small $x^s(t_0) = x^u(t_0) > 0$ such that we are in the linear regime.

To obtain a decay rate for $\boldsymbol{y}^\ddagger(t_0)$, we now consider a linear, equidistant ensemble parameterized by

$$(3-14) \quad \boldsymbol{y}^{\text{ens}}(\alpha, t) = -\boldsymbol{y}^s(t) + \alpha \boldsymbol{y}^u(t),$$

where $\alpha \in [0, 1]$. The ensemble is constructed parallel to the unstable manifold—see Figure 3-5. The value $\alpha^{\text{DS}}(t)$ where $\boldsymbol{y}^{\text{ens}}$ pierces the DS at time t describes the fraction of reactants in the ensemble. Initially, the ensemble touches the DS at $\alpha^{\text{DS}}(t_0) = 1$. As time goes by, however, the ensemble will be stretched and $\alpha^{\text{DS}}(t)$ will therefore decay exponentially. More precisely, α^{DS} is proportional to the number of reactants N and therefore leads to a decay rate

$$(3-15) \quad k_m(t_0) = -\left. \frac{d}{dt} \ln[\alpha^{\text{DS}}(t)] \right|_{t=t_0} = -\dot{\alpha}^{\text{DS}}(t_0)$$

at time t_0 in analogy to Equation (3-12). In this picture, we can now determine the two contributions

$$(3-16) \quad k_m(t_0) = k_m^{\text{ens}}(t_0) + k_m^{\text{DS}}(t_0)$$

to the total decay rate introduced earlier.

For the first part k_m^{ens} , we assume that the ensemble stays in the x - p_x section associated with $\boldsymbol{y}^\ddagger(t)$. As a result, the point where the ensemble pierces the DS is fixed at $x^{\text{DS}}(t) = 0$ for all times t . This is an effectively one-dimensional model. We start by looking at the linearized dynamics near the NHIM as described in Section 2-4. With the origin at $\boldsymbol{y}^\ddagger = \mathbf{0}$, Equation (2-14) can be written as

$$(3-17) \quad \frac{d}{dt} \boldsymbol{y}(t) = \boldsymbol{J}(t) \boldsymbol{y}(t),$$

where $\boldsymbol{J}(t)$ is the Jacobian of the system's equations of motion evaluated on the trajectory \boldsymbol{y}^\ddagger . The fundamental matrix $\boldsymbol{\sigma}(t)$ obtained by integrat-

ing $\dot{\sigma}(t) = J(t) \sigma(t)$ with $\sigma(t_0) = \mathbf{1}_{2d}$ can then be used to propagate the ensemble from time t_0 to a later time t via

$$\boldsymbol{\gamma}^{\text{ens}}(\alpha, t) = \boldsymbol{\sigma}(t) \boldsymbol{\gamma}^{\text{ens}}(\alpha, t_0). \quad (3-18)$$

We are interested in the point α^{DS} where $\boldsymbol{\gamma}^{\text{ens}}(\alpha, t)$ pierces the DS at $x^{\text{DS}}(t) = 0$, i. e.,

$$\boldsymbol{\sigma}(t) \boldsymbol{\gamma}^{\text{ens}}(\alpha^{\text{DS}}(t), t_0) \cdot \hat{\mathbf{x}} \stackrel{!}{=} 0. \quad (3-19)$$

Inserting the ensemble's parameterization defined in Equation (3-14) yields the reactant fraction

$$\alpha^{\text{DS}}(t) = \frac{\sigma_{x,x}(t) x^{\text{u}}(t_0) + \sigma_{x,p_x}(t) p_x^{\text{s}}(t_0)}{\sigma_{x,x}(t) x^{\text{u}}(t_0) + \sigma_{x,p_x}(t) p_x^{\text{u}}(t_0)}, \quad (3-20)$$

where we have used $x^{\text{s}}(t_0) = x^{\text{u}}(t_0)$. This intermediate result can be substituted into Equation (3-15). Since we are only interested in the instantaneous rate at $t = t_0$, we can simplify the expression using $\boldsymbol{\sigma}(t_0) = \mathbf{1}_{2d}$ as well as $\dot{\sigma}_{x,p_x}(t_0) = J_{x,p_x}(t_0)$ and arrive at

$$k_{\text{m}}^{\text{ens}}(t_0) = J_{x,p_x} \frac{p_x^{\text{u}}(t_0) - p_x^{\text{s}}(t_0)}{x^{\text{u}}(t_0)}. \quad (3-21)$$

A geometric interpretation of $k_{\text{m}}^{\text{ens}}$ can be found in Reference [2].

The second contribution k_{m}^{DS} in Equation (3-16) stems from the fact that in systems with more than one degree of freedom the ensemble may leave the x - p_x section associated with $\boldsymbol{\gamma}^{\ddagger}(t)$. An ensemble moving out-of-plane can mostly be treated as described above by projecting it back onto the x - p_x section. Since the position of the DS $x^{\text{DS}}(\mathbf{y}, \mathbf{p}_y)$ is dependent on the orthogonal modes, however, this may lead to the ensemble intersecting with the DS at $\tilde{x}^{\text{DS}} \neq 0$.

To quantify the effect on k_{m} , consider a small time step δt . In the linear regime, the change $\delta\alpha$ caused by the ensemble drifting out-of-plane can be written as

$$\delta\alpha^{\text{DS}}(t_0) = \frac{\tilde{x}^{\text{DS}}(t_0 + \delta t) - x^{\text{DS}}(t_0)}{x^{\text{u}}(t_0)}, \quad (3-22)$$

where $x^u(t_0)$ accounts for normalization. Using Equation (3-15) and the fact that $x^{\text{DS}}(t_0) = 0$, we obtain

$$(3-23) \quad k_m^{\text{DS}}(t_0) = -\frac{\delta \alpha^{\text{DS}}(t_0)}{\delta t} = -\frac{\tilde{x}^{\text{DS}}(t_0 + \delta t)}{x^u(t_0) \delta t}.$$

The quantities δt and x^u can be freely chosen within certain limits, while $\tilde{x}^{\text{DS}}(t_0 + \delta t)$ can be determined numerically by propagating the particle $\boldsymbol{\gamma}^{\text{ens}}(1, t_0)$ initially located on the DS for δt units of time and projecting it back onto the NHIM using the BCM [92]. By combining the contributions (3-21) and (3-23) according to Equation (3-16), we finally arrive at the instantaneous decay rate $k_m(t; \boldsymbol{\gamma}^\ddagger)$ for a trajectory $\boldsymbol{\gamma}^\ddagger$ on the NHIM given in Equation (3-13).

(c) Floquet rate method

The LMA is significantly cheaper to evaluate than a full ensemble propagation. The numerical effort required, however, can still render it impractical when analyzing many trajectories. When only time-averaged rate constants of periodic orbits are sought-after, a more tractable approach is provided by the *Floquet rate method* first introduced in Reference [103] and later extended in References [2, 88, 174]. It determines the rate constant

$$(3-24) \quad k_F = \mu^u - \mu^s$$

for an orbit on the NHIM with period T via the difference between the Floquet exponents

$$(3-25) \quad \mu^{u,s} = \frac{1}{T} \ln |m^{u,s}|$$

as described in Section 2-4.

The Floquet multipliers m^s and m^u correspond to the stable and unstable manifolds of the NHIM. A defining property of a NHIM is that it is normally hyperbolic (cf. Section 2-1), which means that the decay away from it dominates any eventual internal instabilities [128]. Thus, we can assume that m^s and m^u are the smallest and largest eigenvalues of the monodromy matrix, respectively. Furthermore, the monodromy matrix of any Hamiltonian system is symplectic, which implies that $m^s = 1/m^u$. In such cases, we can simplify Equation (3-24) to

$$(3-26) \quad k_F = 2\mu^u.$$

The Floquet rate method can be generalized to aperiodic trajectories by rewriting Equation (3-24) as

$$k_F \Delta t = \ln |m^u| - \ln |m^s|, \quad (3-27)$$

where the period T has been replaced by an arbitrary time Δt . One can then evaluate the right-hand side of Equation (3-27) for sufficiently long times Δt and apply a linear regression [2] to determine the average slope k_F .

3-6 Integrating the Langevin equation

We now continue with the algorithms used in systems that are subject to noise and friction. A wide variety of numerical integration methods for such systems has been developed over the years [177, 178]. In this work, we employ the *LF-Middle* scheme described in Reference [179] for all Langevin-based calculations (cf. Section 2-2). A single integration step $t \mapsto t + \delta t$ with this scheme reads

$$\mathbf{p}'_{n+1/2} = \mathbf{p}_{n-1/2} + \mathbf{F}(\mathbf{q}_n, t_n) \delta t, \quad (3-28a)$$

$$\mathbf{q}_{n+1/2} = \mathbf{q}_n + \mathbf{M}^{-1} \mathbf{p}'_{n+1/2} \frac{\delta t}{2}, \quad (3-28b)$$

$$\mathbf{p}_{n+1/2} = \text{thermostat}_n(\mathbf{p}'_{n+1/2}), \quad (3-28c)$$

$$\mathbf{q}_{n+1} = \mathbf{q}_{n+1/2} + \mathbf{M}^{-1} \mathbf{p}_{n+1/2} \frac{\delta t}{2}, \quad (3-28d)$$

$$\text{and } t_{n+1} = t_n + \delta t, \quad (3-28e)$$

where thermostat_n denotes one of the thermostat steps defined below. LF-Middle is a leapfrog-type scheme, meaning that the momenta \mathbf{p} always lag behind by half a time step between integration steps. This makes it easy and efficient to implement but requires some care when accurate values for \mathbf{p} need to be processed.

The thermostat step (3-28c) incorporates both random forces $\boldsymbol{\xi}$ (noise) and dissipative forces $-\gamma \mathbf{p}$ (friction) from the environment. For memoryless Langevin baths (LE), this step can be written as [177, 178]

$$\mathbf{p}_{n+1/2} = e^{-\gamma \delta t} \mathbf{p}'_{n+1/2} + \sqrt{k_B T (1 - e^{-2\gamma \delta t})} \mathbf{M}^{1/2} \boldsymbol{\xi}_n. \quad (3-29)$$

The GLE thermostat requires another state variable \mathbf{s}_n with initial value $\mathbf{s}_0 = \mathbf{0}$ that serves as the bath's memory. The thermostat update for friction kernel (2-7) can then be implemented via the three-step procedure [139,

$$(3-30a) \quad \mathbf{p}_{n+1/2}'' = \mathbf{p}_{n+1/2}' + \mathbf{s}_n \frac{\delta t}{2},$$

$$(3-30b) \quad \mathbf{s}_{n+1} = \theta \mathbf{s}_n - (1-\theta)\gamma \mathbf{p}_{n+1/2}'' + \sqrt{2k_B T \gamma \frac{(1-\theta)^2}{\delta t}} \mathbf{M}^{1/2} \boldsymbol{\xi}_n,$$

$$(3-30c) \quad \text{and } \mathbf{p}_{n+1/2} = \mathbf{p}_{n+1/2}'' + \mathbf{s}_{n+1} \frac{\delta t}{2},$$

where $\theta = \exp(-\delta t/\tau)$.

3-7 Mean first-passage times

In Kramers's scenario described in Section 2-3, rates are determined via a classical flux-over-population formula. An alternative ansatz for escape rates can be derived from *mean first-passage times* (MFPTs) [180–186]. Here, we first define a domain associated with the reactant state. Its boundary is equivalent to the DS in flux-over-population methods. An ensemble of states is then prepared within this reactant domain and propagated as described in Section 3-6 until it leaves said domain. The time Δt_j it takes a single state to do so is called its first-passage time, and its inverse ensemble average

$$(3-31) \quad k_{\text{MFPT}} = \frac{1}{\langle \Delta t_j \rangle_j} = \left(\frac{1}{N} \sum_{j=1}^N \Delta t_j \right)^{-1}$$

constitutes a rate. As shown by Reimann, Schmid, and Hänggi [182], this ansatz is mathematically equivalent to Kramers's escape rate provided that both methods assume the same boundary (or DS) of the reactant domain. And just like with the flux-over-population rate discussed in Section 2-3, the boundary has to be chosen carefully to not risk over- or underestimation of the rate.

Part II

APPLICATIONS & PERSPECTIVE

Versions of [transition-state theory](#) can be applied to a wide variety of physical and chemical systems. In this second part, we present selected examples of applications in prototypical and real-world models.

BIFURCATIONS IN A TWO-DIMENSIONAL MODEL SYSTEM

Essential parts of this chapter have previously been published by the author in References [3, 5].

TST was originally developed for the description of chemical reactions. Real-world chemical systems, however, can be very complex. This complexity is hindering when one wants to demonstrate the application of certain numerical methods. And it is not even necessary, as many of the interesting phenomena that can occur near a chemical reaction's TS can still be observed and investigated in simpler systems. Furthermore, many of the methods we developed or adapted as part of this and previous work [1–3, 5] are not restricted to chemical physics but can be applied to a variety of systems [6, 10, 11, 87]. For these reasons, we do not start with a real chemical-reaction model. Instead, we begin by exploring a prototypical model system that features a nonlinear reaction pathway divided by a rank-1 saddle. Thus, we include the most important features of a chemical reaction without restricting ourselves too much.

The aim of this chapter is to uncover and resolve nontrivial structures and dynamics on the NHIM as revealed below. Although finding the NHIM in 1-DoF systems may be challenging (cf. Chapter 5), the dynamics on the NHIM itself is trivial. It only consists of one or more individual points without internal structure. If the system is time-invariant, even a 2-DoF system exhibits integrable dynamics on the NHIM because the effective dynamics is one-dimensional and the energy is conserved. Yet, many real physical and chemical systems are time-dependent and nonintegrable. In the following, we therefore investigate a driven 2-DoF system, which is large enough to exhibit nontrivial behavior but small enough to be visualized.

4-1 Two-dimensional model system

For the investigation of the dynamics on the NHIM and the dependence of the dynamics on parameters of the external driving, we use a two-dimensional model system which has already been studied in previous publications [1–3,

5, 87, 91, 96, 108, 174]. The time-dependent potential

$$(4-1) \quad V(x, y, t) = 2 \exp\left\{-[x - \hat{x} \sin(\omega_x t)]^2\right\} + 2\left[y - \frac{2}{\pi} \arctan(2x)\right]^2$$

describes a two-dimensional, periodically oscillating energy landscape including a rank-1 saddle. The saddle's unstable direction is constructed via a Gaussian barrier along the approximate reaction coordinate x . This barrier separates an unbounded reactant from an unbounded product basin. Besides being physically relevant to chemical reactions, the restriction to unbounded reactant and product basins is a simplification that avoids the global recrossings that would arise if one or both basins were closed. Nevertheless, we emphasize that the presence of closed reactant and product basins would not challenge the methods presented here because the important dynamics is happening in the saddle region. For more information on how to deal with global recrossings see Reference [127].

To make the saddle time-dependent, the barrier's position is driven time-periodically. Such driving may arise by way of coupling between a time-dependent external field and the dipole associated with the reaction coordinate [83, 105]. Both the driving amplitude \hat{x} and frequency ω_x will be varied in the following sections. In order to expand the system to two DoFs, a harmonic oscillator is added through an orthogonal mode y . This new DoF is coupled via the nonlinear term $\arctan(2x)$, resulting in nonseparable dynamics in the vicinity of the reaction without changing the properties on the reactant and product regions. Further system parameters, such as the strength of the harmonic oscillator or the saddle height and width, are not changed throughout this work and are therefore set to fixed values. For simplicity, we use dimensionless units.

This prototypical potential, which can be used to describe chemical reactions qualitatively, is depicted in Figure 4-1 at eight different points in time t . In the following we investigate the dynamics on the NHIM parameterized by the orthogonal modes y , p_y , and time t . As will be shown, periodic trajectories play a particularly important role here. The aim of this chapter is to demonstrate how chemical reactions can be controlled by external driving. We focus on the dependence of the system on the parameters ω_x and \hat{x} since they describe the saddle movement caused by the external driving.

4-2 Overview of phenomena resulting from the driving

Although relatively simple, the model system introduced in the previous section already exhibits rich dynamics. In the following, we first give an

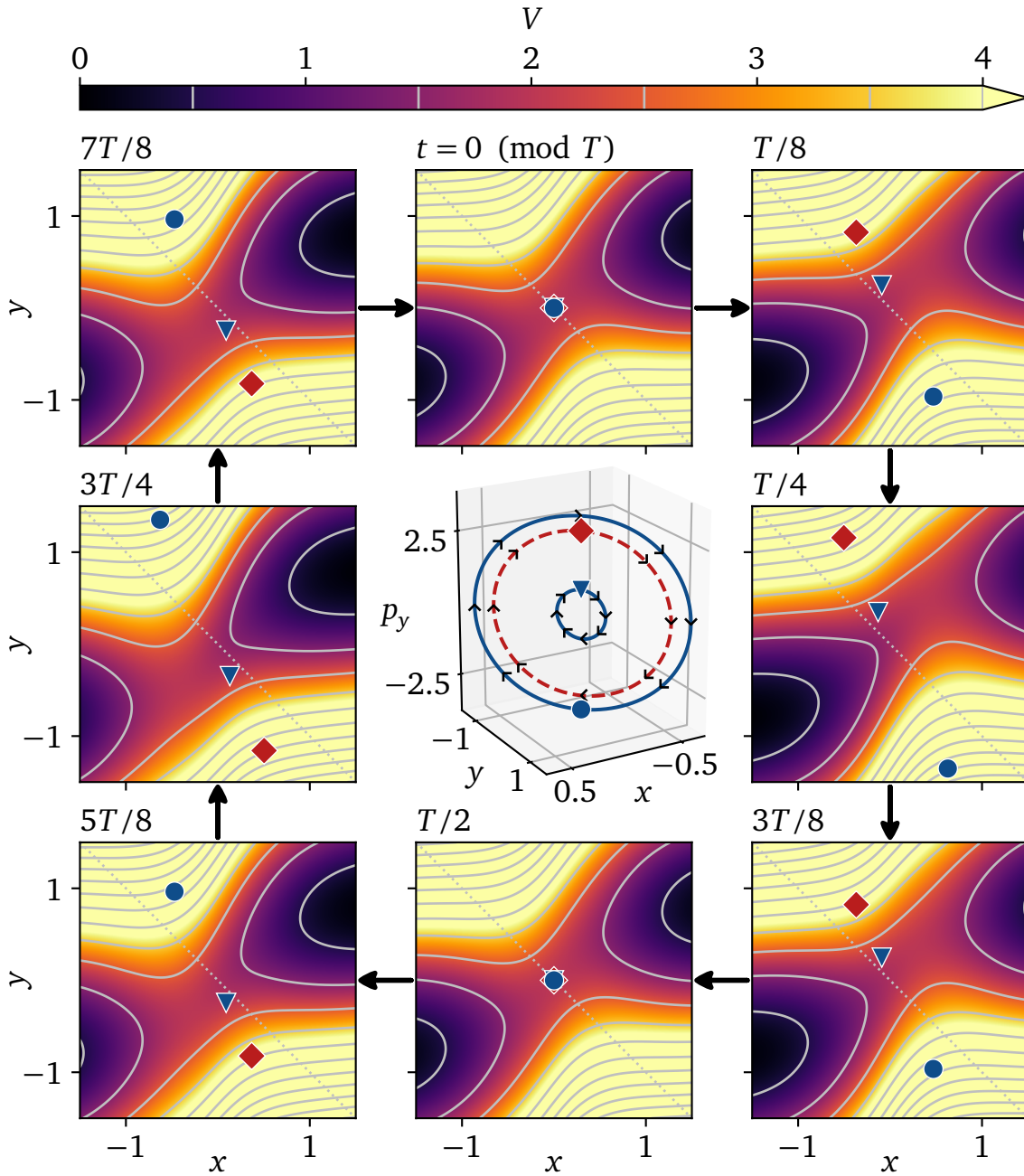


Figure 4-1: Snapshots of the time-dependent potential $V(x, y, t)$ following Equation (4-1) with $\omega_x = 0.77\pi$ and $\hat{x} = 0.4$ over the oscillation period $T = 2\pi/\omega_x$. Diamond, triangle, and circle markers symbolize the positions of three particles with trajectories of period T . Equidistant contour lines with $\Delta V = 1$ are shown in solid gray. A diagonal dotted line per panel serves as a guide to the eye, elucidating the saddle movement. The color scale is capped at $V = 4$. In the center, the periodic trajectories are shown in a three-dimensional subset of the phase space (p_x not shown). Filled markers symbolize positions at $t = 0$ while positions of the particles at the potential snapshots are indicated by black arrow heads pointing in the direction of motion.

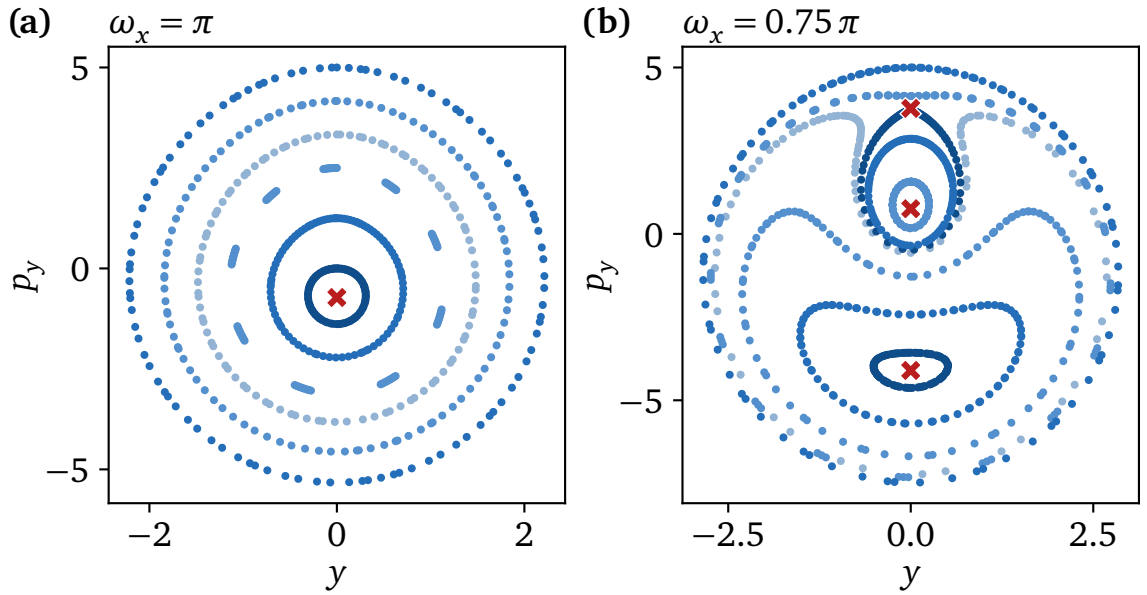


Figure 4-2: Stroboscopic map of selected trajectories (PSOS) started at time $t_0 = 0$ for different frequencies ω_x . The driving amplitude is fixed at $\hat{x} = 0.4$. Crosses indicate fixed points. A color gradient is used to help distinguish neighboring trajectories. **(a)** With $\omega_x = \pi$, a single elliptic fixed point at $(y = 0, p_y \approx -0.72)^\top$ exists. **(b)** When decreasing ω_x to 0.75π , this fixed point moves down to $p_y \approx -4.10$, while a pair of elliptic and hyperbolic fixed points emerges from a saddle-node bifurcation around $\omega_x \approx 0.802\pi$.

overview of the dynamics on the NHIM before discussing various aspects of decay rates in more detail.

(a) Saddle-node bifurcations

We start with a set of driving parameters used in some previous work [1–3, 108], $\omega_x = \pi$ and $\hat{x} = 0.4$. To construct the PSOS, a number of trajectories are started on a specified domain at $t_0 = 0$ and are propagated for 100 periods each. It turns out that a reasonable choice for this domain is the set of points on the p_y axis at $y = 0$. This choice is enough to map the full subspace of the NHIM. That is, given y and p_y , there exists only one x and p_x which keep the phase-space point on the NHIM. Thus, the trajectories are fully specified for a given y , p_y , and t and the restriction of $y = 0$ does not lose any generality in the PSOS shown in Figure 4-2(a).

In the stroboscopic map, we can see a simple structure with a single elliptic fixed point. The elliptical patterns around it indicate that the system's dynamics on the NHIM is regular and nearly integrable. Therefore, trajectories in phase space lie on two-dimensional tori, for which one approximate constant of motion exists [187]. The elliptic fixed point belongs

to an orbit with period $T = 2\pi/\omega_x$. In its neighborhood, resonance gaps can be seen, indicating the existence of periodic orbits with rational winding numbers, i. e., orbits whose period is a rational multiple of the system's period T . Remaining trajectories are quasiperiodic, meaning they have an irrational winding number and that for arbitrary long integration times they would cover the entire torus surface area.

A qualitative change in the system's dynamics occurs in the PSOS when the frequency of driving is decreased to $\omega_x = 0.75\pi$, as can be seen in Figure 4-2(b): The elliptic fixed point from Figure 4-2(a) moves down in p_y . In addition, a pair of fixed points — one elliptic and one hyperbolic — emerges from a so-called saddle-node bifurcation [3, 5, 78, 108, 188–190], as detailed below. As a result, the elliptic structure of the original fixed point gets deformed significantly. While this changes its appearance, it does not lead to chaotic behavior.

From Figure 4-2, it seems natural to assume that there is a bifurcation in the parameter range $0.75\pi < \omega_x < \pi$. To confirm this assumption, we need to examine the fixed points systematically. To do so, fixed points were tracked using a root search algorithm as described in Section 3-4.

Figure 4-3 displays bifurcation diagrams, where the averaged total energy $\langle E[\mathbf{y}^\ddagger] \rangle_t$ of trajectories associated with fixed points is shown as a function of saddle frequency ω_x and driving amplitude \hat{x} . In Figure 4-3(a), the driving frequency is varied between $0.71\pi \leq \omega_x \leq 0.85\pi$. One can clearly see the annihilation of a pair of fixed points — one elliptic and one hyperbolic — in a saddle-node bifurcation at $\omega_x \approx 0.802\pi$. For decreasing frequencies, the original elliptic fixed point from Figure 4-2(a) gets pushed in the negative p_y direction away from the origin, while the new elliptic fixed point formed in the bifurcation slowly converges towards the origin. By contrast, the hyperbolic fixed point's momentum p_y increases for decreasing driving frequencies. Thus, distinguishing the elliptic fixed point near the origin for slow and high driving frequencies must be done with some care.

Bifurcations do not only occur when changing the saddle's frequency but also when altering its driving amplitude. This can be seen in Figure 4-3(b). The saddle frequency was set to $\omega_x = 0.8\pi$, near the parameter where the bifurcation occurs in Figure 4-3(a). Changing the saddle amplitude from $0 < \hat{x} \leq 1.47$ results in two saddle-node bifurcations, one annihilating a fixed-point pair at $\hat{x} \approx 0.47$ and one creating a fixed-point pair at $\hat{x} \approx 0.65$.

(b) Trajectories in position space

Section 4-2 (a) found and investigated a varying number of fixed points on the NHIM. The next step in the classification of the dynamics requires the

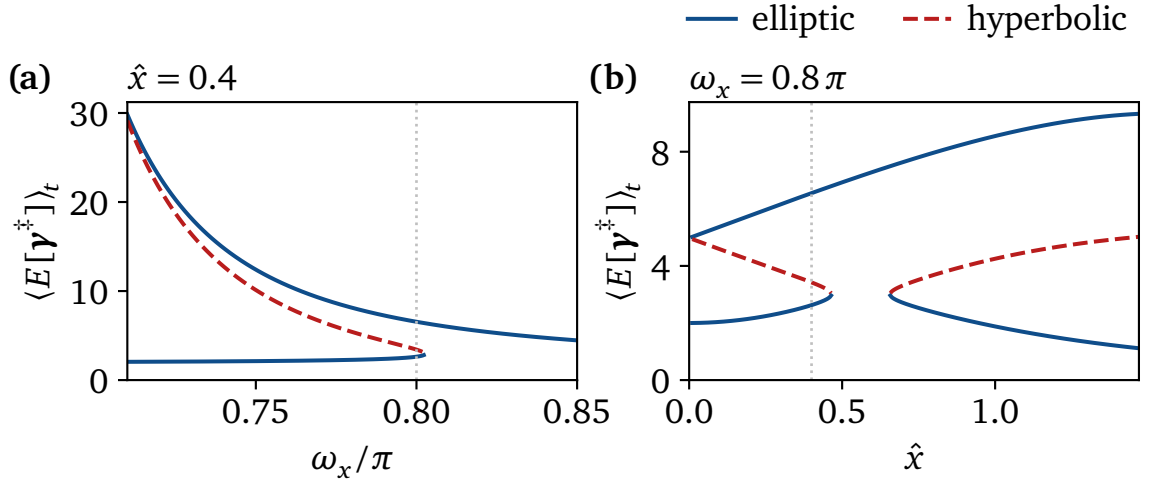


Figure 4-3: (a) Average total energy $\langle E[\mathbf{y}^\ddagger] \rangle_t$ of periodic trajectories \mathbf{y}^\ddagger associated with fixed points (cf. Figure 4-2) as a function of driving frequency ω_x . The driving amplitude is fixed at $\hat{x} = 0.4$. Around $\omega_x \approx 0.802\pi$, a pair of elliptic and hyperbolic fixed points annihilate in a saddle-node bifurcation. (b) Average total energy $\langle E[\mathbf{y}^\ddagger] \rangle_t$ analogous to panel (a) as a function of driving amplitude \hat{x} for $\omega_x = 0.8\pi$. The system exhibits two saddle-node bifurcations around $\hat{x} \approx 0.47$ and $\hat{x} \approx 0.65$. At $\hat{x} = 0$, two orbits have identical potential energies and reversed velocities. Their total energies are therefore degenerate. Vertical lines indicate where the parameter sets of panels (a) and (b) intersect.

characterization of the periodic trajectories associated with these points in position space.

Figure 4-4(a) shows the trajectories associated with the three fixed points in Figure 4-3(a) just below the bifurcation. All three trajectories follow very similar paths roughly orthogonal to the minimum-energy path given by the arctangent in Equation (4-1). The elliptic and hyperbolic fixed points created in the bifurcation belong to trajectories oscillating in phase. By contrast, the trajectory associated with the second elliptic fixed point oscillates in antiphase with a higher amplitude. This is in accordance with its higher mean energy $\langle E[\mathbf{y}^\ddagger] \rangle_t$ as shown in Figure 4-3(a). The slight curvature of the trajectories is caused by the system's nonlinearity.

The nonlinearity is also likely responsible for the bifurcation at $\omega_x \approx 0.802\pi$: In the high-energy limit $\langle E[\mathbf{y}^\ddagger] \rangle_t \rightarrow \infty$, trajectories mostly see an effective potential of the form $V(x, y) = 2y^2$. This potential leads to an eigenfrequency of $\omega = 2 \approx 0.637\pi$ for oscillations along the orthogonal mode y . For lower energies $\langle E[\mathbf{y}^\ddagger] \rangle_t$, however, the barrier and the nonlinear coupling (through the arctangent) need to be taken into account. As a result, the direction of the orthogonal mode changes approximately to $y - x$

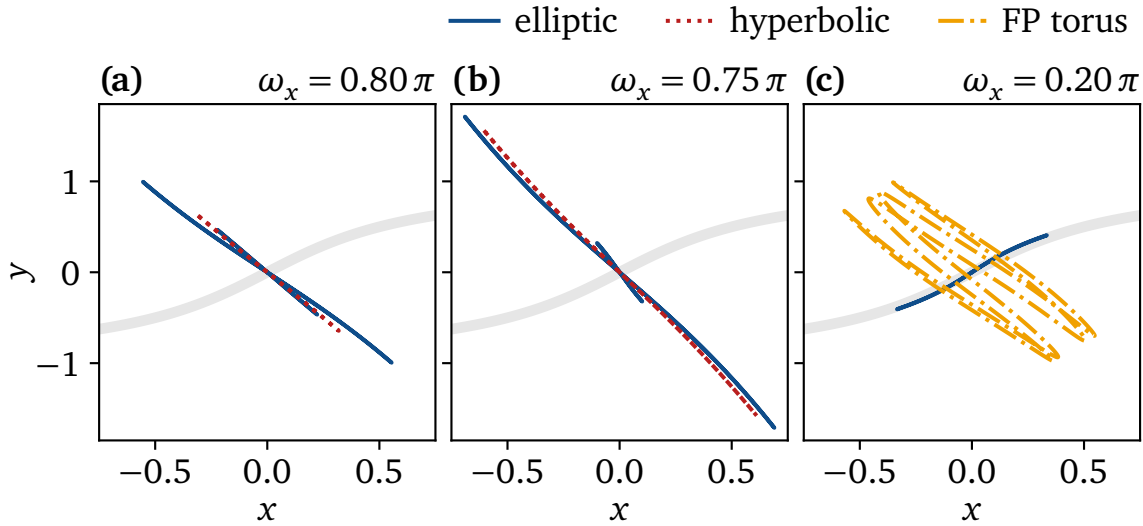


Figure 4-4: Position $(x, y)^\top$ of periodic orbits on the NHIM for different frequencies ω_x . The driving amplitude is fixed at $\hat{x} = 0.4$. The minimum-energy path is shown as a thick, light gray line. **(a)** With a frequency $\omega_x = 0.8\pi$ just below the bifurcation, all three fixed-point trajectories perform a single oscillation per period roughly orthogonal to the minimum-energy path. **(b)** Decreasing the frequency to $\omega_x = 0.75\pi$ leads to the same configuration in principle, although with significant changes to the oscillation amplitudes. **(c)** With $\omega_x = 0.2\pi$ the situation changes fundamentally. The trajectory associated with the central elliptic fixed point now roughly follows the reaction coordinate approximated by the minimum-energy path. In doing so, the trajectory always stays near the saddle point. Trajectories belonging to the fixed-point torus, on the other hand, oscillate in direction of the orthogonal mode. Furthermore, these trajectories oscillate many times per driving period and fan out instead of following the same path back and forth.

with an increased eigenfrequency. The system therefore supports a range of frequencies as a function of energy. Driving the system with a specific frequency ω_x within this range selects the corresponding trajectory and associated fixed point.

In Figure 4-3(a), two branches show a strong increase of the fixed-point energies $\langle E[\mathbf{y}^\ddagger] \rangle_t$ when the driving frequency ω_x is lowered, quickly rising beyond the limits of numerical feasibility. This diverging behavior can also be explained by the aforementioned mechanism since the approximation $V(x, y) = 2y^2$ is only valid for $\langle E[\mathbf{y}^\ddagger] \rangle_t \rightarrow \infty$. The sensitivity of the oscillation amplitude is visible in the dramatic change in the amplitude of the periodic orbits in Figures 4-4(a) and 4-4(b) resulting from the slight reduction in ω_x from 0.8π to 0.75π . The fact that the oscillation of the smaller-amplitude

orbit decreases between the cases in Figures 4-4(a) and 4-4(b) can be attributed to its antiphase oscillation.

Upon lowering the frequency to $\omega_x = 0.2\pi$ [cf. Figure 4-4(c)], only the antiphase fixed point remains. In contrast to Figures 4-4(a) and 4-4(b), its motion now oscillates in phase along the minimum-energy path. In addition, a torus with infinitely many fixed points has emerged. A typical trajectory associated with one fixed point on the torus is shown in Figure 4-4(c). Contrary to all the trajectories shown so far, it oscillates multiple times per period and fans out instead of remaining on a single periodic path. These fixed points can be attributed to a sign change in the torus's winding number.

(c) Resonant tori

Changing the driving frequency to $\omega_x = 0.55\pi$ results in the occurrence of two elliptic fixed points with period $2T$. This can be observed in the PSOS by choosing a proper resolution, as shown in Figure 4-5. Note that the stroboscopic map still records points every T units of time. The fixed point located at the center of the phase space [cf. Figure 4-5(a)] is the elliptic fixed point that emerged from the saddle-node bifurcation in Figure 4-3(a).

The fixed points with period $2T$ can be understood using the Poincaré–Birkhoff fixed-point theorem [187, 191]. It allows the use of the PSOS to predict structural changes of resonant tori when the system is perturbed. Specifically, a change in the driving frequency can be seen in Figure 4-5 as a perturbation which causes some tori with rational winding numbers to be destroyed. It results in an even number of fixed points, alternating between elliptic and hyperbolic ones. Increasing the perturbation of such a system can also tear apart the tori in the vicinity of the $2T$ elliptic fixed points, forming new fixed points. Eventually, this leads to self-similar structures. In principle, one could expect to see such self-similar structures when further zooming the enlarged panels 4-5(b) and 4-5(c). However, we did not continue such zooming here because resolution is limited by numerical precision.

4-3 Decay rate enhancement

We continue by investigating two examples in more detail in which the external driving can be seen to affect the dynamics of the activated complex.

The left column of Figure 4-6 shows the time-averaged total energy $\langle E[\mathbf{y}^\ddagger] \rangle_t$ of trajectories \mathbf{y}^\ddagger on the NHIM for two values of ω_x . At $\omega_x = 0.81\pi$, $\langle E[\mathbf{y}^\ddagger] \rangle_t$ reveals a region in phase space with low-energy trajectories. This region is accompanied by a local maximum in the decay rate k_F , as can

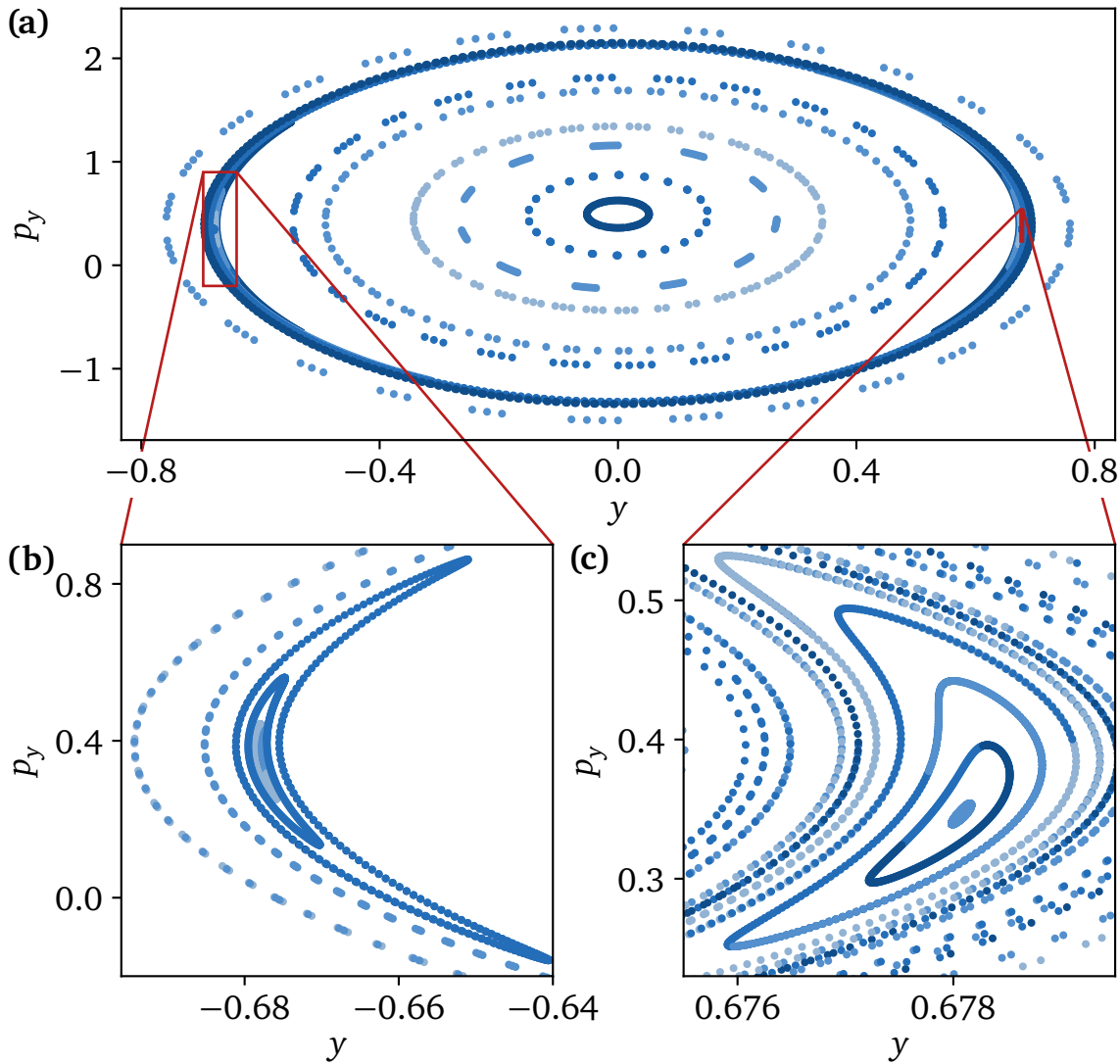


Figure 4-5: Stroboscopic map of trajectories (PSOS) started at time $t_0 = 0$ for driving frequency $\omega_x = 0.55 \pi$ and driving amplitude $\hat{x} = 0.4$. A color gradient is used to help distinguish neighboring trajectories. **(a)** From the overview an elliptic fixed point is clearly visible. **(b)–(c)** Magnified sections of panel **(a)** reveal two more elliptic fixed points. Different magnifications for the left/right-hand side are used since panel **(a)** is symmetric under reflection at $y = 0$.

be seen in the right panel of Figure 4-6(a). The overlaid PSOS highlights an elliptic fixed point belonging to the associated periodic orbit, similar to Figure 4-2(a). It can be seen as the dominant trajectory in the sense that decay rates from this trajectory are also characteristic of neighboring trajectories.

For decreasing ω_x , two new fixed points and, hence, periodic trajectories emerge again, as can be seen in Figure 4-6(b) at $\omega_x = 0.77 \pi$. These trajectories are shown in Figure 4-1 for the elliptic (solid blue lines) and hyperbolic

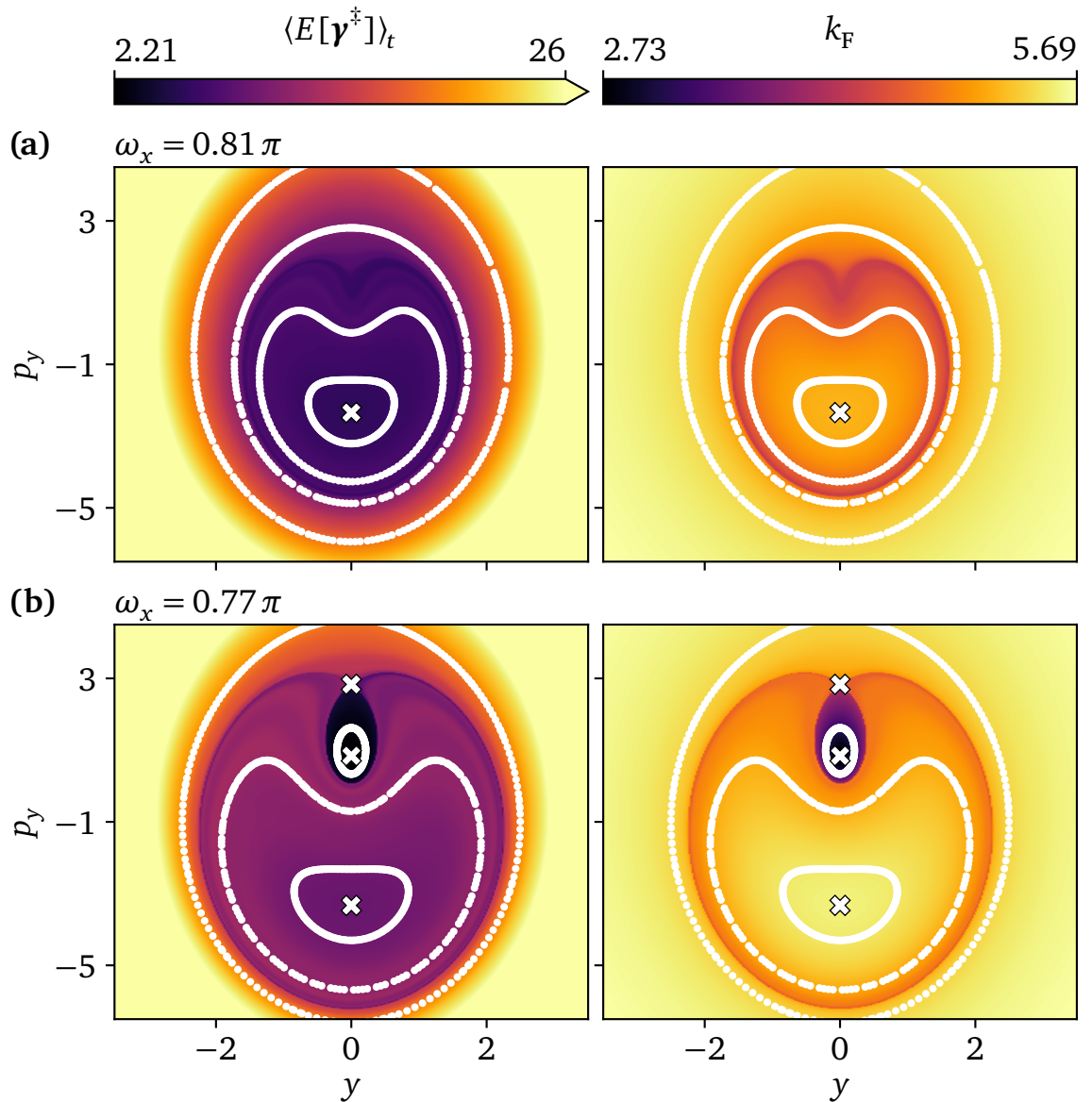


Figure 4-6: Average total energy $\langle E[\boldsymbol{\gamma}^\ddagger] \rangle_t$ (left column, capped at $\langle E[\boldsymbol{\gamma}^\ddagger] \rangle_t = 26$) and Floquet rate constant k_F (right column) of trajectories $\boldsymbol{\gamma}^\ddagger$ started at position $(y, p_y)^\top$ and time $t_0 = 0$ on the NHIM. Shown are typical plots at $\hat{x} = 0.4$ (a) before ($\omega_x = 0.81\pi$) and (b) after ($\omega_x = 0.77\pi$) the bifurcation. To elucidate the structure, a stroboscopic map of selected trajectories (PSOS, white dots) has been overlaid highlighting the existence of one elliptic fixed point before and two elliptic as well as one hyperbolic fixed point after the bifurcation (white crosses). While the elliptic fixed points are always characterized by local minima in $\langle E[\boldsymbol{\gamma}^\ddagger] \rangle_t$, they feature either a local minimum or maximum in k_F .

(dashed red line) fixed points. This saddle-node bifurcation qualitatively changes the dynamics on the **NHIM**. While the new elliptic fixed point is still characterized by a local minimum in $\langle E[\mathbf{y}^\ddagger] \rangle_t$, it now also features a local minimum in k_F instead of a maximum. In addition, its energy $\langle E[\mathbf{y}^\ddagger] \rangle_t$ is much lower compared to the original elliptic fixed point at momentum $p_y = \dot{y} \approx -3$.

The second example for the influence of external driving on the dynamics on the **NHIM** is illustrated in Figure 4-7. At a fixed $\omega_x = \pi$, only a single periodic trajectory was found in the examined parameter regime. Particles near this periodic trajectory exhibit a change in their stability that depends on the system's driving amplitude \hat{x} . We illustrate the change in the stability using the time it takes the particle to reach a distance of $|\Delta x| = 0.05$ from the periodic trajectory. When only a small driving is applied, the particle stays in the saddle region for a relatively long time. This in turn indicates a low decay rate k_F . When increasing the amplitude, stability initially decreases for medium driving only to increase again for large driving. As a result, there must be a local maximum in the system's decay rate k_F allowing for rate enhancement through optimization of \hat{x} .

These two examples demonstrate that the dynamics of trajectories on or near the **NHIM** can be drastically altered through modification of the driving parameters. This is summarized in Figure 4-8 through the calculation of the decay rates k_F as a function of the driving frequency and amplitude. As these are only one-dimensional sections through the two-dimensional space of possible driving parameters, they serve here as examples only. Specifically, they are not meant to represent an exhaustive or exclusive set. As such, any extremal values in one of these sections may not necessarily be extremal in the full parameter space. Nevertheless, the existence of such extrema in sections of parameter space is enough to demonstrate that these systems are sensitive to the driving.

The bifurcation observed in Figures 4-2 and 4-6 is visible in Figure 4-8(a). At larger driving frequencies, there exists a single elliptic fixed point. When lowering ω_x , its rate constant k_F steadily increases. Around $\omega_x = 0.80\pi$, two new fixed points with lower values of k_F emerge in a saddle-node bifurcation. Furthermore, a comparison with the trajectories from Figure 4-1 suggests that high rates are accompanied by large motion in the orthogonal mode $(y, p_y)^\top$.

We demonstrated through Figure 4-7 that there exists a minimum in stability for medium driving. This manifests itself in Figure 4-8(b) by means of a maximum in k_F . When varying ω_x , this extremum persists qualitatively the same, differing mainly in position and height. The varying height of the extremum for different ω_x can be connected to the slope of the upper

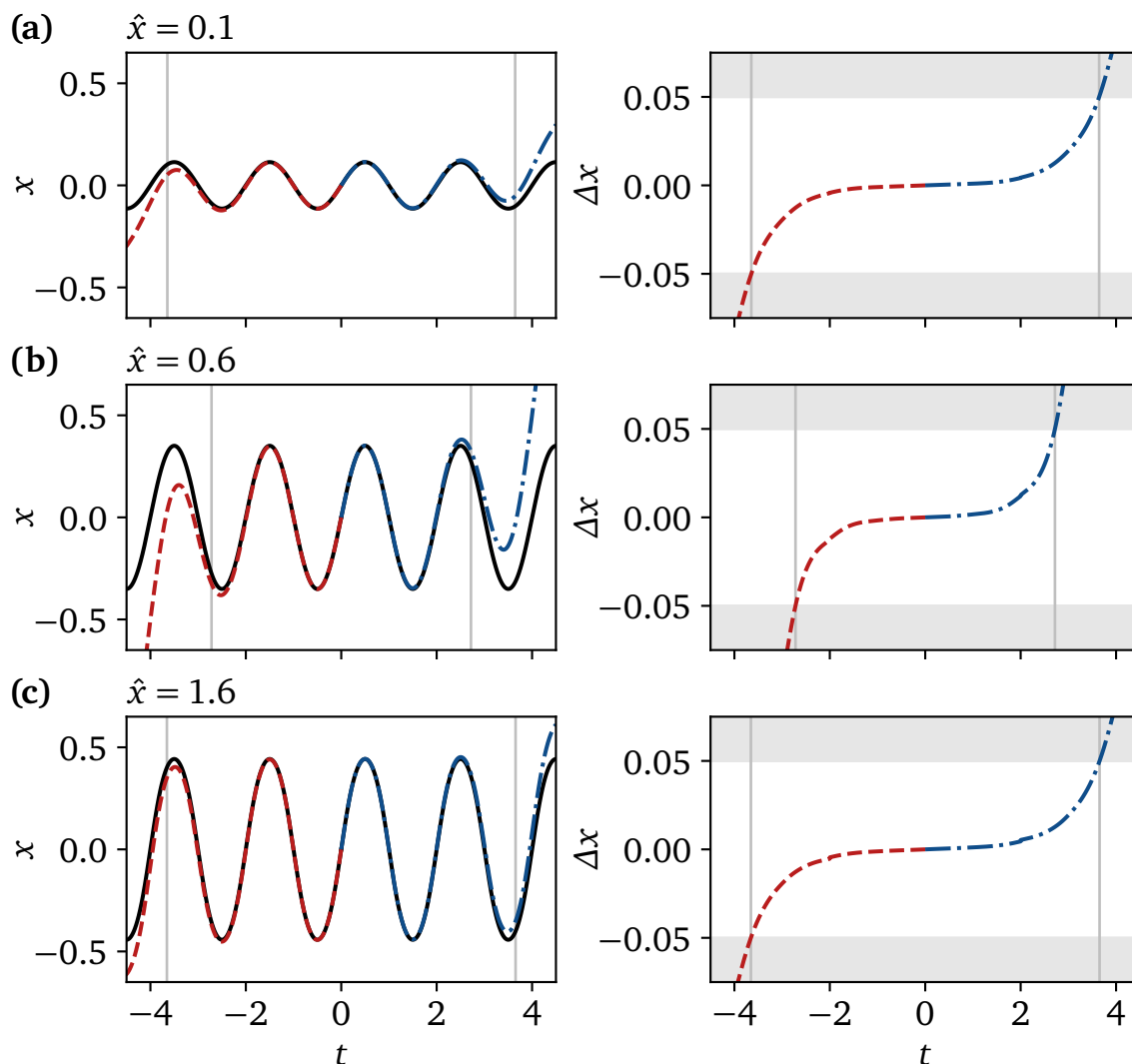


Figure 4-7: Position x over time t of trajectories in systems with **(a)** small ($\hat{x} = 0.1$), **(b)** medium ($\hat{x} = 0.6$), and **(c)** large ($\hat{x} = 1.6$) driving. Driving frequency in all cases is $\omega_x = \pi$. For each parameter set, the periodic trajectory on the NHIM (black solid) as well as a trajectory offset by $\Delta p_x = 10^{-3}$ at $t_0 = 0$ (red dash-dotted/blue dashed) are shown. The style change indicates where the offset trajectories cross from the reactant to the product side. The stability of these trajectories is indicated in the right column by the time interval (vertical lines) where the deviation Δx from the TS is less than 0.05 (nonshaded region). Stability is minimal for medium driving.

curve in Figure 4-8(a). Note that all curves, independent of ω_x , must meet at $k_F(\hat{x} = 0) \approx 2.762$ since a vanishing amplitude is equivalent to the static case.

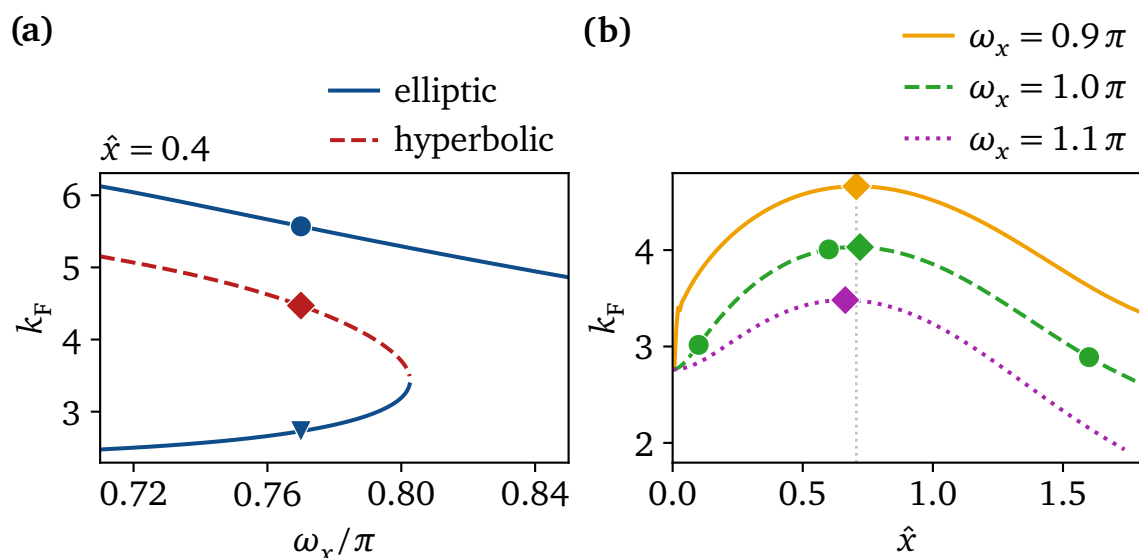


Figure 4-8: (a) Floquet rate k_F as a function of driving frequency ω_x for two elliptic and one hyperbolic fixed point, each corresponding to a periodic trajectory. At $\omega_x \approx 0.802\pi$, two fixed points vanish in a saddle-node bifurcation (cf. Section 4-2). The three markers correspond to the trajectories shown in Figure 4-1. (b) Floquet rate k_F as a function of driving amplitude \hat{x} for three different driving frequencies ω_x . Only a single fixed point (i. e., periodic trajectory) was found per set of parameters considered here. Green circle markers indicate the parameter sets used in Figure 4-7 while diamonds mark each curve’s maximum. The vertical gray line acts as a guide to the eye.

4-4 Reaction geometry

The results reported in the previous sections relate only to the dynamics *on* the NHIM. Making predictions about real chemical reactions, however, requires us to connect to the dynamics *off* the NHIM. More specifically, we need to address when and how the NHIM can influence reactive trajectories, i. e., those connecting the reactant to the product basins.

The NHIM represents — by construction — the minimum energy a trajectory needs while crossing the DS at a given value of the orthogonal modes $(y, p_y)^T$. It is therefore natural to assume that a significant portion of reactants in a thermally distributed ensemble would pass close to the NHIM while reacting. Additionally, for reasons of continuity, we can expect these trajectories to behave similarly to those on the NHIM for some finite time. This provides a possible connection between the dynamics on and off the NHIM.

In a driven system, reactants may gain or lose energy while climbing the potential barrier. A trajectory’s energy $E[\boldsymbol{\gamma}]$ very close to the NHIM can

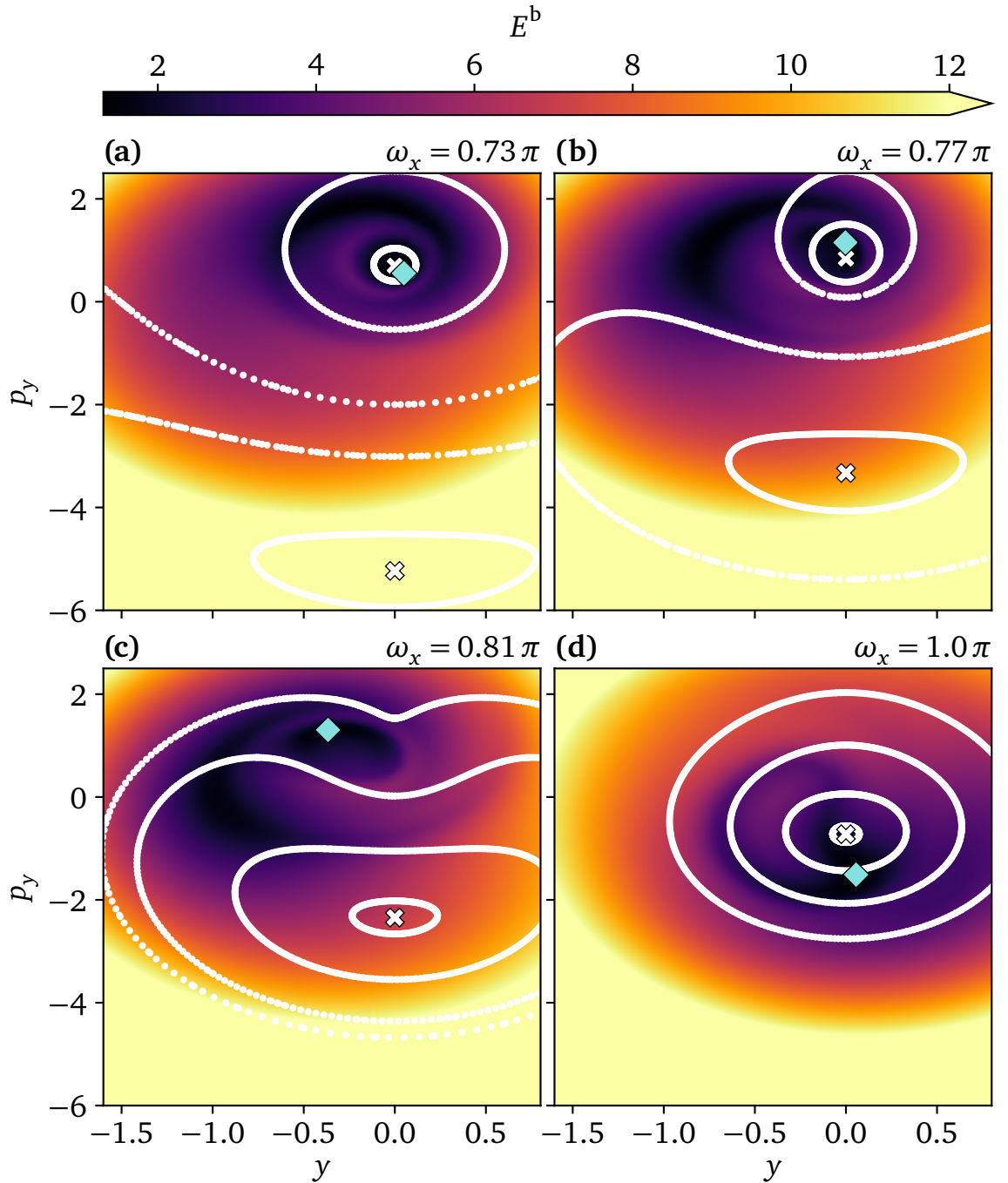


Figure 4-9: Local threshold energy $E^b = \lim_{t \rightarrow -\infty} E[\boldsymbol{\gamma}](t)$ of trajectories $\boldsymbol{\gamma}(t)$ started from position $(y, p_y)^\top$ close to the NHIM at crossing time $t_0 = 0$ and propagated back to the initial time $t \rightarrow -\infty$. A PSOS showing the NHIM's structure is overlaid for comparison. White crosses mark the positions of elliptic fixed points. The diamond marker in each panel is placed at the global spatial minimum $E_{\text{th}}^b(t_0) = \min_{y, p_y} E^b(y, p_y, t_0)$. The panels were calculated for different driving frequencies (a) $\omega_x = 0.73\pi$, (b) $\omega_x = 0.77\pi$, (c) $\omega_x = 0.81\pi$, and (d) $\omega_x = \pi$ as indicated above each panel. The driving amplitude is $\hat{x} = 0.4$ for all panels. The color scale is capped at $E^b = 12$.

thus differ from its initial energy $E^b = \lim_{t \rightarrow -\infty} E[\boldsymbol{\gamma}](t)$ in the reactant basin. The structure of the **NHIM** can be connected to the reactant basins through propagation back in time. For each fixed orthogonal mode $(y, p_y)^\top$ and time t_0 , we first obtain the position $(x, p_x)^\top$ of the **NHIM**. A shift of this point by $\Delta p_x = +10^{-5}$ yields a point on a reactive trajectory which closely passes the **NHIM**. We then propagate the trajectory backward in time until we are sufficiently far away from the moving barrier. The trajectory's energy E^b at this early time — which we refer to as the *local threshold energy* — will then be approximately conserved. Through sampling $(y, p_y)^\top$, we then obtain the distribution of local threshold energies and the corresponding initial points in phase space of the reactive trajectories. Figure 4-9 reports the results of this calculation for crossing time $t_0 = 0$ at four driving frequencies ω_x around the bifurcation shown in Figure 4-8(a). For comparison, the structure of the **NHIM** as revealed by a **PSOS** has been overlaid in each case.

The **PSOS** reveals two elliptic fixed points on the **NHIM** at the driving frequencies below the bifurcation [cf. Figures 4-9(a) and 4-9(b)]. Although the lower one cannot be seen in the structure of the local threshold energy, there is a correlation between E^b and the upper fixed point. This is consistent with the fact that the lower fixed point is associated with higher decay rates and higher average trajectory energies as shown in Figures 4-3(a), 4-6(b) and 4-8(a). Trajectories consequently spend less time near the **NHIM**, and we expect less correlation with the dynamics on the **NHIM**. Conversely, there is a very good match between the *global threshold energy*

$$E_{\text{th}}^b(t_0) = \min_{y, p_y} E^b(y, p_y, t_0) \quad (4-2)$$

and the position of the upper fixed point, i. e., the trajectory on the **NHIM** with the least average energy [cf. Figure 4-6(b)].

Closer to the bifurcation, we find the structure of E^b starting to change [cf. Figures 4-9(b) and 4-9(c)]. Low-energy regions seem to flow out in a counter-clockwise spiral-like structure. The minimum E_{th}^b , however, stays near the upper fixed point. It only starts to move once this fixed point disappears in the bifurcation. Following a counter-clockwise trajectory itself, it moves down towards the remaining fixed point, slowly converging for increasing driving frequency ω_x [cf. Figure 4-9(d)].

If we assume initial energies of a reactant ensemble to be thermally distributed, then we can expect most of these reactants to react via paths related to low- E^b regions at the crossing time t_0 . The bifurcation, therefore, should change the geometry of the reaction dynamics at least qualitatively. This change, as indicated by the movement of the global spatial minimum of the threshold energy E_{th}^b , appears to be smooth across the bifurcation. As a

consequence, we can anticipate that the reaction rates to be presented in the next section will not exhibit a discontinuity around the bifurcation.

4-5 Reaction probability

We now address the degree to which reaction rates — not just decay rates — can be obtained from the structure of the NHIM. Following Farkas and Kramers [27, 111, 182, 192], the reaction rate is determined by the ratio of the reactive flux across a DS divided by the reactant population at steady-state conditions. This presumes a boundary condition in which the reactants are continuously populated at the well according to an equilibrium condition. Here we assume that the reactants are initially thermally distributed, and set the initial distribution in velocities to be that of Boltzmann at temperature T and located in the reactant basin far from the NHIM. The system is then propagated semi-microcanonically — viz., including external driving but neglecting friction and noise. This corresponds to a system which is very weakly coupled to an external bath. The rates that one would obtain in this way are therefore good approximations in cases in which the rate is fast compared to the dissipation.

For numerical expedience, here we obtain the reaction fraction rather than the rates using the flux over population approach. The reactant fraction is the fraction of particles that react — without being reflected and returning to the reactant basin — to products given the initial distribution. The reference ensemble simulation is constructed as follows. For every set of parameters, we initialize an ensemble of 10^7 reactants at position $(x = -8, y = -1)^T$, that is, far from the saddle on the minimum-energy path. Velocities p_x and p_y are chosen according to a Maxwell–Boltzmann distribution of temperature $k_B T = 0.4 \ll E^\ddagger$, where $E^\ddagger = 2$ is the potential energy of the saddle point. Negative velocities result in trajectories that cannot react because the reactant basin is unbounded. We thus include only positive velocities $p_x \geq 0$ by taking the absolute value. The initial time is chosen based on a uniform random distribution. Each reactant is then propagated forward in time until it leaves the reaction region. Trajectories passing $x < -8$ are classified as nonreactive and those passing $x > +4$ as reactive. Besides the fraction of reactive trajectories χ_r^e , we additionally record the minimal initial energy E_{th}^e of the reactive subensemble, referred to as the *ensemble threshold energy*. The results for various values of the driving parameters ω_x and \hat{x} are shown as circle and diamond markers in Figures 4-10 and 4-11.

Alternatively, we can consider the dynamics on the NHIM directly using the spatial minimum E_{th}^b as the effective minimum barrier height; see

Section 4-4. We employ modern global minimization routines to make the determination of E_{th}^{b} as efficient as possible. Specifically, we use simplicial homology global optimization [193] with Sobol’ sampling [194] and the Nelder–Mead simplex method [195] for local optimization as implemented in the Python library SciPy [175]. The resulting E_{th}^{b} is still dependent on the crossing time t_0 . To account for this fact, we consider both the average $\langle E_{\text{th}}^{\text{b}} \rangle_{t_0}$ and the minimum $\min_{t_0} E_{\text{th}}^{\text{b}}$ in t_0 going forward. Both quantities are shown in the left axes of Figures 4-10 and 4-11 for multiple driving-parameter ranges. Unsurprisingly, the minimum ensemble energy E_{th}^{e} is close to but always larger than $\min_{t_0} E_{\text{th}}^{\text{b}}$.

The most straightforward way to obtain a reaction probability from a barrier height is by evaluating the ensemble’s complementary cumulative distribution function — also known as the survival function. In energy space, Maxwell–Boltzmann ensembles follow a χ^2 distribution with argument $2E/(k_{\text{B}}T)$. Here, we report the survival probability $\text{SF}_E^{(2)}$ according to the energy distribution over the two-dimensional configuration space x – y . Curiously, the agreement in the reactive probability (not shown here) was better in the cases reported in Figure 4-11 when we evaluated the survival probability using only the distribution over the reactive degree of freedom x . For reactive trajectories, this circumstance suggests that the nonlinear coupling between x and y is not strong enough to lead to a significant energy exchange between the reaction coordinate and the orthogonal mode. The dynamics on the NHIM, however, is definitely affected by the nonlinear coupling as shown by the bifurcation in Figure 4-8. Finally, we calibrate the resulting curve by linearly scaling it to match the first value of the ensemble calculation. The result is shown in the right axes of Figures 4-10 and 4-11. There is a clear correlation between χ_r^{e} and the survival function of $\min_{t_0} E_{\text{th}}^{\text{b}}$ with very good agreement for $\hat{x} \lesssim 0.8$. The average $\langle E_{\text{th}}^{\text{b}} \rangle_{t_0}$, on the other hand, yields worse results in most cases. It can only slightly beat $\min_{t_0} E_{\text{th}}^{\text{b}}$ for very high driving amplitudes \hat{x} . That is, it appears that the deviations in the reactive percentage between the use of the global reactive flux and the NHIM-based approaches arise because the globality presumed in the latter begins to break down as the particles are driven harder and farther away from the reactive region.

4-6 Conclusion and outlook

We have investigated the constrained dynamics on the NHIM in a time-dependent two-dimensional system. Using PSOSs, we demonstrated the occurrence of structural changes of the dynamics, viz., bifurcations of pe-

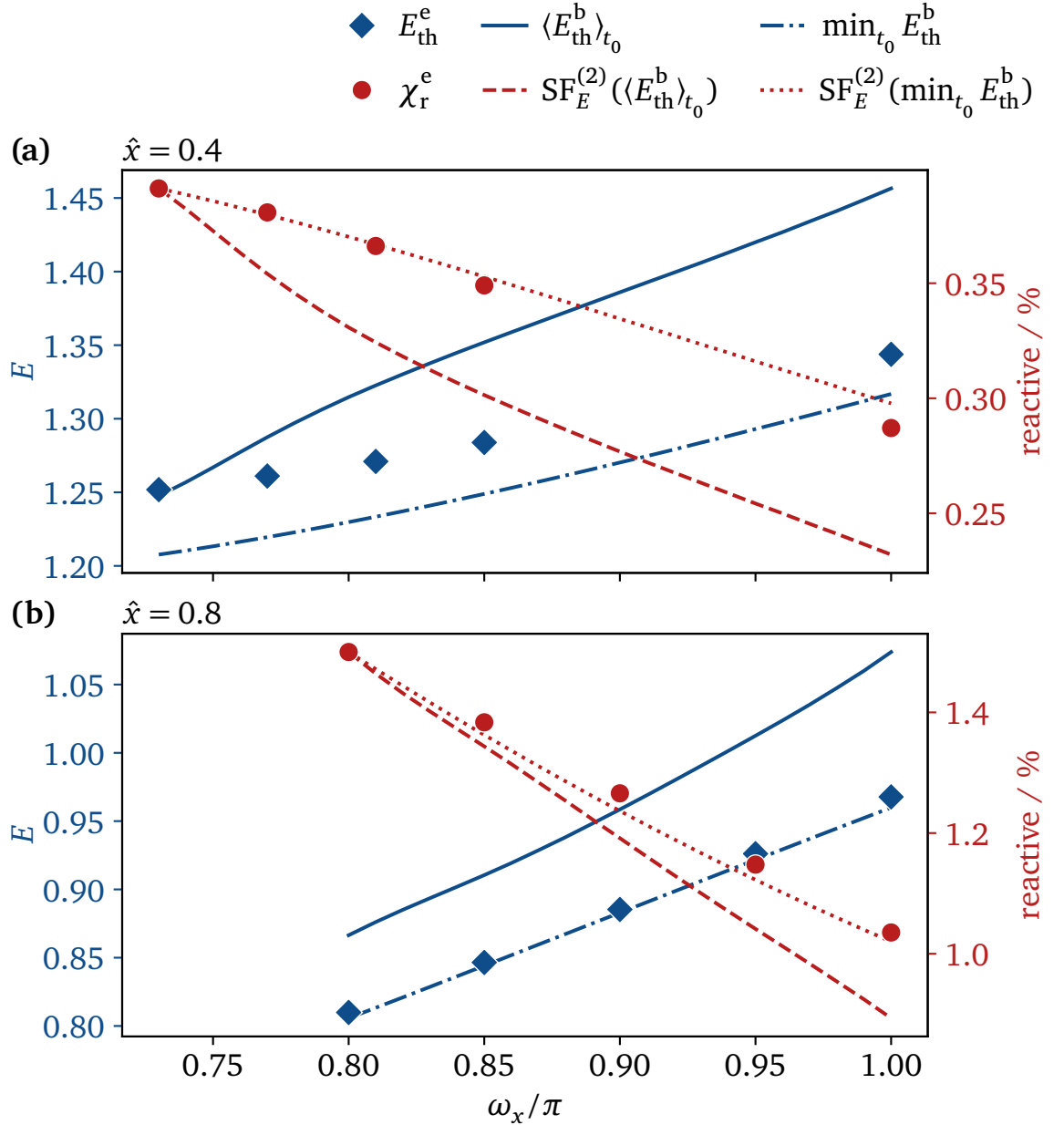


Figure 4-10: Ensemble threshold energy E_{th}^e (diamond markers) and fraction of reactive trajectories χ_r^e (circle markers) for the ensemble calculation described in Section 4-5. Each of the two panels varies driving frequency ω_x while driving amplitude is kept fixed at (a) $\hat{x} = 0.4$ or (b) $\hat{x} = 0.8$, respectively. For comparison, calculations based on the global minimum $E_{\text{th}}^b(t_0) = \min_{y,p_y} E^b(y, p_y, t_0)$ of the local threshold energy E^b akin to Figure 4-9 are shown. Specifically, the average $\langle E_{\text{th}}^b \rangle_{t_0}$ and minimum $\min_{t_0} E_{\text{th}}^b$ in crossing time t_0 are shown with solid and dash-dotted lines, respectively. Evaluating the survival function $\text{SF}_E^{(1)}$ of a one-dimensional Maxwell–Boltzmann distribution in energy space and scaling the results to fit the first ensemble data point yields the dashed and dotted lines, respectively. Parameter ranges differ due to numerical stability.

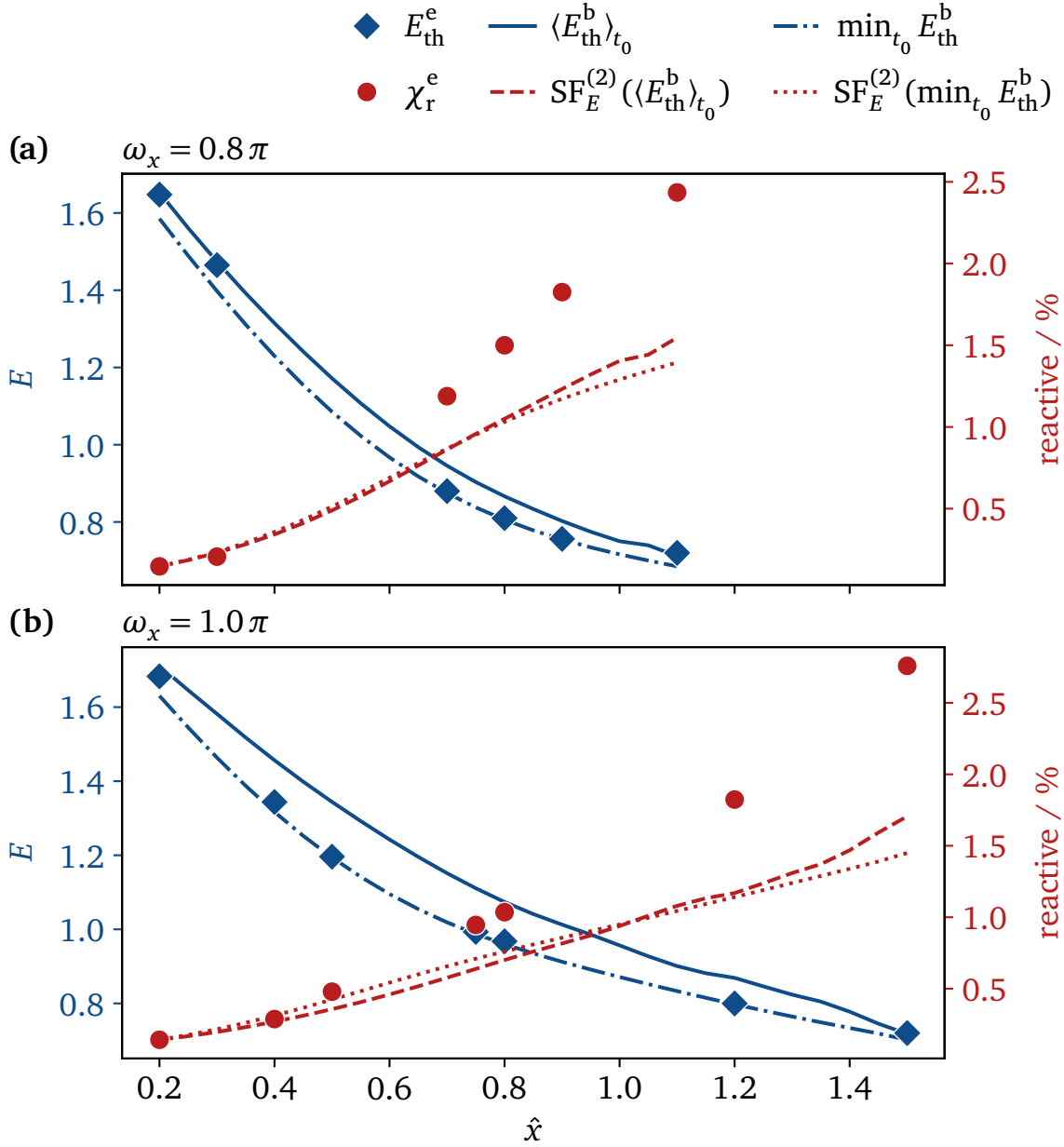


Figure 4-11: Ensemble threshold energy E_{th}^e (diamond markers) and fraction of reactive trajectories χ_r^e (circle markers) for the ensemble calculation described in Section 4-5. Each of the two panels varies driving amplitude \hat{x} while driving frequency is kept fixed at **(a)** $\omega_x = 0.8\pi$ or **(b)** $\omega_x = \pi$, respectively. For comparison, calculations based on the global minimum $E_{\text{th}}^b(t_0) = \min_{y,p_y} E^b(y,p_y,t_0)$ of the local threshold energy E^b akin to Figure 4-9 are shown. Specifically, the average $\langle E_{\text{th}}^b \rangle_{t_0}$ and minimum $\min_{t_0} E_{\text{th}}^b$ in crossing time t_0 are shown with solid and dash-dotted lines, respectively. Evaluating the survival function $\text{SF}_E^{(1)}$ of a one-dimensional Maxwell–Boltzmann distribution in energy space and scaling the results to fit the first ensemble data point yields the dashed and dotted lines, respectively. Parameter ranges differ due to numerical stability.

riodic **TS** trajectories when changing the amplitude or frequency of the external driving. In particular, periodic **TS** trajectories with the same period as the external driving but significantly different parameters such as mean energy compared to the ordinary **TS** trajectory can be created in a saddle-node bifurcation.

The model system investigated in this chapter, featuring a periodically driven rank-1 saddle, is paradigmatic of many chemical reactions in which the reaction takes place along a reaction path which is in turn affected by the mode to which it is most strongly coupled to. We characterized the dependence of the system's dynamics on the parameters of the periodic driving at the saddle, i. e., through its frequency and amplitude. The dynamics of trajectories on the **NHIM** is unstable because of its proximity to the rank-1 saddle, but it can nevertheless be obtained numerically through the use of stabilizing techniques as shown here. The resulting dynamics was analyzed through stroboscopic maps, and observed to be regular for all parameter sets which have been investigated. At low driving frequencies of the saddle, a fixed point with a period twice that of the driving was observed. At higher frequencies, it was also possible to track the fixed points and observe the creation and annihilation of pairs of fixed points in saddle-node bifurcations. The behavior of the periodic trajectories was also projected onto position space leading to the observation that the saddle frequency has a significant influence on the oscillation direction of the trajectories.

We have further demonstrated that decay rates and the reaction geometry can be manipulated by external driving. Based on this, we have found a connection between properties of the **NHIM** and properties of reacting trajectories. This, in turn, has allowed us to predict reaction probabilities without having to propagate large ensembles for each set of parameters, providing further insights into the dynamics of chemical reactions. In the future, these results could be used to control and optimize the reaction rate of chemical reactions. To achieve this goal, however, it is required to extend the methods discussed here to models explicitly describing particular chemical reactions. Promising candidates include the isomerization reactions of LiCN [118–120, 196] — which will be discussed using different methods in Chapter 7 — KCN [197, 198], and ketene [169, 199–202]. Additionally, the results have to be extended to include noise and friction (i. e., Langevin dynamics) in order to be applicable to real chemical reactions.

These results lead to a better understanding of the reaction dynamics of driven reactions. Changes in the parameters of the driving have a huge impact on the system's dynamics and have been seen here and recently [3, 5, 174] to lead to changes in mean energies and decay rates. Indeed, it suggests

that one could control rate constants within a limited range by adjusting the driving of the system.

It remains to characterize the behavior of driven chemical reaction dynamics as a function of other system parameters, including the height and width of the saddle or the various parameters associated with the orthogonal mode. Changing these parameters could lead to further bifurcations, paving the way for the possible observation of a chaotic regime.

SELF-SIMILARITY IN A DRIVEN TWO-SADDLE SYSTEM

Essential parts of this chapter have previously been published by the author in Reference [4].

The focus so far has been on single-barrier reactions. Many complex reactions [21–25], however, have to overcome multiple bottlenecks along the reaction pathway. Such multi-barrier reactions were considered early [203, 204] in the context of quantum-mechanical tunneling through barriers at constant energy. In this so-called *M-problem*, (quasi-)periodic orbits between the barriers give rise to the possibility of an infinite number of returns to the turning point from which tunneling can proceed. The return times are usually not commensurate with the period, either because of coupling to other degrees of freedom — such as from the bath — or because of variations in the potential. In such cases, the coherence in the returns is altered, with return times being sensitive to the exact initial conditions. In this work, we address the ways in which this sensitivity of classical orbits changes the nature of the dynamics.

Problems involving fluctuating [205, 206] or oscillating [176, 207, 208] barriers have also received significant attention leading to, for example, the identification of the phenomenon of resonant activation [209, 210]. While the approaches originally focused on the overdamped regime [176, 205], underdamped systems were later examined [208, 211]. For example, mean first-passage times have been employed to calculate (diffusion) rates in spatially periodic multi-barrier potentials. Therein, various static [185] as well as stochastically driven [212, 213] cases have been characterized primarily through numerical methods.

In the current context, the main challenge in a multi-saddle system comes from the unpredictability of states in the intermediate basin. A reactant entering this region may leave either as a reactant or product depending on the exact initial conditions [77, 214–216]. Historically, this challenge has been approached by categorizing reactions into two classes [43, 215, 217]: *Direct* reactions exhibit a single **TS**. *Complex* reactions, on the other hand, have two clearly separated **TSs**. The potential well between those barriers is assumed to be sufficiently deep that it gives rise to a long-lived collision complex. Trajectories passing through one **TS** enter this collision complex and hence cannot be correlated to trajectories passing through the other **TS**.

In reality, however, a reaction cannot always be uniquely classified. These concerns were addressed in a unified theory by Miller [215], and later refined by Pollak and Pechukas [218] so as to address shallow potential wells. While an important advancement, this theory still treats the saddle’s interactions statistically, thereby neglecting dynamical effects like resonances. Moreover, they considered multistep reactions in which the positions and heights of the barriers are time-independent. Last, there are numerous publications on valley-ridge inflection points, which are typically described by a normal TS followed by a *shared* one [216, 219, 220].

Craven and Hernandez [169] recently examined a four-saddle model of ketene isomerization influenced by a time-dependent external field. They encountered complicated phase-space structures similar to those in systems with closed reactant or product basins [127]. As a result, their analysis was limited to local DSs and no reaction rates were calculated. Moreover, successfully calculating instantaneous rates based on a globally recrossing-free DS attached to the NHIM of a time-dependent multi-saddle system has — to our knowledge — not yet been reported.

In this chapter, we address the challenge of determining the instantaneous TS decay rate for systems that not only feature multiple barriers along the reaction path but that are also time-dependent [4].

5-1 Two-saddle model system

We investigate the properties of multi-barrier systems by considering an open 1-DoF model potential featuring two Gaussian barriers whose saddle points are centered at $x = \pm 1$. Initially, both barriers are placed at the same level. As we are interested in considering the time-dependent case, however, we drive the barrier’s heights $B_\varphi(t)$ sinusoidally in opposite phases. That is, we use the same amplitude and frequency ω for both saddles but opposite initial phases $\varphi \in \{0, \pi\}$. This leads to the potential [173]

$$(5-1a) \quad V(x, t) = B_0(t) e^{-(x+1)^2} + B_\pi(t) e^{-(x-1)^2}$$

$$(5-1b) \quad \text{with } B_\varphi(t) = \frac{7}{4} + \frac{1}{4} \sin(\omega t + \varphi).$$

The oscillation frequency ω is a free parameter that can be varied relative to the other natural timescales of the system at a given fixed total energy. At an arbitrary time, one of the barriers will be larger than the other. For example, when the second barrier is larger, the potential takes a shape such as that shown at the top of Figure 5-1(b). Throughout this chapter, dimensionless

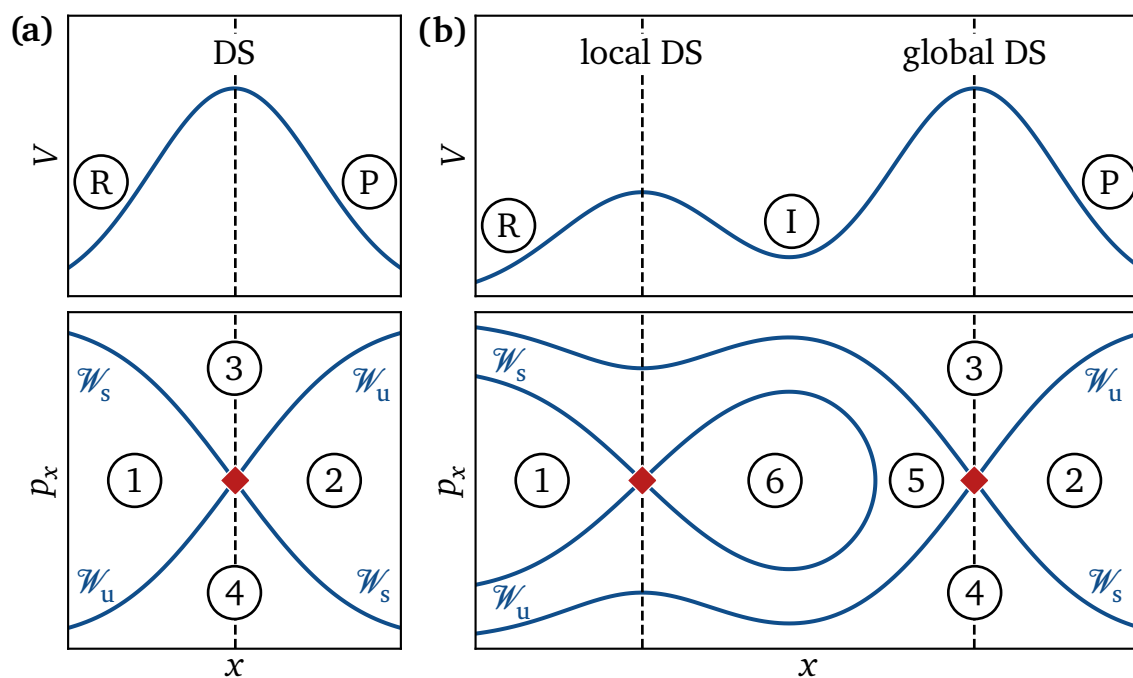


Figure 5-1: Typical structures of static potentials $V(x)$ and their corresponding phase spaces $x-p_x$ with (a) one and (b) two barriers. The potential barriers separate reactant (R) and product (P) states. The two-barrier case features an additional intermediate (I) state in between. The maxima are associated with a hyperbolic fixed point (diamonds) and a dividing surface (indicated by dashed vertical lines) each. The corresponding manifolds divide the phase space into four distinct, numbered regions in panel (a) and six regions in panel (b). See Sections 5-1 and 5-2 (a) for details.

units are used to explore the range of phenomena that can arise from varying the relative timescales of the system and the driving.

Section 3-2 (b) introduced the concept of reactive and nonreactive regions. Given a suitable interaction region around the saddle, it can be used to divide the phase space into four distinct regions depending on the state trajectories originate from and the state they end up in. Such a classification for the initial conditions has to be extended to include the consequences of a local minimum between the saddles of the reacting system of Equation (5-1). A low-energy particle trapped near this local minimum [cf. Figure 5-1(b)] would lead to diverging computation times because it may never leave the interaction region. To solve this problem, an additional termination condition is introduced, whereby any particle that crosses the potential minimum a specified number of times n^* is classified as an intermediate (I) particle. This now leads to three different outcomes per time direction instead of two. Consequently, up to nine different regions in phase space can be distinguished for any given value of n^* .

5-2 Fractal phase space

The phase-space structure of the model system introduced in Section 5-1 is highly dependent on the driving frequency ω . In the following, we give a qualitative overview of the behavior the system can exhibit.

(a) Limiting cases

A static or quasistatic two-saddle system akin to Equation (5-1) with $\omega \rightarrow 0$ exhibits the phase-space structure shown in Figure 5-1(b). The saddle tops are associated with hyperbolic fixed points whose stable and unstable manifolds each form a cross. If the first saddle is smaller than the second one, two of its manifolds constitute a so-called homoclinic orbit. This orbit starts as part of \mathcal{W}_u and ends as part of \mathcal{W}_s , thereby connecting the saddle's fixed point with itself. In this case, the phase space is composed of six regions [173], namely

1. nonreactive reactants $R \rightarrow R$,
2. nonreactive products $P \rightarrow P$,
3. reactive reactants $R \rightarrow P$,
4. reactive products $P \rightarrow R$,
5. particles that react over the first saddle but get reflected at the second $R \rightarrow I \rightarrow R$, and
6. intermediate particles that are trapped between the saddles $I \rightarrow I$.

Likewise, if the driving frequency is sufficiently large ($\omega \rightarrow \infty$), the particle will effectively see an average static potential in which it must cross two similar static barriers of equal height. As the energy is conserved, once the particle crosses the first barrier, it necessarily crosses the second barrier. This results in a phase-space structure similar to that for the static case of Figure 5-1(b) — although with so-called heteroclinic orbits that connect the hyperbolic fixed points mutually.

In such (effectively) static cases, it is straightforward to define a global recrossing-free DS. In a 1-DoF constant-energy system, if (and only if) a particle crosses the highest saddle, it has demonstrated to have enough energy to react over all saddles. Since the largest barrier therefore unambiguously determines whether a particle reacts or not, its associated local DS becomes the global (recrossing-free) DS.

While this holds true for static systems, dynamically driven systems may exhibit much richer dynamics. For example, in the case of an alternating pair of dominant barriers, as in the model of Equation (5-1), the naive DS

jumps discontinuously from one side to the other twice per period. As a result there exist reactive trajectories that never cross the DS. Instead, the latter jumps over the former leading to an inconsistent description of the reaction. Addressing this issue by defining particles between the local DSs as reacting the moment the dominant saddle changes would lead to more problems, e. g., unphysical Dirac delta peaks in the reaction rate. To solve this issue, the system has to be treated as a whole.

(b) Intermediate driving frequency

The limiting cases discussed so far result in effectively static systems. Since we are interested in novel and nontrivial behavior, however, we will now turn to intermediate driving frequencies. These can exhibit varying degrees of complexity as a function of the driving frequency ω . An example of such nontrivial behavior with a highly complex phase space is shown in Figure 5-2. We use the Lagrangian descriptor defined in Section 3-2 (a) for visualization since it is very general and requires little knowledge about the system.

The geometric structure was obtained for the driven potential $V(x, t)$ of Equation (5-1) at an intermediate driving frequency $\omega = \pi$. The general shape of the boundaries separating reactive and nonreactive regions [cf. Figure 5-1(b)] is still vaguely visible. However, the precise position of the crossing points between the stable and unstable manifolds can no longer be determined. This family of crossing points together with the associated stable and unstable manifolds within their vicinity appears as a cross that has arisen from all of these geometric considerations. For simplicity, we define it as a *geometric cross* throughout this work. Note that this term is not meant to be a precise mathematical structure but rather an illustrative concept for describing the complex phase space of the system under study.

The fractal-like geometric crosses seen in the series of Figures 5-2(b) to 5-2(d) for a finite τ suggests a fractal structure at all scales for $\tau \rightarrow \infty$. This structure emerges from particles trapped between the two saddles. For example, a reactant can enter the intermediate region over the left saddle, be reflected multiple times at both saddles, and finally leave the interaction region over the right saddle as a product. The number of reflections is in this case highly dependent on the particular initial conditions as a result of the system being chaotic. In turn, this leads to a discontinuity in the Lagrangian descriptor, and eventually to the self-recurring patterns of a fractal structure.

Figure 5-2 also supports the observation of geometric structures at a given time that are thinner near the dominant saddle compared to the lower energy saddle. In Figure 5-2(a), when the right barrier is dominant, particles initialized near the higher saddle start with higher potential energy and

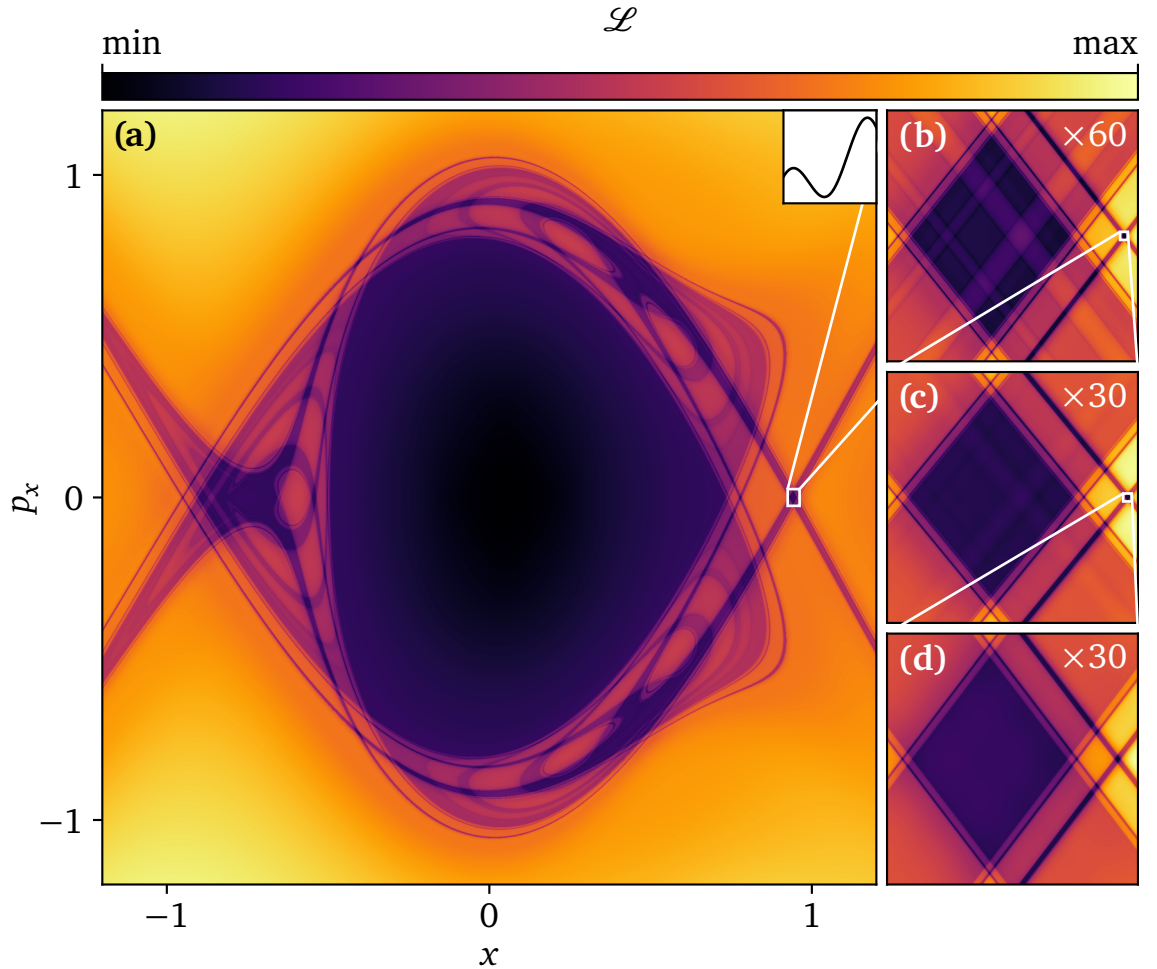


Figure 5-2: Phase-space structure for the time-dependent potential (5-1) with $\omega = \pi$ at $t_0 = 3/2$ as revealed by the Lagrangian descriptor \mathcal{L} given in Equation (3-8) with $\tau = 16$. (a) Although the two geometric crosses seen in Figure 5-1(b) are still present, they now exhibit a complicated substructure involving a vast number of homoclinic and heteroclinic points as well as homoclinic and heteroclinic orbits. The potential at time t_0 is indicated in the top right inset. (b)–(d) The progressively zoomed cutouts exhibit self-recurring structures. Labels in the top right corners indicate the corresponding enlargement from the previous zoom level.

therefore have a lower chance of being reflected. As a result, fewer of these particles linger in the interaction region and the phase-space structures are thinner. While this may be an interesting observation, the geometric cross near the dominant barrier is still highly fractal. There are no isolated, weakly fractal geometric crosses that could reasonably be tracked numerically. Consequently, we cannot make meaningful statements about a globally recrossing-free DS.

(c) Slow driving frequency

The previous sections have shown the range of complexity the model system (5-1) can exhibit. We now need to move from the aesthetically pleasing structures of Figure 5-2 to a more rigorous identification of the globally recrossing-free DS. To do so, we switch to a lower driving frequency $\omega = \pi/10$, which is simpler to analyze but still exhibits nontrivial behavior. Additionally, we employ the concept of reactive regions as described in Sections 3-2 (b) and 5-1 instead of the Lagrangian descriptor. The partitioning of the phase space into nine distinct regions allows us to make quantitative assessments more easily.

Application of this analysis to $V(x, t)$ with $\omega = \pi/10$ leads to the time-dependent regions shown in Figure 5-3. Although fractal-like structures still remain, they are less pronounced and mostly concentrated around whichever saddle happens to be the lower saddle at a given instance. The higher saddle, on the other hand, is accompanied by a clearly visible geometric cross where the four regions known from the one-saddle case (no intermediate states) meet. The regions are also arranged in the same way: $R \rightarrow P$ on top, $R \rightarrow R$ to the left, $P \rightarrow P$ to the right, and $P \rightarrow R$ below. In the following, we refer to this geometric cross as the *primary geometric cross*.

5-3 Geometric cross

We will now analyze the primary geometric cross and its associated TS trajectory in more detail. Its time-dependent position can be tracked precisely over a full period using the algorithms described in Section 3-3. Interestingly, even a given geometric cross is not entirely free of substructures. Instead, it features a fractal-like set of crossing manifolds in its close proximity. Since these additional structures are extremely thin, however, they do not hinder the BCM from finding the desired geometric-cross coordinates up to the desired precision which may be even smaller than the width of some of the substructures. The result is marked as a series of black dots in Figure 5-3. The corresponding trajectory connecting those dots is indicated as a black dashed line.

(a) Global transition-state trajectory

The primary geometric cross associated with the instantaneously higher saddle in Figure 5-3 remains on the barrier nearly as long as the barrier remains dominant. However, when the barriers' heights approach each other, the geometric cross quickly moves from one barrier to the other in the

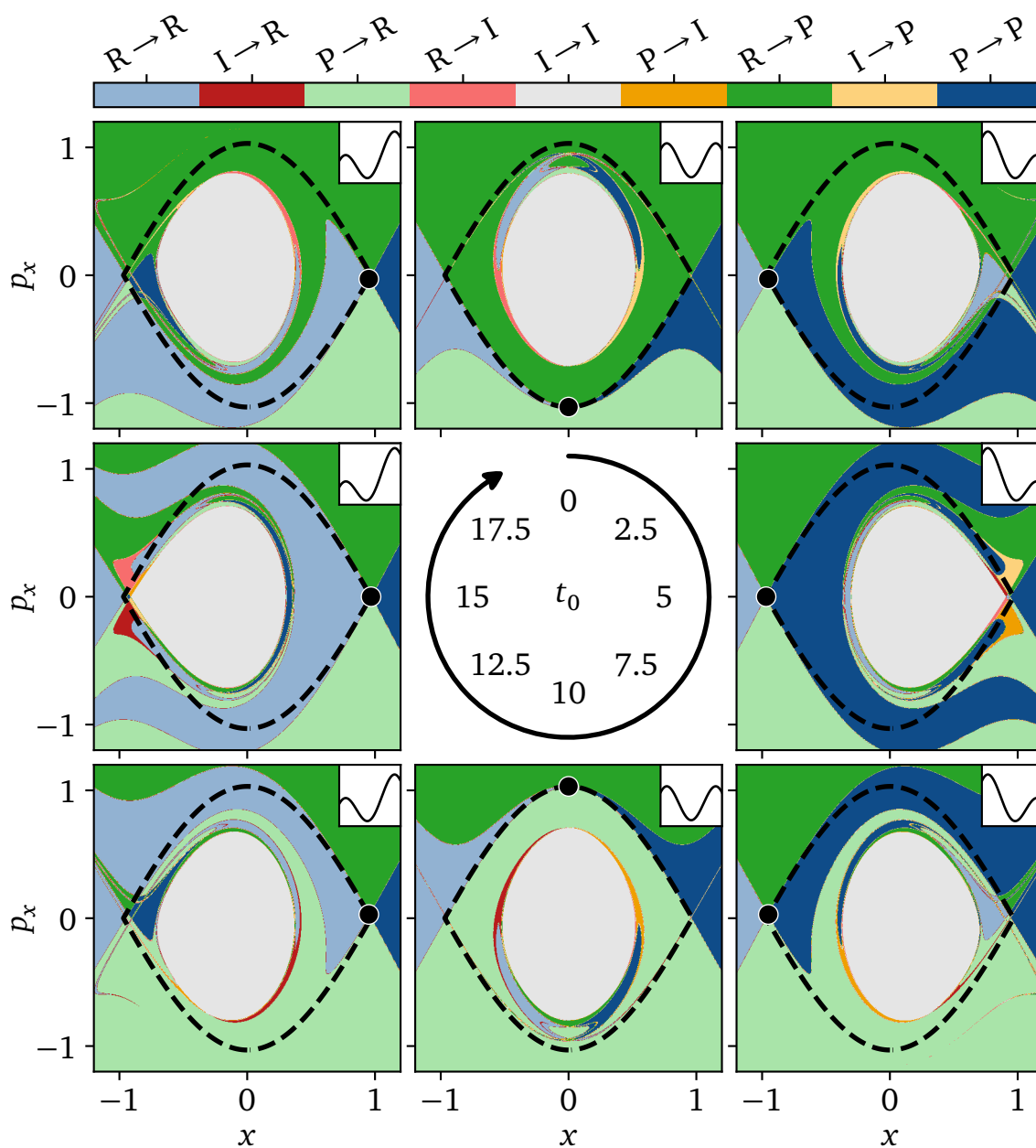


Figure 5-3: Reactive regions for potential (5-1) with $\omega = \pi/10$ as a function of time t_0 (cf. center panel). Trajectories that cross the minimum $n^* = 8$ times are assumed to be captured between the barriers. The color legend at the top indicates whether a particle starts or ends in the reactant (R), intermediate (I), or product (P) state. The position of the point on the **NHIM** associated with the primary geometric cross (black dot) is tracked across a full period (**TS** trajectory, black dashed line). The insets in the upper right corner of each panel illustrate the potential at the corresponding initial time t_0 .

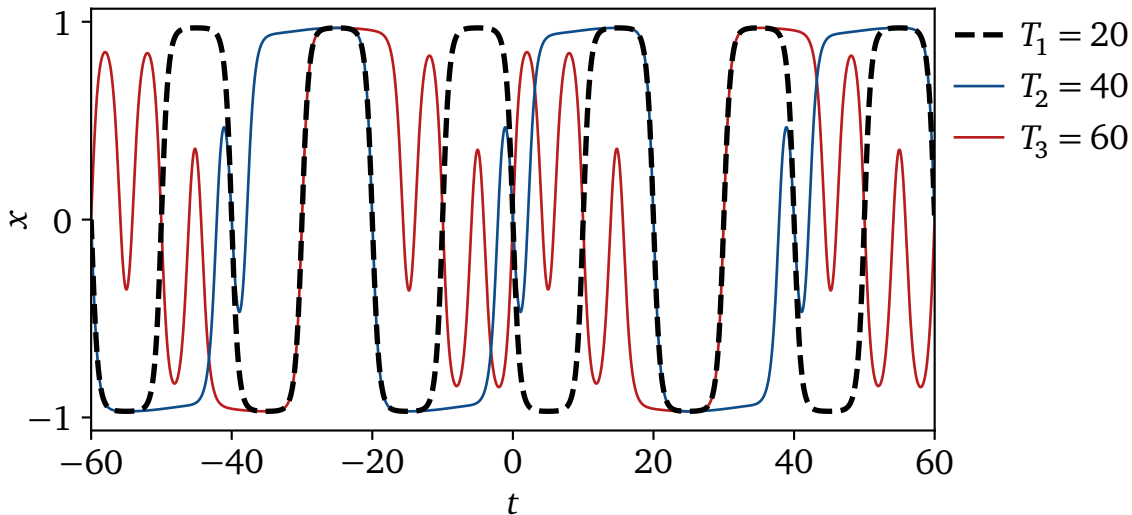


Figure 5-4: Examples of typical periodic trajectories $x(t)$ with periods $T_2 = 40$ (blue) and $T_3 = 60$ (red) for potential (5-1) with $\omega = \pi/10$. The primary TS trajectory from Figure 5-3 with period $T_1 = 20$ (black dashed line) is shown for comparison.

following way. The geometric cross begins to rapidly accelerate towards the middle ($x = 0$). It crosses the local potential minimum exactly when both saddle points are level (e. g., $t_0 = 10$) and continues in the same direction until it is located near the now higher saddle (e. g., $t_0 = 15$). The reverse happens in the following half period, thereby forming a closed trajectory with the same period $T_1 = 20$ as the potential $V(x, t)$ (dashed line in Figure 5-3).

This primary geometric cross marks the position of a particle on an unstable periodic trajectory trapped in the interaction region. The particle on this trajectory oscillates between the saddles with a period of $T_1 = 20$ so that it is always located near the higher saddle. Many other unstable periodic trajectories associated with geometric crosses — i. e., hyperbolic fixed points — in phase space have also been found for particles in the interaction region. Two such trajectories are shown in Figure 5-4. They are typical of an increased degree of structure relative to the primary TS trajectory. All such trajectories together form the system's disjoint, fractal-like time-dependent NHIM. In contrast to the primary TS trajectory, however, all other trajectories have periods larger than T_1 . The only exceptions to this observation are the local TS trajectories in the vicinities of the saddle maxima, which are also part of the global NHIM. These trajectories have the same period T_1 as the potential by construction.

The complex dynamics that arises from the moving barriers is also affected by the degree to which a given trajectory is decoupled from the barriers as it traverses the well between them. Although the energy of the minimum

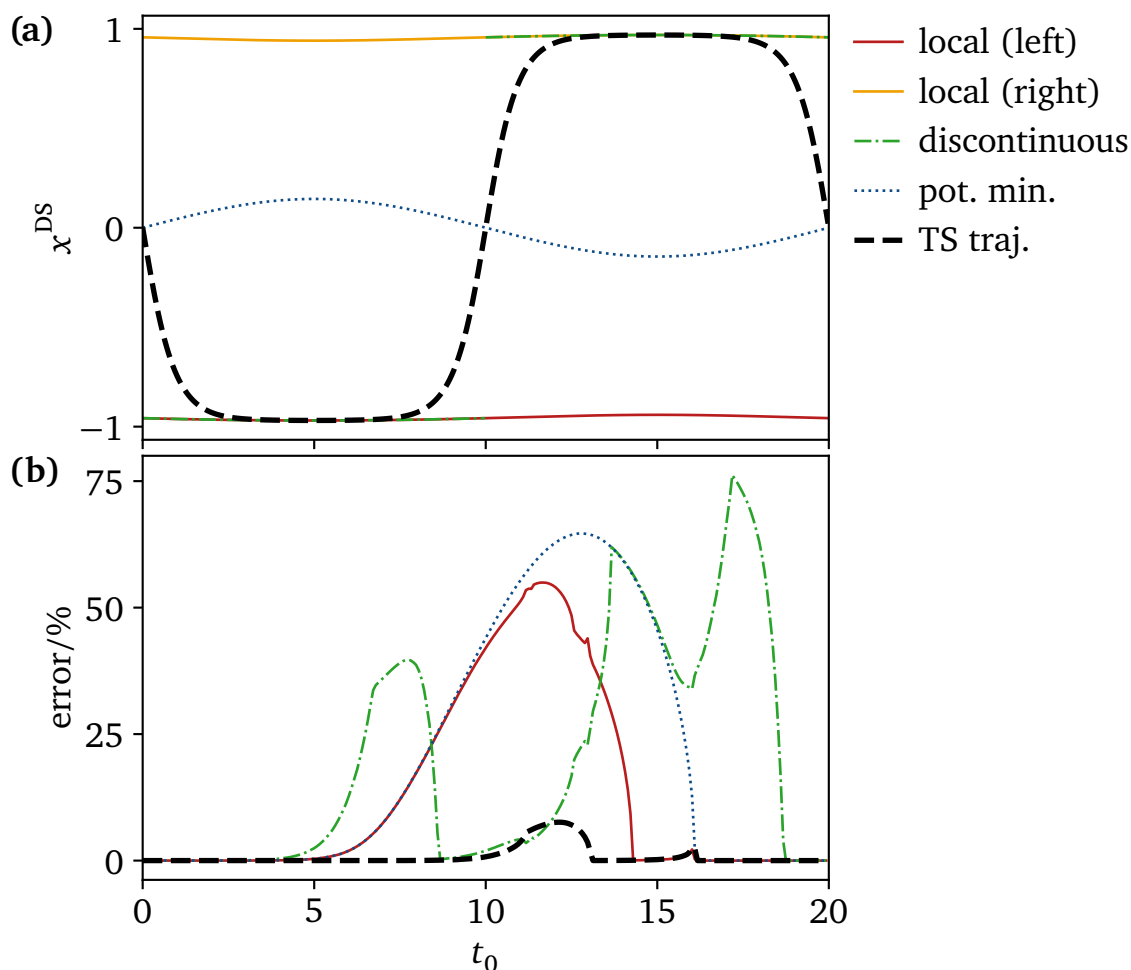


Figure 5-5: (a) Position x^{DS} and (b) percentage of trajectories with recrossings or classification errors as a function of time t_0 for various choices of their assignment as reactive or nonreactive. The assignment is performed according to the crossing of a specified DS associated with either the local (solid) or global (thick dashed) TS trajectories, the instantaneous potential minimum between the saddles (dotted), or the discontinuous TS trajectory jumping between the local ones (dash-dotted). For every t_0 , an ensemble of 10^6 particles with uniformly distributed velocities $1.7 \leq p_x(t_0) \leq 2.1$ is initialized at $x(t_0) = -3$ and propagated for $\Delta t = 80$ time units. The attached DS is parallel to p_x for all times. The right local DS is recrossing-free by construction since particles are started solely to the left of the saddles and is therefore not shown in panel (b). This specific choice for the ensemble is also the reason for the graph's asymmetry.

stays roughly constant, as indicated in Figure 5-3, its position moves back and forth between the barriers as shown in Figure 5-5(a) so that it is always closer to the lower barrier. This can be seen as a manifestation of *Hammond's postulate* [221] applied to the intermediate state and the local TSs. Hammond

conjectured that two consecutive states with similar energy content will likely have a similar molecular structure. We can thus assume that the driving in a corresponding real chemical reaction will time-dependently morph the molecular structure of the intermediate state towards the **TS** of the instantaneously lower barrier.

When the first (left) barrier dominates the dynamics, a locally nonrecrossing **DS** associated with it identifies the trajectories with sufficient energy to cross it, and those continue unabated across the well and the second barrier. As a consequence, a **DS** located at the central well identifies the reactive trajectories equally well (or badly) in this regime. This is demonstrated in Figure 5-5(b) by good identification when the activated particle continues past the second barrier and by rising error quotients when misidentification of trajectories begins to be reflected across both. When the second (right) barrier dominates the dynamics, identifying reactive trajectories at a **DS** at the well allows the evolving trajectories to be reflected by the barrier leading to recrossings. Thus, we find that the reaction dynamics in between the barriers — e. g., at the well — does not go through a single identifiable doorway. In turn, this points to the need for describing the dynamics — even in a local sense — through a geometric picture that spans the two barriers, i. e., the global **NHIM**.

Meanwhile, since the **NHIM** now consists of more than one trajectory, it is not necessarily obvious which of these is most suited for attaching a *global DS*. We can, however, set conditions the global **TS** trajectory should fulfill. First, for symmetry reasons, the trajectory should have the same period $T_1 = 20$ as the potential. Second, the global **TS** trajectory should approach the higher saddle's local **TS** trajectory in the (quasi-)static limit $\omega \rightarrow 0$ [cf. Section 5-2 (a)]. The only trajectory found that matches both criteria is the primary **TS** trajectory introduced previously, see Figure 5-5(a). The large featureless regions surrounding the trajectory in phase space additionally suggest that it affects a significant fraction of the system's dynamics. We will therefore refer to this trajectory as the global **TS** trajectory.

(b) Comparison of dividing surfaces

The next task is to determine the degree to which the global **TS** trajectory gives rise to a recrossing-free **DS**. Numerically, this can be tested by attaching a **DS** to it as specified in the caption of Figure 5-5, propagating an ensemble initialized near it, and recording the number and direction of **DS** crossings (or not) that transpire thereafter in the propagated trajectories. For simplicity, we consider only the most challenging cases in which the ensemble's initial energies are chosen to be between the saddles' minimum and maximum

heights. The usual error in the DS is signaled by the existence of more than one crossing for the trajectories, and the fraction of such recrossings is used below as a measure for the DS's quality.

For simplicity, we limit ourselves to DSs defined by $x = x^{\text{DS}}(t)$, i. e., parallel to p_x . The results of this analysis are shown in Figure 5-5(b). As can be seen, the global DS associated with the time-dependent geometric cross features error rates that are significantly reduced compared to the local DS fixed at the left barrier. One possible DS could be constructed by placing it at the instantaneous potential minimum — shown as the dotted curve in Figure 5-5(a). It would be expected to be ineffective given that rates are usually determined by rate-limiting barriers, not valleys, in between reactants and products. Indeed, the recrossing errors found for this DS, shown in Figure 5-5(b), were high and even worse than those from the use of the DS fixed at the left barrier. But the highest error rate comes from the naive attempt to treat the DS associated with the instantaneously higher saddle point as the global one. In this case, errors can arise from events beyond the recrossing of the DS. That is, there now exists the possibility that the discontinuous instantaneous DS can jump over the trajectory. It is the combination of recrossing and classification errors that leads to the jagged and large deviations in the % error seen for the naive discontinuous DS. As discussed in Appendix A, this can lead to *misclassification* of the reactivity of the trajectory.

Finally, we consider a local DS fixed at the right barrier. This choice would lead to no recrossing or classification errors for trajectories moving in the forward direction (from reactants to products). However, it would fail badly for trajectories moving in the backward direction by symmetry with our finding for the forward trajectories crossing the DS at the left barrier. Thus, the use of the global DS associated with the TS trajectory best captures the time-dependent geometry of the reaction.

Although this TS-trajectory DS is much better than any alternatives considered so far, it still exhibits an amount of recrossings that cannot be explained by numerical imprecision alone. Instead, recrossings are caused by the fractal-like phase-space structure of the system: Figure 5-6(a), for example, shows the phase-space structure at time $t_0 = 0.25$. We can see a relatively large patch of nonreactive reactants (labeled R → R, light blue) to the right of the DS. Particles in this patch leave the interaction region to the reactant (left) side forward and backward in time. Consequently, they need to cross the DS at least twice, which counts as a recrossing. An analogous argument can be applied to P → P regions to the left of the DS. The fractal-like phase-space structure thus leads to numerous problematic

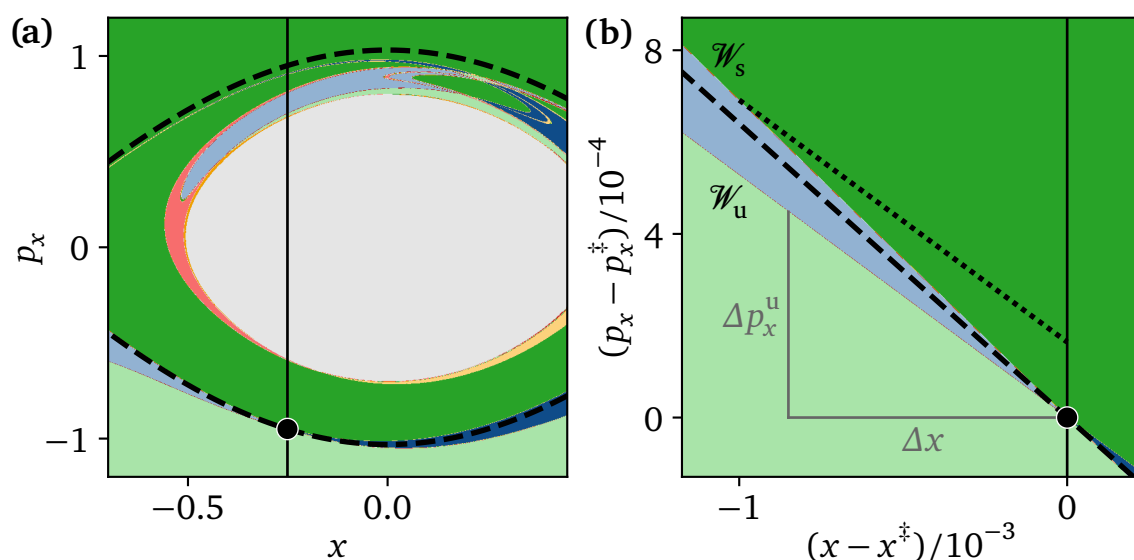


Figure 5-6: Reactive regions analogous to Figure 5-3 at $t_0 = 0.25$ with the addition of the DS (solid black line). **(a)** The simplest choice of a DS parallel to p_x leads inevitably to recrossings as indicated. **(b)** The immediate region of the TS trajectory [shown as a dot in panel (a)] is enlarged to reveal the geometry of the ensemble (densely dotted) used in the rate calculations of Section 5-4. The ensemble is sampled equidistantly on a line parallel to the unstable manifold \mathcal{W}_u at distance $x - x^\ddagger = -1 \times 10^{-3}$ from the TS trajectory at $x^\ddagger(t_0)$. The manifolds \mathcal{W}_u and \mathcal{W}_s are given by the boundaries between reactive and nonreactive regions. The differential of \mathcal{W}_u is indicated by the sides Δx and Δp_x^u of the slope.

patches of vastly different sizes. Hence, two distinct peaks appear in the classification error reported in Figure 5-5(b).

A totally recrossing-free DS, by contrast, would necessarily have to divide the phase space such that $R \rightarrow R$ regions are always on the reactant side, and $P \rightarrow P$ regions always on the product side. This is not possible with a planar DS of any orientation due to the system's fractal-like nature. A globally recrossing-free DS—if it exists—would have to curve as time passes because the entirety of the phase space between the saddle points has a clockwise rotating structure (including periodic trajectories on the NHIM, cf. Figures 5-3 and 5-4). The periodicity of this system would then result in a fractal, spiral-like DS. Thus, the next step in generalizing this theory would require the identification of a nonplanar DS anchored at the TS trajectory which we leave as a challenge to future work.

5-4 Decay rates

We can now calculate decay rates k for the activated complex using the global TS-trajectory DS defined in Section 5-3. The patches leading to recrossing [cf. Section 5-3 (b)] are unproblematic in this case because the ensemble was selected close to the NHIM and thereby necessarily far from them, as can be seen in Figure 5-6. The few recrossings that do still occur are artifacts from the numerical error in the propagation, and are sufficiently small in number that their effect is smaller than the numerical precision of the calculation.

In the following, we consider the three different possible approaches defined in Section 3-5 in order to demonstrate their equivalence in multi-saddle systems. An example for the initial reactant ensemble and manifold geometry can be found in Figure 5-6(b). While the application of the LMA and the Floquet method to our model system are straightforward, applying the ensemble rate method poses a challenge: A finite ensemble of reactants — e. g., of size 10^5 as implemented here — will mostly react within a short time — e. g., 2 to 5 units of time in the case shown here — compared to the period of driving $T_1 = 20$. Resolving the whole period with a single ensemble would therefore require an exponentially growing ensemble size. This would not be numerically feasible. Instead, multiple ensembles have been started at times t_j incremented at equal intervals $\Delta t = 1$. An instantaneous rate $k_e(t; t_j)$ can be obtained for each ensemble j . The instantaneous rate for the whole period $k_e(t)$ — independent of t_j — can then be recovered by concatenating the segments of each $k_e(t; t_j)$ for t from t_j to t_{j+1} . Compared to the first option, this approach scales linearly with the system's period instead of exponentially leading to vastly decreased computing times and increased numerical stability.

The results are shown in Figure 5-7. Since the ensemble and manifold rates $k_e(t)$ and $k_m(t)$ are not constant in time, we additionally show the average

$$(5-2) \quad \langle k \rangle_t = \frac{1}{T_1} \int_0^{T_1} dt k(t)$$

over one period T_1 of the TS trajectory.

Figure 5-7 shows a large variation in the instantaneous reaction rate in the interval $0.13 \lesssim k(t) \lesssim 3.85$. Two features are distinctive. First, the rate $k(t)$ shows mostly flat plateaus during the time the TS trajectory is located near a saddle. This can be explained using Figure 5-3: Although the phase-space structure as a whole is undergoing significant changes during, e. g., $2.5 \leq t \leq 7.5$, the local vicinity around the TS trajectory stays almost unaffected. Second, there are deep dips in $k(t)$ while the TS trajectory

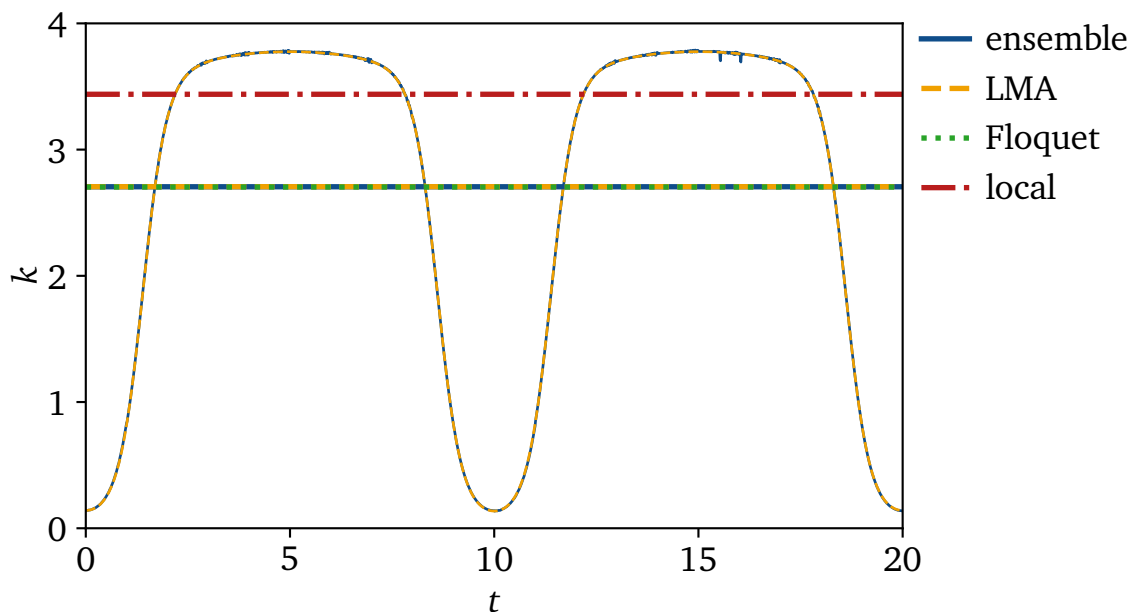


Figure 5-7: Various instantaneous reaction rates k parameterized by time t and associated with the global TS trajectory of the potential (5-1) with $\omega = \pi/10$, and driving period $T_1 = 20$. The ensemble rate $k_e(t)$ (blue solid) is obtained by propagation of 20 ensembles of 10^5 particles each as described in Section 3-5 (a). The manifold rate $k_m(t)$ (yellow dashed) is obtained using Equation (3-13). The Floquet rate constant k_F (green dotted) is obtained from Equation (3-24). The mean rates $\langle k_e \rangle_t$ and $\langle k_m \rangle_t$ (thick horizontal lines) are averaged over the period as defined in Equation (5-2). For comparison, the Floquet rate constant k_F^{loc} (red dash-dotted) of a single barrier's local TS trajectory is also shown.

moves between the saddles (as seen at around $t \in \{10j \mid j \in \mathbb{Z}\}$). As can be seen in Figures 5-3 and 5-6, these times are characterized by much more shallow geometric crosses with a low difference in the slopes of the stable and unstable manifolds. This effect is particularly apparent in Figure 5-6(b).

The same observations can also be interpreted another way. By comparing Figure 5-7 to Figure 5-5(a), we can see a clear correlation between the velocity of the TS trajectory and the instantaneous rate $k(t)$: the faster the TS trajectory moves, the lower the rate drops.

As can be seen in Figure 5-7 and Table 5-1, $\langle k_e \rangle_t$, $\langle k_m \rangle_t$, and k_F are in excellent agreement, which illustrates the equivalence of all three methods. The local Floquet rate constant k_F^{loc} of a single saddle, on the other hand, differs significantly from k_F , even though both saddles are identical. While the local rate constant can thus be used as an upper limit for the overall rate constant, there is no straightforward way to derive a global rate constant from it. Thus, global methods employing the full TS trajectory are necessary

Table 5-1: Values of the decay rate constants discussed in Figure 5-7. The averaged ensemble and LMA rate constants $\langle k_e \rangle_t$ and $\langle k_m \rangle_t$ match the Floquet rate constant to within less than +0.1 %. The local (single barrier) Floquet rate constant, however, differs by +27 %.

Description	Symbol	Value
Global TS trajectory		
ensemble propagation	$\langle k_e \rangle_t$	2.7055
manifold geometry (LMA)	$\langle k_m \rangle_t$	2.7062
Floquet stability analysis	k_F	2.7036
Local TS trajectory		
Floquet stability analysis	k_F^{loc}	3.4384

if accurate rates for multi-saddle systems are desired. All three methods in this section satisfy this requirement, and are consequently in agreement.

5-5 Conclusion and outlook

In this chapter, we have characterized the reaction geometry and determined the associated decay rates in an oscillatory (or time-dependent) two-saddle system.

The first set of central results of this work lies in revealing the phase-space structure of the two-saddle model system. While the structure of stable and unstable manifolds is straightforward for (quasi-)static ($\omega \rightarrow 0$) or very fast ($\omega \rightarrow \infty$) oscillating systems, intermediate frequencies lead to a fractal-like phase space. In this case, the existence of a completely recrossing-free DS is questionable. For lower oscillation frequencies, however, an isolated geometric cross with negligible substructure — referred to as the *primary* geometric cross — emerges. This structure is part of the NHIM and can now be referred to as a *global* TS trajectory in contrast to the *local* TS trajectories associated with the respective single barriers. The global TS trajectory oscillates between the two local TS trajectories with the same frequency as the potential and can be used to attach a mostly recrossing-free DS.

The second set of central results of this work involves the determination of the decay rates of the oscillatory (or time-dependent) two-saddle model system. Using the DS acquired in the first part, we can propagate ensembles of particles, record a time-dependent reactant population, and finally derive an instantaneous reaction rate parameterized by time according to Refer-

ence [2]. Alternatively, the same result can be achieved purely by analyzing the time-dependent phase-space geometry. For comparison, a rate constant can be obtained from the global TS trajectory by means of Floquet stability analysis. This method is in excellent agreement with the average of each instantaneous rate.

While these results mark an important step in the treatment of time-dependent multi-saddle systems, many questions still remain unanswered: First, we restricted ourselves to two-saddle systems with one DoF. To be applicable to real-world systems, however, the methods presented here will have to be generalized at least to more DoFs because few chemical reactions can be treated accurately when reduced to just one coordinate. Second, it will be important to investigate the influence of minor manifold crossings on the rate constant. This is particularly necessary for cases of time-dependent barriers found here in which there is no longer an equivalent to the primary geometric cross. This is even more challenging when the alternation between barriers is driven at high frequencies (cf. Figure 5-2).

The applicability of our results to real-world systems also remains to be demonstrated. It remains unclear whether it is possible to treat systems without a primary geometric cross. That chemical reactions can be represented with potentials exhibiting the challenges discussed here, is illustrated by the isomerization of ketene via formylmethylene and oxirene which has been modeled via a four-saddle potential [169, 199–202]. The isomerization reaction of triangular KCN via a metastable linear $K-C\equiv N$ configuration can similarly be described by a two-saddle system [197, 198]. Thus, the analysis of time-dependent driven potentials resolved here, when applied to these and other chemical reactions, should provide new predictive rates for driven chemical reactions of interest.

THE MOON'S INFLUENCE ON STABILITY NEAR SUN-EARTH L_2

Essential parts of this chapter have previously been published by the author in Reference [6].

It is well known that a balance of forces between bodies in space can lead to stable or unstable fixed points in which a small body, such as a craft or satellite, experiences no net forces in a particular moving frame. The geostationary points arising from the cancellation of the gravitational force of the Earth and a satellite's centrifugal force is a well-known example. At these fixed points, the satellite remains forever fixed above a particular point on the Earth's surface as both rotate in tandem. Five fixed points are known to exist in the *circular restricted three-body problem (CR3BP)*, where a probe of negligible mass is considered moving under the influence of two primary bodies such as the Sun and the Earth. These fixed points are called the libration or Lagrange points L_1 to L_5 [222, 223], as schematically illustrated in Figure 6-1(a). The three collinear libration points L_1 to L_3 are unstable because small deviations from the exact position increase with time leading to the decay of the satellite away from them. However, the other two triangular libration points L_4 and L_5 can be stable because of the effects of the Coriolis force if the ratio of the masses of the two primaries is sufficiently large [222, 224] — as is the case for our Solar System.

The dynamics of planetary systems becomes much more complicated as soon as a third primary such as the Moon is considered [225–229]. In this case, the stability and position of the libration points in the rotating frame are influenced by the Moon's gravitational force. That is, the Moon's rotation around the Earth causes a time-dependent periodic driving of the satellite, and it is a nontrivial question whether or not the satellite can still stay forever in the local vicinity of a libration point. In this chapter, we address this question with respect to the libration point L_2 . We characterize the dynamics and stability of a satellite near this point in a generic star-planet system while explicitly considering the effects from a moon's rotation around the planet. The dynamics near the unstable libration points is determined by a rank-1 saddle of the potential. Therefore, to investigate the dynamics close to the saddle we again resort to the use of TST [19, 26, 35, 38, 40, 43].

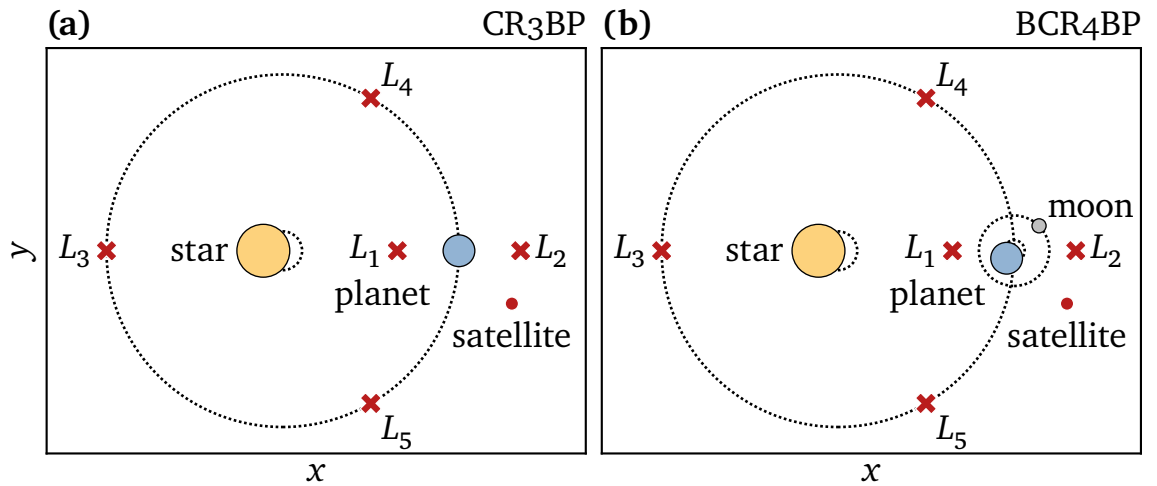


Figure 6-1: (a) Schematic of a generic solar system in the **CR₃BP**. A star and its planet are on circular orbits about their mutual barycenter. (b) Schematic of a generic solar system in the **BCR₄BP**. A planet and its moon are on circular orbits about their mutual barycenter. This planet–moon barycenter and the star both move around the total center of mass. In both cases, (a) and (b), other bodies — e. g., satellites or asteroids — are assumed to have negligible mass. All orbits are coplanar. Without the moon, the system is known to give rise to the five libration points, marked L_1 to L_5 , associated with the stability of additional objects such as a satellite or asteroid. The unstable point L_2 is the focus of this work. In the special case of our Solar System, these bodies refer to the Sun, the Earth and the Moon. Here, we consider a broader range of cases and list the corresponding parameters in Table 6-1.

6-1 Solar system model

We focus on planetary systems with three primary bodies to illustrate the use of **TST** in celestial mechanics [6, 60]. Unfortunately, there does not exist a general closed-form solution for such three-body problems [230] that would provide a rigorous benchmark. We therefore base our calculations on the well-known *bicircular restricted four-body problem* (**BCR₄BP**) which models three primaries on fixed circular orbits in the same two-dimensional plane [225–228]. The two lighter primaries—referred to as planet and moon—orbit their mutual barycenter in an inner nested two-body problem. In turn, this planet–moon barycenter and the heaviest primary—the star— orbit the total system’s center of mass as shown in Figure 6-1(b). Although this center of mass is itself a barycenter for the whole system, we will avoid referring to it as such through the text to avoid confusion. In the outer nested two-body problem, the planet and moon are treated as a single body located at their barycenter. The dynamics of the probe body (for example an asteroid

or satellite) is governed by the primaries' gravitational forces. Its mass is assumed to be so small that its gravitational force on other bodies can be neglected.

(a) Libration points in the star–planet system

A system consisting of two bodies interacting via gravitational forces — in our case a star and a planet — features five points where the gravitational forces and the centrifugal force on a probe mass nullify each other. These equilibrium points are called the libration or Lagrange points L_1 to L_5 . Figure 6-1 schematically shows the position of L_1 to L_5 relative to the celestial bodies. The libration points rotate with the same frequency as the primaries, and therefore the probe mass' position relative to the bodies is constant. This makes them very interesting for space exploration and research [231–233]. Adding a lighter third primary — i. e., a moon orbiting the planet — causes a time-dependent perturbation of the libration points. See Section 6-3 for a more detailed discussion.

The libration points differ by their stability properties. The local potentials near L_1 to L_3 are rank-1 saddles with one unstable DoF in the radial direction and one stable DoF perpendicular to the radial direction. Trajectories near L_1 to L_3 are therefore *unstable*. The libration points L_4 and L_5 show as rank-2 saddles with two unstable directions. Contrary to first intuition, however, trajectories near L_4 and L_5 are *Lyapunov stable* for sufficiently large star–planet mass ratios [222, 224] because of the contributions from the velocity-dependent Coriolis force [224, 234]. However, trajectories near the collinear libration points L_1 to L_3 are not stabilized in similar fashion despite the effects from the Coriolis force.

In this chapter we focus on the stability of satellites near L_2 and how they are influenced by a moon. In our Solar System, L_2 is especially interesting for astrophysics since it is located far enough from Sun, Earth, and Moon to minimize noise but still close enough to Earth for communication. It has been the target of multiple past and present space missions, e. g., the *Wilkinson Microwave Anisotropy Probe* [112], the *Herschel* mission [113], the *James Webb Space Telescope* [114], and the *Planck* spacecraft [115]. In addition, it features a rank-1 saddle which can be readily described using the framework of TST as summarized in Chapter 2.

(b) Parameters and model variants

We use dimensionless units derived from a synodic reference frame with respect to the star and the planet–moon barycenter. The star–barycenter

Table 6-1: Summary of the configuration parameters and derived values used in the strong-driving and Solar System models considered here. We use dimensionless units derived from a synodic coordinate system with respect to the star and the planet–moon barycenter. The star–barycenter distance, star–barycenter angular frequency, and total mass of all primaries are used as units for length, frequency, and mass, respectively. The satellite is assumed to be an infinitesimal mass point. Its mass gets canceled from the equations of motion, and there is no need to specify it. See Section 6-1 (c) for further details.

Description	Symbol	Strong driv.	Solar System
planet–moon distance	a	0.1	2.570×10^{-3}
primary mass param.	μ	0.1	3.040×10^{-6}
secondary mass param.	$\tilde{\mu}$	0.1	1.215×10^{-2}
star mass	$M_S = 1 - \mu$	0.9	0.999997
barycenter mass	$M_B = \mu$	0.1	3.040×10^{-6}
planet mass	$M_P = \mu(1 - \tilde{\mu})$	0.09	3.003×10^{-6}
moon mass	$M_M = \mu\tilde{\mu}$	0.01	3.695×10^{-8}
synodic moon frequency	$\omega = \sqrt{\mu/a^3} - 1$	9	12.387

distance, the star–barycenter angular frequency, and the total mass of all primaries act as units for length, frequency (inverse time), and mass, respectively. The gravitational constant follows as $G = 1$. In this coordinate system, the total center of mass is at the origin with the star and the barycenter located at $(-\mu, 0)^\top$ and $(1 - \mu, 0)^\top$, respectively. The primary mass parameter μ is defined as the barycenter mass (i. e., sum of planet and moon mass) in units of the system’s total mass. The planet and moon orbit with distance a and angular frequency ω around their barycenter. The secondary mass parameter $\tilde{\mu}$ is defined analogously as the moon mass divided by the barycenter mass, cf. Table 6-1.

The **BCR4BP** is only an approximation to the real dynamics. We can recover strict Newtonian motion of the primaries by removing the moon, i. e., by setting $\tilde{\mu} = 0$. This limiting case is equivalent to the **CR3BP** and will be referred to as the time-invariant or *static* system because the resulting potential is time-independent in the synodic frame. In contrast, models with $\tilde{\mu} \neq 0$ will be called *driven*. Although the star’s position can still be fixed, the moon now perturbs the potential time-dependently even in the synodic frame; the planet moves as well to balance the moon’s motion.

In this work, we consider two parameterizations of the BCR₄BP listed in Table 6-1:

1. In the *strong-driving model*, the mass parameters are taken as $\mu = \tilde{\mu} = 0.1$ and the planet–moon distance as $a = 0.1$. The chosen values lead to a stronger perturbation of L_2 and allow for easier visualization. This parameter set is characteristic of the more extreme mass ratios that have been observed in extrasolar systems. An example is the brown dwarf 2M1207A and its companion planet 2M1207b [235] located in the constellation Centaurus with masses around $60 M_J$ and $5 M_J$ (M_J being the Jovian mass), respectively. Therein the mass parameter is $\mu \approx 0.077$, which is comparable to the value in our parameter set.
2. In our *Solar System*, the masses of the Sun, the Earth, the Moon, and the relative distances between them are well known. It provides a comparison to the strong-driving model, and demonstrates the applicability of our methods.

(c) Potential and equations of motion

The bodies have normalized masses

$$M_S = 1 - \mu, \quad M_B = \mu, \quad M_P = \mu(1 - \tilde{\mu}), \quad \text{and} \quad M_M = \mu\tilde{\mu}, \quad (6-1)$$

where

$$0 \leq \mu, \tilde{\mu} \leq 1 \quad \text{and} \quad M_S + M_B = M_S + M_P + M_M = 1. \quad (6-2)$$

They are located at positions

$$\begin{aligned} \mathbf{R}_S &= -\mu\hat{\mathbf{x}}, & \mathbf{R}_B &= (1 - \mu)\hat{\mathbf{x}}, \\ \mathbf{R}_P &= \mathbf{R}_B - a\tilde{\mu}\hat{\boldsymbol{\theta}}, & \mathbf{R}_M &= \mathbf{R}_B + a(1 - \tilde{\mu})\hat{\boldsymbol{\theta}}, \end{aligned} \quad (6-3)$$

where

$$\hat{\boldsymbol{\theta}} = \begin{pmatrix} \cos\theta \\ \sin\theta \end{pmatrix} \quad \text{with} \quad \theta = \omega t \quad \text{and} \quad \omega = \sqrt{\mu/a^3} - 1, \quad (6-4)$$

in the synodic coordinate system. Using the position of the satellite \mathbf{r} relative to the primaries

$$\mathbf{r}_k = \mathbf{r} - \mathbf{R}_k \quad \text{for} \quad k \in \{S, P, M\}, \quad (6-5)$$

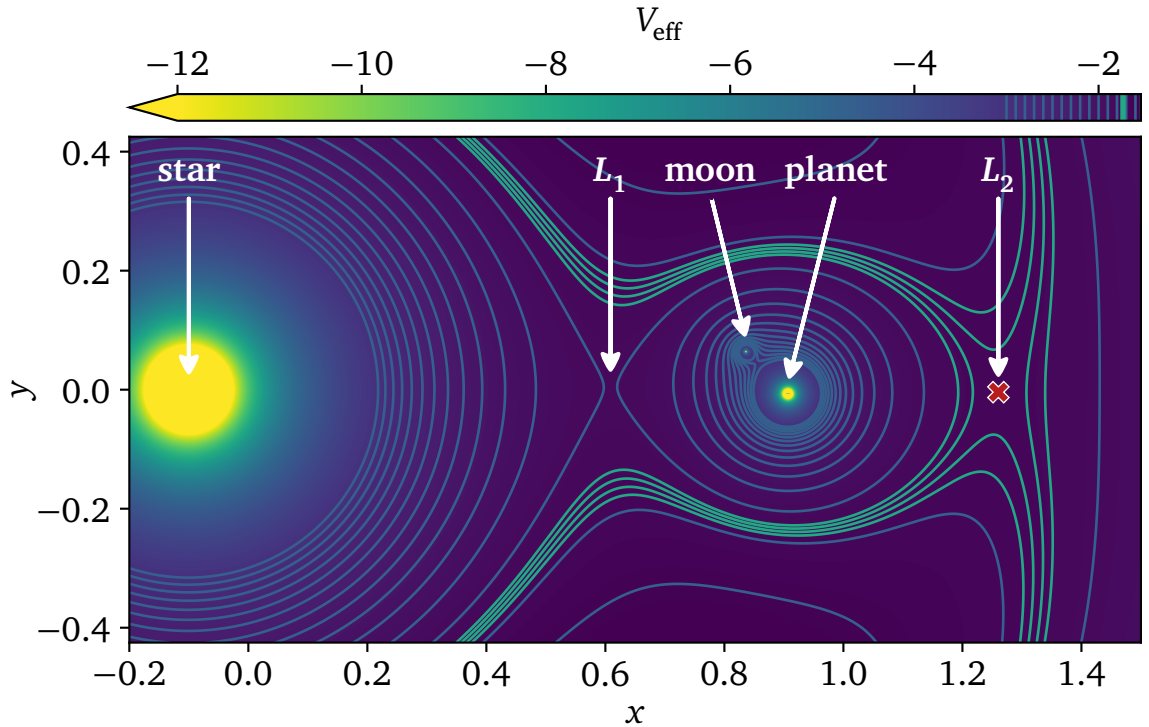


Figure 6-2: Effective potential $V_{\text{eff}}(x, y, t)$ according to Equation (6-6) at $t = 3T/8$ for the strong-driving model. The color map is capped at $V_{\text{eff}} = -12$ since the potential is divergent at the positions of the system's star, planet, and moon (filled yellow circles). A cross indicates the dynamical position of the saddle point near L_2 . We caution the reader that this point does not necessarily correspond to an equilibrium position due to the potential's time dependence. More equipotential lines are shown near L_2 to elucidate the saddle structure.

the effective potential can be written as

$$(6-6) \quad -V_{\text{eff}} = \Omega = \frac{r^2}{2} + \frac{1-\mu}{r_S} + \frac{\mu(1-\tilde{\mu})}{r_P} + \frac{\mu\tilde{\mu}}{r_M}.$$

This potential for the parameters of the strong-driving model is shown in Figure 6-2.

The equations of motion for $\mathbf{r} = (x, y)^T$ can be derived from the effective potential as

$$(6-7) \quad \dot{p}_x = \ddot{x} - 2\dot{y} = \frac{\partial \Omega}{\partial x} \quad \text{and} \quad \dot{p}_y = \ddot{y} + 2\dot{x} = \frac{\partial \Omega}{\partial y},$$

where

$$\frac{\partial \Omega}{\partial j} = j - \sum_{k \in \{S, P, M\}} \frac{M_k}{r_k^3} \mathbf{r}_k \cdot \hat{\mathbf{j}} \quad \text{for } j \in \{x, y\}. \quad (6-8)$$

The terms $-2\dot{y}$ and $+2\dot{x}$ in the equations of motion (6-7) account for the Coriolis force.

The second-order equations of motion can be reformulated as a first-order system

$$\dot{x} = v_x, \quad \dot{y} = v_y, \quad \dot{v}_x = \ddot{x}, \quad \text{and} \quad \dot{v}_y = \ddot{y} \quad (6-9)$$

with \ddot{x} and \ddot{y} given in Equation (6-7). The Jacobian \mathbf{J} of this first-order system reads

$$\mathbf{J} = \begin{pmatrix} 0 & 0 & 1 & 0 \\ 0 & 0 & 0 & 1 \\ J_{v_x, x} & J_{v_x, y} & 0 & 2 \\ J_{v_y, x} & J_{v_y, y} & -2 & 0 \end{pmatrix} \quad (6-10)$$

with

$$J_{v_j, j} = \frac{\partial \dot{v}_j}{\partial j} = 1 + \sum_{k \in \{S, P, M\}} \left[\frac{3M_k}{r_k^5} (\mathbf{r}_k \cdot \hat{\mathbf{j}})^2 - \frac{M_k}{r_k^3} \right] \quad \text{for } j \in \{x, y\} \quad (6-11a)$$

and

$$J_{v_x, y} = J_{v_y, x} = \frac{\partial \dot{v}_x}{\partial y} = \sum_{k \in \{S, P, M\}} \frac{3M_k}{r_k^5} (\mathbf{r}_k \cdot \hat{\mathbf{x}})(\mathbf{r}_k \cdot \hat{\mathbf{y}}). \quad (6-11b)$$

It describes the linearized motion of satellites relative to a reference trajectory as required for decay rate calculations (cf. Section 3-5).

6-2 Reframing TST in terms of celestial mechanics

The star–planet–moon system — described by the effective potential (6-6) — features a rank-1 saddle point at L_2 , as shown in Figure 6-2, which can act as bottleneck of the dynamics. This makes it a prime candidate for the application of TST models (see, e. g., References [58, 59, 236]). It may seem strange at first to apply a framework developed in the context of chemical reactions to an astrophysical problem. Many concepts from the geometrical formulation of TST, however, bear a striking resemblance to those used in

celestial mechanics. It is merely a matter of rephrasing the concepts of one theory in the context of the other.

In typical scenarios for a chemical reaction, a rank-1 saddle point separates reactants from products, and can be used to characterize the flux and associated reaction rate. In the planetary system, reactants roughly correspond to satellites or asteroids inside the planet's Hill sphere [223, 236], and the reaction corresponds to the escape from this sphere, or vice versa. The unstable states between reactants and products form the **TS**. Thus, geometrically, the **TS** is a boundary (or **DS**) between the reactant and product regions which in the current context corresponds to the **DS** between incoming or outgoing directions of the satellite. In planetary systems, this includes all libration point orbits.

In the context of libration points, the terms reactive and nonreactive can be reframed as *transit* and *nontransit* orbits, respectively [227, 237]. Trajectories on the stable manifold \mathcal{W}_s are bound to the saddle's vicinity for $t \rightarrow \infty$ while trajectories on the unstable manifold \mathcal{W}_u are bound for $t \rightarrow -\infty$. These properties play an important role in the determination of efficient transfer orbits for spacecrafts [227, 228, 237–239]. Even the concept of the **NHIM** has previously been employed in celestial mechanics [226], although not under that name. It plays an important role in determining whether a given state is considered a reactant or product—viz., pre- or post-escape in the present celestial models [58, 59, 236].

As usual, the reaction coordinate x (in the rotating frame) describes the saddle's unstable direction and indicates the progress of the reaction. Similarly, the stable direction y is referred to as the orthogonal mode.

6-3 Dynamics on the **NHIM** and the L_2 orbit

The dynamics on the **NHIM** of the periodically driven model system takes place in an effectively two-dimensional phase space. An established method for the visualization of such systems is the stroboscopic map, a special case of the **PSOS**. We propagate satellites on the **NHIM**. Instead of recording the whole trajectory, however, we only record one point every system period $T = 2\pi/\omega$. Trajectories with period T therefore manifest as fixed points in the **PSOS** (cf. Section 3-4).

Figure 6-3(a) shows the stroboscopic **PSOS** of the driven model system's **NHIM** around L_2 . One can see concentric toroidal structures, suggesting regular behavior. Trajectories associated with these tori are mostly quasiperiodic. The tori surround an elliptic fixed point, whose associated periodic trajectory is shown in Figure 6-4(a). This orbit has the same period as the moon's synodic orbit. It can be seen as the generalization of the static L_2 point

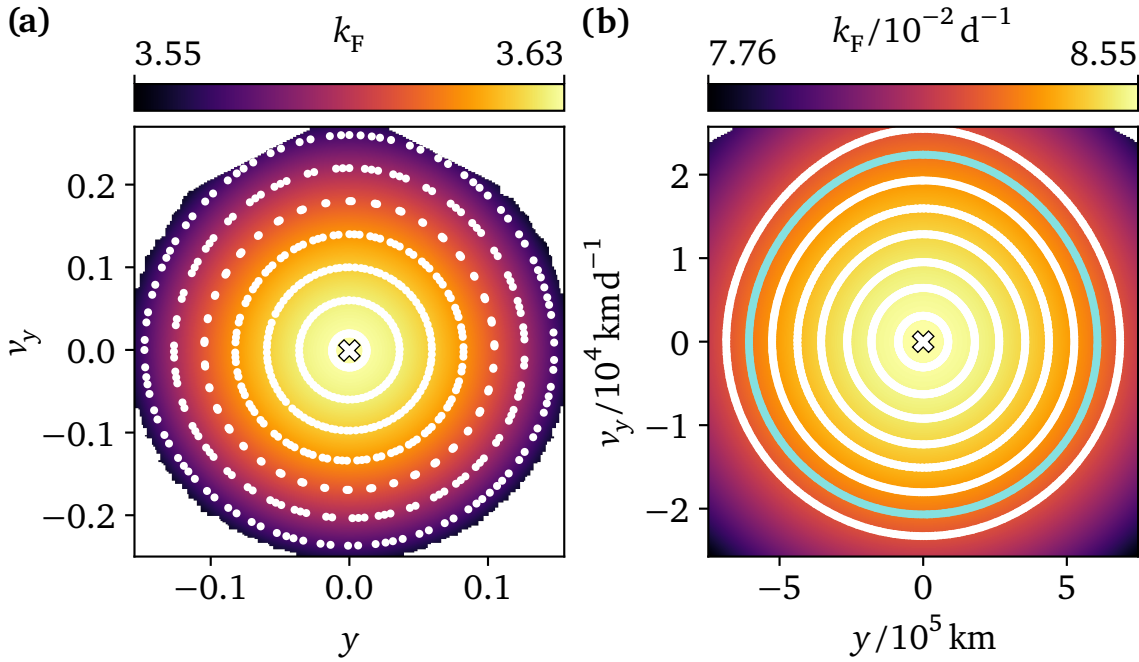


Figure 6-3: (a) Stroboscopic PSOS of the strong-driving model with trajectories propagated over 100 periods on the NHIM starting at initial time $t_0 = 0$. The system exhibits regular dynamics as shown by the concentric tori. In its center, an elliptic fixed point (cross marker) reveals the existence of a periodic orbit with the system’s period T . This periodic orbit replaces the static L_2 point from the CR3BP. Floquet rates k_F of trajectories \mathbf{y}^\ddagger started at t_0 are overlaid. Their maximum coincides with the fixed point. (b) The Solar System model exhibits the same qualitative behavior. The second-outermost torus is highlighted in cyan; its trajectory is discussed further in Figure 6-4.

from the CR3BP. Similar observations have been made before, e. g., in Reference [226] for the triangular libration points. In the following, we will therefore refer to this trajectory as the L_2 orbit. It has been shown previously [2, 8, 87] that elliptic fixed points are typically associated with extrema in the averaged decay rate. Consequently, there exists a region around the fixed points with similar decay rates. Thus, to characterize the escape of satellites in the present time-dependent system, we must first determine the L_2 orbit and then calculate the decay from it as we do in the following section.

An analogous PSOS for the Solar System model is shown in Figure 6-3(b), with the L_2 orbit being shown in Figure 6-4(c). Both exhibit the same structure as the strong-driving model but with a much lower orbit diameter of $\Delta x \approx 2.6 \times 10^{-7}$ simulation units. This roughly corresponds to 40 km in SI units, which is rather small considering the usual scales between bodies in our Solar System. For comparison, Figure 6-4(e) shows the same L_2 orbit but

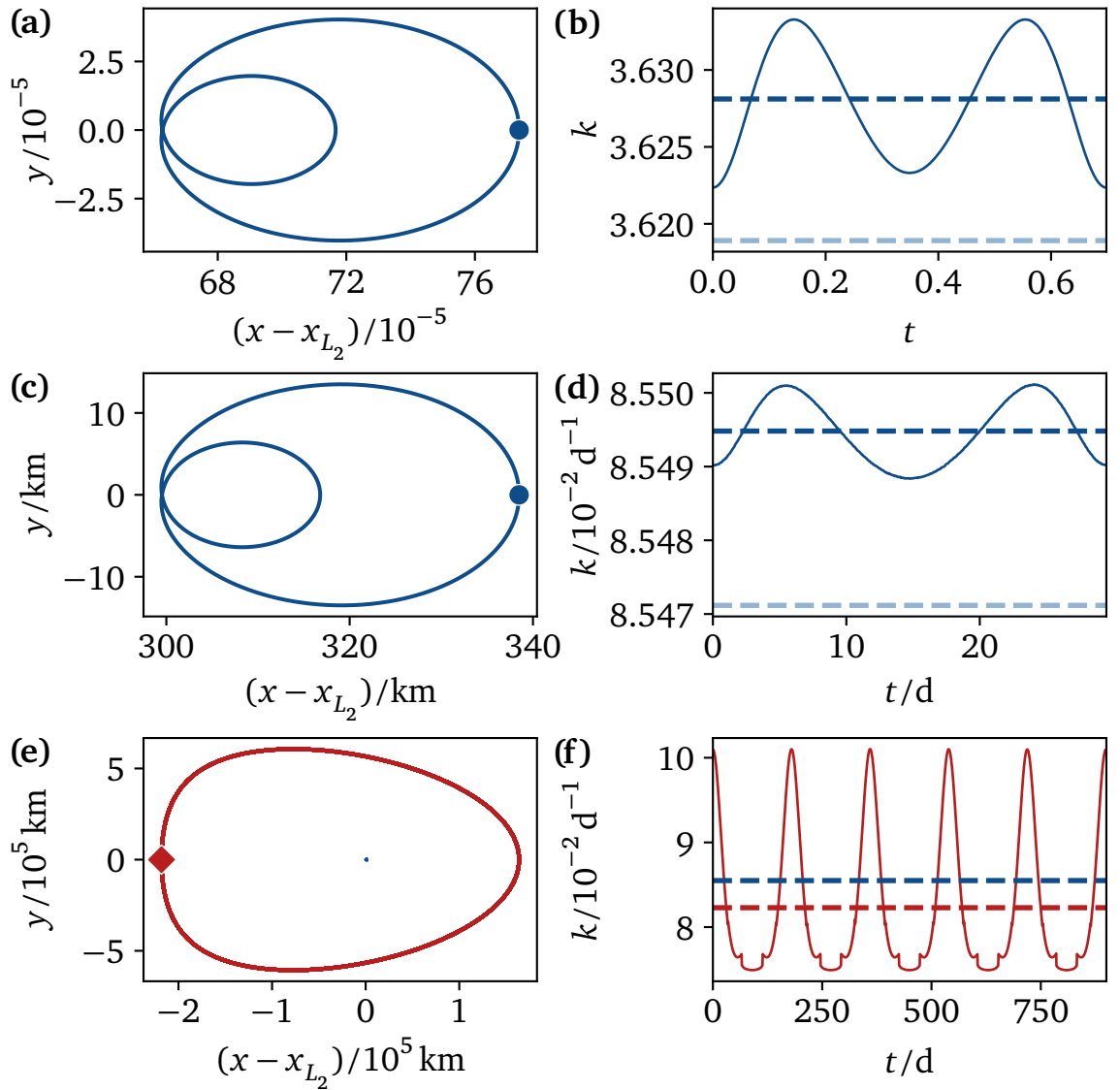


Figure 6-4: Selected orbits in position space x - y and their associated decay rates $k(t)$. The orbits shown here correspond to the fixed points or are highlighted in color in Figure 6-3. The positions at $t_0 = 0$ are marked, with satellites moving clockwise from there on. **(a)** The periodic orbit associated with the L_2 in the strong-driving model. Positions $x - x_{L_2}$ are relative to the location of the L_2 point in the CR₃BP. **(b)** Instantaneous decay rate k_m as a function of time t and averaged rate $\langle k_m \rangle_t$ for the trajectory from panel (a) (solid and dashed dark blue). The decay rate constant k_F of the corresponding CR₃BP is shown in light blue. **(c)** The periodic orbit in the Solar System model analogous to panel (a). **(d)** Decay rates for the Solar System model analogous to panel (b). **(e)** The quasiperiodic orbit highlighted in Figure 6-3(b). In addition, the Solar System's L_2 orbit from panel (c) is shown as a small dot to illustrate the vastly differing scales. **(f)** Analogous decay rates for panel (e). The average decay rate (red dashed) for this orbit is lower than the rate for the periodic orbit in panel (d). A longer time t is shown as the rate, just like its orbit, is quasiperiodic, even though the effect is hardly visible.

Table 6-2: Numeric values for the averaged rate constants shown in Figure 6-4 for the corresponding orbits shown in Figure 6-3. Not all possible combinations of system, orbit, and method are listed because they were not calculated so as to avoid the unnecessary computational expense.

Description	Symbol	Strong driv.	Solar System (d^{-1})
<i>L</i> ₂ orbit			
ensemble propagation	$\langle k_e \rangle_t$	3.628 145	
manifold geometry (LMA)	$\langle k_m \rangle_t$	3.628 115	$8.549 482 \times 10^{-2}$
Floquet stability analysis	k_F	3.628 116	$8.549 479 \times 10^{-2}$
<i>L</i> ₂ orbit, static system ($\tilde{\mu} = 0$)			
Floquet stability analysis	k_F	3.618 910	$8.547 117 \times 10^{-2}$
Quasiperiodic orbit			
manifold geometry (LMA)	$\langle k_m \rangle_t$		$8.228 925 \times 10^{-2}$

with the addition of the quasiperiodic orbit associated with the highlighted torus from Figure 6-3(b). Two differences stand out: First, the diameter of the quasiperiodic orbit is more than four orders of magnitude greater. Specifically, it is about 382 100 km wide in *x* direction, which is very close to the Earth–Moon distance of 384 400 km in our model. Second, this orbit does not feature a loop in its left half. Instead, it is merely oblate on the left and prolate on the right-hand side of Figure 6-4(e), similar to the shape of an egg.

6-4 Stability of satellites

At this point, we are able to analyze the stability of satellites close to the *L*₂ in our system. For this purpose, we calculate decay rates of satellites following the *L*₂ orbit with the three methods presented in Section 3-5. The ensemble rate method has been configured to propagate 32 ensembles of 1024 satellites each. The ensembles are initialized at a maximum distance of $\delta x = 2 \times 10^{-4}$ simulation units from the *L*₂ orbit. We use $\delta x = 10^{-5}$ when determining the slopes of the stable and unstable manifolds for the LMA.

The instability of the *L*₂ orbits as determined by the decay rate is shown in Figures 6-4(b) and 6-4(d). Numeric values for the averaged rate constants are summarized in Table 6-2. As can be seen, all methods are in excellent agreement. The relative deviation between mean rates in the driven system

is

$$(6-12) \quad \left| \frac{k_a - k_b}{k_b} \right| < 10^{-5}, \quad \text{where } k_a, k_b \in \{ \langle k_e \rangle_t, \langle k_m \rangle_t, k_F \}.$$

This confirms the accuracy of the results since all three methods have vastly different numerical implementations.

We show results for both the L_2 orbit of the driven system (with moon, $\tilde{\mu} > 0$) and the L_2 point of the static system (without moon, $\tilde{\mu} = 0$) as defined in Section 6-1. In the latter case, we restrict our analysis to the Floquet rate method as the instantaneous rate in static systems is constant in time and does not yield additional information.

In the comparison to the static system ($\tilde{\mu} = 0$) in Figure 6-4(b), we find a +0.3% increase in the average decay rate of the driven system. That is, the moon generally destabilizes satellites close to the L_2 orbit. During one period of the orbit, L_2 is most stable around $t \bmod T \in \{0, T/2\}$, i. e., when the planet, moon and L_2 are collinear. At these points in time, either the planet or the moon are at their point of minimal distance from L_2 , therefore exerting the strongest forces on satellites near L_2 . Stronger forces push the position of L_2 further out. This is consistent with the course of the L_2 orbit shown in Figure 6-4(a), which reaches maxima in x around $t \bmod T \in \{0, T/2\}$. The lower decay rates entail that satellites near but not on the NHIM depart slower from L_2 . Consequently, fewer course corrections are needed around these points in time.

The limiting case that merges the planet and moon into a single effective body can be achieved by setting $\tilde{\mu} = 0$. This keeps the system's total mass fixed and only changes the mass distribution between planet and moon. Alternatively, we can consider the case in which the star-planet mass ratio M_S/M_P is kept fixed by setting the mass parameter $\mu = 0.09/0.99$. The resulting Floquet rate constant now reads $k_F \approx 3.665$. In this case, the addition of a moon leads to a -1.0% decrease of the rate constant. Hence, the effect of the moon is similar to a static system with an increased planet mass. The resulting stronger forces being exerted on satellites push the L_2 further out.

The calculations of the LMA rates and the Floquet rate constants were also performed for the Solar System model. The results for the L_2 orbit, shown in Figure 6-4(d), are qualitatively identical to those of the strong-driving model discussed above. The decay rate oscillations and the relative deviation between the static and the driven systems, however, are quantitatively smaller by an order of magnitude. In comparison, the quasiperiodic orbit shown in Figure 6-4(e) exhibits two interesting properties: First, its decay rate features much larger oscillations. This is consistent with the larger orbit

diameter as a larger part of the phase space is traversed, and so more varied structures may be taken into account. Second, the average decay rate is about -3.7% lower compared to the L_2 orbit which is large enough to have significant influence on the stability of real-world satellites. This effect is even more apparent in Figure 6-3, where colored backgrounds show the average decay rates behind the PSOSs. The increased stability suggests that the number and/or size of course correction maneuvers could be reduced by parking satellites on one of the outer orbits around L_2 instead of one close to the L_2 orbit.

6-5 Conclusion and outlook

In summary, we have demonstrated that the methods from TST can be used to analyze the dynamics of satellites in planetary systems. Specifically, we analyzed a generic solar system model based on the BCR4BP. We showed how TST approaches can be used to elucidate the dynamics of satellites in the vicinity of the star–planet libration point L_2 , and to determine the extent to which they are influenced by the presence of a moon.

Two sets of parameters were investigated. The first was chosen to show a more significant effect while still resembling real, experimentally observed extrasolar systems. Although there has not yet been a confirmed moon observed around exoplanets [240, 241], this work provides a basis for describing the L_2 of such systems in the future. For comparison, the calculations were repeated for parameters resembling our Solar System. Our calculations revealed that — contrary to first intuition — the L_2 orbit is not the most stable configuration. In fact, orbits on the NHIM get less unstable the farther away from the L_2 orbit they are. We further found that a moon has a destabilizing effect on satellites near L_2 when compared to a system in which planet and moon are merged into a single body. Interestingly, the decay rate when the planet and moon are collinear with the star and L_2 is lower than the average rate, suggesting a reduced need for stabilization by a satellite at that instant.

The rate of instability calculated in this chapter describes how fast trajectories depart from the invariant manifold at L_2 when they are not located exactly on said manifold. In principle, this rate therefore relates to the amount of fuel needed to actively stabilize a satellite on a specific orbit. When using system parameters typical of our Solar System, the methods presented here could be used to optimize the orbits of satellites with respect to fuel consumption.

KRAMERS RATES OF LITHIUM-CYANIDE ISOMERIZATION

This chapter is based on Reference [7] but provides additional data and other enhancements to augment the analysis of the original publication.

We now return from our excursion to celestial mechanics in Chapter 6 and turn towards chemistry again. Specifically, we look at the isomerization of lithium cyanide as it has been the subject of previous studies [7, 116, 118–120, 196] and thus allows us to compare our results. The lithium-cyanide molecule consists of a lithium cation Li^+ revolving around a cyanide anion CN^- . The ionic bond between Li and CN is fluxional, meaning that the lithium can orbit the cyanide relatively easily [242]. This leads to two linear isomer configurations



where the lithium cation is bound to either the carbon or the nitrogen atom, connected by a bridged form with the Li connected to both C and N.

In the following, we do not only consider the LiCN system in isolation, but we account for an external argon bath [118, 119, 196] using the LE and GLE formalisms described in Section 2-2. This is in contrast to References [8, 87], where the dynamics of an isolated lithium-cyanide molecule was investigated. References [8, 87] particularly focused on the stability of the TS as revealed by decay rates and how they are influenced by an external driving. Here, we instead focus on Kramers-style reaction rates, the difference of which is discussed in detail in Section 2-3. Such rates have previously been calculated by García-Müller et al. [118, 119, 196] using PGH theory and AAMD simulations (cf. Section 2-3), by Junginger et al. [120] using LE and GLE reactive-flux calculation, and by Schleeh et al. [7, 116] using MFPT [cf. Equation (3-31)] rates based on the LE. However, some questions remained, especially in the latter references; these will be taken up again below.

In this chapter, we investigate the MFPT reaction rate of lithium-cyanide isomerization. Specifically, we focus on the backward reaction $\text{LiCN} \rightarrow \text{LiNC}$. We make extensive use of Hartree atomic units, which are based on the reduced Planck constant \hbar , the elementary charge e , the Bohr radius a_0 , and the electron rest mass m_e . Units for energy and time follow as $E_h = \hbar^2 m_e^{-1} a_0^{-2}$ and $\hbar E_h^{-1}$, respectively.

7-1 Lithium-cyanide model

The mathematical model this chapter is based on goes back to the work of Es-sers, Tennyson, and Wormer [117, 243]. They performed self-consistent-field calculations [244–246] to obtain the potential-energy surface V for a 2-DoF model of the LiCN molecule (cf. Appendix B). The following simplifications were made:

- The center-of-mass motion is decoupled, which reduces the DoFs from nine to six.
- The total angular momentum is assumed to be zero, reducing the description to four DoFs.
- The resulting model is restricted to a two-dimensional plane, leaving three DoFs.
- The triple bond of the cyanide compound $\text{C}\equiv\text{N}$ is very rigid. Assuming that its length is fixed to $r_{\text{NC}} = 2.186 a_0$ leads us to the final 2-DoF model.

Figure 7-1 shows the resulting configuration. The coordinate system's origin in this model is placed at the cyanide compound's center of mass. The molecule's state is then fully determined by the orientation ϑ of the cyanide CN relative to the lithium atom and the distance R of Li from the origin. In these coordinates, the noiseless Hamiltonian reads

$$(7-2) \quad \mathcal{H} = \frac{p_R^2}{2\mu_1} + \frac{p_\vartheta^2}{2m_\vartheta(R)} + V(R, \vartheta)$$

with the canonical mass (moment of inertia)

$$(7-3) \quad m_\vartheta(R) = \left(\frac{1}{\mu_1 R^2} + \frac{1}{\mu_2 r_{\text{NC}}^2} \right)^{-1}$$

and the reduced masses

$$(7-4) \quad \mu_1 = \left(\frac{1}{M_{\text{Li}}} + \frac{1}{M_{\text{C}} + M_{\text{N}}} \right)^{-1} \quad \text{and} \quad \mu_2 = \left(\frac{1}{M_{\text{C}}} + \frac{1}{M_{\text{N}}} \right)^{-1}.$$

In our calculations we assume pure ${}^7\text{Li}$, ${}^{12}\text{C}$, and ${}^{14}\text{N}$ isotopes with atomic masses [247] $M_{\text{Li}} = 7.016003 \text{ u}$, $M_{\text{C}} = 12 \text{ u}$, and $M_{\text{N}} = 14.003074 \text{ u}$, respectively.

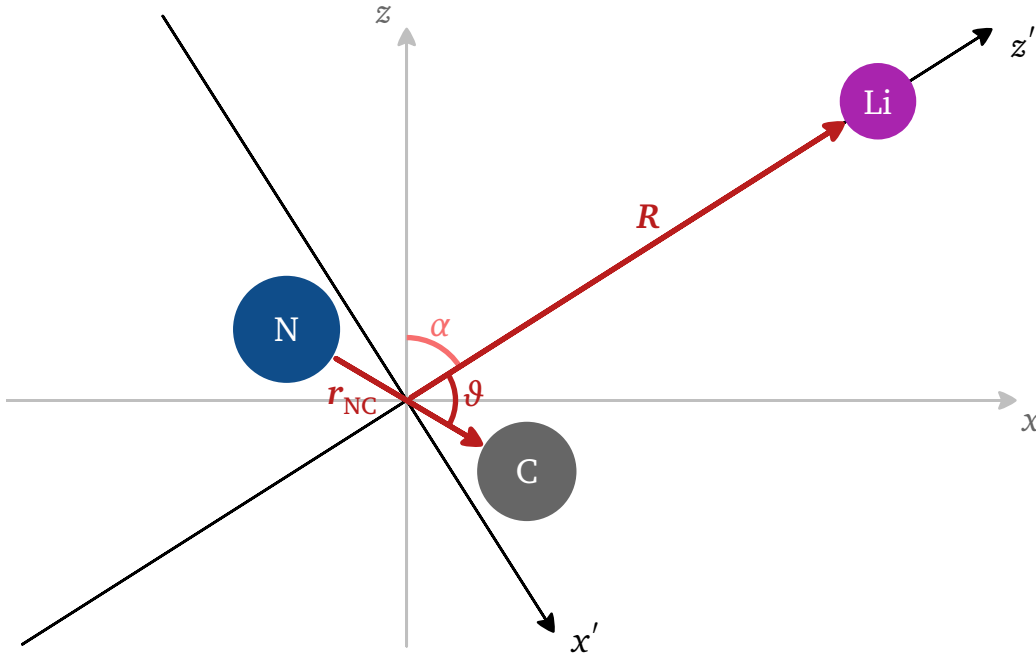


Figure 7-1: The $\text{LiNC} \rightleftharpoons \text{LiCN}$ isomerization model in Jacobi coordinates. The origin of the space-fixed Cartesian coordinate system x - z is placed at the cyanide compound's center of mass. A body-fixed Cartesian coordinate system x' - z' can be defined by rotating the space-fixed axes by angle α such that z' is aligned with \mathbf{R} . The bond between N and C is so rigid that $r_{\text{NC}} = |\mathbf{r}_{\text{NC}}|$ is constant in good approximation. In this body-fixed frame, the Jacobi coordinates $\vartheta = \angle(\mathbf{r}_{\text{NC}}, \mathbf{R})$ and $R = |\mathbf{R}|$ are sufficient to describe the system's configuration. The angles α and ϑ are mutually dependent due to angular momentum conservation.

The equations of motion follow from the Hamiltonian (7-2) as

$$\begin{aligned} \dot{\vartheta} &= \frac{p_{\vartheta}}{m_{\vartheta}(R)}, & \dot{p}_{\vartheta} &= -\frac{dV(R, \vartheta)}{d\vartheta} + \mathcal{E}_{\vartheta}, \\ \dot{R} &= \frac{p_R}{\mu_1}, & \text{and } \dot{p}_R &= \frac{p_{\vartheta}^2}{\mu_1 R^3} - \frac{dV(R, \vartheta)}{dR} + \mathcal{E}_R, \end{aligned} \tag{7-5}$$

where \mathcal{E}_{ϑ} and \mathcal{E}_R represent the appropriate noise and friction terms from Equation (2-1) for the LE or Equation (2-3) for the GLE formalism. The system's mass matrix, which is required for the definition of $\mathcal{E} = (\mathcal{E}_{\vartheta}, \mathcal{E}_R)^{\top}$, reads $\mathbf{M} = \text{diag}(m_{\vartheta}, \mu_1)$.

Readers interested in a more in-depth description of the system, including a derivation of the noiseless equations of motion, are referred to Reference [87].

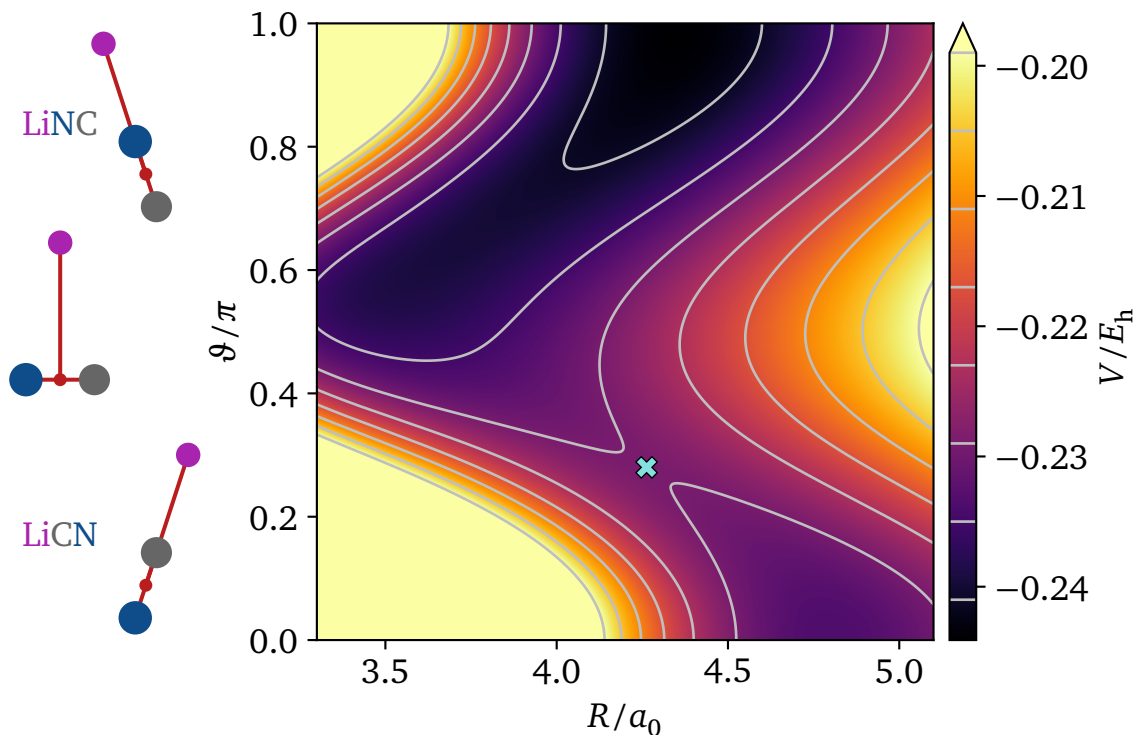


Figure 7-2: Potential-energy surface $V(\vartheta, R)$ as defined in Appendix B. The system consists of two isomer configurations separated by a saddle point at $V(0.2922\pi, 4.2197a_0) = -0.22886E_h$ (cyan cross). The LiNC configuration at $V(\pi, 4.3487a_0) = -0.24461E_h$ is energetically favorable while the LiCN configuration lies significantly higher at $V(0, 4.7947a_0) = -0.23421E_h$. The configurations for LiCN at $\vartheta = 0$, an intermediate state at $\vartheta = \pi/2$, and LiNC at $\vartheta = \pi$ are sketched in space-fixed coordinates on the left-hand side. Their orientation α changes depending on ϑ due to conservation of total angular momentum.

The self-consistent-field potential V [117] is shown in Figure 7-2. Two local minima reveal the linear isomer configurations LiNC and LiCN, whereas the saddle in between (cyan cross) corresponds roughly to the bridged form. The LiNC configuration is the stable ground state. While preparing Reference [7], we found that we were unable to exactly reproduce the figures published in Reference [117] using the numeric parameters from the same article. However, consensus could be achieved by adapting two parameters that seemed to be misprinted. These findings — along with a reproduction of the potential’s analytic form — are discussed in Appendix B.

7-2 Summary of previous results

Initial investigations of MFPT rates in the LiNC \rightleftharpoons LiCN system have previously been published in References [7, 116]. Therein, MFPT rates for the backward reaction were calculated using memoryless LE simulations. The results were compared against PGH calculations (cf. Section 2-3) with and without memory [119] as well as reactive-flux calculations based on LE, GLE [120], and AAMD [119] thermostats. All PGH rates [119] were based on the GLE [cf. Equation (2-3)], but they used two different values for the bath parameter α . Specifically, $\alpha = 1.323 \times 10^6 \hbar^2 E_h^{-2}$ was used to match the memory observed in the AAMD simulations and $\alpha = 1.5625 \hbar^2 E_h^{-2}$ to emulate a memoryless bath. The latter setting corresponds to a memory timescale $\tau = \alpha\gamma = 7.8125 \times 10^{-3} \hbar E_h^{-1}$ that is very short even for the highest friction $\gamma = 5 \times 10^{-3} E_h \hbar^{-1}$ considered here. For comparison, typical first-passage times are $\Delta t \gg 10^3 \hbar E_h^{-1}$ for all investigated parameter sets.

The results from Reference [7] are reproduced in Figure 7-3. First, the PGH and MFPT rates k parameterized by the friction γ were compared. Figure 7-3(a) shows $k(\gamma)$ for a memoryless solvent at temperatures between 300 K and 600 K. Both the PGH and the MFPT method manage to resolve the turnovers. Their general shape matches very well; their scale, however, differs significantly. Hence, the MFPT rates had to be divided by a factor of 5 in References [7, 116] and Figure 7-3(a) to compare the shapes. A similar behavior can be observed at higher temperatures.

Figure 7-3(b) summarizes the temperature dependence of the maximal rate at the turnover for the various methods mentioned above. As can be seen, the PGH rates with and without memory match very well throughout the temperature range, suggesting that memory effects do not play an important role. They are also in good agreement with the AAMD rates, which indicates that PGH theory may still be applicable in this system at temperatures well above the barrier height [118]. The reactive-flux rates from Reference [120], however, behave differently. Whereas GLE-based simulations yield reasonable agreement with PGH and AAMD calculations, the usage of a memoryless LE thermostat results in rates that are roughly half an order to an order of magnitude too large. Reference [120] thus scaled them by a factor of 5, which inspired References [7, 116] to do the same for some of their LE MFPT rates (cf. Figure 7-3(a)). While these MFPT rates — shown unscaled in Figure 7-3(b) — mark an improvement over the LE reactive-flux rates, they still deviate significantly from both the PGH and the AAMD rates. Thus, it was suspected in References [7, 116, 120] that the missing treatment of memory effects in the LE framework was responsible for this discrepancy after all. PGH theory does not directly propagate ensembles of trajectories,

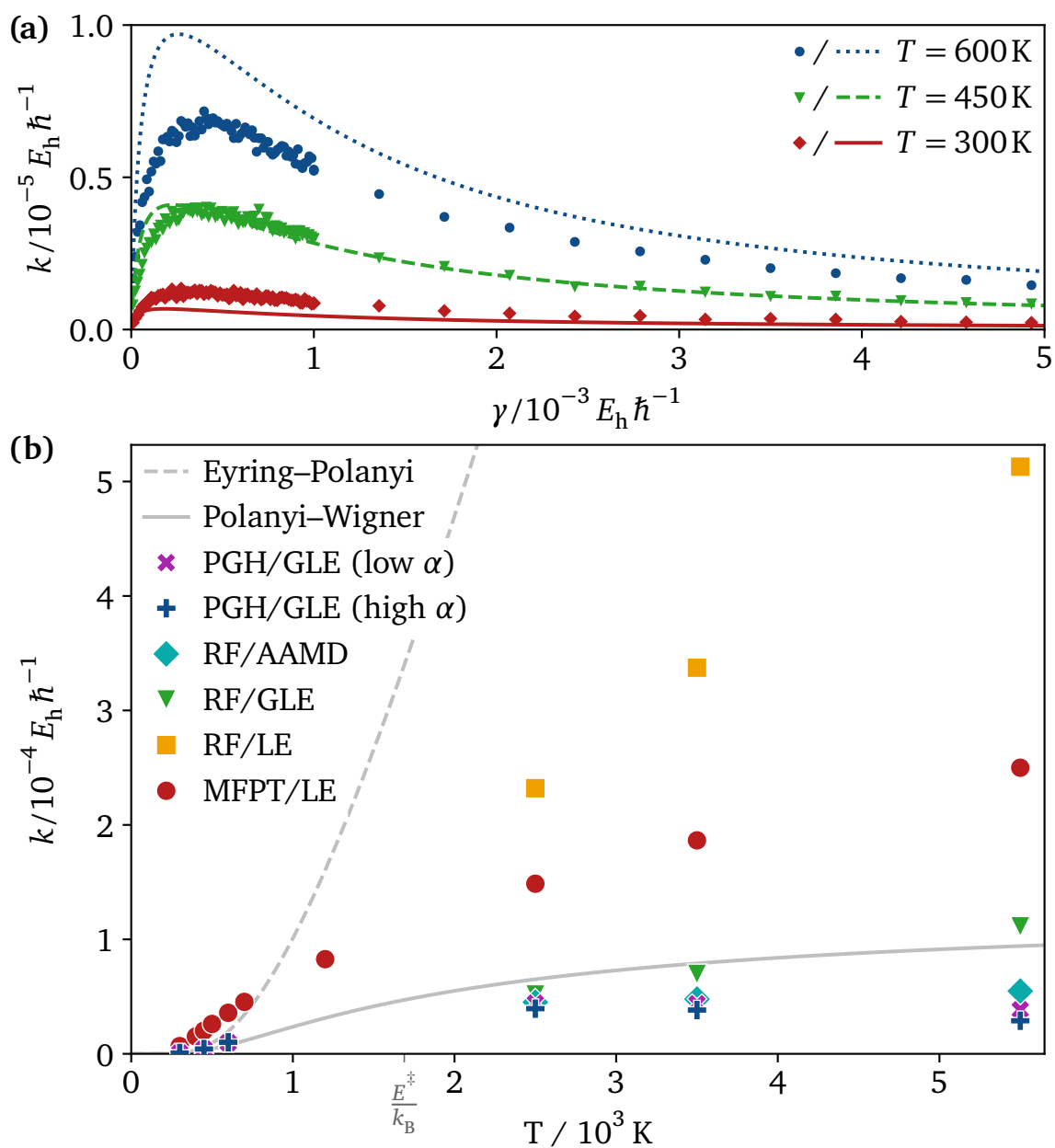


Figure 7-3: Reproduction of the data from Figures 4 and 5 of Reference [7]. **(a)** Reaction rate k of $\text{LiCN} \rightarrow \text{LiNC}$ parameterized by friction γ . Markers show results from the MFPT/LE calculations. These rates have been divided by 5 as in the original publication. Lines indicate unscaled rates obtained from PGH theory with bath parameter $\alpha = 1.5625 \hbar^2 E_h^{-2}$ (almost memoryless). **(b)** Rate maxima k of $\text{LiCN} \rightarrow \text{LiNC}$ as a function of temperature T . The abbreviation “RF” means *reactive flux*. The PGH calculations use $\alpha = 1.5625 \hbar^2 E_h^{-2}$ for rates without and $\alpha = 1.323 \times 10^6 \hbar^2 E_h^{-2}$ for rates with memory. See main text for more information on the different rate methods.

Table 7-1: Influence of the potential of mean force on the PGH rate. The rates based on the bare potential k_{bare} [248] are higher than those based on the potential of mean force k_{PMF} [119] for all temperatures T investigated here. In all cases, we compare the rate at the Kramers turnover with bath parameter $\alpha = 1.323 \times 10^6 \hbar^2 E_{\text{h}}^{-2}$.

T/K	$k_{\text{bare}}/E_{\text{h}} \hbar^{-1}$	$k_{\text{PMF}}/E_{\text{h}} \hbar^{-1}$
2500	4.448×10^{-5}	3.947×10^{-5}
3500	4.634×10^{-5}	3.824×10^{-5}
5500	4.145×10^{-5}	2.887×10^{-5}

so it might behave differently in this regard. Ultimately, we lacked the data to prove or disprove this conjecture in Reference [7].

In addition to the discrepancy discussed above, Schleeh et al. [7] also glossed over the fact that there are two types of potential-energy surfaces on which LE and GLE calculations can be based. The basic surface as described in Appendix B is known as the *bare potential*. It is determined purely from self-consistent field calculations or similar methods and forms the basis for our MFPT simulations, both old and new, as it is readily available. This surface, however, neglects the effects of the solvent on the free energy, i. e., it neglects how the presence of a solvent changes the effective potential-energy surface [119]. To compensate, a so-called *potential of mean force* [249, 250] can be used. This surface would be more accurate, but requires full AAMD simulations to determine. Unfortunately, References [7, 116] are not clear about this issue. They use the original PGH data from Reference [119], which is based on the potential of mean force, for the high-temperature regime with memory. Simultaneously, they add new PGH data at lower temperatures and data without memory based on the bare potential. The impact of this mishap is quantified in Table 7-1. Rates k_{PMF} based on the potential of mean force are clearly lower than their bare-potential equivalents k_{bare} . Yet, this difference is not nearly enough to explain the discrepancies seen in Figure 7-3. So although this is a relatively minor issue with no qualitative impact on the results and conclusions, the inconsistency should still be resolved. The following sections will therefore only compare with bare-potential PGH rates [248] to match the MFPT calculations.

A peculiar behavior in the low- to mid-temperature regime provokes further suspicion: Figure 7-3(b) shows that the PGH rates closely follow the Polanyi–Wigner rate [cf. Equation (C-2) in Section C-1] for temperatures $k_{\text{B}}T$ below the barrier height E^{\ddagger} . Meanwhile, the MFPT rates rise much earlier

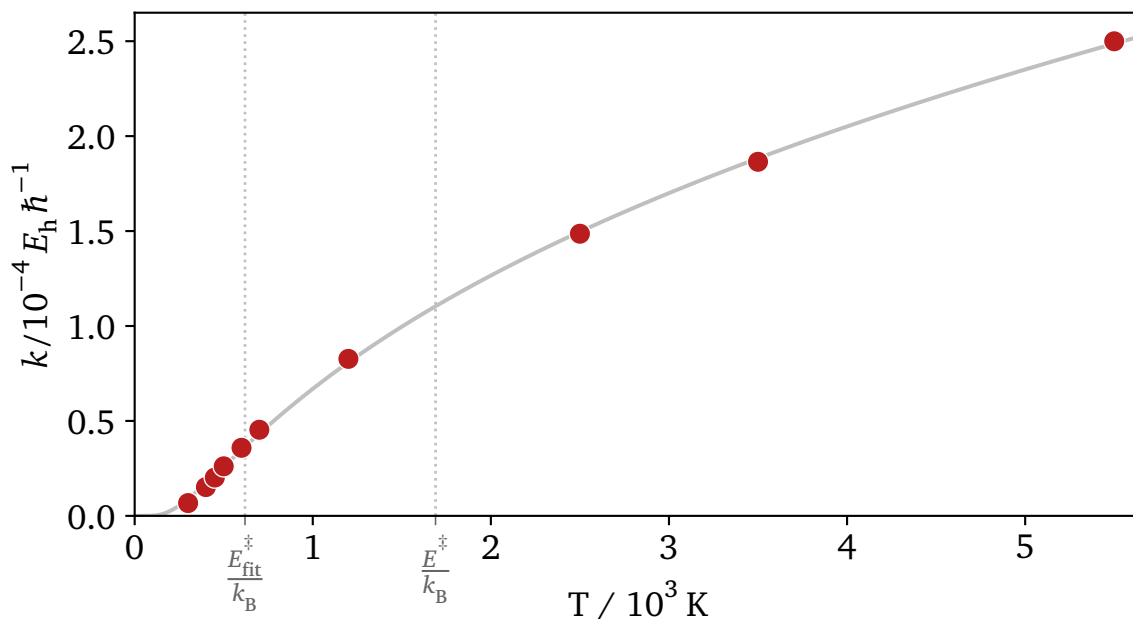


Figure 7-4: MFPT rate k from Figure 7-3(b) as a function of temperature T (markers). The modified Arrhenius equation is in excellent agreement when using the tuned parameters $n_{\text{fit}} = 0.473$ and $E_{\text{fit}}^{\ddagger}/k_{\text{B}} = 619.5$ K (solid line). The fitted value $E_{\text{fit}}^{\ddagger}/k_{\text{B}}$ is far lower than the barrier height $E^{\ddagger}/k_{\text{B}} = 1689.3$ K as indicated via the dotted vertical lines,

and faster. We can model this temperature dependence using the empirical modified Arrhenius equation [251]

$$(7-6) \quad k(T) = AT^n \exp\left(-\frac{E^{\ddagger}}{k_{\text{B}}T}\right),$$

where the parameters A and n are commonly determined via fitting procedures. The Polanyi–Wigner rate can be seen as a special case of this more general expression; it can be recovered by setting A to the reactant well’s vibrational frequency and $n = 0$.

We can now fit Equation (7-6) to the MFPT data from Figure 7-3(b) by tuning A , n , and E^{\ddagger} . A function optimization with the Levenberg–Marquardt algorithm `scipy.optimize.curve_fit(method='lm')` from SciPy [175] yields the solid curve shown in Figure 7-4 with parameters $n_{\text{fit}} = 0.473$ and $E_{\text{fit}}^{\ddagger}/k_{\text{B}} = 619.5$ K. (The pre-exponential A is of little interest for our argument.) The fit reveals two relevant clues. First, we can approximate the rate at high temperatures with

$$(7-7) \quad k(T) \propto \sqrt{T} \quad \text{for} \quad k_{\text{B}}T \gg E^{\ddagger},$$

implying that the system behaves ballistically in this regime. This is not surprising and was already conjectured in References [7, 116]. Indeed surprising, though, is the alleged barrier height of only $E_{\text{fit}}^{\ddagger}/k_{\text{B}} = 619.5 \text{ K}$, which is far lower than the expected $E^{\ddagger}/k_{\text{B}} = 1689.3 \text{ K}$. Such a big deviation suggests a problem with the implementation of either the equations of motion or the stochastic integration algorithm.

Last but not least, the way in which the GLE bath parameters were chosen is inconsistent between the reactive-flux and the PGH simulations. The friction γ is varied in both cases. But whereas reactive-flux fixes τ leaving $\alpha = \tau/\gamma$ to vary, PGH fixes α and leaves $\tau = \alpha\gamma$ varying. This issue has already been present in Reference [120], where the Langevin-based reactive-flux rates were published for the first time. Hence, we will neglect these rates from here on.

The deviations and problems mentioned above motivate to revisit the problem. This chapter is dedicated to addressing the mentioned issues by means of new MFPT simulations. For this task, a new software package supporting LE and GLE thermostats was written. This package does not inherit any components from the previous in-house code used in References [7, 116] so as to provide an independent view on the problem at hand. Readers interested in the open-source code of the new package are referred to Section D-2 in the appendix.

7-3 Kramers turnover

In his seminal paper [111], Kramers showed that the reaction rate rises linearly with γ in the low-friction regime while it decays towards zero for moderate-to-high friction [27] (cf. Section 2-3). Consequently, there must be a turnover in between these limits as discussed in Section 2-3. We begin by resolving this Kramers turnover, as we did in Reference [7]. All MFPT calculations that follow are based on the numerical methods presented in Sections 3-6 and 3-7, and use integration steps of size $\delta t = 0.1 \hbar E_{\text{h}}^{-1}$

Our simulations are based on ensembles of 2048 states initially located at the LiCN minimum. As detailed in Section 3-7, the MFPT method requires us to define a condition that specifies when the propagation of states is to be stopped. We refer to this condition as the *absorbing boundary*. Here, we define that a reactant has definitively turned into a product once it reaches $\vartheta \geq 0.6\pi$. This boundary is indicated as a dashed line in Figure 7-5. By placing it so far on the product side, we ensure that a reacting state is unlikely to return to the reactant well before reaching the LiNC state. With the absorbing boundary in place, we can finally calculate MFPT rates. An

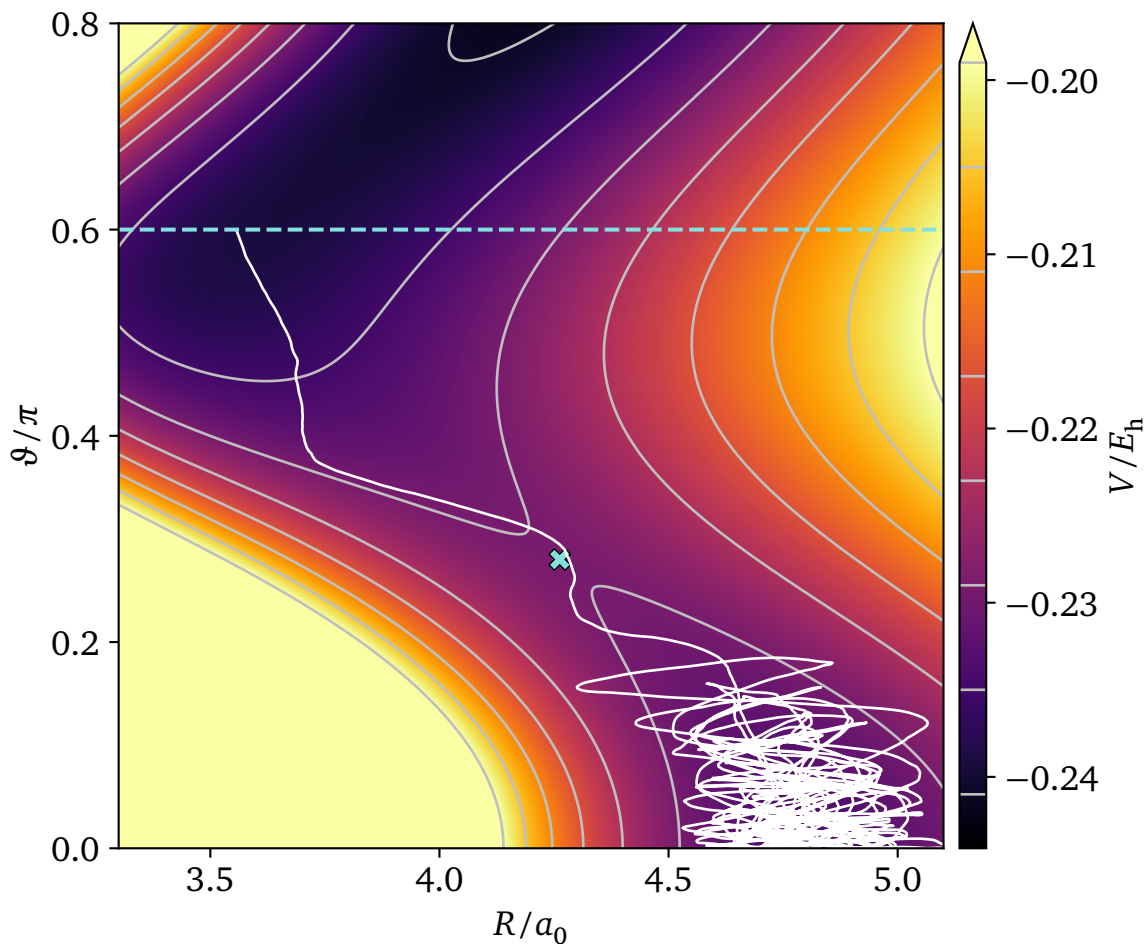


Figure 7-5: Example trajectory for the $\text{LiCN} \rightarrow \text{LiNC}$ reaction in a memoryless bath with temperature $T = 600\text{K}$ and friction $\gamma = 3.25 \times 10^{-4} E_h \hbar^{-1}$. For reference, the potential-energy surface $V(\vartheta, R)$ from Figure 7-2 is underlaid. The trajectory dwells in the LiCN basin for a relatively long time before escaping over the saddle. Propagation in MFPT calculations is stopped once the absorbing boundary $\vartheta = 0.6\pi$, indicated by a horizontal dashed line, is reached.

example for a typical trajectory at $T = 600\text{K}$ is also shown in Figure 7-5. Trajectories at this temperature are usually *activated*, meaning that the thermal energy is lower than the activation energy. The trajectory therefore dwells in the reactant basin for a relatively long time before escaping to the product well. Repeating such calculations for the whole ensemble yields a single rate according to Equation (3-31). The Kramers turnover can then be resolved by propagating one ensemble for each value of the friction γ .

The results are shown in Figure 7-6. As can be seen in Figure 7-6(a), we have excellent agreement between PGH and MFPT rates based on the LE at $T = 300\text{K}$. The turnover peak is slightly shifted to higher γ for increasing temperatures, but the methods are still in very good agreement. Impor-

tantly, this consensus does not rely on any rescaling of the rate. By contrast, References [7, 116, 120] had to divide some of their rates by a factor of 5 to achieve a satisfying match with the **PGH** and **AAMD** rates, as shown in Figure 7-3(a).

The situation is rather similar if memory effects are considered, see Figure 7-6(b). Rates for $T = 300\text{K}$ are still in excellent agreement, and turnovers are still slightly shifted to higher γ for larger T . But whereas the height of turnovers stays almost the same, the rate drops much slower for increasing friction γ compared to the memoryless case. This effect is more pronounced for the **PGH** rates, leading to a noticeable deviation in the decreasing slope at $T = 600\text{K}$. Importantly, this difference does not imply that there is a problem with the **MFPT** calculations. Indeed, **PGH** theory as applied here makes a number of assumptions that simplify the problem — e. g., approximating the minimum-energy path using parabolas — so our **MFPT** calculations could very well be more accurate. Overall, the good agreement between both methods is remarkable.

7-4 Temperature dependence

Now that we have verified that **MFPT** and **PGH** rates are in good agreement at low temperatures, we can consider higher temperatures. This allows us to compare our **MFPT** calculations with the **AAMD** results introduced earlier. Specifically, we do so by studying the temperature dependence of the Kramers-turnover rates. Looking only at the turnover has one big advantage: **AAMD** simulations do not have a coarse-gained friction parameter γ . Instead, a friction effect is caused by collisions with solvent particles, i. e., argon atoms [118, 119, 196]. A higher argon density leads to more collisions and, hence, a higher effective friction. By only looking at the maximal rate, we remove the need to find exact relations between solvent density and friction parameter, making the comparison less error-prone.

MFPT rates are calculated by sampling and averaging first-passage times. This is a stochastic process, and so the rate is only exact for an infinitely sized ensemble, which is not realizable in practice. Thus, the rate fluctuates, as can be seen in Figure 7-6. There are two options to prevent overestimation of the rate maximum caused by these fluctuations. First, the ensemble size could be increased. This would yield ideal results but may not be feasible because of the increased computational cost. Alternatively, we can smooth $k(\gamma)$ numerically. Here, we employ Savitzky–Golay filters [252] with window size 9 and polynomial degree 3 to correct for outliers. This type of filter operates on windows $[j - n, j + n]$ containing the sample to be smoothed at index j plus n samples before and after, for a total of $2n + 1$ samples

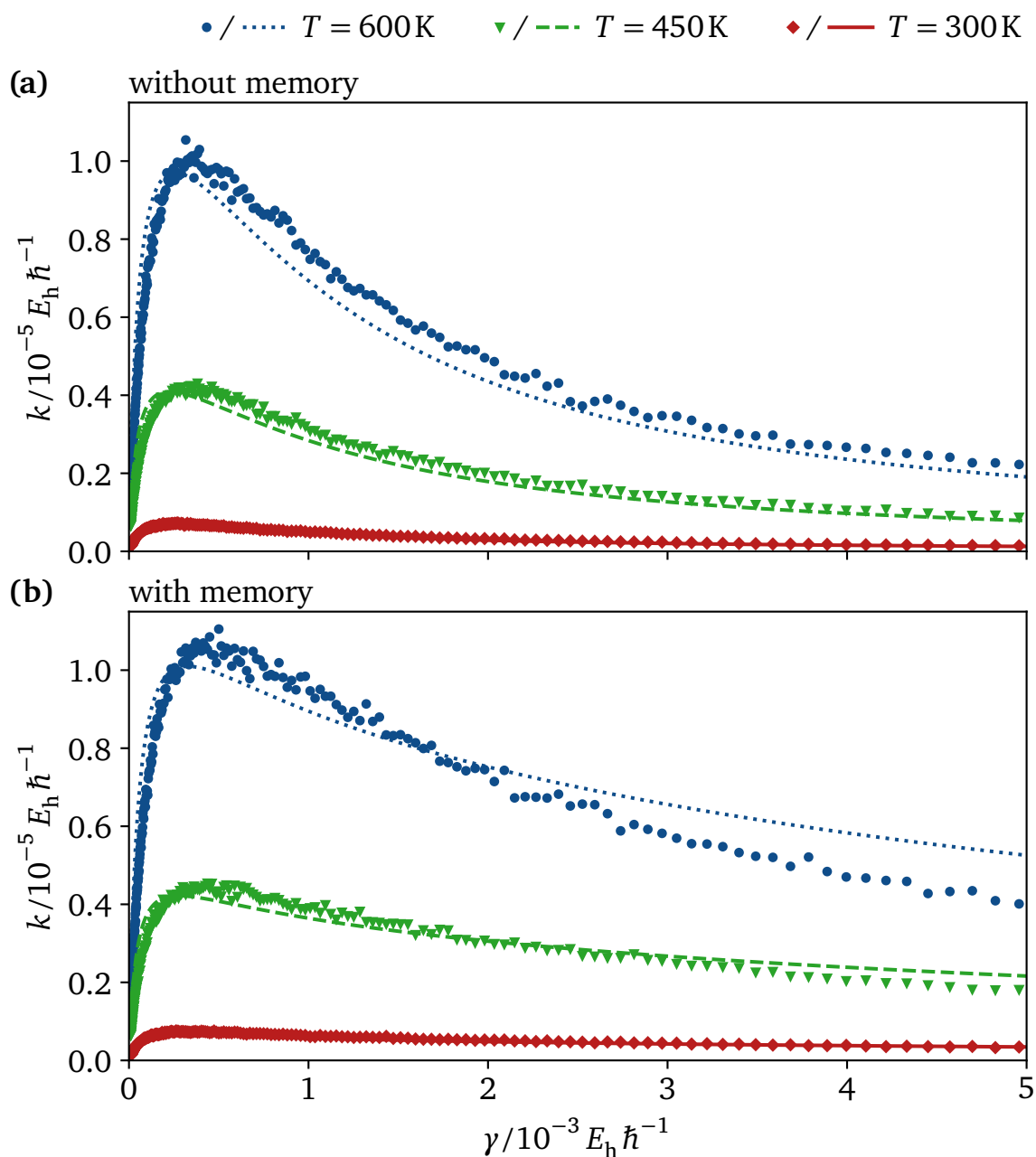


Figure 7-6: MFPT rates k of $\text{LiCN} \rightarrow \text{LiNC}$ parameterized by friction γ (markers). The absorbing boundary is defined as $\vartheta \geq 0.6\pi$. The interaction with the solvent is modeled using (a) the LE—corresponds to $\alpha = 0$ —and (b) the GLE with $\alpha = 1.313 \times 10^6 \hbar^2 E_h^{-2}$. For comparison, lines show PGH rates based on the GLE with $\alpha = 1.5625 \hbar^2 E_h^{-2}$ and $\alpha = 1.323 \times 10^6 \hbar^2 E_h^{-2}$ in panels (a) and (b), respectively. The friction γ is sampled logarithmically. Contrary to Figure 7-3(a), the values have not been divided by 5. Despite this, there is very good agreement between both methods (see text).

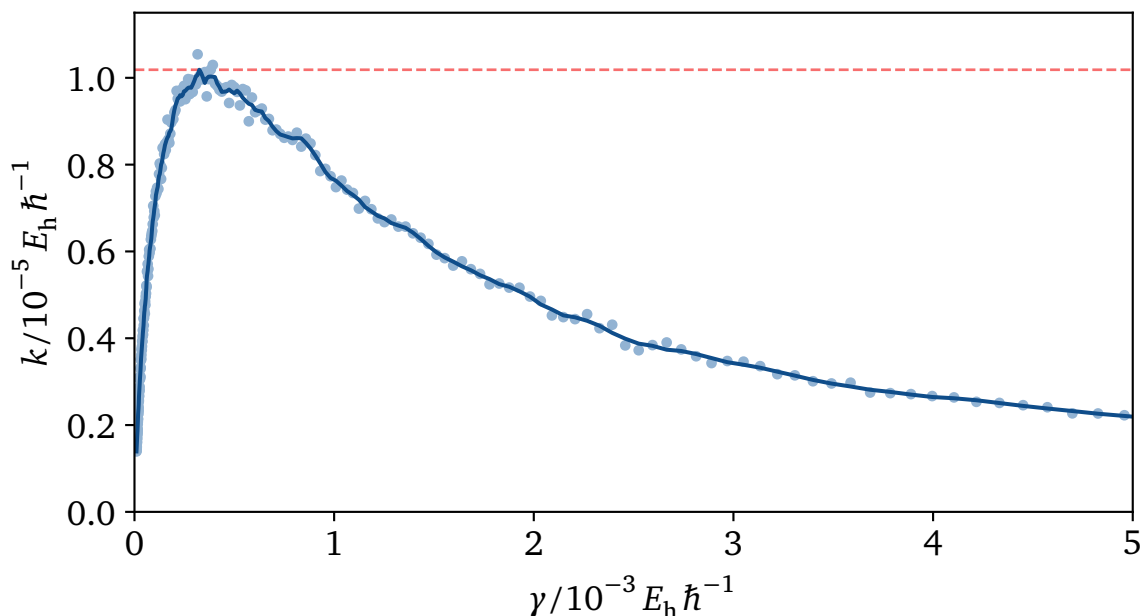


Figure 7-7: MFPT rate k of the $\text{LiCN} \rightarrow \text{LiNC}$ isomerization reaction parameterized by friction γ at $T = 600\text{K}$ without memory [light blue dots, cf. Figure 7-6(a)]. The rate $k(\gamma)$ is noisy because finite ensembles have to be used in numerical calculations. This, however, can lead to an overestimation of the rate. To compensate, we first apply a Savitzky–Golay filter [252] with window size 9 and polynomial degree 3 (blue solid line, see Section 7-4). The maximum (red dashed line) then evaluates to $k = 1.02 \times 10^{-5} E_h \hbar^{-1}$ at $\gamma = 3.25 \times 10^{-4} E_h \hbar^{-1}$ in this example.

($n = 4$ in our case). The new value is produced by fitting a polynomial of degree $d < 2n + 1$ to those samples, and by evaluating the fitted polynomial at the location of sample j . This procedure can be repeated by shifting the window sample by sample to filter the whole input. The result is illustrated in Figure 7-7. Although not perfect, the Savitzky–Golay filter still reduces the overestimation significantly. This filtering is performed for all turnovers $k(\gamma)$, and thus forms the foundation for the following analysis.

(a) Comparison of MFPT with PGH and AAMD rates

The filtered MFPT rate maxima for the LE and the GLE are shown in Figures 7-8(a) and 7-9 along with the corresponding (unfiltered) PGH and AAMD rates. The new MFPT rates improve significantly on the previous results from Figure 7-3. They match very well with the PGH rates at low temperatures (cf. Figure 7-9) and deviate much less from PGH and AAMD rates at high temperatures [cf. Figure 7-8(a)]. In addition, the new calculations show only small differences between LE and GLE baths, which is

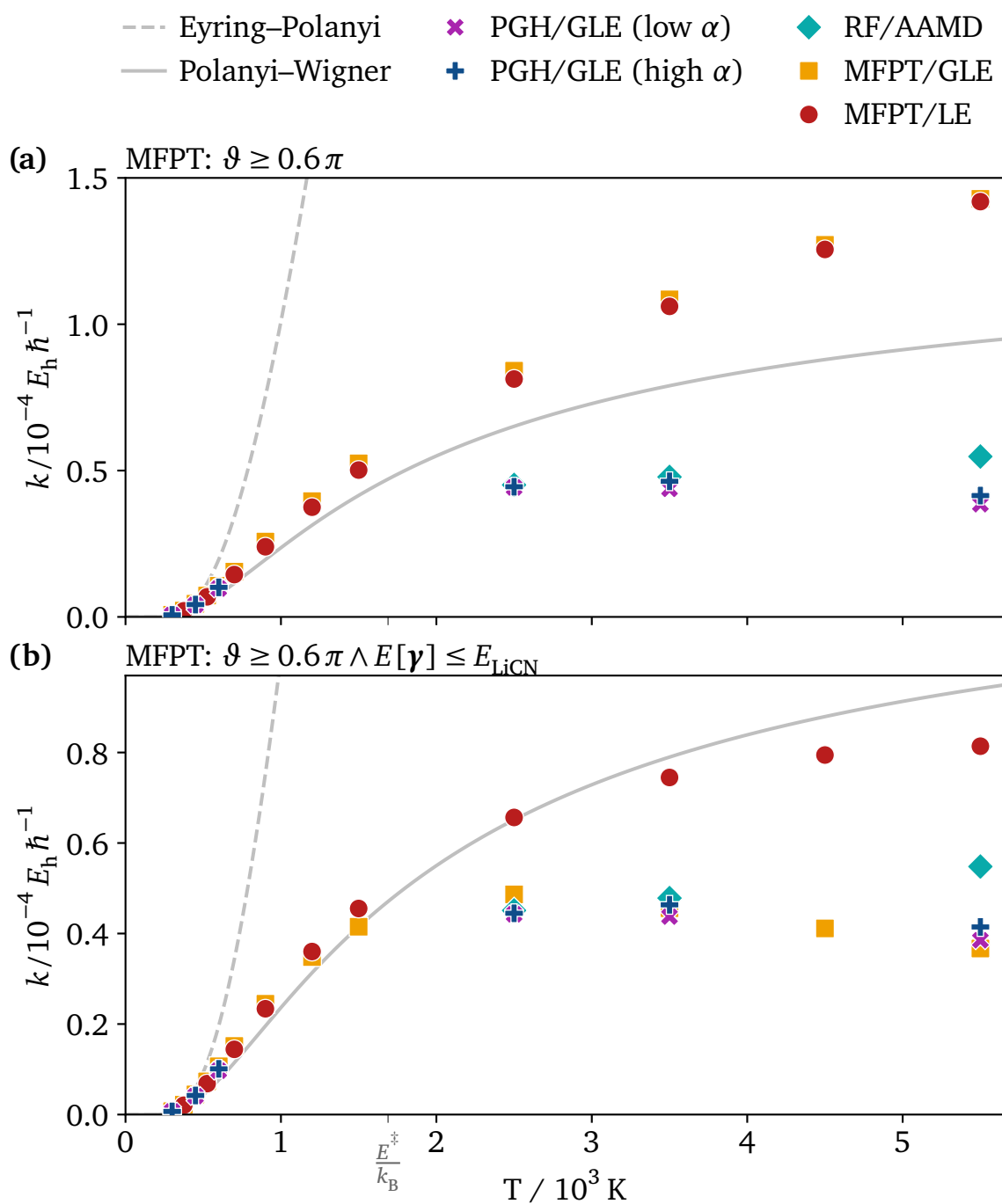


Figure 7-8: Rate maxima k of $\text{LiCN} \rightarrow \text{LiNC}$ parameterized by temperature T . The data presented here is akin to Figure 7-3(b) but uses the new MFPT calculations (cf. Figure 7-6). The abbreviation “RF” means *reactive flux*. (a) The absorbing boundary is defined via the termination condition $\vartheta \geq 0.6\pi$. (b) MFPT trajectories additionally have to satisfy the termination condition $E[\gamma] \leq E_{\text{LiCN}}$, i. e., their total energy has to drop below the LiCN minimum before propagation is allowed to stop.

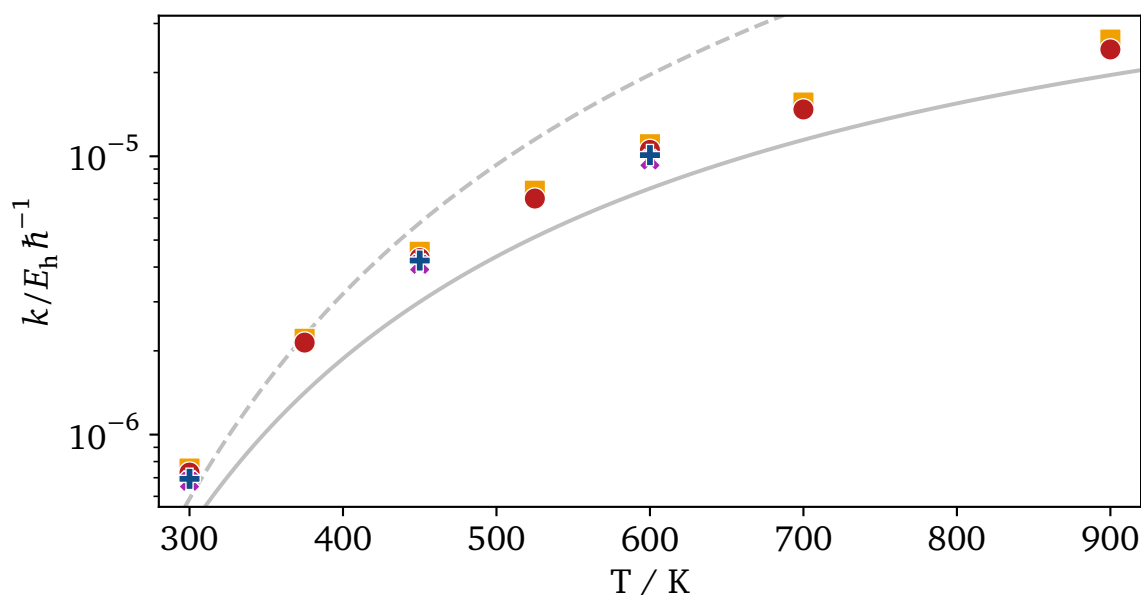


Figure 7-9: Rate maxima k of $\text{LiCN} \rightarrow \text{LiNC}$ parameterized by temperature T . Shown is an enlarged excerpt from the low-temperature region of Figure 7-8(a). **PGH** and **MFPT** results are in very good agreement, and lie mostly between the Eyring–Polanyi and Polanyi–Wigner rates.

consistent with the **PGH** behavior. So far, this challenges the conjecture about the missing solvent memory being responsible for overlarge rates, and further hints towards implementation issues in some of the previous work [7, 116].

For comparison, **TST** rates determined from the Eyring–Polanyi and Polanyi–Wigner expressions have also been added (cf. Appendix C). While both fit very well at low temperatures, Eyring–Polanyi rates diverge quickly for rising T . Indeed, typical **TST** rate theories are only valid for $k_{\text{B}}T \ll E^{\ddagger}$ and begin to break down for thermal energies near or above the barrier height, which is particularly apparent here. This makes it all the more surprising that the **PGH** rates still seem to work so well for the high temperatures considered here. There is good agreement with **AAMD** for all but the highest-temperature sample. Meanwhile, the Polanyi–Wigner expression provides reasonable rates as well, always staying between the **MFPT** and the **PGH** rates at higher temperatures. The rate converges towards the reactant well’s vibrational frequency $\omega_0/2\pi \approx 1.28 \times 10^{-4} E_{\text{h}} \hbar^{-1} \approx 5.29 \times 10^{12}$ THz in the high-temperature limit. (This value is valid for small to medium oscillations; larger oscillations have a slightly lower frequency because of the well’s anharmonicity.)

There are numerous possible sources for the deviations at high temperatures. Perhaps most obvious is the fact that our **MFPT** calculations are based on the bare potential. This neglects the effects of the solvent on the free

energy, as detailed in Section 7-2. Calculating the potential of mean force, however, would increase computational cost and complexity significantly as it relies on full AAMD simulations. In our case, this would defeat the purpose of using the cheaper LE and GLE frameworks in the first place.

A second source is given by statistical errors, which affect both MFPT and AAMD calculations. MFPT calculations are sufficiently cheap so as to minimize these effects (cf. Figure 7-7). The AAMD simulation, though, rely on much fewer ensembles with fewer trajectories per ensemble, hence we can expect larger statistical fluctuations.

Finally, the value of the GLE memory parameter α may not be ideal. This issue again relates to the observation that Reference [120] fixed the memory timescale $\tau = \alpha\gamma$ while References [7, 116, 118, 119, 196] fixed α . Investigating the influence of these parameters on the MFPT rates will be a worthwhile future task.

The deviations observed at high temperatures raise another issue. Namely, how do we define a rate? So far, our MFPT calculations simply used an absorbing boundary in position space. This definition does not discriminate between ballistic and activated trajectories, which may or may not be desired. Meanwhile, the exact details of the AAMD reactive-flux calculations — how is the DS chosen; are ballistic trajectories filtered out? — are not clear from the original publications [118, 119]. This makes it harder to compare the results with our MFPT simulations.

(b) Influence of ballistic trajectories

The occurrence of ballistic trajectories in rate calculations is not a new problem. There is significant precedence in literature [158, 185, 211] of using a state's total energy to constrain the absorbing boundary. Specifically, the first passage is only considered to be complete once, in addition to any other criteria, the total energy falls below a prescribed threshold energy. Figure 7-8(b) repeats the calculations from Figure 7-8(a) taking such a total-energy constraint into account.

The MFPT rates can clearly be seen to drop with both thermostats. This is to be expected since the additional termination condition can only increase first-passage times, and so k goes down. This time, however, a significant difference between LE and GLE solvents emerges. For the LE, the energy threshold only causes the rate growth to slow down, but it is not able to halt it. Systems with memory, on the other hand, seem to be affected much more strongly. Here, the rate of reaction reaches a maximum around $T = 2500\text{K}$ before decreasing again for even higher temperatures. This can be explained by the increasing number of ballistic trajectories at higher temperatures in

combination with the periodic reaction coordinate ϑ . At these temperatures, average trajectories are so fast that they do not only surmount the barrier once, but they instead circle around multiple times before getting caught again in one of the wells. Memory in the GLE formalism effectively reduces the friction of such trajectories, which helps to keep momentum and amplifies the effect. In principle, this could explain at least part of the differences between GLE or AAMD rates and the overlarge LE rates from References [7, 120]. For all the reasons mentioned above, however, it is unlikely to be the sole cause.

The GLE MFPT results shown in Figure 7-8(b) reproduce the behavior of PGH theory well. Both the low- α and high- α PGH rates reach a maximum around 2500 K and 3500 K, respectively, although the effect is less pronounced. This consensus is surprising as PGH theory does not explicitly include any energy constraint as we did for the MFPT calculations. Then again, we are seriously stretching the limits of PGH theory's validity at these high temperatures, so this agreement may just be a coincidence.

7-5 Conclusion and outlook

In this chapter, we revisited the calculation of MFPT escape rates for the $\text{LiCN} \rightarrow \text{LiNC}$ isomerization reaction. We were able to significantly improve on our earlier results [7] using new in-house simulation software developed recently (cf. Section D-2).

At low temperatures, the new results match very well with PGH theory as well as with the Eyring–Polanyi and Polanyi–Wigner expressions. This is important evidence for the new implementation working correctly. Yet, rates at high temperatures are still higher than those determined via PGH theory and AAMD simulations. Deviations from PGH theory are not very surprising in this regime. Pollak, Grabert, and Hänggi assumed that the thermal energy $k_{\text{B}}T$ is small compared to the barrier height E^{\ddagger} , and so their theory is outside its range of validity. Indeed surprising, however, is that the PGH rates do match the AAMD rates well. Whether this is by chance or whether PGH theory is still applicable in this regime will have to be answered through future research.

Disregarding PGH theory, there are a number of possible reasons for why our MFPT results could differ from the AAMD ones. First, our calculations coarse-grained the solvent via the GLE. This approximation may have been too coarse to sufficiently capture the interaction with the argon solvent as implemented in the AAMD simulations. Related to this, we were only able to use a bare potential-energy surface in this work. More accurate results could have been obtained using a potential of mean force. Approximating

the 9-DoF LiCN molecule via a 2-DoF model may have introduced further errors. All of these points could be improved upon in future work.

Another possible reason is the treatment of ballistic trajectories. Excluding them, which we achieve by limiting the total energy of product states in the MFPT formalism, can partially correct the observed deviations. The resulting rates agree much better with the reference data. Whether this correction is physically sensible depends on the question one seeks to answer and, therefore, on what one defines as *the rate*. The original AAMD-rate publications [118, 119] are not very detailed regarding the reactive-flux calculations. Although this is less important for activated trajectories, it can have very significant effects for ballistic ones. So while AAMD does have a credit of trust — it is the most fundamental method after all — neither the MFPT nor the AAMD results can definitively be considered right or wrong without specifying the problem to be solved.

REVIEW AND FUTURE PERSPECTIVE

In this thesis, we used the advanced framework of **TST** as described in Part I to investigate a selection of systems with rank-1 saddle. Specifically, we explore two driven model systems with one two-dimensional saddle or two one-dimensional saddles, a celestial-mechanics system, and a simple chemical reaction in Part II. These systems have in common that they are low-dimensional, featuring at most two **DoFs**. This facilitates visualization, but is still enough to allow for complex dynamics. Most of the methods used in this work can, in principle, be applied to systems with arbitrarily many **DoFs**. Yet, doing so may get a lot more difficult. To become feasible, methods like the **BCM** might need modifications or extensions making them more robust. Developing these methods further could open the door to novel applications in more complex systems.

Our investigations focused on the construction of a recrossing-free **DS** from the dynamical properties of the saddle, the properties of the associated **NHIM** and **TS**, and the rate of trajectories passing through this **TS**. We were able to define two qualitatively different types of rates depending on whether only the vicinity of the **NHIM** or the whole potential landscape was considered.

8-1 Decay rates in driven systems

Decay rates describe the stability of trajectories near the **NHIM** (cf. Section 3-5). They can be used to map the **NHIM**'s structure, which is especially interesting in driven scenarios. We have shown in Chapter 4 that variations of the driving parameters can alter the **NHIM** significantly through, e. g., saddle-node bifurcations of fixed points. These results lead to a better understanding of the reaction dynamics in these systems. Indeed, it suggests that one could control reaction pathways and, thus, reaction rates within a limited range by adjusting the driving of the system. For these results to become applicable to real chemical reactions, though, they must be generalized to include effects like noise and friction as caused, for instance, by a solvent. This will not be an easy task for these effects will cause the **NHIM** to collapse to a single trajectory over time [9, 116]. Hence, future research will be well-advised to focus initially on the limit of weak noise and friction. It will be even more challenging to incorporate the results from the multi-saddle

system discussed in Chapter 5. This, however, will be an important task since many—even very simple—chemical reactions like the isomerizations of ketene [169, 199–202] and triangular potassium cyanide [197, 198] can be described by potential-energy surfaces with multiple saddles.

Besides the generalization of the results to thermal systems, future research should also seek for models where the presented methods can be applied directly. This complementary approach was pursued in Chapter 6. Here, the stability revealed by the decay rate allowed us to assess the relative fuel consumption of satellites on orbits near one of the collinear libration points L_1 to L_3 . This is especially useful near the Sun–Earth point L_2 as it has been the target of many past and present space probes [112–115].

This example demonstrates how science can be advanced by exchanging ideas between different disciplines like TST and celestial mechanics. And celestial mechanics is not the only field where TST methods can be applied to; spintronics, for instance, has been shown to be amenable as well [10, 11, 50–52]. A unique property of macrospin systems is that the Landau–Lifshitz–Gilbert equation [253, 254], which describes the time-evolution of spin states, is a first-order differential equation that does not include momenta. It can be reduced to a two-dimensional phase space in spherical coordinates, where one of the angles takes the role of the momentum. Only the inclusion of inertial effects [255, 256] adds proper momenta back. Yet, both variants can be treated using TST methods. Such interdisciplinary work is reminiscent of Haken’s idea of synergetics [257]. To really advance both TST and the other disciplines, however, it will not be enough to simply demonstrate our methods in those other fields. Instead, researchers will have to work together to achieve their full potential.

8-2 Absolute reaction rates in thermal systems

The other type of rate, the absolute reaction rate, describes how fast trajectories move from a reactant well on one side of the DS to a product well on the other side and vice versa. This concept is usually applied to systems that are coupled to a thermal bath, chemical reactions being a prime example.

As hinted at in the previous section, we were able to uncover a limited connection between the structures revealed by decay rates on the one hand and the dynamics of trajectories linking the reactant to the product well on the other hand. Still, it is yet unclear whether a method can be developed that utilizes decay rates in a meaningful way to calculate accurate reaction rates. This will be especially challenging at higher temperatures where many trajectories will cross the DS far from the NHIM. Thus, the stability properties of the NHIM lose significantly in importance in this regime.

Nevertheless, pursuing this research further may reveal interesting details about the geometry of reaction pathways, and not just about the rate of a reaction.

Finally, our investigations shed some light on a handful of open questions concerning the reaction rate of the $\text{LiCN} \rightarrow \text{LiNC}$ isomerization reaction. We exposed a number of inconsistencies between calculations with different methods [7, 116, 119, 120] that seemed to be caused by either implementation issues or rates being calculated for effectively different processes, e. g., by using different sets of parameters. Through new GLE-based MFPT calculations, we showed how the definition of the DS (or absorbing boundary condition) can have a massive influence on the resulting rate, especially when considering solvent memory at high temperatures. This effect might have contributed to the deviations observed in References [7, 116, 120]. It led us to debate the question of when a reaction process is actually complete. Whether it is enough to cross the barrier or whether a trajectory also has to be captured in the product basin makes for a qualitatively different process, and the correct choice depends on the physical or chemical question to be answered. By making sure that equivalent definitions for the DS and the parameters are used, future work could provide a more meaningful comparison between the different methods.

Appendices

FLAWS OF DISCONTINUOUS DIVIDING SURFACES

A

Essential parts of this appendix have previously been published by the author in Reference [4].

In Chapter 5, a system with two barriers — each associated with a **DS** — was discussed. In such a system, it may seem natural to define a global **DS** via the local **DS** associated with the instantaneously higher saddle point, cf. Figure 5-1(b). This naive **DS**, however, can jump discontinuously from one side to the other if the heights of the saddle points vary with time. There are multiple ways in which such a discontinuous **DS** can misclassify a trajectory:

- A nonreactive trajectory is classified as reactive (labeled “N as R” in Figure A-1). This can happen when a reactant enters the central region between the saddles while the **DS** is located near the left saddle. If this happens shortly before the **DS** jumps to the right, the particle can get reflected at the right barrier and leave the central region on the reactant side.
- A reactive trajectory is classified as nonreactive (labeled “R as N” in Figure A-1). This can happen when a reactant enters the central region while the **DS** is located near the right saddle. The **DS** can then jump discontinuously over the particle to the left saddle — which is not counted as a crossing — before the particle leaves the central region to the right as a product. The classification is thus inconsistent.
- Further inconsistencies are possible (labeled “incons.” in Figure A-1). This is the case, e. g., when a reactant enters the central region while the **DS** is located near the right saddle, and leaves it again to the reactant side while the **DS** is near the left saddle. As a result, a backward reaction is recorded even though the particle started as a reactant. Similarly, it is possible to detect two forward reactions over the same **DS** without an intermediate backward reaction. It is unclear which reaction is to be counted as the *real* one.
- The trajectory crosses the **DS** multiple times, i. e., it exhibits recrossings (labeled “recross.” in Figure A-1). This can happen when a particle enters and leaves the central region on the reactant side while the **DS** is near the left saddle, resulting in two crossings.

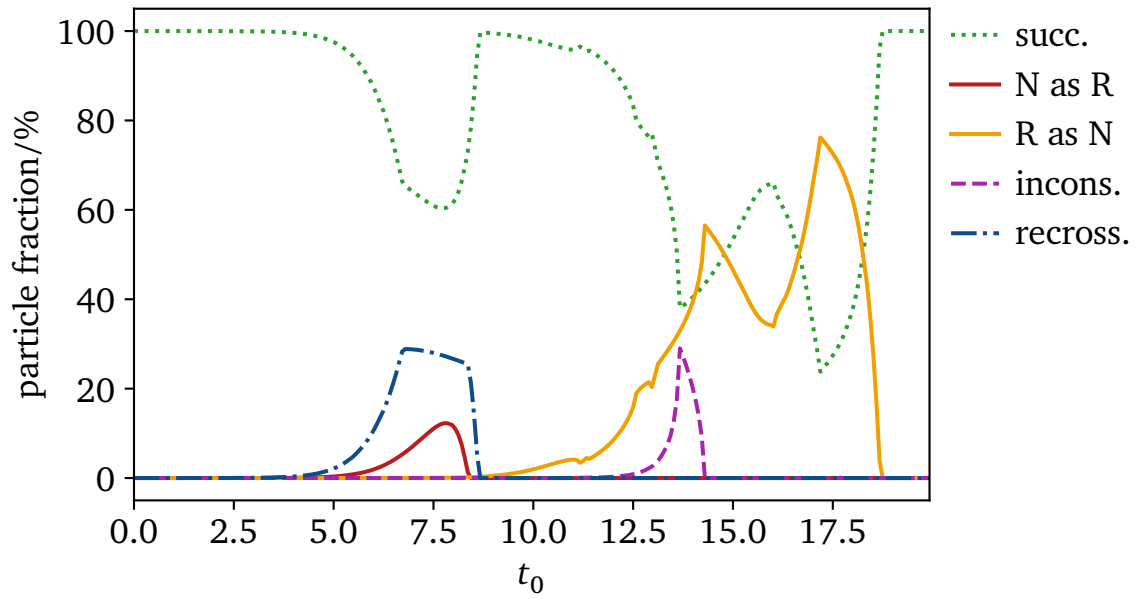


Figure A-1: Fraction of trajectories with (see text) and without (labeled “succ.”) errors as a function of time t_0 for the discontinuous DS from Figure 5-5.

The distributions of these errors in the context of Section 5-3 are shown in Figure A-1. They sum up to the error reported in Figure 5-5(b) for the discontinuous DS.

LITHIUM-CYANIDE POTENTIAL-ENERGY SURFACE

Essential parts of this appendix have previously been published by the author in Reference [7].

The LiNC \rightleftharpoons LiCN potential-energy surface used in Chapter 7 was initially published in Reference [117]. It consists of two parts, a damped long-range energy plus a short-range energy. Both terms involve several numeric parameters, two of which were found to be erroneous [7] in the original publication. Here, we summarize the potential with the correct parameters.

The long-range part is composed of the electrostatic energy

$$E_{\text{el}}(R, \vartheta) = \sum_{L=0}^{\infty} R^{-L-1} P_L(\cos \vartheta) \langle Q_{L,0} \rangle \quad (\text{B-1})$$

and the induction energy

$$E_{\text{ind}}(R, \vartheta) = \sum_{l_1, l_2=0}^{\infty} R^{-l_1-l_2-2} \sum_{L=|l_1-l_2|}^{l_1+l_2} P_L(\cos \vartheta) C_{l_1, l_2, L}. \quad (\text{B-2})$$

Table B-1: Expectation values $\langle Q_{L,0} \rangle$ of the CN^- multipole moments used in Equation (B-1) and induction energy coefficients $C_{l_1, l_2, L}$ used in Equation (B-2). Originally published in Reference [117] and (partially) Reference [243]. The bold value $C_{2,1,3}$ differs from the original publication. All values are given in Hartree atomic units.

L	$\langle Q_{L,0} \rangle$	$C_{1,1,L}$	$C_{2,1,L}$	$C_{2,2,L}$	$C_{3,1,L}$	$C_{3,2,L}$	$C_{3,3,L}$
0	-1.000	-10.53		-57.49			-458.2
1	-0.2151		-10.31			-101.45	
2	-3.414	-3.17		-35.71	-35.56		-353.7
3	-3.819		1.866			-37.62	
4	-15.84			5.23	5.95		-112.6
5	-14.29					-14.23	
6	-43.82						-108.3

Table B-2: Parameters A_L , B_L , and C_L found for the analytical expression of the short-range interaction in Equation (B-5). The bold value C_2 differs from that in the original publication in Reference [117], but all the other values are the same. All values are given in Hartree atomic units.

L	A_L	B_L	C_L
0	-1.38321	0.14001	0.207892
1	-2.95791	1.47977	-0.011613
2	-4.74203	1.81199	-0.017181
3	-1.88853	1.28750	0.027728
4	-4.41433	2.32297	-0.070693
5	-4.02565	2.77538	-0.137720
6	-5.84259	3.48085	-0.186331
7	-2.61681	2.65559	-0.005882
8	-6.34466	4.34498	-0.152914
9	15.2023	-6.54925	1.302568

Here, P_L is the Legendre polynomial of order L , $\langle Q_{L,0} \rangle$ denotes the expectation value of the order- L CN^- multipole moment, and $C_{l_1, l_2, L}$ are the induction coefficients. Numeric values for $\langle Q_{L,0} \rangle$ and $C_{l_1, l_2, L}$ are given in Table B-1. The damping is represented by

$$(B-3) \quad F(R) = 1 - \exp\left[-a(R - R_0)^2\right]$$

with fit parameters $a = 1.5156 a_0^{-2}$ and $R_0 = 1.9008 a_0$, where a_0 is the Bohr radius.

The short-range term can be written as

$$(B-4) \quad E_{\text{SR}}(R, \vartheta) = \sum_{L=0}^{\infty} D_L(R) P_L(\cos \vartheta),$$

where the analytic form

$$(B-5) \quad D_L(R) = \exp\left(-A_L - B_L R - C_L R^2\right)$$

has been fitted to self-consistent field calculations. Numeric values for the fit parameters A_L , B_L , and C_L are given in Table B-2.

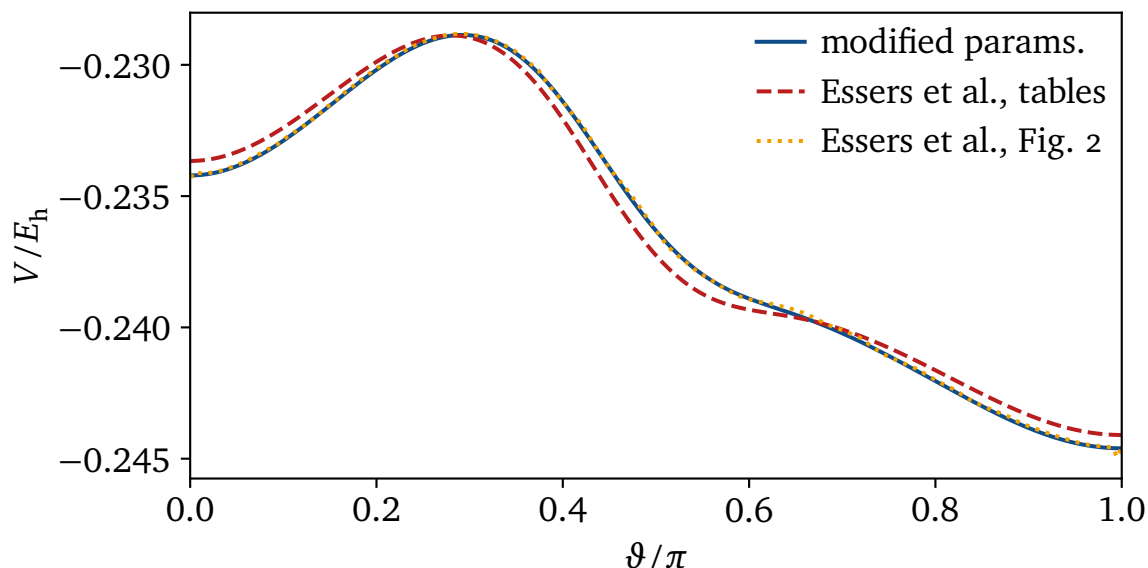


Figure B-1: Potential energy V as a function of angle ϑ on the minimum-energy path of the $\text{LiNC} \rightleftharpoons \text{LiCN}$ isomerization reaction. Plotting the potential (B-6) using the parameters published in Reference [117] yields the dashed curve. This curve differs visibly from the one shown in Figure 2 of the same article, reproduced here as the dotted line. Modifying the parameters as detailed in the text results in much better agreement, as illustrated by the solid line.

Combining long- and short-range energies, the final potential-energy surface reads

$$V(R, \vartheta) = [E_{\text{el}}(R, \vartheta) + E_{\text{ind}}(R, \vartheta)] F(R) + E_{\text{SR}}(R, \vartheta). \quad (\text{B-6})$$

We noticed a discrepancy [7] while comparing the minimum-energy path calculated using the parameters published in Reference [117] with Figure 2 of the same article. As shown in Figure B-1, the two curves differ visibly. Two parameters in the original source code [258], $C_{2,1,3}$ in Equation (B-2) and C_2 in Equation (B-5), differ significantly from the originally published values [117], possibly due to errors introduced during the paper’s production process. The correct values — shown in bold in Tables B-1 and B-2 — yield a much better agreement with Figure 2 from Reference [117].

An implementation of the potential in the Python programming language [259] using the same parameters as the original source code [258] can be found on GitHub [260]. See also Section D-3.

APPROXIMATIVE REACTION-RATE FORMULAS

Essential parts of this appendix have previously been published by the author in Reference [7].

Most approximative reaction-rate formulas follow the Arrhenius form [27, 109]

$$k(T) = \nu(T) \exp\left(-\frac{E^\ddagger}{k_B T}\right), \quad (\text{C-1})$$

where ν is a possibly temperature-dependent prefactor, E^\ddagger is the reaction's barrier height or activation energy, k_B is the Boltzmann constant, and T is the temperature. In the following we present two important TST variants of this equation.

C-1 Polanyi–Wigner rate

One of the earliest results of TST is the unimolecular rate equation derived, among others, by Polanyi and Wigner in 1928 [143]. It follows the Arrhenius rate law (C-1) with the pre-exponential factor $\nu(T)$ given by the vibrational frequency $\omega_0/2\pi$ of the reactant well [27]

$$k(T) = \frac{\omega_0}{2\pi} \exp\left(-\frac{E^\ddagger}{k_B T}\right), \quad (\text{C-2})$$

where E^\ddagger is the internal energy difference between the barrier and the reactant of the isolated system. This equation has been derived in various contexts. It can, e. g., be recovered from the underdamped regime $\omega^\ddagger k_B T/E^\ddagger \ll \gamma \ll \omega^\ddagger$ of Kramers's medium-to-high-viscosity rate [111, 145]

$$k(T) = \left[\sqrt{\left(\frac{\gamma}{2\omega^\ddagger}\right)^2 + 1} - \frac{\gamma}{2\omega^\ddagger} \right] \frac{\omega_0}{2\pi} \exp\left(-\frac{E^\ddagger}{k_B T}\right), \quad (\text{C-3})$$

where γ is the friction and ω^\ddagger is the inverse barrier frequency. Equation (C-2) can therefore be seen as an upper bound for the rate at the turnover in Kramers's original theory for a *solvated* reaction [27].

C-2 Eyring–Polanyi rate

The usual (or modern) form for the classical TST rate equation is given by the Eyring–Polanyi equation [26, 110, 144]

$$(C-4) \quad k(T) = \frac{\kappa k_{\text{B}} T}{h} \exp\left(-\frac{\Delta G^\ddagger}{k_{\text{B}} T}\right)$$

with $\kappa = 1$, where κ is the transmission coefficient, h is Planck's constant, and ΔG^\ddagger is the Gibbs energy of activation in the context of a solvent.

The Gibbs energy of activation can be approximately determined from the enthalpy of activation ΔH^\ddagger via

$$(C-5) \quad \Delta G^\ddagger = \Delta H^\ddagger - T \Delta S^\ddagger,$$

where ΔS^\ddagger is the entropy of activation. In turn, the enthalpy of activation for an unimolecular gas-phase reaction can be written as

$$(C-6) \quad \Delta H^\ddagger = E^\ddagger - k_{\text{B}} T.$$

The energy of activation E^\ddagger and the entropy of activation ΔS^\ddagger can finally be determined from the minimum-energy path and the potential of mean force of the reaction [118, 119] by equating the latter with the Gibbs energy.

The transmission coefficient κ in the Eyring–Polanyi equation describes the fraction of states that cross the DS between reactants and products at most once, i. e., those that do not recross. This quantity cannot be determined from straightforward statistical mechanics and is therefore of great interest [110] in the general case. In TST, it is assumed to be approximately one [27]. This approximation is valid if the temperature is not too high or if the friction is sufficiently strong.

SOFTWARE

All results in this thesis have been obtained using software libraries developed in-house at the Institute for Theoretical Physics I. These libraries are either written directly in Python [259] or at least provide Python bindings. The in-house libraries are combined with renowned third-party libraries such as NumPy [261], SciPy [175], and Matplotlib [262] to achieve the final results.

Parts of the software developed by the author have been made open-source. The following sections introduce these projects briefly.

D-1 RODEO

The *RODEO* project is a closed-source library that has been developed internally at the Institute for Theoretical Physics I. It was initiated by Matthias Feldmaier and further advanced with Robin Bardakcioglu and this thesis' author. Variants of this project provided the basis for Chapters 4 to 6 as well as various publications and theses [1–11, 51, 52, 60, 87, 94–96, 98, 99, 108, 116, 173].

RODEO is implemented as a Python library with a CUDA-enabled [263] C++ [264] backend. This allows it to be fast and efficient in many scenarios while still being relatively easy to use. However, this comes at the cost of high complexity, making it difficult to showcase algorithms and procedures. Thus, a simplified reimplementations of the most important parts has been published on GitHub [265]. It is written purely in Python, giving us a lot of freedom for code design and enabling anyone to play around with the implemented algorithms.

Researchers interested in using this project are invited to have a look at the documentation and the sample scripts included in Reference [265].

D-2 mfptlib

The focus of the MFPT calculations in Chapter 7 differs quite a lot from most of our earlier research. For example, all core algorithms in RODEO (cf. Section D-1) need to be able to propagate trajectories backward in time. This requirement is fundamentally incompatible with the idea of solvent-induced memory, where the friction at time t_0 may depend on momenta at previous times $t < t_0$.

To solve this conflict, the *mfptlib* project was devised. This library is split into a Python frontend and a C++ backend just like RODEO but does not include CUDA support. It implements different integration algorithms as well as thermostats with and without memory to efficiently propagate ensembles of trajectories in the [GLE](#) framework. With *mfptlib*, first-passage times of whole ensembles can be calculated with few lines of simple Python code. The architecture is flexible enough so that new physical systems, numerical integrators, and thermal baths can be implemented easily in the C++ backend.

The project's source code can be found on [GitHub \[266\]](#).

D-3 Lithium-cyanide isomerization potential

An optimized C++ implementation of the $\text{LiNC} \rightleftharpoons \text{LiCN}$ isomerization potential [\[117\]](#) with parameters from Reference [\[258\]](#) (cf. Appendix [B](#)) is provided with the *mfptlib* project (cf. Section [D-2](#)). The focus on run-time performance in this project entails that the implementation is not always as clear as it could be. Therefore, an additional Python-only implementation has been written that closely follows the equations from the original publication so as to minimize the chance for implementation errors. This reference implementation is used inside the test suite of *mfptlib* to verify the optimized implementation. A standalone version has been published on [GitHub \[260\]](#) as supplemental material for Reference [\[7\]](#).

SYMBOLS AND NOTATION

The following sections summarize the symbols that are used repeatedly throughout this thesis or that are common in the literature. We separate the list into symbols used in thermal contexts — e. g., Section 2-2 and Chapter 7 — and those used in nonthermal or deterministic contexts.

General notation

The following conventions are used throughout this work:

X	scalar
\mathbf{X}	vector or matrix
\hat{X}	unit vector in X direction
ΔX	difference in variable X
δX	very small difference in variable X
$\langle X \rangle_t$	average of quantity $X(t)$ over variable t
\dot{X}	time-derivative of variable X

Symbols in nonthermal contexts

The following symbols are relevant in deterministic contexts:

E	energy
k	decay rate
k_e	decay rate (ensemble method)
k_F	decay rate (Floquet method)
k_m	decay rate (LMA)
\mathcal{L}	Lagrangian descriptor
N	number of reactants
p	momentum
p^\ddagger	momentum of (a trajectory on) the NHIM
q	general position, i. e., x or y

T	driving period
t	time
V	potential energy
v	velocity
\mathcal{W}_s	stable manifold
\mathcal{W}_u	unstable manifold
x	reaction coordinate
x^\ddagger	x position of (a trajectory on) the NHIM
x^{DS}	x position of the DS
y	orthogonal mode
y^\ddagger	y position of (a trajectory on) the NHIM
\boldsymbol{y}	trajectory, i. e., $(\boldsymbol{q}, \boldsymbol{p})^T$ or $(x, y, p_x, p_y)^T$
\boldsymbol{y}^\ddagger	trajectory on the NHIM
τ	integration time for the Lagrangian descriptor [cf. Equation (3-8)]

Symbols in thermal contexts

The following symbols are relevant in thermal contexts with noise and friction:

a_0	Bohr radius
E^\ddagger	energy of activation
E_h	Hartree energy
ΔG^\ddagger	Gibbs energy of activation
h	Planck constant
\hbar	reduced Planck constant ($= h/2\pi$)
ΔH^\ddagger	enthalpy of activation
k	reaction rate
k_B	Boltzmann constant
ΔS^\ddagger	entropy of activation
T	temperature
V	potential energy
α	bath parameter

Γ	friction kernel
γ	friction coefficient
κ	transmission coefficient
ν	pre-exponential factor in TST rate equations (cf. Appendix C)
τ	memory timescale ($= \alpha\gamma$)
ω_0	vibrational frequency of the reactant well
ω^\ddagger	inverse barrier frequency

GLOSSARY

all-atom molecular dynamics (AAMD)

A numerical ansatz for the simulation of a molecule in a solvent. [AAMD](#) does not coarse-grain the molecule or the solvent (as in the [LE](#)), but instead simulates the motion of and interaction with every single atom.

bicircular restricted four-body problem (BCR4BP)

An extension of the [CR3BP](#) featuring a third primary body. Analytical solvability is maintained by introducing a hierarchy of circular two-body problems. See [Figure 6-1](#) for more details.

binary-contraction method (BCM)

A numerical method determining the position of the [NHIM](#) based on four interleaved bisection procedures. See [Section 3-3 \(a\)](#) for more details.

circular restricted three-body problem (CR3BP)

A simplification of the classical three-body problem that recovers analytical solvability by assuming that one of the three bodies has negligible mass. This probe body has no influence on the motion of the two primary bodies. The circular version further restricts the primary bodies to circular orbits. See [Figure 6-1](#) for more details.

degree of freedom (DoF)

An independent variable or coordinate of a mathematical model. Usually used to describe the number of independent position coordinates, i. e., the dimensionality of the configuration space.

dividing surface (DS)

A surface dividing the phase space into a reactant and a product region according to some predefined criterion. There may be (infinitely) many valid choices for any given system. See [Chapter 2](#) for more details.

generalized Langevin equation (GLE)

A generalized version of the [LE](#) that allows for non-Gaussian noise and friction with memory. See [Section 2-2](#) for more details.

Langevin equation (LE)

A stochastic equation of motion describing a system coupled to a thermal bath. It incorporates Gaussian noise and memoryless friction. See Section 2-2 for more details.

local manifold analysis (LMA)

A numerical method to calculate the decay rate of trajectories near the NHIM using the geometry of the stable and unstable manifolds. See Section 3-5 (b) for more details.

mean first-passage time (MFPT)

The first-passage time is the duration it takes some initial state to reach a predefined condition for the first time. The condition can be arbitrary but typically involves the reaction coordinate x in chemical systems. Averaging the first-passage time over an ensemble of initial states yields the MFPT. Its inverse constitutes a reaction rate. See Section 3-7 for more details.

normally hyperbolic invariant manifold (NHIM)

The generalization of a hyperbolic fixed point — including stable and unstable manifolds — to arbitrarily many DoFs. Invariant manifolds are subspaces that cannot be entered or left. A state initialized on a NHIM may move within that NHIM but may never deviate from it (except for numerical errors). Similarly, states started off the NHIM may approach it via the stable manifold, but they may never reach it. Normally hyperbolic roughly means that the instability or decay away from (normal to) the NHIM dominates any possible instabilities within the NHIM itself [128]. See Section 2-1 for more details.

Poincaré surface of section (PSOS)

A technique that can be used to visualize regular and chaotic behavior of higher-dimensional systems in a two-dimensional plane. A special case, the stroboscopic map, is used throughout this work. See Section 3-4 for more details.

Pollak–Grabert–Hänggi (PGH)

In 1940, Kramers [111] published a theory that provides expressions for reaction rates in the low- and high-friction limits, and predicts an unspecified turnover in between. Pollak, Grabert, and Hänggi [146] later connected Kramers’s limiting cases, fully resolving the turnover, and generalized his ideas to include memory effects based on the GLE. See Section 2-3 for more details.

transition state (TS)

Traditionally used to describe the set of configurations in between the reactant and the product state, i. e., those located on the codimension-1 **DS** in phase space. The more mathematical literature, however, uses this phrase to refer to the ensemble of states bound indefinitely to the saddle region, i. e., those located on the codimension-2 **NHIM**. See footnote 6 of Reference [33] for a more detailed discussion. In this work, we adapt the former definition for the **TS** but use the phrase *TS trajectory* for trajectories bound to the **NHIM**.

transition-state theory (TST)

The framework of theories revolving around the **TS**.

BIBLIOGRAPHY

- [1] M. Feldmaier, P. Schraft, R. Bardakcioglu, J. Reiff, M. Lober, M. Tschöpe, A. Junginger, J. Main, T. Bartsch, and R. Hernandez, “Invariant manifolds and rate constants in driven chemical reactions,” *J. Phys. Chem. B* **123**, 2070–2086 (2019).
- [2] M. Feldmaier, R. Bardakcioglu, J. Reiff, J. Main, and R. Hernandez, “Phase-space resolved rates in driven multidimensional chemical reactions,” *J. Chem. Phys.* **151**, 244108 (2019).
- [3] M. Kuchelmeister, J. Reiff, J. Main, and R. Hernandez, “Dynamics and bifurcations on the normally hyperbolic invariant manifold of a periodically driven system with rank-1 saddle,” *Regul. Chaotic Dyn.* **25**, 496–507 (2020).
- [4] J. Reiff, M. Feldmaier, J. Main, and R. Hernandez, “Dynamics and decay rates of a time-dependent two-saddle system,” *Phys. Rev. E* **103**, 022121 (2021).
- [5] J. Reiff, R. Bardakcioglu, M. Feldmaier, J. Main, and R. Hernandez, “Controlling reaction dynamics in chemical model systems through external driving,” *Physica D* **427**, 133013 (2021).
- [6] J. Reiff, J. Zatsch, J. Main, and R. Hernandez, “On the stability of satellites at unstable libration points of sun–planet–moon systems,” *Commun. Nonlinear Sci. Numer. Simul.* **104**, 106053 (2022).
- [7] M. M. Schlee, J. Reiff, P. L. García-Müller, R. M. Benito, F. Borondo, J. Main, and R. Hernandez, “Mean first-passage times for solvated LiCN isomerization at intermediate to high temperatures,” *J. Chem. Phys.* **156**, 034103 (2022).
- [8] M. Feldmaier, J. Reiff, R. M. Benito, F. Borondo, J. Main, and R. Hernandez, “Influence of external driving on decays in the geometry of the LiCN isomerization,” *J. Chem. Phys.* **153**, 084115 (2020).
- [9] R. Bardakcioglu, J. Reiff, M. Feldmaier, J. Main, and R. Hernandez, “Thermal decay rates of an activated complex in a driven model chemical reaction,” *Phys. Rev. E* **102**, 062204 (2020).
- [10] J. Mögerle, R. Schuldt, J. Reiff, J. Main, and R. Hernandez, “Transition state dynamics of a driven magnetic free layer,” *Commun. Nonlinear Sci. Numer. Simul.* **105**, 106054 (2022).

- [11] M. Maihöfer, J. Reiff, J. Main, and R. Hernandez, “Transition state theory characterizes thin film macrospin dynamics driven by an oscillatory magnetic field: inertial effects,” *Commun. Nonlinear Sci. Numer. Simul.* **115**, 106764 (2022).
- [12] P. Waage and C. M. Guldberg, “Studier over Affiniteten,” Norwegian, *Forhandlinger: Videnskabs-Selskabet i Christiana*, 35–45 (1864).
- [13] P. Waage, “Yderligere Forsøg til Bestemmelse af Lovene for Affiniteten,” Norwegian, *Forhandlinger: Videnskabs-Selskabet i Christiana*, 92–94 (1864).
- [14] C. M. Guldberg, “Lovene for Affiniteten,” Norwegian, *Forhandlinger: Videnskabs-Selskabet i Christiana*, 111–120 (1864).
- [15] P. Waage and C. M. Gulberg, “Studies concerning affinity,” from the Norwegian, trans. by H. I. Abrash, *J. Chem. Educ.* **63**, 1044 (1986).
- [16] J. H. van 't Hoff, *Etudes de dynamique chimique*, French (Frederik Muller & Co., Amsterdam, 1884), <https://archive.org/details/etudesdedynamiqu00hoff>.
- [17] D. G. Truhlar, W. L. Hase, and J. T. Hynes, “Current status of transition-state theory,” *J. Phys. Chem.* **87**, 2664–2682 (1983).
- [18] R. A. Marcus, “Skiing the reaction rate slopes,” *Science* **256**, 1523–1524 (1992).
- [19] D. G. Truhlar, B. C. Garrett, and S. J. Klippenstein, “Current status of transition-state theory,” *J. Phys. Chem.* **100**, 12771–12800 (1996).
- [20] T. Komatsuzaki and R. S. Berry, “Dynamical hierarchy in transition states: Why and how does a system climb over the mountain?” *Proc. Natl. Acad. Sci. U.S.A.* **98**, 7666–7671 (2001).
- [21] E. V. Anslyn and D. A. Dougherty, *Modern physical organic chemistry* (University Science Books, Sausalito, CA, 2005), ISBN: 978-1-891-38931-3.
- [22] M. R. Harper, K. M. Van Geem, S. P. Pyl, G. B. Marin, and W. H. Green, “Comprehensive reaction mechanism for n-butanol pyrolysis and combustion,” *Combust. Flame* **158**, 16–41 (2011).
- [23] S. T. Chill, J. Stevenson, V. Ruehle, C. Shang, P. Xiao, J. D. Farrell, D. J. Wales, and G. Henkelman, “Benchmarks for characterization of minima, transition states, and pathways in atomic, molecular, and condensed matter systems,” *J. Chem. Theory Comput.* **10**, 5476–5482 (2014).

- [24] Z. C. Kramer, B. K. Carpenter, G. S. Ezra, and S. Wiggins, "Reaction path bifurcation in an electrocyclic reaction: Ring-opening of the cyclopropyl radical," *J. Phys. Chem. A* **119**, 6611–6630 (2015).
- [25] B. Chen, R. Hoffmann, and R. Cammi, "The effect of pressure on organic reactions in fluids — a new theoretical perspective," *Angew. Chem. Int. Ed.* **56**, 11126–11142 (2017).
- [26] H. Eyring, "The activated complex in chemical reactions," *J. Chem. Phys.* **3**, 107–115 (1935).
- [27] P. Hänggi, P. Talkner, and M. Borkovec, "Reaction-rate theory: Fifty years after Kramers," *Rev. Mod. Phys.* **62**, 251–341 (1990).
- [28] G. A. Natanson, B. C. Garrett, T. N. Truong, T. Joseph, and D. G. Truhlar, "The definition of reaction coordinates for reaction-path dynamics," *J. Chem. Phys.* **94**, 7875–7892 (1991).
- [29] D. G. Truhlar and B. C. Garrett, "Multidimensional transition state theory and the validity of Grote–Hynes theory," *J. Phys. Chem. B* **104**, 1069–1072 (2000).
- [30] T. Bartsch, R. Hernandez, and T. Uzer, "Transition state in a noisy environment," *Phys. Rev. Lett.* **95**, 058301 (2005).
- [31] T. Bartsch, T. Uzer, and R. Hernandez, "Stochastic transition states: Reaction geometry amidst noise," *J. Chem. Phys.* **123**, 204102 (2005).
- [32] E. Pollak and P. Talkner, "Reaction rate theory: What it was, where is it today, and where is it going?" *Chaos* **15**, 026116 (2005).
- [33] H. Waalkens, R. Schubert, and S. Wiggins, "Wigner's dynamical transition state theory in phase space: Classical and quantum," *Nonlinearity* **21**, R1–R118 (2008).
- [34] T. Bartsch, J. M. Moix, R. Hernandez, S. Kawai, and T. Uzer, "Time-dependent transition state theory," in *Advances in chemical physics*, Vol. 140, edited by S. A. Rice (John Wiley & Sons, Hoboken, NJ, 2008) Chap. 4, pp. 191–238.
- [35] E. Wigner, "Calculation of the rate of elementary association reactions," *J. Chem. Phys.* **5**, 720–725 (1937).
- [36] R. Hernandez, T. Uzer, and T. Bartsch, "Transition state theory in liquids beyond planar dividing surfaces," *Chem. Phys.* **370**, 270–276 (2010).
- [37] S. Kawai and T. Komatsuzaki, "Robust existence of a reaction boundary to separate the fate of a chemical reaction," *Phys. Rev. Lett.* **105**, 048304 (2010).

- [38] R. G. Mullen, J.-E. Shea, and B. Peters, “Communication: An existence test for dividing surfaces without recrossing,” *J. Chem. Phys.* **140**, 041104 (2014).
- [39] O. Sharia and G. Henkelman, “Analytic dynamical corrections to transition state theory,” *New J. Phys.* **18**, 013023 (2016).
- [40] S. Wiggins, “The role of normally hyperbolic invariant manifolds (NHIMS) in the context of the phase space setting for chemical reaction dynamics,” *Regul. Chaotic Dyn.* **21**, 621–638 (2016).
- [41] K. S. Pitzer, F. T. Smith, and H. Eyring, *The transition state*, Special Publications (Chemical Society, London, 1962).
- [42] B. C. Garrett and D. G. Truhlar, “Generalized transition state theory. Classical mechanical theory and applications to collinear reactions of hydrogen molecules,” *J. Phys. Chem.* **83**, 1052–1079 (1979).
- [43] P. Pechukas, “Transition state theory,” *Annu. Rev. Phys. Chem.* **32**, 159–177 (1981).
- [44] D. G. Truhlar, A. D. Issacson, and B. C. Garrett, “Generalized transition state theory,” in *Theory of chemical reaction dynamics*, Vol. 4, edited by M. Baer (CRC Press, Boca Raton, FL, 1985) Chap. 2, pp. 65–137.
- [45] J. T. Hynes, “Chemical reaction dynamics in solution,” *Annu. Rev. Phys. Chem.* **36**, 573–597 (1985).
- [46] A. Nitzan, “Activated rate processes in condensed phases: The Kramers theory revisited,” in *Advances in chemical physics: Evolution of size effects in chemical dynamics*, Vol. 70.2, edited by I. Prigogine and S. A. Rice (John Wiley & Sons, New York, NY, 1988) Chap. 11, pp. 489–555.
- [47] B. J. Berne, M. Borkovec, and J. E. Straub, “Classical and modern methods in reaction rate theory,” *J. Phys. Chem.* **92**, 3711–3725 (1988).
- [48] C. Jaffé, D. Farrelly, and T. Uzer, “Transition state theory without time-reversal symmetry: Chaotic ionization of the hydrogen atom,” *Phys. Rev. Lett.* **84**, 610–613 (2000).
- [49] G. Jacucci, M. Toller, G. DeLorenzi, and C. P. Flynn, “Rate theory, return jump catastrophes, and the center manifold,” *Phys. Rev. Lett.* **52**, 295–298 (1984).
- [50] R. Schuldt, “Zeitabhängige Theorie des Übergangszustands und Methode der Lagrangedeskriptoren für ein getriebenes Spin-System,” German, Master’s thesis (Universität Stuttgart, Stuttgart, 2017).

- [51] J. Mögerle, “Ratenkonstanten für den Spinflip in einem getriebenen Zweischichtenmodell,” German, Bachelor’s thesis ([Universität Stuttgart, Stuttgart, 2019](#)).
- [52] M. Maihöfer, “Übergangsraten eines getriebenen Spinsystems unter Berücksichtigung von Relaxation,” German, Master’s thesis ([Universität Stuttgart, Stuttgart, 2021](#)).
- [53] T. Komatsuzaki and R. S. Berry, “Regularity in chaotic reaction paths. I. Ar₆,” *J. Chem. Phys.* **110**, 9160–9173 (1999).
- [54] T. Komatsuzaki and R. S. Berry, “Chemical reaction dynamics: Many-body chaos and regularity,” in *Advances in chemical physics*, Vol. 123, edited by I. Prigogine and S. A. Rice (John Wiley & Sons, New York, NY, 2002) Chap. 2, pp. 79–152.
- [55] M. Toller, G. Jacucci, G. DeLorenzi, and C. P. Flynn, “Theory of classical diffusion jumps in solids,” *Phys. Rev. B* **32**, 2082–2095 (1985).
- [56] A. F. Voter, F. Montalenti, and T. C. Germann, “Extending the time scale in atomistic simulation of materials,” *Annu. Rev. Mater. Res.* **32**, 321–346 (2002).
- [57] H. P. de Oliveira, A. M. Ozorio de Almeida, I. Damião Soares, and E. V. Tonini, “Homoclinic chaos in the dynamics of a general Bianchi type-IX model,” *Phys. Rev. D* **65**, 083511 (2002).
- [58] C. Jaffé, S. D. Ross, M. W. Lo, J. Marsden, D. Farrelly, and T. Uzer, “Statistical theory of asteroid escape rates,” *Phys. Rev. Lett.* **89**, 011101 (2002).
- [59] H. Waalkens, A. Burbanks, and S. Wiggins, “Escape from planetary neighbourhoods,” *Mon. Not. R. Astron. Soc.* **361**, 763–775 (2005).
- [60] J. C. J. Zatsch, “Berücksichtigung der Mondrotation beim Asteroideneinfang an Lagrangepunkten,” German, Bachelor’s thesis ([Universität Stuttgart, Stuttgart, 2019](#)).
- [61] C. Huepe, S. Métens, G. Dewel, P. Borckmans, and M. E. Brachet, “Decay rates in attractive Bose–Einstein condensates,” *Phys. Rev. Lett.* **82**, 1616–1619 (1999).
- [62] C. Huepe, L. S. Tuckerman, S. Métens, and M. E. Brachet, “Stability and decay rates of nonisotropic attractive Bose–Einstein condensates,” *Phys. Rev. A* **68**, 023609 (2003).
- [63] A. Junginger, J. Main, G. Wunner, and M. Dorwarth, “Transition state theory for wave packet dynamics: I. Thermal decay in metastable Schrödinger systems,” *J. Phys. A* **45**, 155201 (2012).

- [64] A. Junginger, M. Dorwarth, J. Main, and G. Wunner, “Transition state theory for wave packet dynamics: II. Thermal decay of Bose–Einstein condensates with long-range interaction,” *J. Phys. A* **45**, 155202 (2012).
- [65] A. Junginger, M. Kreibich, J. Main, and G. Wunner, “Transition states and thermal collapse of dipolar Bose–Einstein condensates,” *Phys. Rev. A* **88**, 043617 (2013).
- [66] A. J. Lichtenberg and M. A. Liebermann, *Regular and stochastic motion*, Applied Mathematical Sciences 38 (Springer, New York, NY, 1983), ISBN: 978-1-4757-4257-2.
- [67] R. Hernandez and W. H. Miller, “Semiclassical transition state theory. A new perspective,” *Chem. Phys. Lett.* **214**, 129–136 (1993).
- [68] R. Hernandez, “Application of semiclassical methods to reaction rate theory,” PhD thesis (University of California, Berkeley, CA, 1993).
- [69] S. Wiggins, *Normally hyperbolic invariant manifolds in dynamical systems*, Applied Mathematical Sciences 105 (Springer, New York, NY, 1994), ISBN: 978-1-4612-4312-0.
- [70] E. Ott, *Chaos in dynamical systems*, 2nd ed. (Cambridge University Press, Cambridge, 2002), ISBN: 978-0-511-80326-0.
- [71] S. Kawai, H. Teramoto, C.-B. Li, T. Komatsuzaki, and M. Toda, “Dynamical reaction theory based on geometric structures in phase space,” in *Advancing theory for kinetics and dynamics of complex, many-dimensional systems: Clusters and proteins*, edited by T. Komatsuzaki, R. S. Berry, and D. M. Leitner, Advances in Chemical Physics 145 (John Wiley & Sons, Hoboken, NJ, 2011) Chap. 4, pp. 123–169.
- [72] G. Haller, T. Uzer, J. Palacián, P. Yanguas, and C. Jaffé, “Transition state geometry near higher-rank saddles in phase space,” *Nonlinearity* **24**, 527–561 (2011).
- [73] C.-B. Li, A. Shoujiguchi, M. Toda, and T. Komatsuzaki, “Definability of no-return transition states in the high-energy regime above the reaction threshold,” *Phys. Rev. Lett.* **97**, 028302 (2006).
- [74] H. Teramoto, G. Haller, and T. Komatsuzaki, “Detecting invariant manifolds as stationary Lagrangian coherent structures in autonomous dynamical systems,” *Chaos* **23**, 043107 (2013).
- [75] P. Pechukas and E. Pollak, “Trapped trajectories at the boundary of reactivity bands in molecular collisions,” *J. Chem. Phys.* **67**, 5976–5977 (1977).

- [76] E. Pollak and P. Pechukas, “Transition states, trapped trajectories, and classical bound states embedded in the continuum,” *J. Chem. Phys.* **69**, 1218–1226 (1978).
- [77] E. Pollak, M. S. Child, and P. Pechukas, “Classical transition state theory: A lower bound to the reaction probability,” *J. Chem. Phys.* **72**, 1669–1678 (1980).
- [78] C.-B. Li, M. Toda, and T. Komatsuzaki, “Bifurcation of no-return transition states in many-body chemical reactions,” *J. Chem. Phys.* **130**, 124116 (2009).
- [79] H. Teramoto, M. Toda, and T. Komatsuzaki, “Dynamical switching of a reaction coordinate to carry the system through to a different product state at high energies,” *Phys. Rev. Lett.* **106**, 054101 (2011).
- [80] H. Teramoto, M. Toda, and T. Komatsuzaki, “Breakdown mechanisms of normally hyperbolic invariant manifolds in terms of unstable periodic orbits and homoclinic/heteroclinic orbits in Hamiltonian systems,” *Nonlinearity* **28**, 2677–2698 (2015).
- [81] H. Teramoto, M. Toda, M. Takahashi, H. Kono, and T. Komatsuzaki, “Mechanism and experimental observability of global switching between reactive and nonreactive coordinates at high total energies,” *Phys. Rev. Lett.* **115**, 093003 (2015).
- [82] P. Talkner, E. Hershkovitz, E. Pollak, and P. Hänggi, “Controlling activated surface diffusion by external fields,” *Surf. Sci.* **437**, 198–206 (1999).
- [83] G. E. Murgida, D. A. Wisniacki, P. I. Tamborenea, and F. Borondo, “Control of chemical reactions using external electric fields: The case of the $\text{LiNC} \rightleftharpoons \text{LiCN}$ isomerization,” *Chem. Phys. Lett.* **496**, 356–361 (2010).
- [84] F. Revuelta, R. Chacón, and F. Borondo, “Towards AC-induced optimum control of dynamical localization,” *EPL* **110**, 40007 (2015).
- [85] G. E. Murgida, F. J. Arranz, and F. Borondo, “Quantum control of isomerization by robust navigation in the energy spectrum,” *J. Chem. Phys.* **143**, 214305 (2015).
- [86] A. Shukla and S. Keshavamurthy, “One versus two photon control of dynamical tunneling: Influence of the irregular floquet states,” *J. Phys. Chem. B* **119**, 11326–11335 (2015).
- [87] M. Feldmaier, “Phase-space resolved decay rates of driven systems near the transition state,” PhD thesis (Universität Stuttgart, Stuttgart, 2020).

- [88] F. Revuelta, G. T. Craven, T. Bartsch, F. Borondo, R. M. Benito, and R. Hernandez, “Transition state theory for activated systems with driven anharmonic barriers,” *J. Chem. Phys.* **147**, 074104 (2017).
- [89] C. Mendoza and A. M. Mancho, “Hidden geometry of ocean flows,” *Phys. Rev. Lett.* **105**, 038501 (2010).
- [90] A. M. Mancho, S. Wiggins, C. Jezabel, and C. Mendoza, “Lagrangian descriptors: A method for revealing phase space structures of general time dependent dynamical systems,” *Commun. Nonlinear Sci. Numer. Simul.* **18**, 3530–3557 (2013).
- [91] M. Feldmaier, A. Junginger, J. Main, G. Wunner, and R. Hernandez, “Obtaining time-dependent multi-dimensional dividing surfaces using Lagrangian descriptors,” *Chem. Phys. Lett.* **687**, 194–199 (2017).
- [92] R. Bardakcioglu, A. Junginger, M. Feldmaier, J. Main, and R. Hernandez, “Binary contraction method for the construction of time-dependent dividing surfaces in driven chemical reactions,” *Phys. Rev. E* **98**, 032204 (2018).
- [93] J. P. Schraft, “Neural networks for the approximation of time-dependent dividing surfaces in transition state theory,” Master’s thesis (Universität Stuttgart, Stuttgart, 2017).
- [94] R. Bardakcioglu, “Time-dependent transition state theory to determine dividing surfaces and reaction rates in multidimensional systems,” Master’s thesis (Universität Stuttgart, Stuttgart, 2018).
- [95] M. J. Lober, “Parameter dependent rates in transition state theory for periodically driven systems,” Bachelor’s thesis (Universität Stuttgart, Stuttgart, 2018).
- [96] M. Tschöpe, “Application of neural networks to determine the transition state trajectory in periodically driven systems with two or more degrees of freedom,” Master’s thesis (Universität Stuttgart, Stuttgart, 2018).
- [97] T. Mielich, “Machine learning methods for the computation of rate constants in driven chemical reactions,” Master’s thesis (Universität Stuttgart, Stuttgart, 2019).
- [98] M. J. Lober, “Dimensionality reduction of manifolds of dynamical systems with a rank-1 saddle by application of autoencoder artificial neural networks,” Master’s thesis (Universität Stuttgart, Stuttgart, 2021).

- [99] P. Mishra, “Predicting instantaneous decay rates at the transition state using neural networks and investigating their usefulness for the reaction rates of arbitrary ensembles,” Master’s thesis ([Universität Stuttgart, Stuttgart, 2021](#)).
- [100] A. Junginger and R. Hernandez, “Lagrangian descriptors in dissipative systems,” *Phys. Chem. Chem. Phys.* **18**, 30282–30287 (2016).
- [101] T. Bartsch, T. Uzer, J. M. Moix, and R. Hernandez, “Identifying reactive trajectories using a moving transition state,” *J. Chem. Phys.* **124**, 244310 (2006).
- [102] S. Kawai and T. Komatsuzaki, “Dynamic pathways to mediate reactions buried in thermal fluctuations. I. Time-dependent normal form theory for multidimensional langevin equation,” *J. Chem. Phys.* **131**, 224505 (2009).
- [103] G. T. Craven, T. Bartsch, and R. Hernandez, “Communication: Transition state trajectory stability determines barrier crossing rates in chemical reactions induced by time-dependent oscillating fields,” *J. Chem. Phys.* **141**, 041106 (2014).
- [104] G. T. Craven, T. Bartsch, and R. Hernandez, “Persistence of transition state structure in chemical reactions driven by fields oscillating in time,” *Phys. Rev. E* **89**, 040801(R) (2014).
- [105] G. T. Craven, T. Bartsch, and R. Hernandez, “Chemical reactions induced by oscillating external fields in weak thermal environments,” *J. Chem. Phys.* **142**, 074108 (2015).
- [106] A. Junginger and R. Hernandez, “Uncovering the geometry of barrierless reactions using Lagrangian descriptors,” *J. Phys. Chem. B* **120**, 1720–1725 (2016).
- [107] A. Junginger, G. T. Craven, T. Bartsch, F. Revuelta, F. Borondo, R. M. Benito, and R. Hernandez, “Transition state geometry of driven chemical reactions on time-dependent double-well potentials,” *Phys. Chem. Chem. Phys.* **18**, 30270–30281 (2016).
- [108] M. Kuchelmeister, “Untersuchung der Dynamik auf der normal hyperbolisch invarianten Mannigfaltigkeit eines periodisch getriebenen Systems mit Rang-1-Sattel,” German, Bachelor’s thesis ([Universität Stuttgart, Stuttgart, 2019](#)).
- [109] S. Arrhenius, “Über die Reaktionsgeschwindigkeit bei der Inversion von Rohrzucker durch Säuren,” German, *Z. Phys. Chem.* **4U**, 226–248 (1889).

- [110] H. Eyring, “The activated complex and the absolute rate of chemical reactions,” *Chem. Rev.* **17**, 65–77 (1935).
- [111] H. A. Kramers, “Brownian motion in a field of force and the diffusional model of chemical reactions,” *Physica* **7**, 284–304 (1940).
- [112] C. L. Bennett, M. Bay, M. Halpern, G. Hinshaw, C. Jackson, N. Jarosik, A. Kogut, M. Limon, S. S. Meyer, L. Page, et al., “The *Microwave Anisotropy Probe* mission,” *Astrophys. J.* **583**, 1–23 (2003).
- [113] M. Harwit, “The Herschel mission,” *Adv. Space Res.* **34**, 568–572 (2004).
- [114] J. P. Gardner, J. C. Mather, M. Clampin, R. Doyon, M. A. Greenhouse, H. B. Hammel, J. B. Hutchings, P. Jakobsen, S. J. Lilly, K. S. Long, et al., “The James Webb Space Telescope,” *Space Sci. Rev.* **123**, 485–606 (2006).
- [115] P. A. R. Ade, N. Aghanim, M. I. R. Alves, C. Armitage-Caplan, M. Arnaud, M. Ashdown, F. Atrio-Barandela, J. Aumont, H. Aussel, C. Baccigalupi, et al. (Planck Collaboration), “*Planck* 2013 results. I. Overview of products and scientific results,” *Astron. Astrophys.* **571**, A1 (2014).
- [116] M. M. Schlee, “Thermal rates for driven isomerization reactions,” Master’s thesis (Universität Stuttgart, Stuttgart, 2021).
- [117] R. Essers, J. Tennyson, and P. E. S. Wormer, “An SCF potential energy surface for lithium cyanide,” *Chem. Phys. Lett.* **89**, 223–227 (1982).
- [118] P. L. García-Müller, F. Borondo, R. Hernandez, and R. M. Benito, “Solvent-induced acceleration of the rate of activation of a molecular reaction,” *Phys. Rev. Lett.* **101**, 178302 (2008).
- [119] P. L. García-Müller, R. Hernandez, R. M. Benito, and F. Borondo, “Detailed study of the direct numerical observation of the Kramers turnover in the $\text{LiNC} \rightleftharpoons \text{LiCN}$ isomerization rate,” *J. Chem. Phys.* **137**, 204301 (2012).
- [120] A. Junginger, P. L. García-Müller, F. Borondo, R. M. Benito, and R. Hernandez, “Solvated molecular dynamics of LiCN isomerization: All-atom argon solvent versus a generalized Langevin bath,” *J. Chem. Phys.* **144**, 024104 (2016).
- [121] M. Born and R. Oppenheimer, “Zur Quantentheorie der Molekeln,” German, *Ann. Phys.* **389**, 457–484 (1927).
- [122] K. Fukui, “Formulation of the reaction coordinate,” *J. Phys. Chem.* **74**, 4161–4163 (1970).
- [123] S. Kato and K. Fukui, “Reaction ergodography. Methane–tritium reaction,” *J. Am. Chem. Soc.* **98**, 6395–6397 (1976).

- [124] W. H. Miller, “‘Direct’ and ‘correct’ calculation of canonical and microcanonical rate constants for chemical reactions,” *J. Phys. Chem. A* **102**, 793–806 (1998).
- [125] T. Komatsuzaki and R. S. Berry, “Regularity in chaotic reaction paths II: Ar₆. Energy dependence and visualization of the reaction bottleneck,” *Phys. Chem. Chem. Phys.* **1**, 1387–1397 (1999).
- [126] C. B. Li, A. Shojiguchi, M. Toda, and T. Komatsuzaki, “Dynamical hierarchy in transition states of reactions,” *Few-Body Syst.* **38**, 173–179 (2006).
- [127] A. Junginger, L. Duvenbeck, M. Feldmaier, J. Main, G. Wunner, and R. Hernandez, “Chemical dynamics between wells across a time-dependent barrier: Self-similarity in the Lagrangian descriptor and reactive basins,” *J. Chem. Phys.* **147**, 064101 (2017).
- [128] S. Wiggins, L. Wiesenfeld, C. Jaffé, and T. Uzer, “Impenetrable barriers in phase-space,” *Phys. Rev. Lett.* **86**, 5478–5481 (2001).
- [129] D. G. Truhlar and B. C. Garrett, “Variational transition state theory,” *Annu. Rev. Phys. Chem.* **35**, 159–189 (1984).
- [130] S. Naik, V. J. García-Garrido, and S. Wiggins, “Finding NHIM: Identifying high dimensional phase space structures in reaction dynamics using Lagrangian descriptors,” *Commun. Nonlinear Sci. Numer. Simul.* **79**, 104907 (2019).
- [131] T. Uzer, C. Jaffé, J. Palacián, P. Yanguas, and S. Wiggins, “The geometry of reaction dynamics,” *Nonlinearity* **15**, 957–992 (2002).
- [132] P. Schraft, A. Junginger, M. Feldmaier, R. Bardakcioglu, J. Main, G. Wunner, and R. Hernandez, “Neural network approach to time-dependent dividing surfaces in classical reaction dynamics,” *Phys. Rev. E* **97**, 042309 (2018).
- [133] G. S. Ezra and S. Wiggins, “Sampling phase space dividing surfaces constructed from normally hyperbolic invariant manifolds (NHIMs),” *J. Phys. Chem. A* **122**, 8354–8362 (2018).
- [134] R. Kubo, “The fluctuation-dissipation theorem,” *Rep. Prog. Phys.* **29**, 255–284 (1966).
- [135] D. S. Lemons and A. Gythiel, “Paul Langevin’s 1908 paper ‘On the theory of Brownian motion’ [‘Sur la théorie du mouvement brownien,’ *C. R. Acad. Sci. (Paris)* **146**, 530–533 (1908)],” *Am. J. Phys.* **65**, 1079–1081 (1997).
- [136] R. Zwanzig, *Nonequilibrium statistical mechanics* (Oxford University Press, New York, NY, 2001), ISBN: 978-0-19-514018-7.

- [137] N. Pottier, *Nonequilibrium statistical physics: Linear irreversible processes* (Oxford University Press, Oxford, 2010), ISBN: 978-0-19-955688-5.
- [138] P. Hänggi, “Generalized Langevin equations: A useful tool for the perplexed modeller of nonequilibrium fluctuations?” In *Stochastic dynamics*, edited by L. Schimansky-Geier and T. Pöschel, Lecture Notes in Physics 484 (Springer, Berlin and Heidelberg, 1997), pp. 15–22.
- [139] A. D. Baczewski and S. D. Bond, “Numerical integration of the extended variable generalized Langevin equation with a positive Prony representable memory kernel,” *J. Chem. Phys.* **139**, 044107 (2013).
- [140] M. H. Duong and X. Shang, “Accurate and robust splitting methods for the generalized Langevin equation with a positive Prony series memory kernel,” *J. Comput. Phys.* **464**, 111332 (2022).
- [141] N. G. van Kampen, “Itô versus Stratonovich,” *J. Stat. Phys.* **24**, 175–187 (1981).
- [142] W. Moon and J. S. Wettlaufer, “On the interpretation of Stratonovich calculus,” *New J. Phys.* **16**, 055017 (2014).
- [143] M. Polanyi and E. Wigner, “Über die Interferenz von Eigenschwingungen als Ursache von Energieschwankungen und chemischer Umsetzungen,” German, *Z. Phys. Chem.* **139A**, 439–452 (1928).
- [144] K. J. Laidler and M. C. King, “Development of transition-state theory,” *J. Phys. Chem.* **87**, 2657–2664 (1983).
- [145] V. I. Mel’nikov and S. V. Meshkov, “Theory of activated rate processes: Exact solution of the Kramers problem,” *J. Chem. Phys.* **85**, 1018–1027 (1986).
- [146] E. Pollak, H. Grabert, and P. Hänggi, “Theory of activated rate processes for arbitrary frequency dependent friction: Solution of the turnover problem,” *J. Chem. Phys.* **91**, 4073–4087 (1989).
- [147] S. Linkwitz, H. Grabert, E. Turlot, D. Estève, and M. H. Devoret, “Escape rates in the region between the Kramers limits,” *Phys. Rev. A* **45**, R3369–R3372 (1992).
- [148] S. Singh, R. Krishnan, and G. W. Robinson, “Critical phenomena and scaling behavior in theories of activated barrier crossing,” *Phys. Rev. Lett.* **68**, 2608–2611 (1992).
- [149] S. C. Tucker, “The reactive flux method in the energy diffusion regime. I. Effect of slow vibrational energy relaxation,” *J. Chem. Phys.* **101**, 2006–2015 (1994).

- [150] E. Pollak and J. Ankerhold, “Improvements to Kramers turnover theory,” *J. Chem. Phys.* **138**, 164116 (2013).
- [151] E. Pollak and R. Ianconescu, “Finite barrier corrections to the PGH solution of Kramers’ turnover theory,” *J. Chem. Phys.* **140**, 154108 (2014).
- [152] Y. Shigemitsu and Y. Ohga, “Accelerated molecular dynamics study of Z/E isomerization of azobenzene: Kramers’ theory validation,” *J. Solut. Chem.* **43**, 1746–1754 (2014).
- [153] L. P. Lindoy, A. Mandal, and D. R. Reichman, “Resonant cavity modification of ground-state chemical kinetics,” *J. Phys. Chem. Lett.* **13**, 6580–6586 (2022).
- [154] B. J. Alder and T. E. Wainwright, “Studies in molecular dynamics. I. General method,” *J. Chem. Phys.* **31**, 459–466 (1959).
- [155] D. Frenkel and B. Smit, *Understanding molecular simulation: From algorithms to applications*, 2nd ed. (Academic Press, San Diego, CA, 2002), ISBN: 978-0-12-267351-1.
- [156] D. C. Rapaport, *The art of molecular dynamics simulation*, 2nd ed. (Cambridge University Press, Cambridge, 2004-04), ISBN: 978-0-511-81658-1.
- [157] M. Griebel, G. Zumbusch, and S. Knapek, *Numerical simulation in molecular dynamics: Numerics, algorithms, parallelization, applications* (Springer, Berlin and Heidelberg, 2007), ISBN: 978-3-540-68095-6.
- [158] R. F. Grote and J. T. Hynes, “The stable states picture of chemical reactions. II. Rate constants for condensed and gas phase reaction models,” *J. Chem. Phys.* **73**, 2715–2732 (1980).
- [159] S. C. Tucker, M. E. Tuckerman, B. J. Berne, and E. Pollak, “Comparison of rate theories for generalized Langevin dynamics,” *J. Chem. Phys.* **95**, 5809–5826 (1991).
- [160] E. Pollak and P. Talkner, “Transition-state recrossing dynamics in activated rate processes,” *Phys. Rev. E* **51**, 1868–1878 (1995).
- [161] E. Pollak, S. C. Tucker, and B. J. Berne, “Variational transition-state theory for reaction rates in dissipative systems,” *Phys. Rev. Lett.* **65**, 1399–1402 (1990).
- [162] G. Floquet, “Sur les équations différentielles linéaires à coefficients périodiques,” French, *Ann. Sci. Éc. Norm. Supér.*, 2nd ser. **12**, 47–88 (1883).

- [163] P. Cvitanović, R. Artuso, R. Mainieri, G. Tanner, and G. Vattay, *Chaos: Classical and quantum*, 17th ed. (Niels Bohr Institute, Copenhagen, 2020), <https://ChaosBook.org/>.
- [164] W. C. Swope, H. C. Andersen, P. H. Berens, and K. R. Wilson, “A computer simulation method for the calculation of equilibrium constants for the formation of physical clusters of molecules: Application to small water clusters,” *J. Chem. Phys.* **76**, 637–649 (1982).
- [165] E. Hairer, C. Lubich, and G. Wanner, “Geometric numerical integration illustrated by the Störmer–Verlet method,” *Acta Numer.* **12**, 399–450 (2003).
- [166] B. Delacroix, A. Bouarab, L. Fradette, F. Bertrand, and B. Blais, “Simulation of granular flow in a rotating frame of reference using the discrete element method,” *Powder Technol.* **369**, 146–161 (2020).
- [167] C. Runge, “Ueber die numerische Auflösung von Differentialgleichungen,” German, *Math. Ann.* **46**, 167–178 (1895).
- [168] M. Kutta, “Beitrag zur näherungsweise Integration totaler Differentialgleichungen,” German, *Z. Math. Phys.* **46**, 435–453 (1901).
- [169] G. T. Craven and R. Hernandez, “Deconstructing field-induced ketene isomerization through Lagrangian descriptors,” *Phys. Chem. Chem. Phys.* **18**, 4008–4018 (2016).
- [170] Y. Nagahata, F. Borondo, R. M. Benito, and R. Hernandez, “Identifying reaction pathways in phase space via asymptotic trajectories,” *Phys. Chem. Chem. Phys.* **22**, 10087–10105 (2020).
- [171] G. T. Craven and R. Hernandez, “Lagrangian descriptors of thermalized transition states on time-varying energy surfaces,” *Phys. Rev. Lett.* **115**, 148301 (2015).
- [172] D. E. Knuth, *The art of computer programming: Sorting and searching*, 2nd ed., Vol. 3 (Addison-Wesley, Reading, MA, 1998), ISBN: 978-0-201-89685-5.
- [173] J. Reiff, “Dynamik und Trennflächen für getriebene Systeme mit zwei zeitabhängigen Sattelpunkten,” German, Master’s thesis (Universität Stuttgart, Stuttgart, 2018).
- [174] M. Tschöpe, M. Feldmaier, J. Main, and R. Hernandez, “Neural network approach for the dynamics on the normally hyperbolic invariant manifold of periodically driven systems,” *Phys. Rev. E* **101**, 022219 (2020).

- [175] P. Virtanen, R. Gommers, T. E. Oliphant, M. Haberland, T. Reddy, D. Cournapeau, E. Burovski, P. Peterson, W. Weckesser, J. Bright, et al. (SciPy 1.0 Contributors), “SciPy 1.0: Fundamental algorithms for scientific computing in Python,” *Nat. Methods* **17**, 261–272 (2020).
- [176] J. Lehmann, P. Reimann, and P. Hänggi, “Surmounting oscillating barriers,” *Phys. Rev. Lett.* **84**, 1639–1642 (2000).
- [177] B. Leimkuhler and C. Matthews, *Molecular dynamics: With deterministic and stochastic numerical methods*, Interdisciplinary Applied Mathematics 39 (Springer, Cham, 2015), ISBN: 978-3-319-16375-8.
- [178] J. Fass, D. Sivak, G. Crooks, K. Beauchamp, B. Leimkuhler, and J. Chodera, “Quantifying configuration-sampling error in Langevin simulations of complex molecular systems,” *Entropy* **20**, 318 (2018).
- [179] Z. Zhang, X. Liu, K. Yan, M. E. Tuckerman, and J. Liu, “Unified efficient thermostat scheme for the canonical ensemble with holonomic or isokinetic constraints via molecular dynamics,” *J. Phys. Chem. A* **123**, 6056–6079 (2019).
- [180] P. Hänggi and P. Talkner, “Non-Markov processes: The problem of the mean first passage time,” *Z. Phys. B* **45**, 79–83 (1981).
- [181] R. Müller, P. Talkner, and P. Reimann, “Rates and mean first passage times,” *Physica A* **247**, 338–356 (1997).
- [182] P. Reimann, G. J. Schmid, and P. Hänggi, “Universal equivalence of mean first-passage time and Kramers rate,” *Phys. Rev. E* **60**, R1–R4 (1999).
- [183] S. Redner, *A guide to first-passage processes* (Cambridge University Press, Cambridge, 2001-08), ISBN: 978-0-511-60601-4.
- [184] J. L. Vega, R. Guantes, and S. Miret-Artés, “Mean first passage time and the Kramers turnover theory in activated atom–surface diffusion,” *Phys. Chem. Chem. Phys.* **4**, 4985–4991 (2002).
- [185] T. D. Shepherd and R. Hernandez, “An optimized mean first passage time approach for obtaining rates in activated processes,” *J. Chem. Phys.* **117**, 9227–9233 (2002).
- [186] S. Park, M. K. Sener, D. Lu, and K. Schulten, “Reaction paths based on mean first-passage times,” *J. Chem. Phys.* **119**, 1313–1319 (2003).
- [187] S. Wimberger, *Nonlinear dynamics and quantum chaos: An introduction*, Graduate Texts in Physics (Springer, Cham, 2014), ISBN: 978-3-319-06343-0.

- [188] F. Borondo, A. A. Zembekov, and R. M. Benito, “Quantum manifestations of saddle-node bifurcations,” *Chem. Phys. Lett.* **246**, 421–426 (1995).
- [189] F. Borondo, A. A. Zembekov, and R. M. Benito, “Saddle-node bifurcations in the LiNC/LiCN molecular system: Classical aspects and quantum manifestations,” *J. Chem. Phys.* **105**, 5068–5081 (1996).
- [190] M. Iñarraea, J. F. Palacián, A. I. Pascual, and J. P. Salas, “Bifurcations of dividing surfaces in chemical reactions,” *J. Chem. Phys.* **135**, 014110 (2011).
- [191] H. G. Schuster and W. Just, *Deterministic chaos: An introduction*, 4th ed. (Wiley-VCH, Weinheim, 2005), ISBN: 978-3-527-60480-7.
- [192] L. Farkas, “Keimbildungsgeschwindigkeit in übersättigten Dämpfen,” German, *Z. Phys. Chem.* **125U**, 236–242 (1927).
- [193] S. C. Endres, C. Sandrock, and W. W. Focke, “A simplicial homology algorithm for Lipschitz optimisation,” *J. Glob. Optim.* **72**, 181–217 (2018).
- [194] I. M. Sobol’, “On the distribution of points in a cube and the approximate evaluation of integrals,” *USSR Comput. Maths. Math. Phys.* **7**, 86–112 (1967).
- [195] J. A. Nelder and R. Mead, “A simplex method for function minimization,” *Comput. J.* **7**, 308–313 (1965).
- [196] P. L. García-Müller, R. Hernandez, R. M. Benito, and F. Borondo, “The role of the CN vibration in the activated dynamics of LiNC \rightleftharpoons LiCN isomerization in an argon solvent at high temperatures,” *J. Chem. Phys.* **141**, 074312 (2014).
- [197] H. Párraga, F. J. Arranz, R. M. Benito, and F. Borondo, “Ab initio potential energy surface for the highly nonlinear dynamics of the KCN molecule,” *J. Chem. Phys.* **139**, 194304 (2013).
- [198] H. Párraga, F. J. Arranz, R. M. Benito, and F. Borondo, “Above saddle-point regions of order in a sea of chaos in the vibrational dynamics of KCN,” *J. Phys. Chem. A* **122**, 3433–3441 (2018).
- [199] J. D. Gezelter and W. H. Miller, “Resonant features in the energy dependence of the rate of ketene isomerization,” *J. Chem. Phys.* **103**, 7868–7876 (1995).
- [200] I. S. Ulusoy, J. F. Stanton, and R. Hernandez, “Effects of roaming trajectories on the transition state theory rates of a reduced-dimensional model of ketene isomerization,” *J. Phys. Chem. A* **117**, 7553–7560 (2013).

- [201] F. A. L. Mauguière, P. Collins, G. S. Ezra, S. C. Farantos, and S. Wiggins, “Roaming dynamics in ketene isomerization,” *Theor. Chem. Acc.* **133**, 1507 (2014).
- [202] I. S. Ulusoy and R. Hernandez, “Revisiting roaming trajectories in ketene isomerization at higher dimensionality,” *Theor. Chem. Acc.* **133**, 1528 (2014).
- [203] W. H. Miller, “Semiclassical treatment of multiple turning-point problems — phase shifts and eigenvalues,” *J. Chem. Phys.* **48**, 1651–1658 (1968).
- [204] W. H. Miller, “Periodic orbit description of tunneling in symmetric and asymmetric double-well potentials,” *J. Phys. Chem.* **83**, 960–963 (1979).
- [205] C. R. Doering and J. C. Gadoua, “Resonant activation over a fluctuating barrier,” *Phys. Rev. Lett.* **69**, 2318–2321 (1992).
- [206] J. Maddox, “Surmounting fluctuating barriers,” *Nature* **359**, 771–771 (1992).
- [207] J. Lehmann, P. Reimann, and P. Hänggi, “Surmounting oscillating barriers: Path-integral approach for weak noise,” *Phys. Rev. E* **62**, 6282–6303 (2000).
- [208] J. Lehmann, P. Reimann, and P. Hänggi, “Activated escape over oscillating barriers: The case of many dimensions,” *Phys. Status Solidi B* **237**, 53–71 (2003).
- [209] C. Van den Broeck, “Simple stochastic model for resonant activation,” *Phys. Rev. E* **47**, 4579–4580 (1993).
- [210] P. Hänggi, “Escape over fluctuating barriers driven by colored noise,” *Chem. Phys.* **180**, 157–166 (1994).
- [211] T. D. Shepherd and R. Hernandez, “Chemical reaction dynamics with stochastic potentials below the high-friction limit,” *J. Chem. Phys.* **115**, 2430–2438 (2001).
- [212] T. D. Shepherd and R. Hernandez, “Activated dynamics across aperiodic stochastic potentials,” *J. Phys. Chem. B* **106**, 8176–8181 (2002).
- [213] J. M. Moix, T. D. Shepherd, and R. Hernandez, “A phenomenological model for surface diffusion: Diffusive dynamics across incoherent stochastic aperiodic potentials,” *J. Phys. Chem. B* **108**, 19476–19482 (2004).
- [214] R. De Vogelaere and M. Boudart, “Contribution to the theory of fast reaction rates,” *J. Chem. Phys.* **23**, 1236–1244 (1955).

- [215] W. H. Miller, “Unified statistical model for ‘complex’ and ‘direct’ reaction mechanisms,” *J. Chem. Phys.* **65**, 2216–2223 (1976).
- [216] B. K. Carpenter, “Potential energy surfaces and reaction dynamics,” in *Reactive intermediate chemistry*, edited by R. A. Moss, M. S. Platz, and M. Jones Jr. (John Wiley & Sons, New York, NY, 2005) Chap. 21, pp. 925–960.
- [217] P. Pechukas, “Statistical approximations in collision theory,” in *Dynamics of molecular collisions: Part B*, edited by W. H. Miller, Modern Theoretical Chemistry 2 (Springer, Boston, MA, 1976) Chap. 6, pp. 269–322.
- [218] E. Pollak and P. Pechukas, “Unified statistical model for ‘complex’ and ‘direct’ reaction mechanisms: A test on the collinear H + H₂ exchange reaction,” *J. Chem. Phys.* **70**, 325–333 (1979).
- [219] J. Rehbein and B. K. Carpenter, “Do we fully understand what controls chemical selectivity?” *Phys. Chem. Chem. Phys.* **13**, 20906–20922 (2011).
- [220] P. Collins, B. K. Carpenter, G. S. Ezra, and S. Wiggins, “Nonstatistical dynamics on potentials exhibiting reaction path bifurcations and valley-ridge inflection points,” *J. Chem. Phys.* **139**, 154108 (2013).
- [221] G. S. Hammond, “A correlation of reaction rates,” *J. Am. Chem. Soc.* **77**, 334–338 (1955).
- [222] L. Steg and J. P. De Vries, “Earth-moon libration points: Theory, existence and applications,” *Space Sci. Rev.* **5**, 210–233 (1966).
- [223] C. D. Murray and S. F. Dermott, *Solar system dynamics* (Cambridge University Press, Cambridge, 2000), ISBN: 978-1-139-17481-7.
- [224] A. Wintner, *The analytical foundations of celestial mechanics*, Princeton Mathematical Series 5 (Princeton University Press, Princeton, NJ, 1941).
- [225] J. Cronin, P. B. Richards, and L. H. Russell, “Some periodic solutions of a four-body problem,” *Icarus* **3**, 423–428 (1964).
- [226] C. Simó, G. Gómez, À. Jorba, and J. Masdemont, “The bicircular model near the triangular libration points of the RTBP,” in *From Newton to chaos: Modern techniques for understanding and coping with chaos in n-body dynamical systems*, edited by A. E. Roy and B. A. Steves, NATO ASI Series 336 (Springer, Boston, MA, 1995), pp. 343–370.
- [227] W. S. Koon, M. W. Lo, J. E. Marsden, and S. D. Ross, “Low energy transfer to the moon,” *Celest. Mech. Dyn. Astron.* **81**, 63–73 (2001).

- [228] Q. Guo and H. Lei, “Families of Earth–Moon trajectories with applications to transfers towards Sun–Earth libration point orbits,” *Astrophys. Space Sci.* **364**, 43 (2019).
- [229] R. B. Negri and A. F. B. A. Prado, “Generalizing the bicircular restricted four-body problem,” *J. Guid. Control Dyn.* **43**, 1173–1179 (2020).
- [230] J. Barrow-Green, *Poincaré and the three body problem*, History of Mathematics 11 (American Mathematical Society, Providence, RI, 1997), ISBN: 978-0-8218-0367-7.
- [231] B. Fleck, “First results from SOHO,” *Astrophys. Space Sci.* **258**, 57–75 (1997).
- [232] M. Armano, H. Audley, G. Auger, J. T. Baird, M. Bassan, P. Binetruy, M. Born, D. Bortoluzzi, N. Brandt, M. Caleno, et al., “Sub-femto-g free fall for space-based gravitational wave observatories: LISA Pathfinder results,” *Phys. Rev. Lett.* **116**, 231101 (2016).
- [233] S. Kraft, K. G. Puschmann, and J. P. Luntama, “Remote sensing optical instrumentation for enhanced space weather monitoring from the L1 and L5 Lagrange points,” in *International conference on space optics—ICSO 2016*, edited by B. Cugny, N. Karafolas, and Z. Sodnik, 10562 (International Society for Optics and Photonics, 2017), pp. 115–123.
- [234] K. B. Bhatnagar and P. P. Hallan, “Effect of perturbations in Coriolis and centrifugal forces on the stability of libration points in the restricted problem,” *Celest. Mech.* **18**, 105–112 (1978).
- [235] L. Ricci, P. Cazzoletti, I. Czekala, S. M. Andrews, D. Wilner, L. Szűcs, G. Lodato, L. Testi, I. Pascucci, S. Mohanty, et al., “ALMA observations of the young substellar binary system 2M1207,” *Astron. J.* **154**, 24 (2017).
- [236] S. A. Astakhov, A. D. Burbanks, S. Wiggins, and D. Farrelly, “Chaos-assisted capture of irregular moons,” *Nature* **423**, 264–267 (2003).
- [237] W. S. Koon, M. W. Lo, J. E. Marsden, and S. D. Ross, “Heteroclinic connections between periodic orbits and resonance transitions in celestial mechanics,” *Chaos* **10**, 427–469 (2000).
- [238] K. C. Howell, “Families of orbits in the vicinity of the collinear libration points,” *J. Astronaut. Sci.* **49**, 107–125 (2001).
- [239] G. Gómez, M. Marcote, and J. M. Mondelo, “The invariant manifold structure of the spatial Hill’s problem,” *Dyn. Syst.* **20**, 115–147 (2005).

- [240] A. Teachey and D. M. Kipping, “Evidence for a large exomoon orbiting Kepler-1625b,” *Sci. Adv.* **4**, eaav1784 (2018).
- [241] K. Rodenbeck, R. Heller, M. Hippke, and L. Gizon, “Revisiting the exomoon candidate signal around Kepler-1625 b,” *Astron. Astrophys.* **617**, A49 (2018).
- [242] P. Von Ragué Schleyer, A. Sawaryn, A. E. Reed, and P. Hobza, “The remarkable structure of lithium cyanide/isocyanide,” *J. Comput. Chem.* **7**, 666–672 (1986).
- [243] P. E. S. Wormer and J. Tennyson, “Ab initio SCF calculations on the potential energy surface of potassium cyanide (KCN),” *J. Chem. Phys.* **75**, 1245–1252 (1981).
- [244] J. C. Slater, “A generalized self-consistent field method,” *Phys. Rev.* **91**, 528–530 (1953).
- [245] H. Ehrenreich and M. H. Cohen, “Self-consistent field approach to the many-electron problem,” *Phys. Rev.* **115**, 786–790 (1959).
- [246] F. Jensen, *Introduction to computational chemistry*, 3rd ed. (John Wiley & Sons, Chichester, West Sussex, 2017), ISBN: 978-1-118-82599-0.
- [247] M. Wang, G. Audi, F. G. Kondev, W. J. Huang, S. Naimi, and X. Xu, “The AME2016 atomic mass evaluation (II). Tables, graphs and references,” *Chin. Phys. C* **41**, 030003 (2017).
- [248] P. L. García-Müller, “PGH rates of the LiCN \rightarrow LiNC reaction,” private communication, 2021.
- [249] A. R. Leach, *Molecular modelling: Principles and applications*, 2nd ed. (Prentice Hall, Harlow, 2001), ISBN: 978-0-582-38210-7.
- [250] M. E. Tuckerman, *Statistical mechanics: Theory and molecular simulation* (Oxford University Press, Oxford, 2010), ISBN: 978-0-19-852526-4.
- [251] A. D. McNaught and A. Wilkinson, *Compendium of chemical terminology: IUPAC recommendations*, edited by V. Gold, 2nd ed. (Blackwell Science, Oxford, 1997), ISBN: 978-0-86542-684-9.
- [252] A. Savitzky and M. J. E. Golay, “Smoothing and differentiation of data by simplified least squares procedures,” *Anal. Chem.* **36**, 1627–1639 (1964).
- [253] T. L. Gilbert, “A phenomenological theory of damping in ferromagnetic materials,” *IEEE Trans. Magn.* **40**, 3443–3449 (2004).
- [254] C. Abert, “Micromagnetics and spintronics: Models and numerical methods,” *Eur. Phys. J. B* **92**, 120 (2019).

- [255] M.-C. Giornei, J. M. Rubí, and J.-E. Wegrowe, “Magnetization dynamics in the inertial regime: Nutation predicted at short time scales,” *Phys. Rev. B* **83**, 020410(R) (2011).
- [256] M. Fähnle, D. Steiauf, and C. Illg, “Generalized Gilbert equation including inertial damping: Derivation from an extended breathing Fermi surface model,” *Phys. Rev. B* **84**, 172403 (2011).
- [257] H. Haken, “Synergetics: An overview,” *Rep. Prog. Phys.* **52**, 515–553 (1989).
- [258] J. Tennyson, “LiCN/LiNC potential surface procedure,” private communication via F. Borondo, 1989.
- [259] Python Software Foundation, *Python*, version 3, <https://www.python.org/>.
- [260] J. Reiff, *LiNC \rightleftharpoons LiCN isomerization potential surface*, GitHub, 2021-06-04, <https://github.com/joreiff/licn-potential>.
- [261] C. R. Harris, K. J. Millman, S. J. van der Walt, R. Gommers, P. Virtanen, D. Cournapeau, E. Wieser, J. Taylor, S. Berg, N. J. Smith, et al., “Array programming with NumPy,” *Nature* **585**, 357–362 (2020).
- [262] J. D. Hunter, “Matplotlib: A 2D graphics environment,” *Comput. Sci. Eng.* **9**, 90–95 (2007).
- [263] NVIDIA, *CUDA toolkit*, <https://developer.nvidia.com/cuda-toolkit>.
- [264] ISO/IEC JTC 1/SC 22, *Programming languages—C++*, ISO/IEC 14882:2020 (International Organization for Standardization, Geneva, 2020-12), <https://www.iso.org/standard/79358.html>.
- [265] J. Reiff, *RODEO*, GitHub, 2022-12-13, <https://github.com/joreiff/rodeo>.
- [266] J. Reiff, *mfptlib*, GitHub, 2022-12-12, <https://github.com/joreiff/mfptlib>.

ZUSAMMENFASSUNG IN DEUTSCHER SPRACHE

Ein zentrales Ziel der Reaktionskinetik ist die akkurate Bestimmung chemischer Reaktionsraten. Hierbei handelt es sich nicht nur um eine abstrakte Fragestellung aus der Grundlagenforschung [17–20], sondern auch um ein Problem mit praktischer Relevanz für reale Reaktionsprozesse [21–25]. Die Optimierung von Raten durch äußeres Treiben bietet ein großes Potenzial für zukünftige technische Anwendungen.

Um diesem Ziel ein Stück näherzukommen, beschäftigt sich die vorliegende Arbeit mit verschiedenen Aspekten des Ratenbegriffs im Kontext der Theorie des Übergangszustands (engl. *transition-state theory*, TST) [19, 20, 26–47]. Wir nehmen dafür ein System an, in dem ein Rang-1-Sattel einen Reaktant- von einem Produktzustand trennt. Der Fokus liegt auf der Entwicklung und Anwendung von Methoden auf unterschiedliche physikalische wie chemische Systeme.

Insbesondere beschäftigen wir uns mit der geometrischen Formulierung der TST [66–71], mit deren Hilfe beispielsweise die Stabilität von Trajektorien auf dem Sattel bestimmt werden kann. Die zugehörige Metrik bezeichnen wir als *Zerfallsrate* [2, 4, 6]. Diese Rate kann in der Raumfahrt genutzt werden, um die Orbits von Satelliten nahe der Lagrange-Punkte L_1 bis L_3 im Hinblick auf den Treibstoffverbrauch zu optimieren [6, 60]. Zerfallsraten erlauben darüber hinaus, die Struktur der instabilen Dynamik auf dem Sattel aufzuzeigen [3, 5, 108]. Diese Struktur kann wiederum im begrenzten Maße mit der Dynamik zwischen Reaktant- und Produktbassin korreliert werden [5].

Zerfallsraten können prinzipiell auch für chemische Systeme berechnet werden [87, 116]. Allerdings sind die Ergebnisse hier deutlich schwerer zu interpretieren und experimentell zu validieren. Stattdessen untersuchen wir in diesem Kontext *absolute Reaktionsraten*, speziell die Isomerisierungsrate von Lithiumcyanid [117]. Diese Reaktion wurde bereits zuvor von verschiedenen Gruppen untersucht, wobei jedoch teils widersprüchliche Ergebnisse erzielt wurden [7, 116, 118–120]. Hier greifen wir die Berechnungen aus Referenzen [7, 116] wieder auf. Die neuen Ergebnisse passen deutlich besser zu den Referenzwerten aus Referenzen [7, 118, 119], selbst bei Temperaturen, bei denen die thermische Energie die Barrierenhöhe übersteigt. In diesem Regime stellt sich jedoch generell die Frage, wie genau die Reaktionsrate de-

finiert wird. Die Antwort kann einen signifikanten Einfluss auf das Ergebnis haben, was es erschwert, mittels verschiedener Methoden bestimmte Raten miteinander zu vergleichen.

Teil I: Theorie & Methoden

Die TST [19, 20, 26–47] hat sich bewährt, um Aspekte der Reaktionskinetik in Systemen mit Rang-1-Sattel zu beschreiben. Die Berechnung von Reaktionsraten in solchen Systemen basiert dabei auf der Unterscheidung von zwei unterschiedlichen Zuständen – Reaktant und Produkt – auf einer Potentialfläche [121], die durch eine Trennfläche (engl. *dividing surface*, DS) nahe dem Sattel separiert werden. Der normierte Fluss durch diese Fläche [124] gibt die Rate wieder. Methoden der TST können vielseitig eingesetzt werden, beispielsweise in der Atomphysik [48], in der Festkörperphysik [10, 11, 49], zur Beschreibung von Cluster-Bildung [53, 54] und Diffusion [55, 56], im Kontext von Kosmologie [57] und Himmelsmechanik [6, 58–60] sowie bei Bose-Einstein-Kondensaten [61–65]. Die Beschreibung zeitlich getriebener Systeme ist dabei erheblich anspruchsvoller, da die DS hier ebenfalls zeitabhängig wird [30, 31, 34]. Dennoch kann die DS auch hier mittels verschiedener Methoden [1, 87–92] bestimmt werden.

Kapitel 2: Theorie des Übergangszustands

Die Methode, die wir in dieser Arbeit einsetzen wollen, basiert dabei auf der geometrischen Formulierung der TST [40]. Diese Variante nutzt Konzepte aus der Theorie dynamischer Systeme, um formal exakte DSs zu konstruieren, die höchstens einmal von jeder Trajektorie gekreuzt werden. Diese Eigenschaft ist wichtig, um Reaktionsraten nicht zu überschätzen.

Betrachten wir zunächst das System aus Abbildung 2-1(a). Gezeigt ist die Umgebung eines typischen Rang-1-Sattels in einem System mit einem Freiheitsgrad (engl. *degree of freedom*, DoF). Reaktanten (R) sind dabei von Produkten (P) durch den auf der DS lokalisierten Übergangszustand (engl. *transition state*, TS) [19, 26, 35, 43] getrennt. Die meisten Trajektorien eines solchen Systems lassen sich in eine von vier Klassen einteilen, nämlich nichtreaktive Reaktanten und Produkte unterhalb [Bereiche 1 und 2 in Abbildung 2-1(b)] sowie vor- und rückreaktive Trajektorien oberhalb der Aktivierungsenergie [Bereiche 3 und 4 in Abbildung 2-1(b)]. Im Phasenraum werden diese vier Bereiche durch die sogenannten *stabilen und instabilen Mannigfaltigkeiten* \mathcal{W}_s und \mathcal{W}_u getrennt. Hierbei handelt es sich um kritische Trajektorien, die sich für $t \rightarrow +\infty$ respektive $t \rightarrow -\infty$ dem Sattelpunkt

annähern, ohne diesen jemals zu erreichen. Sie gehören zu einem hyperbolischen Fixpunkt, der *normal-hyperbolisch invarianten Mannigfaltigkeit* (engl. *normally hyperbolic invariant manifold*, NHIM) [66–70, 130]. Alle formal exakten DSs müssen an diesem Fixpunkt verankert werden [128, 131, 133], andernfalls sind Mehrfachkreuzungen von Trajektorien [73, 78, 125, 126] unausweichlich [siehe graue DS in Abbildung 2-1(b)].

In statischen Systemen beschreibt die NHIM die Trajektorie eines Teilchens, das exakt auf dem Sattelpunkt bzw. der Spitze der Barriere ruht und bei der kleinsten Störung herunterfallen würde. Analoge Betrachtungen können auch für zeitlich getriebene Systeme angestellt werden, wobei sich die nun ebenfalls zeitabhängige NHIM im Allgemeinen jedoch vom Sattelpunkt löst. Dennoch behält sie ihre Funktion in der Konstruktion von DSs bei.

Das hier gezeichnete Bild lässt sich problemlos auf Systeme mit d DoFs erweitern. Die instabile Richtung des Sattels wird dann als Reaktionskoordinate x bezeichnet, während die anderen (stabilen) Richtungen unter dem Begriff der orthogonalen Moden y zusammengefasst werden. Eine DS im $2d$ -dimensionalen Phasenraum ist hier $(2d - 1)$ -dimensional, hat also Kodimension 1. Die NHIM ist entsprechend $(2d - 2)$ -dimensional mit Kodimension 2. Mit gut gewählten Koordinaten zeigt jeder Schnitt $x-p_x$ bei fixierten orthogonalen Moden y und Impulsen p_y die in Abbildung 2-1(b) gezeigte Struktur.

Die geometrische Formulierung der TST eignet sich hervorragend, um die Dynamik eines Systems auf dem Sattel zu beschreiben. Eine klassische Berechnung des Flusses durch die zugehörige DS führt dabei auf das Konzept von *Zerfallsraten* [6, 8, 87, 103], die ein Maß für die Instabilität von Trajektorien darstellen. Diese müssen unterschieden werden von *absoluten Reaktionsraten* [109–111, 146], bei denen zusätzlich berücksichtigt wird, dass Trajektorien zunächst einmal überhaupt den Sattel erklimmen müssen, bevor sie die DS kreuzen können. Zudem beruhen Letztere in der Regel auf der Kopplung des Systems mit einem thermischen Bad. In dieser Arbeit beschäftigen wir uns mit Zerfallsraten in Kapitel 4 bis 6 und mit absoluten Reaktionsraten in Kapitel 7.

Ein wichtiger Schritt in der Bestimmung absoluter Reaktionsraten gelang Kramers im Jahr 1940 [111], als er seine Überlegungen zur *Fluchtrate* über einen Sattel veröffentlichte. In dieser wegweisenden Arbeit leitete er analytische Ausdrücke für die absolute Reaktionsrate her, wobei sich diese jedoch auf die Grenzfälle kleiner und großer Reibung beschränkten. Bei mittlerer Reibung sagte Kramers ein Maximum in der Rate vorher, ohne es jedoch quantifizieren zu können. Diese Lücke wurde später von *Pollak, Grabert und Hänggi* (PGH) [146] geschlossen, die Kramers' Theorie zudem auf die *generalisierte Langevin-Gleichung* (engl. *generalized Langevin equa-*

tion, GLE) verallgemeinerten (siehe unten). Letztlich stellt aber auch die PGH-Rate nur eine Näherung dar, da sie unter anderem die Reaktion auf einen eindimensionalen Prozess reduziert [27].

Allgemeingültiger lassen sich Raten durch Ensemblesimulationen basierend auf Langevin- [134–138] oder atomistischer Molekulardynamik (engl. *all-atom molecular dynamics*, AAMD) [154–157] berechnen. Hierfür wird analog zu Kramers' Grundidee ein konstanter Fluss an Reaktanten in das System eingeleitet und der sich einstellende Fluss durch eine DS gemessen. Sobald eine Trajektorie die DS erreicht und damit zum Produkt wird, wird diese aus der Simulation entfernt (*absorbierende Randbedingungen* [158]). Das Verhältnis aus Fluss und Reaktanten-Gleichgewichtspopulation bildet die Rate.

Um auf diese Weise akkurat Raten berechnen zu können, ist eine DS vonnöten, die möglichst wenige Mehrfachkreuzungen aufweist. So würde beispielsweise eine Trajektorie, die direkt nach dem Kreuzen der DS vom thermischen Bad zurückgeworfen wird, die Rate verfälschen. Die geometrische Formulierung könnte prinzipiell genutzt werden, um eine ideale DS für dieses Szenario zu berechnen [9, 94]. Dies wäre jedoch numerisch extrem aufwendig, da die resultierende DS auch von der exakten Dynamik des Bads abhängig wäre. In der Praxis werden daher einfachere Näherungen angewendet [129, 158, 159, 161].

Die Wahl der DS ist insbesondere bei hohen Temperaturen ausschlaggebend. Hierbei muss auch die physikalische oder chemische Fragestellung berücksichtigt werden, die beantwortet werden soll. So kann es je nach Situation sinnvoll sein, eine Reaktion nur als solche zu werten, wenn die Trajektorie nach dem Überqueren des Sattels auch im Produktbassin eingefangen wird und nicht unmittelbar wieder zurück reagiert [149, 160]. Abschnitt 7-4 (b) zeigt anhand der Isomerisierung von Lithiumcyanid, dass eine solche Bedingung einen enormen Effekt auf die beobachtete Reaktionsrate haben kann.

Die Berechnung absoluter Reaktionsraten setzt typischerweise den Kontakt zu einem thermischen Bad voraus, was Effekte wie Rauschen und Reibung zur Folge haben kann. Im Rahmen dieser Arbeit modellieren wir derartige Effekte mithilfe der GLE

$$\begin{aligned}
 (2-3a) \quad & \dot{\mathbf{q}}(t) = \mathbf{M}^{-1} \mathbf{p}(t) \\
 (2-3b) \quad & \text{und } \dot{\mathbf{p}}(t) = \mathbf{F}(\mathbf{q}(t), \mathbf{p}(t), t) - \int_{t_0}^t dt' \Gamma(t-t') \mathbf{p}(t') + \boldsymbol{\zeta}(t),
 \end{aligned}$$

wobei \mathbf{M} die Massenmatrix, Γ den Reibungs-Kernel und $\boldsymbol{\zeta}$ ein zufälliges Rauschen darstellen. Reibung und Rauschen hängen dabei über das Fluktuations-

Dissipations-Theorem [134, 136]

$$\langle \zeta_j(t) \zeta_k(t') \rangle = k_B T M_{jk} \Gamma(t - t') \quad (2-4)$$

zusammen. Im Folgenden beschränken wir uns auf den Kernel [139, 140]

$$\Gamma(s) = \frac{1}{\alpha} \exp\left(-\frac{s}{\alpha\gamma}\right) \quad (2-7)$$

mit Reibungskoeffizient γ und Badparameter α . Dieser lässt ein exponentiell abklingendes Gedächtnis mit charakteristischer Zeitskala $\tau = \alpha\gamma$ zu. Im Limes $\alpha \rightarrow 0$ ergibt sich die gedächtnislose **Langevin-Gleichung** (engl. *Langevin equation*, LE) mit weißem Rauschen und Reibungs-Kernel

$$\Gamma(s) = 2\gamma \delta(s). \quad (2-5)$$

Kapitel 3: Numerische Methoden

Um die in Kapitel 2 vorgestellten Strukturen numerisch aufzulösen, müssen Trajektorien propagiert werden. Hierfür greifen wir in Kapitel 4 und 5 auf das *Velocity-Verlet*-Verfahren [164] zurück und bedienen uns ins in Kapitel 6 dem *Runge-Kutta*-Algorithmus in vierter Ordnung [167, 168].

Aufbauend hierauf lässt sich beispielsweise der *Lagrange-Deskriptor* [89, 90, 100, 106, 169, 171]

$$\mathcal{L}(\mathbf{q}_0, \mathbf{v}_0, t_0) = \int_{t_0-\tau}^{t_0+\tau} dt \|\mathbf{v}(t; \mathbf{q}_0, \mathbf{v}_0, t_0)\|_2 \quad (3-8)$$

definieren. Die hier gezeigte klassische Variante misst die Bogenlänge einer Trajektorie im Zeitintervall $t_0 - \tau \leq t \leq t_0 + \tau$. Weitere Varianten sind möglich [90], werden in dieser Arbeit jedoch nicht thematisiert. Die stabilen und instabilen Mannigfaltigkeiten zeigen sich in dieser Metrik als lokale Minima, wie in Abbildung 3-2(a) zu erkennen ist. Der Lagrange-Deskriptor lässt sich sehr universell einsetzen; eine genaue numerische Auswertung der Strukturen in \mathcal{L} ist im Allgemeinen jedoch relativ schwierig.

Sehr viel einfacher fällt dies über das Konzept der *reaktiven (und nichtreaktiven) Bereiche* [1, 87, 92]. Hierbei wird der Ortsraum zunächst in einen Reaktant-, einen Produkt- und einen Zwischenbereich eingeteilt. Trajektorien im Zwischenbereich werden daraufhin so lang vorwärts und rückwärts in der Zeit propagiert, bis sie im Reaktant- oder Produktbereich landen. Abhängig davon, aus welchem Bereich sie kamen und in welchem sie enden, können die Anfangsbedingungen $(\mathbf{q}_0, \mathbf{v}_0, t_0)$ im Phasenraum einer von

vier Klassen zugeordnet werden (siehe Abbildung 3-2(b)). Dies entspricht wiederum exakt der in Abschnitt 2-1 vorgestellten Klassifizierung.

Diese Klassifizierung lässt sich nun verwenden, um mittels einer einfachen Bisektion [172] die stabilen und instabilen Mannigfaltigkeiten aufzulösen. Verknüpft man vier solcher Bisektionsverfahren, so erhält man die in Abbildung 3-3 gezeigte **binäre Kontraktionsmethode** (engl. *binary-contraction method, BCM*) [92], mit deren Hilfe die genaue Position der **NHIM** bestimmt werden kann.

Obwohl die **NHIM** ein mathematisch invarianter Unterraum ist, entfernen sich Trajektorien in der Praxis exponentiell schnell aufgrund numerischer Ungenauigkeiten. Die **BCM** kann dazu verwendet werden, um Trajektorien numerisch zu stabilisieren, indem diese regelmäßig zurück auf die **NHIM** projiziert werden. Dies ermöglicht die Untersuchung der Dynamik auf der **NHIM**, was ein Schwerpunkt der Kapitel 4 und 6 ist. Zur Visualisierung dieser Dynamik eignet sich dabei insbesondere die stroboskopische Abbildung — ein Spezialfall eines **Poincaré-Schnitts** (engl. *Poincaré surface of section, PSOS*) [66].

Die Stabilität von Trajektorien auf der **NHIM** lässt sich schließlich mithilfe von Zerfallsraten quantifizieren. Zur Berechnung dieser haben sich vor allem drei Methoden bewährt [2, 4–6, 8–11, 87, 103]:

1. Die **Ensemble-Ratenmethode** [2, 176] berechnet instantane (d. h. zeit aufgelöste) Raten, indem eine große Anzahl von Teilchen nahe der **NHIM** propagiert wird. Das Ensemble wird dabei wie in Abbildung 3-5 gezeigt initialisiert, um Konsistenz mit der Floquet-Rate zu gewährleisten. Aus dem zeitlichen Verlauf der Reaktantenpopulation N ergibt sich schließlich die Rate zu

$$(3-12) \quad k_e(\mathbf{y}, \mathbf{p}_y, t; t_0) = -\frac{d}{dt} \ln[N(\mathbf{y}, \mathbf{p}_y, t; t_0)].$$

Dieses Verfahren hat den Vorteil, dass es konzeptionell recht einfach ist und nur wenige Annahmen über die Dynamik enthält. Dafür ist es jedoch sehr rechenintensiv und weist tendenziell höhere numerische Ungenauigkeiten auf als die folgenden Methoden.

2. Die **lokale Mannigfaltigkeiten-Analyse** (engl. *local manifold analysis, LMA*) [2, 6] nutzt die linearisierte Dynamik in der Nähe der **NHIM** aus, um die Ensemble-Ratenmethode zu beschleunigen und numerische Fehler zu reduzieren. Anstatt Ensembles zu propagieren, müssen hier lediglich die Steigungen der stabilen und instabilen Mannigfaltigkeiten p_x^s/x^s und p_x^u/x^u berechnet werden. Aus der Differenz ergibt sich

sodann die Rate

$$k_m(t; \mathbf{y}^\ddagger) = J_{x, p_x}(t) \frac{p_x^u(t) - p_x^s(t)}{x^u(t)} - \frac{x^{\text{DS}}(t + \delta t)}{x^u(t) \delta t}, \quad (3-13)$$

wobei der letzte Term eine mögliche lokale Kopplung von Reaktionskoordinate und orthogonalen Moden – beispielsweise durch die Coriolis-Kraft –berücksichtigt.

3. Gemittelte Raten von periodischen Trajektorien lassen sich noch effizienter auch mittels Floquet-Theorie berechnen [88, 103]. Hierzu müssen lediglich die größten und kleinsten Eigenwerte der Monodromiematrix bestimmt werden. Die Differenz der zugehörigen Floquet-Exponenten

$$k_F = \mu^u - \mu^s \quad (3-24)$$

entspricht der Zerfallsrate der Trajektorie. Diese Betrachtung lässt sich mittels linearer Regression auch auf quasiperiodische Trajektorien ausweiten [2, 174].

Bei den in Teil II untersuchten Systemen liefern alle drei Methoden übereinstimmende Ergebnisse. Dies bestätigt, dass die unterschiedlichen Annahmen, die für die verschiedenen Methoden gemacht wurden, hier gerechtfertigt sind.

In Kapitel 7 untersuchen wir die Reaktionsrate einer chemischen Reaktion. Hierfür wird das System nicht mehr nur in Isolation betrachtet, sondern zusätzlich die Interaktion mit einem thermischen Bad modelliert (siehe Abschnitt 2-2). Für die Lösung der resultierenden stochastische Bewegungsgleichung greifen wir auf das *LF-Middle*-Verfahren zurück. Aufbauend hierauf lassen sich nun Raten berechnen.

Neben Ratengleichungen, die auf dem Fluss durch eine DS basieren, gibt es noch weitere Ansätze. So zeigten Reimann, Schmid und Hänggi [182] beispielsweise, dass äquivalente Raten ebenfalls via *mittleren Erstdurchgangszeiten* (engl. *mean first-passage time*, MFPT) [180–186] berechnet werden können. Hierzu werden Bedingungen definiert, wann eine Reaktion abgeschlossen ist, und die Zeiten Δt_j für jede Trajektorie j gemessen, bis diese Bedingungen zum ersten Mal erfüllt sind. Die Rate ergibt sich daraus zu

$$k_{\text{MFPT}} = \frac{1}{\langle \Delta t_j \rangle_j} = \left(\frac{1}{N} \sum_{j=1}^N \Delta t_j \right)^{-1}. \quad (3-31)$$

Teil II: Anwendungen & Ausblick

Im zweiten Teil präsentieren wir nun ausgesuchte Beispiele von Anwendungen in prototypischen und von der echten Welt inspirierten Systemen.

Kapitel 4: Bifurkationen in einem zweidimensionalen Modellsystem

Wir beginnen mit einem einfachen, getriebenen Modellsystem mit zwei nichtlinear gekoppelten DoFs [1–3, 5, 87, 91, 108, 174]

$$(4-1) \quad V(x, y, t) = 2 \exp\left\{-[x - \hat{x} \sin(\omega_x t)]^2\right\} + 2\left[y - \frac{2}{\pi} \arctan(2x)\right]^2,$$

wobei \hat{x} und ω_x die Amplitude und Frequenz des externen Treibens darstellen. Dieses Treiben lässt die Position des Rang-1-Sattels wie in Abbildung 4-1 dargestellt oszillieren, was zu einer reichhaltigen Dynamik in dessen Nähe führt.

Abbildung 4-2 demonstriert, welchen Einfluss eine Änderung der Frequenz ω_x auf die NHIM haben kann. Während bei $\omega_x = \pi$ nur ein elliptischer Fixpunkt im PSOS zu erkennen ist, weist derselbe Ausschnitt bei $\omega_x = 0.75 \pi$ zusätzlich je einen elliptischen und einen hyperbolischen Fixpunkt auf. Derartige Paare können, wie Abbildung 4-3 demonstriert, aus Sattel-Knoten-Bifurkation [3, 5, 78, 108, 188–190] heraus erzeugt oder vernichtet werden. Sie haben einen signifikanten Einfluss auf die Stabilität von Trajektorien innerhalb der NHIM und sind daher von großem Interesse in der Theorie dynamischer Systeme.

Um den Einfluss solcher Bifurkationen weiter zu verdeutlichen, können wir den PSOS zusätzlich mit verschiedenen Eigenschaften der Trajektorien auf der NHIM hinterlegen. Dies wurde in Abbildung 4-6 für die durchschnittliche Energie $\langle E[\mathbf{y}^\ddagger] \rangle_t$ sowie die Floquet-Zerfallsrate k_F nahe der Bifurkation umgesetzt. Deutlich zu erkennen spiegeln $\langle E[\mathbf{y}^\ddagger] \rangle_t$ und k_F die Struktur des PSOS wider. Zusätzlich lassen sich jedoch auch Plateaus nahe der elliptischen Fixpunkte identifizieren, die auf eine einheitliche Dynamik schließen lassen. Diese sind mitunter scharf von ihrer Umgebung getrennt, was für eine schlagartige Änderung der Dynamik spricht. Wenn ein solches Plateau im Zuge einer Bifurkation entsteht oder verschwindet, so kann dies einen Sprung in der Stabilität des Systems hervorrufen, wie Abbildung 4-8(a) zeigt. Dieses Wissen kann genutzt werden, um Systeme hinsichtlich verschiedener Eigenschaften zu steuern und zu optimieren.

Die bisherige Betrachtung spielte sich ausschließlich auf der NHIM ab. Für chemische Prozesse ist es jedoch entscheidend, dass die gewonnenen Erkenntnisse auch auf Trajektorien abseits der NHIM übertragen werden

können. Hierzu starten wir Trajektorien mit einem Versatz $\Delta p_x = +10^{-5}$ zur **NHIM** und propagieren diese rückwärts in der Zeit, bis sie im (offenen) Reaktantbassin ankommen. Die dort gemessene Anfangsenergie gibt Aufschluss darüber, wie viel Energie notwendig ist, um den Sattel zu einer bestimmten Zeit und an einem bestimmten Ort zu überqueren.

Das Ergebnis ist in **Abbildung 4-9** für verschiedene Frequenzen des externen Treibens dargestellt. Es zeigt sich eine deutliche Korrelation mit der Struktur der **NHIM**, hier repräsentiert durch den **PSOS**. Insbesondere befindet sich die Position mit minimaler zugehöriger Anfangsenergie meist in unmittelbarer Umgebung zum stabilsten elliptischen Fixpunkt, wie ein Vergleich mit **Abbildung 4-6** zeigt. Der Übergang unmittelbar nach der Bifurkation verläuft jedoch kontinuierlich und nicht sprunghaft. Mit zunehmender Entfernung von der **NHIM** verstärkt sich dieser Effekt – die Strukturen verwaschen.

Basierend auf dieser Betrachtung ist es sogar möglich, in eingeschränktem Maße Reaktionswahrscheinlichkeiten vorherzusagen. Hierzu wird ein Ensemble mit Maxwell-Boltzmann-verteilter Anfangsgeschwindigkeit im Reaktantbassin initialisiert und der Anteil an Trajektorien χ_r^e gemessen, der die Barriere überwindet. Ein ähnlicher Wert lässt sich aus dem globalen (räumlichen und zeitlichen) Minimum der Anfangsenergie abschätzen. Dieser Schätzwert stimmt, insbesondere bei Variation der Frequenz des Treibens, erstaunlich gut mit dem simulierten Ergebnis überein (siehe **Abbildungen 4-10** und **4-11**).

Kapitel 5: Selbstähnlichkeit in einem getriebenen Zweisattelsystem

Kapitel 4 beschäftigte sich mit nur einem Sattel. In vielen komplexen Reaktionen [21–25] müssen jedoch mehrere Hindernisse entlang des Reaktionspfads überwunden werden. Die Interaktion zwischen diesen Barrieren [4, 77, 173, 214–216] kann dabei bereits in den einfachsten Systemen eine hochgradig komplexe Dynamik zur Folge haben. Insbesondere wollen wir uns in diesem Kapitel mit der Frage beschäftigen, ob – und wenn ja, wie – in solchen Mehrsattelsystemen eine global exakte **DS** definiert werden kann.

Diese Fragestellung untersuchen wir anhand des eindimensionalen Potentials [4, 173]

$$V(x, t) = B_0(t) e^{-(x+1)^2} + B_\pi(t) e^{-(x-1)^2} \quad (5-1a)$$

$$\text{mit } B_\varphi(t) = \frac{7}{4} + \frac{1}{4} \sin(\omega t + \varphi), \quad (5-1b)$$

wobei zwei Gauß-Barrieren mit Frequenz ω gegenphasig getrieben werden. Im statischen Fall ergibt sich eine sehr einfache Phasenraumstruktur [siehe Abbildung 5-1(b)]. Beide Sättel weisen lokal die bekannte Kreuzstruktur auf. Letzten Endes entscheidet aber stets die höchste Barriere über die Reaktivität einer Trajektorie; die zugehörige lokale *DS* wird hier gleichzeitig zur globalen *DS*. Die (diskrete) *NHIM* des Gesamtsystems setzt sich dabei aus den Sattelpunkten der Einzelsättel zusammen. Ähnlich sieht der Fall $\omega \rightarrow \infty$ aus, da hier effektiv wieder ein statisches Potential wirkt.

Erheblich komplexer ist die Situation, wenn mit einer endlichen Frequenz getrieben wird. Abbildung 5-2 zeigt dazu die mittels Lagrange-Deskriptor aufgedeckte Phasenraumstruktur bei $\omega = \pi$. Um die Position der Sättel bei $x \approx \pm 1$ sind zwar immer noch kreuzartige Strukturen zu erkennen, welche wir im Folgenden allgemein als *geometrische Kreuze* bezeichnen wollen. Diese weisen jedoch eine detaillierte, fraktale Substruktur auf, was die Bestimmung der *NHIM* schwierig macht. Hierbei hilft es auch nicht, dass die *NHIM* nun aus unendlich vielen, aber immer noch diskreten, Punkten besteht.

Bemerkenswert ist dennoch, dass das geometrische Kreuz des momentan höheren Sattels dünner ausgeprägt ist. Um den Effekt zu verstärken, verlangsamen wir das Treiben auf $\omega = \pi/10$. Abbildung 5-3 zeigt die zeitabhängige Phasenraumstruktur, nun wieder über die reaktiven Bereiche. Hier sticht erneut der momentan höhere Sattel mit seiner klaren Struktur hervor. Dieses *primäre geometrische Kreuz* bewegt sich zwischen den Sätteln, ohne mit anderen Strukturen in Kontakt zu kommen. Zu diesem Kreuz gehört eine *TS*-Trajektorie, die mit genau der Periode des Treibens zwischen den Sätteln schwingt (siehe Abbildung 5-4). Eine an dieser *TS*-Trajektorie verankerte *DS* führt im Vergleich zu erheblich weniger Mehrfachkreuzungen, wie Abbildung 5-5 zeigt. Ganz ausschließen lassen sich solche Mehrfachkreuzungen bei planaren *DSs* jedoch nie, was erneut an der fraktalen Struktur des Phasenraums liegt (siehe Abbildung 5-6).

Berechnet man die Zerfallsrate für die primäre *TS*-Trajektorie, so fällt abschließend ein interessantes Detail auf. Gemäß Abbildung 5-7 weist die Rate immer dann dramatische Einbrüche auf, wenn sich die Trajektorie gerade vom einen zum anderen Sattel bewegt. Wie in Abschnitt 3-5 (b) diskutiert wird, hängt dies eng mit der schmalen Form des Kreuzes zu diesen Zeitpunkten zusammen, was in Abbildung 5-6(b) gut zu sehen ist.

Kapitel 6: Einfluss des Mondes auf die Stabilität nahe des Sonne-Erde-Lagrangepunkts L_2

Eine konkretere Interpretation der Zerfallsrate ist möglich, wenn wir uns der Himmelsmechanik zuwenden [6, 60]. Betrachten wir dazu die Bewegung

eines Satelliten in einem Sonnensystem, das neben dem Stern auch noch aus einem Planeten mit einem Mond besteht. Um in einem solchen System einen Rang-1-Sattel identifizieren zu können, auf den sich die [TST](#) anwenden lässt, müssen einige Approximationen gemacht werden. Zum einen wird die Masse des Satelliten vernachlässigt, sodass dessen Bewegung keinen Einfluss auf die drei Primärkörper hat. Zum anderen werden die Primärkörper in einer Hierarchie von zirkularen Zweikörperproblemen angeordnet, sodass Mond und Planet ihren gemeinsamen Schwerpunkt umkreisen. Dieses *Baryzentrum* wiederum bewegt sich zusammen mit dem Stern auf einer Umlaufbahn um den Gesamtschwerpunkt des Systems. In einem passenden synodischen Koordinatensystem sind Stern und Baryzentrum fix, während sich Planet und Mond auf Kreisbahnen bewegen. Ein solches Modell, dargestellt in [Abbildung 6-1](#), ist in der Literatur als [bizirkulares eingeschränktes Vierkörperproblem](#) (engl. *bicircular restricted four-body problem*, [BCR4BP](#)) [[225–228](#)] bekannt.

In einem klassischen Zweikörperproblem sind fünf Punkte bekannt, an denen sich in synodischen Koordinaten alle Kräfte aufheben. Diese sogenannten Librationspunkte L_1 bis L_5 [[222](#), [223](#), [231–233](#)], auch Lagrange-Punkte genannt, werden im [BCR4BP](#) durch den Mond gestört, sodass Kräfte hier nicht mehr verschwinden. Dennoch lassen sich auch mit Mond weiterhin Satelliten in der Nähe parken, was sich mithilfe des effektiven Potentials nachvollziehen lässt. Dieses weist dank der Zentrifugalbarriere eine Sattelform nahe der kollinearen Librationspunkte L_1 bis L_3 auf (siehe [Abbildung 6-2](#)). Folglich existiert eine zugehörige [NHIM](#) [[226](#)], die sämtliche Orbits enthält, die sich dauerhaft nahe dem Sattel aufhalten. Die [NHIM](#) wird durch die Bewegung des Mondes zwar beeinflusst, aber nicht zerstört.

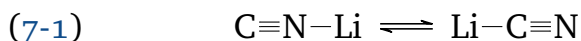
Hier konzentrieren wir uns auf den Sonne-Erde- L_2 -Punkt, da dieser von großer Relevanz für die Astrophysik ist [[112–115](#)]. Wir parametrisieren das Modell mit zwei unterschiedlichen Parametersätzen, einerseits basierend auf unserer Sonne, der Erde und ihrem Mond, und andererseits mit extremeren Testparametern, die aber gerade noch realistisch erscheinen [[235](#)]. Genaue Werte für die einzelnen Parameter finden sich in [Tabelle 6-1](#). Bei der resultierenden Struktur der [NHIM](#) – zu sehen in [Abbildung 6-4](#) – zeigen sich große Ähnlichkeiten zu [Kapitel 4](#), insbesondere [Abbildung 4-2\(a\)](#). Die vom [PSOS](#) aufgedeckten Tori gehören zu größtenteils quasiperiodischen Bahnen nahe dem L_2 . Der Fixpunkt selbst gehört wiederum zu einer periodischen Bahn, die wir als L_2 -Orbit bezeichnen wollen, da sie den L_2 -Punkt in diesem generalisierten Kontext ersetzt; im Grenzfall ohne Mond geht der L_2 -Orbit in den L_2 -Punkt über.

Dass Zerfallsraten die Stabilität einer Bahn angeben, lässt sich im Kontext der Himmelsmechanik schließlich ganz praktisch interpretieren. Künstliche

oder natürliche Satelliten können in der Praxis niemals exakt auf der **NHIM** platziert werden und driften daher exponentiell schnell ab. Sonden, die nahe L_2 platziert werden sollen, müssen daher regelmäßig Kurskorrekturen vornehmen. Die Zerfallsrate des Orbits gibt Aufschluss über die Stärke der Drift und stellt damit letztlich auch ein Maß für den Treibstoffverbrauch eines Satelliten dar. Durch Optimierung des Orbits können in einer echten Mission Treibstoff gespart und dadurch Kosten gesenkt und Missionsdauern verlängert werden.

Kapitel 7: Kramers-Raten der Isomerisierung von Lithiumcyanid

Nach diesem Ausflug in die Astrophysik wenden wir uns erneut der Chemie – genauer gesagt der Isomerisierungsrate von Lithiumcyanid – zu. Die Reaktion



in einem Argon-Bad [118, 119, 196] war bereits mehrfach Gegenstand theoretischer Untersuchungen [7, 118–120, 196]. Hierbei zeigten sich größere Abweichungen zwischen verschiedenen Methoden, deren Ursprung nicht endgültig geklärt werden konnte. In diesem Kapitel legen wir dar, warum die in Referenz [7] veröffentlichten **MFPT**-Raten problematisch sind, und präsentieren neue Ergebnisse, die besser mit denen anderer Methoden [118, 119, 196] übereinstimmen.

Das Modell, das dafür zum Einsatz kommt [117, 243], ist in Abbildung 7-1 zu sehen. Da die Dreifachbindung des Cyanids sehr starr ist, reicht es aus, die Konfiguration über den Abstand R und den Winkel ϑ des Lithium-Atoms relativ zum Cyanid zu beschreiben. Die LiCN- und LiNC-Konfigurationen bei $\vartheta = 0$ und $\vartheta = \pi$ zeigen sich als lokale Minima im zugehörigen Potential (siehe Abbildung 7-2), wobei LiNC den stabileren Zustand darstellt.

Abbildung 7-3 fasst die Ergebnisse zusammen, die zuvor mit diesem Modell erzielt wurden. Insbesondere konzentrieren wir uns hier auf die **PGH**-Raten aus Referenzen [7, 119, 248] sowie die **MFPT**-Raten aus Referenz [7]. Zum Vergleich dienen Raten aus **AAMD**-Simulationen, die ebenfalls Referenz [119] entstammen.

Im Vergleich wird deutlich, dass sich die Verläufe der Raten k als Funktion der Reibung γ in ihrer Form sehr ähneln. Die Skalierung, erkennbar an der Höhe der Maxima, weicht jedoch teilweise stark ab. So mussten die **MFPT**-Raten durch einen Faktor 5 geteilt werden, um einigermaßen mit der **PGH**-Rate übereinzustimmen. Der Verlauf in Abhängigkeit der Temperatur T zeigt ähnliche Abweichungen. Bei genauerem Hinsehen fällt auf, dass sich

die MFPT-Raten zwar mit einer modifizierten Arrhenius-Gleichung [251]

$$k(T) = AT^n \exp\left(-\frac{E^\ddagger}{k_B T}\right) \quad (7-6)$$

beschreiben lassen, jedoch nur, wenn eine Aktivierungsenergie von $E_{\text{fit}}^\ddagger/k_B \approx 619.5\text{K}$ angenommen wird. Dieser Wert steht im deutlichen Widerspruch zur eigentlichen Barrierenhöhe von $E^\ddagger/k_B = 1689.3\text{K}$ und lässt ein tiefergehendes Problem mit der Implementierung vermuten.

Um dem nachzugehen, wurden sämtliche MFPT-Berechnungen nochmals mit einem komplett neuen Simulationsprogramm wiederholt. Wie Abbildung 7-6(a) zeigt, stimmen die neuen Ergebnisse bei niedrigen Temperaturen sehr gut mit der PGH-Rate überein, auch ohne Reskalierung um einen Faktor 5. Die Erweiterung auf die GLE-Dynamik mit Gedächtnis liefert ähnlich vielversprechende Resultate [siehe Abbildung 7-6(b)]. Bei hohen Temperaturen kommt es jedoch immer noch zu Abweichungen, wie in Abbildung 7-8(a) zu erkennen ist, auch wenn diese bereits erheblich niedriger ausfallen. Interessanterweise stimmen die PGH-Raten selbst in diesem Regime mit $k_B T > E^\ddagger$ noch relativ gut mit den AAMD-Raten überein, obwohl die PGH-Theorie – wie für TST-Methoden üblich – eigentlich $k_B T \ll E^\ddagger$ voraussetzt.

Solch hohe Temperaturen werfen jedoch auch die Frage nach der genauen Definition der Rate auf. Verlangen wir beispielsweise, dass Trajektorien im Produktbassin gefangen werden müssen, bevor wir sie als reagiert werten, so hat dies einen erheblichen Einfluss auf unsere MFPT-Raten [siehe Abbildung 7-8(b)]. Einerseits führt dies dazu, dass die Raten sinken, da ballistische Trajektorien erheblich länger propagiert werden. Andererseits sind jetzt auch erhebliche Abweichungen zwischen LE- und GLE-basierten Raten erkennbar, da das Gedächtnis des Bads ballistische Trajektorien begünstigt. Ob eine solche Modifikation sinnvoll ist, hängt davon ab, welche physikalische Frage beantwortet werden soll, und könnte Gegenstand zukünftiger Forschung sein.

Kapitel 8: Zusammenfassung und Ausblick

Kernthema dieser Arbeit war die Dynamik von Trajektorien auf einem sowie über einen Rang-1-Sattel einer Potentialfläche. Die Dynamik auf dem Sattel führt dabei auf das Konzept der NHIM, worüber sich eine DS definieren lässt. Betrachtet man den normierten Fluss durch diese DS, so erhält man Zerfallsraten, die die Stabilität von Trajektorien nahe der NHIM beschreiben. Dieselbe Grundidee, den normierten Fluss durch die DS zu betrachten, führt

jedoch auf absolute Reaktionsraten, wenn die komplette Dynamik zwischen Reaktant- und Produktbassin betrachtet wird. In letzterem Fall wird dabei für gewöhnlich die Kopplung an ein thermisches Bad berücksichtigt.

Mit Zerfallsraten kann unter anderem die Struktur der **NHIM** aufgedeckt werden. Diese Struktur kann zu einem gewissen Grad mit der Dynamik zwischen Reaktant- und Produktbassin korreliert werden. Es gibt jedoch noch keinerlei Ansätze, mit denen die Zerfallsrate selbst in die Berechnung von absoluten Reaktionsraten einbezogen werden könnte; ob dies möglich ist, ist derzeit offen. Zukünftige Forschung sollte diese Verbindung dennoch nicht vernachlässigen, da hierdurch interessante Details zu Reaktionspfaden aufgezeigt werden könnten. Um für chemische Systeme relevant zu sein, müssen die Ergebnisse jedoch verallgemeinert werden, um thermische Effekte zu berücksichtigen.

Wie Kapitel 6 am Beispiel der Astrophysik zeigt, lassen sich Methoden wie die Zerfallsrate aktuell viel direkter außerhalb der Chemie nutzen. Auch die Anwendung in der Spintronik wurde bereits demonstriert [10, 11, 50–52]. Es könnte sich daher lohnen, verstärkt nach weiteren derartigen Systemen Ausschau zu halten. Um die verschiedenen Disziplinen wirklich weiterbringen zu können, reicht es jedoch nicht aus, **TST**-Methoden blind auf andere Systeme anzuwenden. Stattdessen sollte mit Wissenschaftlern der jeweiligen Fachrichtungen kollaboriert werden, um das volle Potenzial einer solchen Forschung zu entfalten.

Die erneute Untersuchung der absoluten Reaktionsrate von $\text{LiCN} \rightarrow \text{LiNC}$ konnte offene Fragen aus früheren Publikationen [7, 116, 120] teilweise beantworten. Durch die Betrachtung von Reaktionsraten bei hohen Temperaturen wurden Fragen nach der genauen Definition der Rate aufgeworfen. Um in einer zukünftigen Arbeit einen fairen Vergleich der Raten zu ermöglichen, muss sichergestellt werden, dass äquivalente Definitionen für die **DS** verwendet werden. Welche der möglichen Definitionen dabei am sinnvollsten ist, hängt von der physikalischen beziehungsweise chemischen Fragestellung ab, die untersucht wird.

DANKSAGUNG

Zahlreiche Personen haben auf die ein oder andere Weise zum Gelingen dieser Dissertation beigetragen. Ihnen möchte ich im Folgenden meinen tiefsten Dank aussprechen:

- Zunächst wäre hier natürlich mein Doktorvater Prof. Dr. Jörg Main zu nennen. Er begleitet mich an der Universität Stuttgart nun schon seit meiner Bachelorarbeit 2016 und hatte in dieser Zeit immer ein offenes Ohr für Fragen und Probleme aller Art. Diskussionen blieben dabei stets konstruktiv und auf Augenhöhe, wodurch man sich bereits als Student wertgeschätzt und als Teil eines Teams gefühlt hat. Zudem ermöglichte er mir mehrere USA-Aufenthalte im Rahmen des TraX-Projekts. Ich musste zwar erst überzeugt werden, möchte die Erfahrungen im Nachhinein jedoch nicht mehr missen. Lieber Jörg, durch dein Engagement hast du diese Arbeit in vielerlei Hinsicht erst möglich gemacht. Du hast mir die nötige Führung und Hilfestellung, aber auch genügend Freiraum gegeben, um meine Promotion erfolgreich zu absolvieren. Hierfür bin ich dir zu tiefstem Dank verpflichtet!
- Anschließend möchte ich sogleich mit meinem Dank für Prof. Dr. Udo Seifert, der den Mitbericht für diese Dissertation übernommen hat.
- Im Hinblick auf meine Verteidigung darf natürlich auch Prof. Dr. Ronny Nawrodt nicht fehlen. Er übernahm nicht nur den Prüfungsvorsitz, sondern ermöglichte mir auch, meiner Faszination für die Astronomie in der Sternwarte der Universität Stuttgart nachzugehen. Lieber Ronny, ich hoffe, du schaffst es noch lange Zeit, den Praktikumsversuch zur Astrophysik zu erhalten. Er ist wirklich eine Bereicherung für das Physikstudium in Stuttgart!
- Ich habe den Weg eines Doktoranden in der [TST](#) glücklicherweise nicht vollkommen alleine bestreiten müssen. Stattdessen wurde ich zumindest auf der ersten Hälfte von Matthias Feldmaier und Robin Bardakcioglu begleitet. Dies hat mir meinen Einstieg enorm erleichtert. Lieber Matthias, lieber Robin, vielen Dank für die intensive und produktive Zusammenarbeit, bei der aber auch der Spaß und die Freude nie zu kurz kamen. Ich habe die Zeit mit euch sehr geschätzt und hoffe, auch weiterhin den Kontakt halten zu können!
- Neben den oben genannten Personen war meine Zeit am ITP1 in großen Teilen geprägt durch die Arbeit mit den unterschiedlichsten

Studenten, von denen ich über die Jahre hinweg einige betreuen durfte. Mitunter haben sich aus dieser Betreuung sehr gute Freundschaften entwickelt; zu erwähnen wären hier vor allem Jonas Zatsch, Johannes Mögerle und Manuel Kuchelmeister, die wie selbstverständlich anboten, die vorliegende Dissertation Korrektur zu lesen. Forschungsergebnisse von fünf Studenten – neben Jonas, Johannes und Manuel auch Michael Maihöfer und Micha Schlee – konnten letztlich in Fachzeitschriften publiziert werden, was gerade bei Bachelorarbeiten alles andere als selbstverständlich ist. Ich danke euch allen daher herzlich für die gute und erfolgreiche Zusammenarbeit, auch wenn ihr mir manchmal den ein oder anderen Nerv gekostet habt!

- All the publications mentioned above were authored together with our collaborator and friend Prof. Rigoberto Hernandez as part of the TraX project. This entailed countless hours of scientific discussions, debates about the wording of our manuscripts, and always a new idea for just one more thing. He also was so kind to host us in Baltimore numerous times throughout this project. And when the COVID-19 pandemic struck, we continued seamlessly via video conferences. Dear Rigoberto, together with Amy and Gobi, you always made us feel right at home whenever we were in Baltimore. I am deeply grateful for the productive time on campus, and also very much enjoyed the fun times off campus. You are a busy man, but you always tried to devote as much time as possible to us whenever we had the chance to visit you. I am much obliged to you. Dear Amy, thank you for inviting us into your home so many times – your dinner was always delicious! And Gobi, I wish you the best of luck for your studies. I really hope to see all of you back at some point.
- Im Zuge unserer Besuche bei Prof. Hernandez konnte ich auch Dr. Thomas Bartsch näher kennenlernen. Lieber Thomas, vielen Dank für all die hilfreichen Diskussionen zur [TST](#) und die Ausflüge nach getaner Arbeit! Es war eine schöne Zeit mit dir und den anderen TraX-Kollegen in Baltimore.
- Speaking about TraX, we did not just collaborate with Thomas and Rigoberto but also with our Spanish colleagues Dr. Pablo García-Müller, Prof. Rosa Benito, and Prof. Florentino Borondo. Dear Pablo, Rosa, and Tino, thank you for working with us on the LiCN system! Your expertise was always welcome!
- Ein großer Dank geht auch an meinen guten Freund Daniel Dizdarevic. Sein kritischer Blick für Design und Typografie war mir eine große Hilfe bei der Erstellung dieser Dissertation. Lieber Daniel, auch wenn

ich deine Meinung nicht immer teile, so hat sie mir doch stetes geholfen, mein Design zu entwickeln und zu verbessern. Ohne dich hätte ich das \LaTeX -Monster nicht so leicht bezwungen!

- Seit ein paar Jahren werde ich nun auch von Finn Schmolke begleitet. Er ist nicht nur ein sehr angenehmer und hilfreicher Zimmerkollege, sondern auch ein wirklich guter Freund. Letzteres gilt ebenso für Chris Bühler, Clara Roth, Raphael Ehmann und Hanna Schellenberger. Alle fünf hatten sich angeboten, auf Fehlersuche in der vorliegenden Arbeit zu gehen. Vielen Dank für die hilfreichen Kommentare!
- Mein Dank gilt darüber hinaus auch allen weiteren aktiven wie ehemaligen Mitgliedern des ITP₁, die mich auf dieser Reise begleitet haben. Hierbei möchte ich insbesondere unsere Sekretärin Monika Bund hervorheben. Liebe Frau Bund, haben Sie vielen Dank für den Einsatz, den Sie tagtäglich für das Institut im Allgemeinen und mich im Speziellen zeigen! Ihr Engagement geht teilweise weit über die Aufgaben einer Sekretärin hinaus!
- Neben dem ITP₁ verbrachte ich auch immer wieder Zeit in der Didaktik-Abteilung des PI₅. Egal ob mittags gemeinsam Kochen oder Filmabend mit Pizza – die Didaktik war für mich wie ein zweites Zuhause an der Universität. Danke dafür!
- Nicht zuletzt möchte ich natürlich auch noch einen ganz besonderen Dank an meine Familie aussprechen, die mich von Anfang an in meinem Vorhaben bestärkte und ohne deren langjährige Unterstützung diese Arbeit niemals möglich gewesen wäre. Ich bin euch auf ewig verbunden!

Neben all den Einzelpersonen, die zum Gelingen dieser Arbeit beigetragen haben, möchte ich an dieser Stelle auch noch zwei Organisationen danken, ohne die meine Promotion in dieser Form nicht möglich gewesen wäre:

- Hierzu zählt zum einen die *Deutsche Forschungsgemeinschaft* (DFG), die primär meine Stelle am ITP₁ finanzierte.
- Zum anderen ermöglichte das *TraX*-Projekt im Rahmen des *Horizon 2020 Research and Innovation Program* der Europäischen Union (Marie Skłodowska-Curie Action) den Austausch und die Kollaboration mit einer Vielzahl internationaler Wissenschaftler, die mitunter auch bereits oben erwähnt wurden.

CURRICULUM VITAE

Wissenschaftlicher Werdegang von Johannes Reiff aus Berlin.

Studium und Promotion

- 2013-09 **Bachelor of Science in Physik**
bis 2016-08 *Universität Stuttgart*
- 2016-04 **Bachelorarbeit**
bis 2016-08 *Universität Stuttgart, Institut für Theoretische Physik I*
„Beschreibung \mathcal{PT} -symmetrischer Bose-Einstein-Kondensate mit einem Vier-Mulden-Potential und der Bogoliubov-Backreaction-Methode“
- 2016-10 **Master of Science in Physik**
bis 2018-10 *Universität Stuttgart*
- 2017-10 **Masterarbeit**
bis 2018-10 *Universität Stuttgart, Institut für Theoretische Physik I*
„Dynamik und Trennflächen für getriebene Systeme mit zwei zeitabhängigen Sattelpunkten“
- 2018-11 **Doktor der Naturwissenschaften**
bis 2023-04 *Universität Stuttgart, Institut für Theoretische Physik I*
„Advances in Transition-State Theory and Applications to Driven Systems“

Wissenschaftliche Tätigkeit

- 2018-11 **Wissenschaftlicher Mitarbeiter**
bis 2023-04 *Universität Stuttgart, Institut für Theoretische Physik I*
- 2018-11 **Early-Stage Researcher**
bis 2022-10 *EU-Rahmenprogramm für Forschung und Innovation Horizont 2020, TraX-Projekt*
Internationale Kollaboration inklusive fünf mehrwöchiger USA-Aufenthalte an der Johns Hopkins University in Baltimore.

Präsentationen

- 2018-03 **Posterpräsentation**
DPG-Frühjahrstagung 2018, Berlin
„Dynamics and phase space structure for reactions with multiple saddles“
- 2022-04 **Eingeladener Vortrag**
Prof. Rigoberto Hernandez, Johns Hopkins University, Baltimore
„Transition state theory and its applications to driven systems“
- 2022-05 **Eingeladener Vortrag**
TraX International Workshop 2022, Barcelona
„Transition state theory in driven systems: celestial mechanics“
- 2022-07 **Posterpräsentationen**
American Conference on Theoretical Chemistry 2022, Olympic Valley, CA
„Transition state theory in driven systems: Methods“
„Transition state theory in driven systems: Applications“

Publikationen

- [1] D. Dizdarevic, J. Main, K. Alpin, **J. Reiff**, D. Dast, H. Cartarius und G. Wunner, „Realization of balanced gain and loss in a time-dependent four-mode Bose–Hubbard model“, *Phys. Rev. A* **97**, 013623 (2018).
- [2] M. Feldmaier, P. Schraft, R. Bardakcioglu, **J. Reiff**, M. Lober, M. Tschöpe, A. Junginger, J. Main, T. Bartsch und R. Hernandez, „Invariant manifolds and rate constants in driven chemical reactions“, *J. Phys. Chem. B* **123**, 2070–2086 (2019).
- [3] M. Feldmaier, R. Bardakcioglu, **J. Reiff**, J. Main und R. Hernandez, „Phase-space resolved rates in driven multidimensional chemical reactions“, *J. Chem. Phys.* **151**, 244108 (2019).
- [4] M. Feldmaier, **J. Reiff**, R. M. Benito, F. Borondo, J. Main und R. Hernandez, „Influence of external driving on decays in the geometry of the LiCN isomerization“, *J. Chem. Phys.* **153**, 084115 (2020).
- [5] M. Kuchelmeister, **J. Reiff**, J. Main und R. Hernandez, „Dynamics and bifurcations on the normally hyperbolic invariant manifold of a periodically driven system with rank-1 saddle“, *Regul. Chaotic Dyn.* **25**, 496–507 (2020).

- [6] R. Bardakcioglu, **J. Reiff**, M. Feldmaier, J. Main und R. Hernandez, „Thermal decay rates of an activated complex in a driven model chemical reaction“, *Phys. Rev. E* **102**, 062204 (2020).
- [7] **J. Reiff**, M. Feldmaier, J. Main und R. Hernandez, „Dynamics and decay rates of a time-dependent two-saddle system“, *Phys. Rev. E* **103**, 022121 (2021).
- [8] **J. Reiff**, R. Bardakcioglu, M. Feldmaier, J. Main und R. Hernandez, „Controlling reaction dynamics in chemical model systems through external driving“, *Physica D* **427**, 133013 (2021).
- [9] **J. Reiff**, J. Zatsch, J. Main und R. Hernandez, „On the stability of satellites at unstable libration points of sun–planet–moon systems“, *Commun. Nonlinear Sci. Numer. Simul.* **104**, 106053 (2022).
- [10] M. M. Schlee, **J. Reiff**, P. L. García-Müller, R. M. Benito, F. Borondo, J. Main und R. Hernandez, „Mean first-passage times for solvated LiCN isomerization at intermediate to high temperatures“, *J. Chem. Phys.* **156**, 034103 (2022).
- [11] J. Mögerle, R. Schuldt, **J. Reiff**, J. Main und R. Hernandez, „Transition state dynamics of a driven magnetic free layer“, *Commun. Nonlinear Sci. Numer. Simul.* **105**, 106054 (2022).
- [12] M. Maihöfer, **J. Reiff**, J. Main und R. Hernandez, „Transition state theory characterizes thin film macrospin dynamics driven by an oscillatory magnetic field: inertial effects“, *Commun. Nonlinear Sci. Numer. Simul.* **115**, 106764 (2022).

Ehrenwörtliche Erklärung

Ich erkläre, dass ich diese Dissertation – abgesehen von den ausdrücklich bezeichneten Hilfsmitteln – selbständig verfasst habe.

Stuttgart, den 2. Februar 2023

Johannes Reiff